4-25-2014 12:00 AM

Steam Gasification of Biomass Surrogates: Catalyst Development and Kinetic Modelling

A S M Jahirul Islam Mazumder
The University of Western Ontario

Supervisor
Dr. Hugo de Lasa
The University of Western Ontario

Graduate Program in Chemical and Biochemical Engineering
A thesis submitted in partial fulfillment of the requirements for the degree in Doctor of Philosophy
© A S M Jahirul Islam Mazumder 2014

STEAM GASIFICATION OF BIOMASS SURROGATES: CATALYST DEVELOPMENT AND KINETIC MODELLING

(Thesis format: Monograph)

by

A S M Jahirul Islam Mazumder

Graduate Program in Engineering Science

Department of Chemical and Biochemical Engineering

A thesis submitted in partial fulfillment
of the requirements for the degree of
Doctor of Philosophy

The School of Graduate and Postdoctoral Studies
The University of Western Ontario
London, Ontario, Canada

ABSTRACT

The gradual depletion of fossil fuel and the increased concerns about climate change are stimulating a renewed interest in the efficient utilization of biomass as an energy source. In recent years, biomass steam gasification has become an area of growing interest because it produces a synthesis gas with relatively higher hydrogen content. However, the formation of tars still offers a technical challenge in the commercialization of this technology. The catalytic reforming of biomass tars into gaseous products is an efficient method for tar removal avoiding costly downstream processing. An effective catalyst for biomass gasification should be stable and highly active to produce high quality and tar free synthesis gas at temperatures below 700 °C eliminating the concern of ash agglomeration.

In this regard, this study reports a new fluidizable La_2O_3 promoted Ni/γ-Al_2O_3 catalyst. Catalysts are prepared using a specially designed incipient wetness technique: a multi-step impregnation with direct reduction of metal precursors after each impregnation in fluidized bed conditions. Modified supports and catalysts are characterized using BET specific surface area, XRD, TPR, TPO, H_2-pulse chemisorptions, Pyridine FTIR, NH_3-TPD and CO_2-TPD. Catalytic steam gasification of biomass surrogates (glucose and 2-methoxy-4-methylphenol representing the biomass cellulose and lignin content, respectively) are performed in a CREC Riser Simulator under the expected conditions of a twin circulating fluidized bed gasifier. Experiments are performed at different steam/biomass ratios, temperatures and reaction times.

Characterization results showed that the addition of La_2O_3 up to 5 wt% improves surface area, CO_2 adsorption capacity, Ni reducibility and dispersion, as well as reduces support acidity. As the lanthanum content increased from 5 to 10 wt%, a diminution in dry gas yield and an increase in coking were observed. The formation of undesirable $LaAlO_3$ on the Ni catalyst containing 10 wt% La_2O_3, as found by XRD, was responsible for its poor gasification performance. TPR results showed that excess La_2O_3 content causes: i) the suppression of some of the active nickel and ii) favors agglomeration of surface Ni crystallites which are susceptible to coking.

Using XRD, $La_2O_3 \geq 10$ wt% and temperature above 1000 °C are established as the pre-conditions for $LaAlO_3$ formation. This result points toward the increase of local catalysts bed temperatures during the exothermic reduction of metal nitrates. A higher gas flow rate during the catalyst reduction step minimizes thermal sintering/dehydroxylation of meta-stable γ-Al_2O_3 as well as improves Ni dispersion by effectively removing the heat generated. The relative proportion of octahedral and tetrahedral sites in γ-Al_2O_3 is found to be the indicator of the extent of dehydroxylation. The estimation of this important parameter is confirmed using both H_2 TPR and NH_3-TPD.

Gasification performance of a catalyst is found to be well-correlated as a function of its Ni dispersion and basicity/acidity ratio. It is hypothesized that acid sites of γ-Al_2O_3 are responsible for coke deposition via hydrocarbon cracking, whereas basic sites facilitated coke reforming. A 20% Ni/5% La_2O_3-γAl_2O_3 catalyst is developed, in this study, optimizing catalyst formulation and preparation conditions. This catalyst yields a 98.26% carbon conversion of glucose to permanent gases with no tar formation and negligible coke deposition at 700 °C. In the case of 2-methoxy-4-methylphenol gasification, a 89.75% carbon conversion with tar formation reduced to only 5.7% is achieved using this catalyst. A high-quality synthesis gas (H_2/CO>2) is also attained, which makes it suitable for direct alcohol synthesis.

Changes in the gasification product composition with the variation of operating parameters are found to be in agreement with the thermodynamic model predictions. Moreover, product composition approaches chemical equilibrium as the reaction time is increased indicating that the overall steam gasification process is kinetically controlled. Therefore, a mechanistic based kinetic model is proposed, in order to describe the experimental observations. Statistically significant intrinsic kinetic parameters are estimated, and validated using an independent set of experimental results.

Dedicated to my parents

ACKNOWLEDGMENTS

TABLE OF CONTENTS

LIST OF TABLES

LIST OF FIGURES

CHAPTER 1

INTRODUCTION

1.1 **Background**

Biomass refers to organic materials derived from all living matters. Biomass from plants was the first fuel used by humans to meet their energy demands. In the 19th century, the discovery of fossil fuels helped to industrialize the world and improve the standard of living. Nowadays, the gradual depletion of accessible fossil fuel and increased concerns about climate change are stimulating a renewed interest in the efficient utilization of biomass as an energy source [1–4]. To gradually replace the depleting fossil fuels, biomass is considered as the primary renewable resource given its abundance, its CO_2 neutral emissions and its lower sulfur content. Using biomass as an energy source, zero net emissions of carbon dioxide can be achieved with the released carbon dioxide being recycled back into plants via photosynthesis [4–9].

Different biomass conversion processes are utilized to produce heat and electricity, as well as various chemicals. The biochemical route offers a potential avenue for biomass conversion in small-scale. These processes are relatively slow and selective to the use of specific feedstocks. In contrast, the thermochemical route offers faster conversion and can be applied to a diversity of biomass feedstocks. Biomass gasification is considered as one of the most promising thermochemical processes because of its greater energy efficiency and proven operational history [4,8–13]. Gasification can efficiently and economically convert the low value and highly distributed solid biomass into synthesis gas.

Gasification technology, primarily wood gasifiers, was used to power cars in the early 1920s due to the scarcity of petroleum resources in Sweden. Extensive studies were undertaken during the 1939–1945 period to further refine the design of the wood

gasifiers, gas cleaning, cooling systems and gas turbines to optimize their performance on wood waste [14].

Air, oxygen and steam are usually used as gasifying agents. In recent years, biomass steam gasification has become an area of growing interest because it produces a synthesis gas with relatively higher heating value and higher hydrogen content [1,2,4–6,9,15,16]. Steam gasification of biomass in fluidized beds is a promising approach given its: (i) rapid biomass heating, (ii) effective heat and mass transfer between reacting phases, (iii) uniform gasifier reaction temperature [5,6,10,17]. Moreover, fluidized beds tolerate wide variations in fuel quality as well as broad particle-size distributions.

$$C_n H_{2m} + tars + H_2O \longrightarrow CO + H_2$$

$$CH_4 + H_2O \longleftrightarrow CO + 3H_2 \qquad \Delta H^0 = 205.81 \ kJ/mol$$

$$CH_4 + CO_2 \longleftrightarrow 2CO + 2H_2 \qquad \Delta H^0 = 246.98 \ kJ/mol$$

$$CO + H_2O \longleftrightarrow H_2 + CO_2 \qquad \Delta H^0 = -41.16 \ kJ/mol$$

$$C + H_2O \longleftrightarrow H_2 + CO \qquad \Delta H^0 = 131.29 \ kJ/mol$$

$$C + CO_2 \longleftrightarrow 2CO \qquad \Delta H^0 = 172.46 \ kJ/mol$$

$$C + 2H_2 \longleftrightarrow CH_4 \qquad \Delta H^0 = -74.52 \ kJ/mol$$

$$C_x H_y O_z \xrightarrow{heat} H_2 + CO + CO_2 + H_2O + C_n H_{2m} + C_{(s)} + tars$$
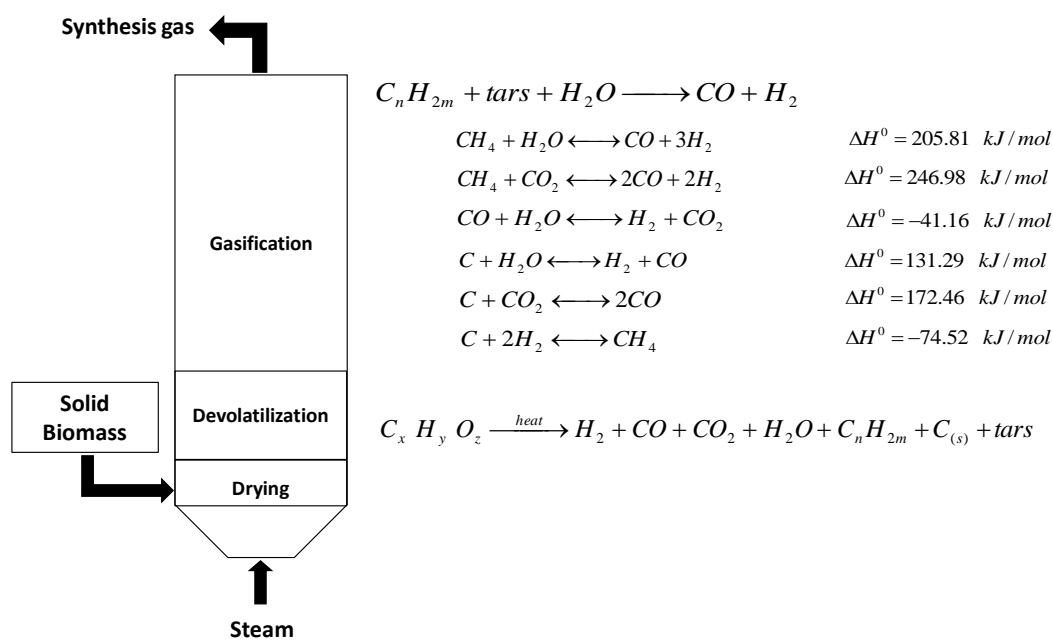
Figure 1.1: Schematic representation of biomass steam gasification process.

Steam gasification of biomass involves a complex network of heterogeneous reactions. The gasification process can be classified into three steps: drying, devolatilization and gasification (Figure 1.1). One can envision biomass gasification as a combination of primary and secondary reactions [2,17–19]. *Primary* reactions break down the vaporized biomass molecules, forming permanent gases, higher hydrocarbons, tars and coke. *Secondary* reactions crack or/and reform the higher hydrocarbons and tars into lighter

hydrocarbons and permanent gases (CO, CO_2, H_2). Furthermore, light hydrocarbons, CO and H_2 can react with steam and CO_2 altering the gas composition depending on gasifier operating conditions.

However, in the implementation of biomass gasification to produce high quality syngas/or hydrogen, the formation of tars still offers a technical challenge [19–22]. Tar formation creates numerous problems in gasifier operation, while conversion of tar adds value to the syngas by increasing the yields of H_2 and/or CO [23–25]. Tar can be converted thermally. However, this typically requires a very high temperature (greater than 1000 °C) which is not economically viable. Furthermore, this also increases the risk of ash agglomeration. Therefore, the catalytic reforming of biomass tars into gaseous products inside the gasifier appears as an effective and efficient method for tar removal, avoiding costly downstream processing for tar disposal [9,20,25].

An effective catalyst for biomass gasification should be stable and highly active, producing high quality and tar free synthesis gas. Dolomite, olivine, zeolites, alkali and noble metals, and Ni-based catalysts have been used for this purpose [1,9,19,25]. The Ni catalyst is one of the most promising catalysts for biomass gasification due to its high reforming activity and affordability [26–30]. Deactivation may be an issue, however, with nickel-based catalysts [25,29–31]. Under the high operating gasification temperatures required to achieve significant feedstock conversions, deactivation of Ni-based catalysts may occur due to coke deposition and crystallite agglomeration. Thus, new catalysts for biomass steam gasification should have the long life required in preventing tar formation, carbon fouling and crystallite agglomeration under the operating conditions of a gasifier[1]. To accomplish this, the use of promoters plays a very important role in minimizing tar formation and in enhancing the stability of Ni-based catalysts [29–32].

Fluidizable γ-Al_2O_3 is one of the most promising supports for a Ni-based catalyst due to its high surface area and mechanical strength. However, γ-Al_2O_3 is not stable at high temperatures due to thermal sintering and phase transformation. Rare earth oxides have been investigated as a γ-Al_2O_3 stabilizer [33–37]. La_2O_3 is a reported inhibitor for γ-

alumina surface area losses. Moreover, La_2O_3 has been used as a promoter of Ni/Al_2O_3 catalysts for steam gasification of biomass and its surrogate species [29,30,32,38–41]. When small amounts of La_2O_3 were added, they dispersed well on γ-Al_2O_3. These lanthanum species enhanced catalytic activity, acting as a Ni dispersion promoter [37,42–51]. There is, however, a limit for lanthanum loading. Excess lanthanum may lead to the formation of undesirable $LaAlO_3$ above 1000 °C [34,43,44,49,52,53]. Moreover, the controlled amount of basic La_2O_3 reduces the acidity and enhances CO_2 adsorption capacity of γ-Al_2O_3 resulting in lower coke formation on the catalyst surface [30,39,46,54–57].

Furthermore, the catalyst preparation method plays a crucial role in influencing structural properties, metal-support interaction, reducibility and dispersion of active phase [58–60]. Conventionally, impregnated metal salts are decomposed to oxides by high temperature calcination in air followed by metal oxide reduction under hydrogen. Surface area, dispersion, and reducibility of nickel can be improved significantly however, by direct decomposition of nickel salts to nickel in a reducing atmosphere without prior calcinations in air [58].

The development of an efficient catalytic steam gasification process also requires insights into gasification kinetics and reaction mechanisms in order to predict the end-reaction products. To date, different types of models have been developed on biomass gasification (mostly on air gasification). Thermodynamic equilibrium models [4,61–67] provide valuable tools to predict the maximum achievable yield of hydrogen or syngas. Underestimation of tars is the main limitation of an equilibrium model. Moreover, most of the reported thermodynamic studies are on air gasification of biomass. There is scarcity in comprehensive equilibrium models for biomass steam gasification. Salaices et al [18] developed a thermodynamic model for biomass steam gasification at atmospheric pressure. However, changes in reactor pressure after biomass conversion were not considered in their model. In the present study, thermodynamic analysis of biomass steam gasification is conducted considering the equilibrium reactor pressure to establish a rigorous comparison with experimental results.

Although these equilibrium models are useful in evaluating the influence of various operating parameters, in most cases, the observed synthesis gas compositions deviate from chemical equilibrium predictions. It is well acknowledged that in an actual process, various gasification reactions cannot reach chemical equilibrium. Therefore, a mechanistic based kinetic model is essential to predict the performance of a steam gasification process. Salaices [68] studied both the thermodynamic and the kinetics of biomass steam gasification using a Ni/α-alumina catalyst.

1.2 Scope of this Study

The present study focuses on the development of a new and improved fludizable biomass steam gasification catalyst to produce high quality synthesis gas reducing tar formation. Process temperature of below 700 °C is proposed considering the energy efficiency, ash agglomeration and catalyst stability issues. A twin circulating fluidized bed gasifier configuration, which is the most proven and viable technology option for large scale biomass processing, is considered in this study. This configuration allows catalytic gasification to take place in one fluidized beds while char combustion and catalyst regeneration take place in the other unit. The concept is successfully implemented using a CREC Riser Simulator [69].

Biomass surrogate species are used in this study instead of real biomass. Glucose is used as the representative of cellulose content in biomass whereas gasification of biomass lignin content/produced tars is studied using 2-methoxy-4-methylphenol. This allows the simulation of the main components of biomass in a controlled manner. The presence of traces amount of sulphur, nitrogen, and other impurities in biomass also remained out of the scope of this study.

A fluidizable high surface area La_2O_3 promoted $Ni/\gamma-Al_2O_3$ is developed in this study. La_2O_3 is selected as a support modifier/promoter, to improve the thermal stability and acid-base properties of $\gamma-Al_2O_3$, as well as to enhance Ni dispersion. A specially designed incipient wetness technique is used for catalyst preparation. This catalyst preparation method involves a multi-step impregnation with direct reduction of metal precursors after

each impregnation in fluidized bed conditions. The effects of catalyst preparation method, formulation and reduction condition are systematically investigated using various well-established characterization techniques. The structure-property and structure-reactivity relationships of the prepared catalysts are established using characterization and gasification results. The best performing catalyst displays encouraging performance in terms of conversion, yield and synthesis gas quality. This catalyst as well remains stable under repeated cycles of gasification and regeneration which are the expected operating conditions of a twin circulating fluidized bed gasifier system. In addition, the performance of this catalyst ranks favorably when compared with equilibrium predictions of a thermodynamic steam gasification model developed in this study.

The newly developed catalyst is also employed to study the effect of various operating parameters. Finally, a phenomenologically based kinetic model is developed considering the significant reactions involved. The statistically significant model parameters are estimated using the experimental glucose gasification results with the variation of temperature. The developed model is also validated using the experimental results obtained with the variation of steam/biomass ratio.

1.3 Thesis Structure

The major findings of this study are organized in the following chapters:

- Chapter 2: Provides a review on biomass characteristics, gasifier design and operation, biomass steam gasification catalysts, thermodynamic and kinetic modelling.

- Chapter 3: Describes the experimental methods and analytical equipments used in this study.

- Chapter 4: Demonstrates the effect of catalyst preparation conditions and the catalyst formulations on the physiochemical properties, reactivity and stability of the prepared catalysts.

- Chapter 5: Reports the thermodynamic model for steam gasification of biomass developed in this study. The experimental gasification results with the variation of operating parameters are also compared with the equilibrium predictions.

- Chapter 6: Illustrates the developed mechanistic kinetic model, parameter estimation and model validation.

- Chapter 7: Provides concluding remarks and recommendations for future work.

CHAPTER 2

LITERATURE REVIEW

2.1 **Introduction**

Biomass is a hydrocarbon material mainly consisting of carbon, hydrogen, oxygen, nitrogen and minerals. It is considered an ideal renewable resource given its abundance, its lower sulfur content and its CO_2 neutral emissions. There are different biomass conversion processes utilized to produce heat and electricity, as well as to convert biomass into various chemical species. Since ancient times, the combustion of biomass has been used to produce energy. However, biomass combustion possesses only 20-40% energy conversion efficiency [11].

The hydrolysis of cellulose with mineral acids or enzymes has already been used for a quite a number of years. However, its commercial use is hindered by problems associated by the following (i) degradation of monomers, (ii) corrosion risk, (iii) handling and storage of acids/ enzymes, (iv) generation of neutralized waste and (v) separation of the product [70,71].

Bio-oils can be produced by heating biomass in the absence of oxygen, known as pyrolysis. Biomass pyrolysis produces tars and chars as by-products. Moreover, high energy requirements, and poor thermal stability and corrosivity of bio-oils which are the major challenges in this conversion process still need to be addressed [1,11].

Gasification or thermochemical transformation of cellulose or lignocellulose into synthesis gas ($CO+ H_2$) is one of the most economical and efficient technologies for the conversion of low value and highly distributed solid biomass into energy [6,8,11,13,15]. In the presence of controlled amounts of oxidant, biomass can be gasified into a gas-phase mixture of hydrogen (H_2), carbon monoxide (CO), carbon dioxide (CO_2), methane (CH_4), and water vapour with small amounts of tars and chars.

Table 2.1: Advantage and disadvantage of different gasifying agents [6,13,72,73]

Oxidants	Pros	Cons
Air	1. Provides partial combustion for gasification heat supply 2. Yields moderate char and tar contents	1. Provides a low heating value (4-6MJ/Nm^3) with large amounts of N_2 in the produced syngas (e.g., approx 50% by volume)
Steam	1. Yields a high heating value syngas (13–20 MJ/Nm^3) 2. Yields a H_2-rich syngas (e.g.,> 50% by volume)	1. Requires indirect or external heat supply for gasification 2. Yields a high tar content in syngas 3. Requires catalytic tar reforming
Carbon dioxide	1. Yields a high heating value syngas 2. Yields high H_2 and CO, and low CO_2 in syngas	1. Requires indirect or external heat supply 2. Requires catalytic tar reforming

The specific fractions of the various species obtained from biomass gasification depend on feedstock properties, process conditions, and gasification medium. Air, oxygen, steam, CO_2 or their mixtures can be used as gasifying agents. Pros and cons of different gasifying agents are summarized in Table 2.1. Gasification with oxygen produces a synthesis gas with net calorific values of 10–15 MJ/Nm^3 [13,15]. Air is normally used instead of oxygen, as the use of oxygen for gasification is expensive. Air gasification gives a gas with very low calorific value (4-6 MJ/Nm^3) due to the nitrogen dilution [15,16]. Steam gasification is an attractive alternative, as it produces a synthesis gas with 13-20 MJ/Nm^3 calorific values [15,16]. Unlike the air/oxygen gasification, biomass steam gasification is an endothermic process, requiring heat to be transferred. The best practice is to make a gasifier self-sufficient in energy (auto-thermal process), where a fraction of biomass is combusted to produce the heat required for endothermic steam gasification.

In recent years, catalytic steam gasification of biomass has become an area of growing interest as it yields higher energy efficiency. The use of suitable catalysts, reduces tars

yield significantly as well as produces a gaseous fuel with relatively high hydrogen content [13,15,16,71,74]. Properties of the feedstock, gasifier configurations and operating conditions, activity and stability of the catalysts used have a significant influence on the quality of the synthesis gas, and tar and char yields from biomass steam gasification. Moreover, the composition/heating value of the produced syngas also depends on the stoichiometry of the gasification process. It is, in this respect, essential to understand the gasification chemistry as well as the thermodynamic equilibrium and the kinetics of gasification reactions. These essential aspects of biomass steam gasification are reviewed in the following sections.

2.2 **Biomass**

Biomass is organic matter derived from plants and waste. Researchers characterize the various types of biomass dividing them in four major categories [75]:

(i)   *Energy crops*. Energy crops are those grown especially for the purpose of producing energy encompassing short-rotation or energy plantations. They comprise of herbaceous energy crops, woody energy crops, industrial crops, agricultural crops and aquatic crops. Typical examples are eucalyptus, willows, and poplars, assorghum, sugar cane, and artichokes, soya beans, sunflowers, cotton, rapeseed such as Salix Viminalis, Miscanthus X Giganteus (MXG) and Andropogon Gerardi. Energy crops are suitable to be used in combustion, pyrolysis and gasification for the production of biofuels, synthesis gas and hydrogen.

(ii)   *Agricultural residues and waste*. Large quantities of agricultural plant residues are produced annually worldwide and are vastly underutilized. The most common agricultural residue is the rice husk, which makes up 25% of rice by mass. Other plant residues include sugar cane fiber (bagasse), coconut husks and shells, groundnut (peanut) shells, and straw. Included in agricultural residue is waste, such as animal manure (e.g., from cattle, chicken, and pigs). Due to the low heating value of the

syngas produced using animal manure, manure is not technically feasible as the only gasifier fuel and other potential options have to be considered. For instance, cow dung can be used as a supplementary fuel blended with a conventional woody biomass, like sawdust [76].

(iii) *Forestry waste and residues*. These wastes and residues include mill wood waste, logging residue, tree and shrub residues. Fuels from wood (wood fuel and charcoal) are derived from natural forests, natural woodlands, and forestry plantations. Wood fuel is the principal source for small-scale industrial energy in the rural areas of developing countries. However, reforestation will be required to meet future energy demands as the world population grows. A possible predominant biomass derived fuel comes from wood-processing industries. The utilization of this residue for energy production at or near its source has the advantage of avoiding expensive transporting costs. Domestic wood fuels are sourced principally from land clearing and logging residues.

(iv) *Industrial and municipal wastes*: This waste encompasses municipal solid waste (MSW), sewage sludge and industry waste. [77] Municipal solid wastes and industrial residues such as black liquor from wood pulping also represent potential biomass feedstocks [78]. They pose however, major problems in gasification technology. Straw and municipal solid wastes may form large amounts of ash deposits in the furnace or convective sections of utility boilers [79].

A significant volume of published articles on gasification using various sources of biomass confirmed that thermal degradation kinetics, reactivity and product characteristics all change with the type of biomass used [80]. The amount and type of char and tar from gasification appear to be composed of different chemical species. These chemical species are a function of the feedstock used and of the different cracking pathways [81]. For example, Kosstrin [82] proved through experiments that the highest yield of tar was 35% from wood, around 60% from paper and only 30% from sawdust.

This was attributed to the fact that gasification products are affected by biomass chemical composition, as well as moisture content, and type of alkali content.

2.2.1 Chemical Characteristic

Every biomass type has carbon, hydrogen and oxygen as major chemical constitutive elements. These element fractions can be quantified using ultimate analysis. The ultimate analyses of thirteen biomass feedstocks are reported in Table 2.2. It is reported using the $C_xH_yO_z$ formula, where x, y and z represent the elemental fractions of C, H and O, respectively. Given the low hydrogen and high oxygen contents, all biomasses display a relative low calorific value. This is a main disadvantage for direct biomass utilization as an energy source. One can also establish that the oxygen available in biomass only allows 65–87wt% of the carbon to be converted into CO, while the remaining 13–35wt% of the carbon requires additional oxygen supply.

Table 2.2: Ultimate analysis of a diverse variety of biomass

Biomass	Ultimate analysis					$C_xH_yO_z{}^a$			Ref
	C	H	O	N	S	x	y	z	
Glucose						1.0	2.00	1.00	
Jute stick	47.18	8.36	44.10	0.36		1.0	2.11	0.70	[83]
Heterotrophic	76.22	11.61	11.24	0.93		1.0	1.81	0.11	[83]
Potato starch	42.50	6.40	50.80	0.00	0.000	1.0	1.79	0.90	[84]
Poplar sawdust	42.70	6.20	50.90	0.10	0.100	1.0	1.73	0.89	[84]
Pine Sawdust	50.26	6.72	42.66	0.16	0.200	1.0	1.59	0.64	[85]
Legume straw	43.30	5.62	50.35	0.61	0.120	1.0	1.55	0.87	[85]
Rice straw	36.90	4.70	32.50	0.30	0.060	1.0	1.52	0.66	[86]
Softwood bark	77.56	8.69	13.30	0.59		1.0	1.34	0.13	[83]
Pine	51.60	4.90	42.60	0.90		1.0	1.13	0.62	[87]
Waste Wood	55.11	6.01	37.99	0.86	0.030	1.0	1.30	0.52	[88]
Coal	75.80	4.40	16.70	1.89	1.220	1.0	0.69	0.17	[89]

[a] *in the $C_xH_yO_z$ formula x, y and z represent the elemental fractions of C, H and O respectively*

Biomass is mainly formed of hemi-cellulose, cellulose and lignin. Cellulose is a glucose polymer, consisting of linear chains of glucopyranose units, with an average molecular weight of around 100,000 Kg/Kmole. Hemi-cellulose is a mixture of polysaccharides, composed almost entirely of sugars such as glucose, mannose, xylose and arabinose with an average molecular weight of 30,000 Kg/Kmole. In contrast to cellulose, hemicellulose is a heterogeneous branched polysaccharide that binds tightly and noncovalently to the surface of each cellulose micro-fibril. Lignin can be regarded as a group of amorphous, high molecular weight, chemically related compounds. The building blocks of lignin are believed to be a three carbon chain attached to rings of six carbon atoms, called phenyl-propanes. Biomass hemicellulose, cellulose and lignin constituents decompose in the temperature ranges of 225-325°C, 305-375°C and 250-500°C, respectively [90].

The relative proportions of cellulose and lignin are two of the determining factors in identifying the suitability of plant species for subsequent processing as energy crops. Woody plant species are typically characterized by slow growth and are composed of tightly bound fibers, giving a hard external surface, while herbaceous plants are usually perennial, with more loosely bound fibers, indicating a lower proportion of lignin. Typical compositions of biomass are shown in Table 2.3. The variation of constituent fractions in biomass gives products with a different heating value. Furthermore, and taking into account that lignin gasification produces more hydrogen than other components of the biomass, pretreatments that improve lignin content are important.

Table 2.3: Typical compositions of biomass [13]

Biomass	Cellulose (wt%)	Hemi-cellulose (wt%)	Lignin (wt%)	Ash (wt%)
Harwood	36.4-50.3	12.7-23.2	16.6-28.6	0.4-9.7
Herbaceous Energy Crops	22.5 - 39.4	13.8 - 28.8	10.9 - 31.9	2.1 - 12.1
Agricultural Residues	30.6 - 43.4	12.2 - 25.5	16.9 - 27.6	2.8 - 13.5
Other wastes	30.7 - 31.4	9.8 - 16.9	15.3 - 16.9	6.6 - 34.2

Regarding biomass constituents, there is still controversy regarding the possible interactions among the different components of biomass during gasification [8,21]. It was observed, in this respect, that the formation of water-soluble tars occurs mainly in the early stages of pure cellulose gasification. This is the case, in contrast with the lower water-soluble tar yields obtained with full biomass. This shows that there are interactions between lignin, cellulose and hemi-cellulose biomass components during gasification.

Moreover, the products of biomass gasification also depend on its inorganic materials content. In order to fully describe biomass characteristics, it is customary to provide, in addition, to the ultimate analysis (percentage of carbon, hydrogen and oxygen), the proximate analysis. This analysis includes the content of moisture, volatile matter, fixed carbon and ash.

While biomass is converted, ash can be traced to the biomass mineral matter content. Depending on the biomass ash content, the available energy of the fuel is reduced proportionately. Moreover, gasification temperature is often above the melting point of biomass ash, especially if the alkali oxide and mineral content of ash is high [7]. Melted ash offers challenges to biomass conversion including sintering, agglomeration, deposition, erosion and corrosion. These are obstacles to economical and viable applications of biomass gasification technologies [6,91]. In contrast, it is well documented that ash contributes towards tars conversion acting as a catalyst [8,91–93].

Moreover ashes, which are continuously produced and normally disposed of in landfills, may have an adverse effect on the environment. Small ash particles may contribute to both air pollution and groundwater pollution through metal leaching. Ash can be used as a pozzolanic material mixed with concrete or cement. This reduces both the consumption of concrete and cement as well as landfill area requirements. This, in turn, can help to decrease the environmental impact caused by concrete and cement manufacturing since both involve high energy consumption and CO_2 emissions.

Moisture is an important constituent in biomass. While water is needed for a suitable gasification, a moisture content which is too high means that more energy consumption to

evaporate the additional moisture and to sustain the gasifier temperature. This results in lower heating value of the product gas [94,95].

2.2.2   Physical Characteristic

Biomass Size

Since pyrolysis and gasification of biomass are thermochemical processes, the temperature and rates of particle heating have pronounced effects on biomass conversion. To achieve this, the smaller the biomass size, the better the fluid-particle heat transfer. If the temperature is uniform throughout the particle, this yields a more controlled gasification. Moreover, whenever the intrinsic kinetics controls the overall gasification process, gasification rates increase exponentially with temperature following Arrhenius' rate law [1]. Maa and Bailie [96] have shown that in the pyrolysis of cellulose, the intrinsic reaction rate controls the overall gasification for particles smaller than 0.2 cm. For particles in the 0.2–6 cm size range, both heat transfer and intrinsic reaction rate have an influence on the gasification. For particles larger than 6 cm, the gasification rate becomes fully controlled by heat transfer. However, one has to be aware that particle size should not be smaller than required as biomass particle size reduction is quite an intensive energy process.

Biomass Structure

A porous biomass facilitates diffusion of the reactants and products under non-restricted molecular transport. Furthermore, when the biomass is highly porous, uniform temperature can be achieved in biomass pellets. This results in homogeneous gasification in all portions of biomass yielding uniform composition of product gases. On the other hand, when biomass is less porous, the temperature may vary from a maximum temperature at the pellet exterior to a minimum value at the center. In those cases, gasification on biomass exterior surfaces may dominate, with biomass external surfaces shrinking throughout the gasification. Due to the non-uniformity of temperature, drying, pyrolysis and gasification, these processes may take place concurrently yielding non-uniform composition of gases [8].

2.3 Chemistry of Gasification

Gasification is a thermochemical conversion process of solid biomass into a gas-phase mixture of carbon monoxide (CO), hydrogen (H_2), carbon dioxide (CO_2), methane (CH_4), organic vapors, tars (benzene and other aromatic hydrocarbons), water vapor, hydrogen sulfide (H_2S), residual solids, and other trace species (HCN, NH_3, and HCl). Upon heating, the biomass dries up, until it reaches 120 °C. Volatiles are produced until it reaches 350 °C and the resulting char is gasified above 350 °C. Therefore, it is customary to classify the entire gasification process into three steps: drying, devolatilization and gasification [90,97]. Gasification itself is a combination of pyrolysis and oxidation reactions. Chemical species are heated up to 500-900 °C in the presence of air, steam, CO_2, or other components. Heat to drive the process is generated either outside the unit or in the same unit via exothermic biomass combustion.

Evans and Milne [97] divided the gasification process into three reaction regimes: primary, secondary, and tertiary regimes. During the primary stage below 500 °C of gasification, solid biomass forms gaseous H_2O, CO_2, oxygenated vapor species and primary oxygenated liquids. The primary oxygenated vapors and liquids include cellulose-derived molecules (such as levoglucosan, hydroxyacetaldehyde), their analogous hemicellulose-derived products, and lignin-derived methoxyphenols. No secondary gas-phase cracking products were observed at this stage [3]. Primary pyrolysis vapors are of rather low molecular weight, representing monomers and fragments of monomers. However, Fu et al [98] reported that the aromatization process starts at 350 °C and continues at higher temperatures.

Secondary reactions take place at 700 to 850 °C. At this stage, the primary vapors and liquids are converted to gaseous olefins, CO, CO_2, H_2, H_2O, and condensable oils such as phenols and aromatics. The gases and remaining tars undergo other secondary reactions such as water-gas shift, methanation, steam-reforming and cracking. However, these reactions in which catalysts are not present are generally too slow. The only exception is the water-gas shift reaction.

Tertiary reactions occur with the further heating of evolved chemical species to 850-1000 °C. Tertiary reactions convert secondary products into CO, CO_2, H_2, H_2O, and polynuclear aromatic hydrocarbons (PAH). PAH compounds include methyl derivatives of aromatics such as methyl acenaphthylene, methyl naphthalene, toluene, and indene. Some tertiary products such as benzene, naphthalene, acenaphthylene, anthracene, phenanthrene and pyrene condense to form a liquid tertiary phase [3].

Table 2.4: Tar maturation scheme [99]

Gasification temperature	400 °C	500 °C	600 °C	700 °C	800 °C	900 °C
Species	Mixed Oxygenates	Phenolic Ethers	Alkyl Phenols	Heterocyclic Ethers	Polynuclear Aromatic Hydrocarbons	Larger Polynuclear Aromatics

During biomass gasification, higher molecular weight hydrocarbons, known as tars, formed in a series of complex reactions. Tar is defined as a complex mixture of condensable hydrocarbons, which includes single ring to 5-ring aromatic compounds along with other oxygen-containing hydrocarbons and complex polynuclear aromatic hydrocarbons (PAH). Tar causes operational challenges as it condenses in exit pipes and on particulate filters leading to blockages and clogged filters. According Milne et al [100], "tar is the most cumbersome and problematic parameter in any gasification commercialization effort". Tar removal or tar conversion, has been reported to be one of the greatest technical challenges in the commercialization of gasification technologies.

The formation of tar is highly dependent on the reaction conditions. The chemical composition of tars is also strongly affected by temperature and residence time. With the increase of reaction temperature and time, secondary reactions occur in the gas phase. Here, oxygenated tar compounds are converted to light hydrocarbons, aromatics, oxygenates and olefins, subsequently forming higher hydrocarbons and larger PAH in tertiary processes [100]. Elliott [99] reviewed the composition of biomass pyrolysis/gasification products from various processes and proposed a tar maturation

scheme. Table 2.4 and Table 2.5 show the expected transition from primary products to phenolic compounds to aromatic hydrocarbons, as a function of process temperature.

Table 2.5: Chemical components in biomass tars [99]

Conventional Flash Pyrolysis (450 –500°C)	High-Temperature Flash Pyrolysis (600–650°C)	Conventional Steam Gasification (700 –800°C)	High-Temperature Steam Gasification (900 –1000°C)
Acids	Benzenes	Naphthalenes	Naphthalene
Aldehydes	Phenols	Acenaphthylenes	Acenaphthylene
Ketones	Catechols	Fluorenes	Phenanthrene
Furans	Naphthalenes	Phenanthrenes	Fluoranthene
Alcohols	Biphenyls	Benzaldehydes	Pyrene
Complex	Phenanthrenes	Phenols	Acephenanthrylene
Oxygenates	Benzofurans	Naphthofurans	Benzanthracenes
Phenols	Benzaldehydes	Benzanthracenes	Benzopyrenes
Guaiacols			PAHs
Syringols			
Complex Phenols			

During gasification, the inorganic components of the biomass are usually converted into ash, which is removed from the bottom of the gasifier (bottom ash), or into fly ash, which leaves with the product gas. The composition of the ash includes CaO, K_2O, P_2O_5, MgO, SiO_2, SO_3, Na_2O, and residual carbon. Volatile halogen elements and alkali elements are mainly found in wet scrubber ash and in fly ash while Si, Ni, Pb, Zn, Cr, Cd, K, S, Mn, Cu elements are typically contained in the ash separator exit, enriched with heavy metals.

Soot and coke are formed during these secondary and tertiary processes. Coke forms from thermolysis of liquids and organic vapors. The homogeneous nucleation of the intermediate chemical species, produced at a high temperature, yields soot in the gas-phase [3]. Among biomass formed products, char retains the morphology of the original lignocelluloses. Char is formed through cross-linking reactions via condensation and water loss with slow pyrolysis yielding more char [101]. The char yield decreases rapidly with increasing temperature until 400 ^{o}C is reached. As the temperature increases, the char becomes progressively more aromatic and high in carbon. This is due to the removal

of hydroxyl, aliphatic C-H bonds and carbonyl and olefinic C=C groups. The release of volatile matter opens spaces in the char pore structure at the higher gasification temperatures. Higher temperatures may also lead to char softening, melting and fusion. The shrinkage of the carbon structure may take place above $500^{o}C$, which is concurrent with the aromatization process [98]. Char that is formed from the primary and secondary reactions regimes continues to pyrolyze and react with steam (i.e. the carbon/steam reaction) producing additional permanent gases.

2.4 Operating Conditions of Gasifiers

The operating conditions play a very important role in biomass gasification in all respects, including carbon conversion, product gas composition, and tar reduction. The most important influencing parameters include gasification temperature, steam/biomass ratio, and residence time. The selection of these parameters also depends on the type of gasifier used. The influence of the operating parameters are summarized in Table 2.6.

2.4.1   Gasification Temperature

Researchers have conducted extensive studies reviewing the influence of temperature on tar production during biomass gasification. To achieve a high carbon conversion of the biomass and a low tar content, a high operating temperature (above 800 °C) in the gasifier is recommended. With the increase in temperature, combustible gas content, gas yield, hydrogen, and heating value all increased significantly, while the tar content decreased sharply.

Fagbemi et al [102] showed that tar yields augmented first while temperature rose up to $600^{o}C$, and then dropped after this temperature was surpassed. At higher temperatures, primary reactions were less significant and secondary reactions (i.e. tar cracking) prevailed. This led to considerable tar decomposition. Temperature not only affects the amount of tar formed, but also the composition of tar by influencing the chemical reactions involved in the gasification network [9]. Yu et al. [103] reported that tar yield was reduced by more than 40% when the temperature was raised from 700 to 900 °C.

With an increase in temperature, the amount of total oxygen-containing components drastically went down, the amount of substituted 1-ring and 2-ring aromatics also decreased, but the formation of 3- and 4-ring aromatics increased rapidly. An almost 40% increase in naphthalene content was reported at 900 °C. Furthermore, in the combustion zone of the gasifier, temperature plays a dominant role in the reactions between char and oxygen.

While this showed that higher temperatures are favorable for biomass gasification [104–106], from an overall process perspective, the reduction of ash agglomeration requires lower temperatures [1,6,91]. This may limit, in practice, gasification temperatures up to 750 °C [1,18]. Moreover, Mahishi and Goswami [107] reported that the hydrogen at chemical equilibrium initially increased with temperature, reached a maximum and then gradually decreased at the highest temperatures. Therefore, several factors including tar content, gas composition determining gas heating value and char conversion should all be taken into consideration and weighted carefully in the selection of the gasifier operating temperature.

Table 2.6: Influence of different operating parameters of a gasifier [6,9,108,109]

Operating parameters	Advantages	Technical Challenges
Temperature Increase	1. Yields reduced char and tar content 2. Yields higher carbon conversion and reduced methane in syngas 3. Yields increases syngas heating value	1. Yields a decreased energy efficiency 2. Increases ash-related problems
Increase of pressure	1. Yields low char and tar content 2. Yields a compressed syngas required for downstream utilization	1. Creates an increased uncertainty given the limited design and operational experience 2. Yields more expensive small scale gasifier
Increase of S/B ratio	1. Yields low char and tar contents	1. Decreases heating value of syngas

2.4.2   Steam/Biomass Ratio

The steam/biomass ratio (S/B) or equivalence ratio (ER) strongly influences the type of gasification products. In case of air gasification, a high equivalence ratio (ER) results in a lower concentration of H_2 and CO as well as in a higher CO_2 content in the product gas. Thus, a higher ER decreases the heating value of the syngas. Increasing the ER also has a beneficial effect on reducing tar formation given the greater availability of oxygen to react with volatiles. This phenomenon is more significant at higher temperatures.

On the other hand, an increase in the steam/biomass ratio is expected to produce higher hydrogen and lower CO fractions as a result of the water-gas shift reaction. In addition, excess steam often drives the cracking of higher hydrocarbons and reforming reactions [109]. Nevertheless, the upper limit of steam/biomass ratio is set by gasification stoichiometry. Exceeding this limit yields excess steam in the product gas. The energy associated with excess steam and the enthalpy losses resulting from the unnecessary production of this steam need to be considered in the system energy balances. Such issues demonstrate the importance of selecting an optimal steam/biomass ratio in biomass steam gasification for achieving high process efficiency.

Herguido et al [110] reported the effect of steam/biomass ratio on the products from biomass steam gasification. They observed an increase in H_2 (as high as 60%) and CO_2 (from 10 to 30%) contents, a sharp decrease in CO (from 35 to 10%) content and a slight decrease in CH_4 content when the S/B ratio was increased from 0.5 to 2.5. It also reduced the tars yield from 8% at S/B = 0.5 to almost nil at S/B = 2.5. However, there was a sharp decrease in the lower heating value which was attributed to the decrease in CO.

Steam gasification requires external energy input as it is a endothermic process. The use of some small amounts of oxygen along with steam can provide the necessary heat for gasification. The process is known as auto-thermal gasification. In view of this, many researchers used steam–oxygen mixtures for biomass gasification. Aznar et al [111] reported more than 85% reduction in the total tar when they increased the (steam+O_2)/biomass ratio termed as gasifying ratio (GR) from 0.7 to 1.2. They also reported that low GR values produced light tars which could be easily converted using a

catalyst. Gil et al [73] recommended H_2O/O_2 ratio of around 3.0 (mol/mol) for auto-thermal gasification. They observed a decrease in H_2 content from 29% to 13%, a decrease in CO content from 50% to 30%, an increase in CO_2 content from 14% to 37%, a slight decrease in CH_4 content from 7% to 5% and a change in C_2 hydrocarbons from 3.5% to 2.3%, when the GR was increased from 0.6 to 1.7. Tar content of the raw gas was also sharply decreased with GR; with less than 5 g/m^3 at a GR of 1.2.

2.4.3   Operating Pressure

Several researchers have investigated pressurized biomass gasification [112]. When the pressure was increased, a reduction in the amount of light hydrocarbons and tars were observed at higher ERs. This occurred with 100% carbon conversion. Although the total amount of tar decreased with greater pressures, the fraction of polycyclic aromatic hydrocarbons increased.

2.4.4   Residence time

Residence time has a significant influence on the amount and composition of the produced tars. According to Kinoshita et al [108], the fraction of oxygen-containing compounds tends to decrease by increasing residence time. Furthermore, yields of one and two aromatic ring compounds (except benzene and naphthalene) decrease with residence time whereas that of three and four ring species increases. Corella et al [113], observed a decrease in the total tar content when the space time was augmented in biomass gasification with a bed of dolomite.

2.5 Design of Gasifiers

Gasifiers can be divided into two principal types: fixed beds and fluidized beds, with variations within each type. The advantages and technical challenges of different gasifier configurations are summarized in Table 2.7. Fixed-bed gasifiers are the oldest and historically most common reactors used to produce syngas because of their simplicity in construction and operation. In the last two decades however, large scale (higher than 10 MW), fixed-bed gasifiers have lost a part of their industrial market appeal. Yet, small

scale (less than 10 MW) fixed-bed gasifiers, which provide a relatively high thermal efficiency and require minimal feedstock pre-treatment, have maintained a commercial interest, especially in the area of locally based power generation. Depending on the direction of airflow, fixed gasifiers are classified as updraft, downdraft, or cross-flow [114].

Table 2.7: Advantages and technical challenges of different types of gasifier [6,8,9,16,17]

Design	Main Advantages	Main Technical Challenges to overcome
Fixed / moving beds	1. Involves a simple and reliable design 2. Suitable for wet biomass 3. Entails favorable economics at small scale	1. Operates at longer residence time 2. Operates with non-uniform temperature distribution 3. Yields high char & tar contents 4. Low biomass processing capacity
Fluidized bed	1. Operates at short residence time 2. High biomass processing capacity 3. Uniform temperature distribution 4. Yields low char or/and tar contents 5. Reduces ash-related problems at low-medium temperatures	1. Yields high particulate dust concentrations in syngas 2. Displays favourable economics on a medium to large scale only

Among the technologies that can be used for thermochemical conversion of biomass, fluidized beds are promising given their flexibility and high efficiency. Fluidized bed (FB) gasification has been used extensively for coal gasification for many years. Its advantage over fixed bed gasifiers is the uniform temperature distribution achieved in the gasification zone. This temperature uniformity is accomplished using a bed of fine granular material (e.g. sand) into which gas is circulated fluidizing the bed. Intense bed

fluidization promoting solid circulation also favors the mixing of the hot bed material, the hot combustion gases and the biomass feed. Fluidized beds can be used for a broad variety of fuels. This flexibility with respect to different fuels is actually another critical advantage of fluidized beds [115]. Loss of adequate fluidization known as defluidization due to particle/ash agglomeration is a major problem in fluidized bed gasifiers operated above 800 °C. Agglomeration can be reduced by lowering and controlling the bed temperature.

Two main types of fluidized bed gasifiers are in current use. These are the following: a) circulating fluidized bed, b) bubbling bed. Circulating fluidized bed gasifiers are able to cope with high capacity biomass throughputs and are used in the paper industry for the gasification of bark and other forestry residues. The bed material is circulated between the reaction vessel and a cyclone separator, where the ash is removed and the bed material and char are returned to the reactor vessel. Circulating fluidised bed gasifiers have proven very reliable with a variety of feedstocks and are relative easy to scale up from a 10 MW up to 100 MW. Even for capacities above 100 MW, there is confidence that the industry would be able to provide reliable gasifiers. This appears to be the preferred system for large-scale applications and is used by most industries. These systems, therefore, have high market attractiveness and are technically well proven. Moreover, circulating fluidized bed gasifiers can be operated at elevated pressures. Therefore, produced gases can be delivered at gas turbine operating pressures without requiring further compression.

Bubbling fluidized bed gasifier consists of a vessel with a grid at the bottom through which air is introduced.   Above the grid, there is a moving bed of fine-grained material into which the pretreated biomass feed is introduced. Bed temperature is maintained in the range of 700–900 °C by controlling the steam/biomass ratio. The biomass is pyrolyzed in the hot bed, forming char, gaseous compounds and tar. The high molecular weight tar is cracked by contact with the hot bed material, giving a product gas with a lower tar content (<1–3 g/Nm^3).

2.6 **Catalysts for Steam Gasification of Biomass**

A considerable volume of research has been conducted with the goal of developing biomass gasification processes in the recent years. However, a serious issue for the broad implementation of this technology is how to deal with the generation of unwanted contaminants (e.g. tar, coke-on-catalyst, particles, nitrogen compounds, alkali metals) [116]. Tar is a complex mixture of condensable hydrocarbons including single ring to 5-ring aromatic compounds. It also includes oxygen-containing hydrocarbon species, which cause blockage, corrosion, as well as reduce overall efficiency of the gasifier [100]. For commercial applications, tar components must be limited to less than 1 g/m^3 of gas at STP conditions.

Tar can be converted thermally. High gasification temperature reduces the formation of tar; but high energy consumption (i.e. high production cost for syngas) makes the process economically unviable [117]. Even at temperatures in excess to 1000 °C, tar cannot be removed completely. Moreover, it is highly desirable, to keep the operating temperature of the gasifier below 750 °C, to prevent ash agglomeration. Ash frequently contains CaO, K_2O, P_2O_5, MgO, SiO_2, SO_3, and Na_2O that can sinter, agglomerate, deposit on surfaces and contributes to erosion and corrosion of the gasifier. Furthermore, alkaline metals react readily in the gasifier with silica forming silicates or with sulfur producing alkali sulfates. This leaves a sticky deposit in the gasifier and in many instances causing bed sintering and defluidization [91,118,119].

Catalytic reforming can be used to convert tar into gaseous products. For more than three decades [9,19,26,100,116,120], it has been the most promising method for tar removal, avoiding costly tar disposal. The use of catalysts during biomass gasification promotes char gasification, changes the product gas composition and reduces the tar yield even at lower temperatures. Moreover, the addition of a catalyst not only influences the gas composition, but also the heating value of the product gas [121].

Thus, given the value of catalysts for gasification, relevant research has been done with the goal of developing stable and highly active catalysts for biomass gasification

producing high quality synthesis gas and /or hydrogen free of tars. Significant amounts of study have been carried out using dolomite, olivine, alkali, nickel and noble metal catalysts for this purpose.

Catalysts have been employed directly in the gasifier and in these cases, they are referred to as *primary catalysts* [9,19,23,122–125]. These primary catalysts such as dolomite, calcined dolomite, olivine, and Ni/Al_2O_3 promote several important chemical reactions such as s steam & dry reforming, and water-gas-shift. Thus, there is the opportunity with primary catalysts to minimize tars, increase both hydrogen and CO_2 yields avoiding altogether complex downstream tar removal operations [126]. Furthermore, the addition of active materials to the bed also helps prevent the solid agglomeration tendencies and subsequent choking of the bed. However, catalysts in the gasifier, particularly the Ni based catalysts, may be affected by deactivation due to carbon deposition on the catalyst surface [26,127].

In spite of the challenges, the use of primary catalysts, in the context of biomass gasification, is gaining much attention nowadays as they reduce the need for expensive downstream operations [9]. Another possible alternative is to have a catalytic process in a reactor placed downstream from the gasifier. In this reactor, product gases are further processed using secondary catalysts [19]. Typical materials that are used as *secondary catalysts* are dolomite and nickel based formulations. These catalysts decrease the tar content of the product gas in the 750-900 °C range [19,26,111,127–130]. Secondary catalysts are effective for hot gas cleaning with the overall cost of the gasification process increasing significantly [117]. According to Asadullah et al [131], when Rh/CeO_2 is used as a secondary catalyst, the formation of CH_4 and CO_2 is in many cases increased significantly and the formation of CO and H_2 may be reduced.

Catalytic biomass gasification is a complex process which includes numerous chemical reactions steps such as pyrolysis, steam gasification and water- gas shift reaction [132]. Contributions to the development of stable and efficient biomass gasification catalysts are reviewed in the next section of this article.

2.6.1 Dolomite, Olivine and Alkali metal Based Catalysts

The use of dolomite, a magnesium ore with the general formula $MgCO_3$ $CaCO_3$, as a primary and/or secondary catalyst in biomass gasification has attracted much attention since it is a cheap disposable catalyst that can significantly reduce the tar content of the product gas from a gasifier. The main issue with dolomite is its fragility; quick attrition occurs in fluidized beds under the prevalent high turbulence conditions [9].

Dalai et al [133] studied the performance of a CaO catalyst by varying the catalyst loading from 0 to 8.9 wt. % during temperature programmed gasification (TPG) and constant temperature gasification (CTG). Experiments showed that the use of CaO as a primary catalyst reduced the maximum gasification temperature by 150 °C. In addition, the total fuel produced, as well as the hydrogen, and carbons yielded were significantly increased with CaO impregnated in cellulose, cedar, and aspen. Furthermore, the rate and the cumulative production of H_2 from CaO impregnated in cedar and aspen were higher than those from CaO impregnated in cellulose both for catalytic as well as for non-catalytic TPG and CTG.

Aznar et al [89], conducted parametric studies using dolomite as a tar cracking catalyst. The feedstock was composed of blends of plastic waste mixed with pine wood sawdust and coal at flow rates of 1-4 Kg/h. Operating variables studied were gasifier bed temperatures (750 – 880 °C), equivalence ratio (0.30 – 0.46), feedstock composition and the influence of secondary air fed into the freeboard. As a result, a gas with medium hydrogen content (up to 15 % dry basis) and low tar content (less than $0.5g/m^3$) was obtained. Additionally, these authors found that the injection of secondary air into the freeboard reduced tar content by 50 %, down to 5 g/m^3. Under these conditions, a clean gas was obtained.

A few studies have been done recently into the catalytic activity of olivine and dolomite for tar elimination. Hu et al [134] tested calcined olivine and calcined dolomite as catalysts in a fixed-bed reactor. Results showed that the catalytic activities of calcined catalysts were higher than those of the untreated ones. A similar system was used by Devi et al [74], who observed that in the case of untreated olivine and calcined dolomite, tar

conversion increased when temperature reached 800 °C to 900 °C. These authors found that water soluble heterocyclic compounds could be 100 % converted at 900 °C. Additionally, the conversion of heavy polyaromatics increased from 48 % to 71 % using 17 wt% untreated olivine mixed with sand at 900 °C; whereas the conversion of heavy polyaromatics reached up to 90 % with 17 wt % of calcined dolomite. Furthermore, a total tar amount of 4.0 g/m^3 could be reduced to 1.5 and 2.2 g/m^3 using calcined dolomite and olivine.

Xu et al [135] demonstrated that, for atmospheric gasification of biomass, CaO could also be used as an effective CO_2 capture material, provided that the reaction temperature was selected appropriately. It was shown that, at temperatures below 730°C, the CaO captured CO_2, yielded a CO_2 in the product gases that was below 10 vol. % and increased as a result, the heating value of the product gases considerably. Furthermore, the addition of CaO increased the H_2 gas content, and decreased the CO concentration, irrespective of the reaction temperature. This result corroborates the commonly known catalytic effect of CaO on CO_2 capture, water-gas-shift reaction and tar reforming/cracking reactions.

Monovalent alkali metals of group 1A are all highly reactive and electropositive. Alkali metals, principally K and to a lesser extent Na, exist naturally in biomass and accumulate in the gasifier ashes. These alkali metals can have a significant impact during pyrolysis, forming a reactive char that enhances gasification. Furthermore, the use of ash itself as a catalyst solves the problem of ash waste handling and gives an added value to the gasification by increasing the gasification rate and reducing the tar content in the produced gas. However, the major disadvantage of these ash based catalysts is their potential activity losses due to particle agglomeration. Sutton et al [19] reported several disadvantages in the direct addition of alkali metals, such as the difficult and the expensive recovery of the catalyst, which increased char content after gasification, and ash disposal problems. On the other hand, Lee et al [136] found that the addition of Na_2CO_3 while using nickel catalysts enhanced rice straw catalytic gasification and significantly increased the formation of permanent gases. The same authors found that the formation of permanent gases depended on the nature of the alkali metal carbonate used with the following reactivity order being assigned: Na ≥ K > Cs > Li.

The beneficial effect of using activated alumina as a secondary catalyst for tar reduction comes from its high catalytic activity, comparable to dolomite [137], although it deactivates by coke faster than dolomite. Juutilainen et al [138] tested the activity of these catalysts also containing zirconia in the selective oxidation of tar and ammonia. This performance was compared with that of nickel and dolomite catalysts. Synthesis gas with toluene as a tar model compound was used as a feed in a fixed bed tube reactor. The presence of oxygen, zirconia and alumina-doped zirconia led to high toluene removal and ammonia conversions at temperatures below 600 °C. These catalysts were active for toluene oxidation below 700 °C and for ammonia oxidation below 650 °C. This showed that the zirconia enhanced the oxidation activity, while alumina improved the oxidation selectivity. At higher temperatures, these ZrO_2/Al_2O_3 catalysts performed even better. The authors concluded that both zirconia and alumina in catalyst formulations promoted toluene and ammonia conversions at lower temperatures.

2.6.2   Nickel Based Catalysts

Among the transition metals (group VIII), nickel is the most widely used in the industry for steam and dry reforming reactions [139]. Commercially available nickel reforming catalysts have been used extensively for biomass gasification [26,111,120,128,140,141]. According to Aznar et al [111], under the conditions of catalytic gasification, nickel catalysts, are more active for heavy hydrocarbon steam-reforming (i.e. C_nH_m +$nH_2O\rightarrow$ n CO+ (n+m/2) H_2) than for light hydrocarbon steam reforming (i.e. CH_4 + $H_2O\rightarrow$ CO+ 2 H_2). These nickel catalysts also promote water-gas-shift reaction (CO+$H_2O\rightarrow CO_2$ + H_2), and are very effective in tar conversion. As a result, these nickel based catalysts reduce tars while increasing H_2/CO ratio, improving synthesis gas quality. According to Olivares et al [123], "nickel reforming catalysts display 8-10 times more reactivity than calcined dolomite".

2.6.2.1   Catalyst Deactivation

When using nickel-based catalysts, several deactivation mechanisms occur including poisoning by sulphur, chlorine, and alkali metals, sintering of Ni particles and coke formation [25]. Ni-based catalysts deactivate rapidly due to coke formation and catalyst

attrition. Coke formation is inherent to steam reforming processes. The high temperatures associated with reforming, promote both higher hydrogen yields and undesirable coke formation. Coking in Ni-based steam reforming catalysts is reasonably well understood [142]. This process is the result of high temperature reactions taking place both in the gas phase and on the catalyst surface. Tars, light and unsaturated hydrocarbons dissociate on catalyst metal surfaces to produce carbon deposits. They block the access to the catalyst pores resulting in a loss of catalyst activity. The formed carbon may be gasified, may encapsulate on the catalyst surface or may diffuse through the nickel to nucleate and precipitate, leading to the formation of carbon whiskers. The formation of carbon whiskers lifts the nickel crystallite from the catalyst surface resulting in sintering. Therefore, nickel-based catalysts deactivate by carbon in two ways: (1) through the encapsulation of nickel crystallites by inactive carbonaceous layers of material, and (2) through the formation of inactive bulk nickel carbide phases [142–146]. Furthermore, there is a tendency for coke to be formed as a result of the increased unsaturation, molecular weight and aromaticity of the feedstock.

Regarding coke formation, it can be minimized through the use of excess steam vis-a-vis of the one required by gasification stochiometry. In this respect, it is possible to estimate a minimum steam/carbon ratio required to avoid coke formation [147]. This provides a very useful guideline to establish the desired operating conditions. However, the practical negative effect of feeding extra steam is that it increases the overall energy costs for plant operation. Therefore and given the above mentioned considerations, it is crucial to maintain as low a steam/C ratio as possible [142].

If coke deposits on the catalyst surface at the same rate that it is removed by combustion, the catalyst surface remains clean. Thus, there is no catalyst deactivation and the catalyst will always be effective in biomass gasification [26,148]. This is the ideal scenario that may happen in auto-thermal gasification where air fluidizes the catalyst and biomass bed, contributing to always keeping the catalyst free of coke. However, coke removal with combustion may also lead to metal oxide formation. The active metal component of the catalyst has to be reduced quickly to prevent poor catalyst activity and selectivity as well as limited catalyst life.

Ni-based catalysts are also prone to deactivation by sulphur. Struis et al [149] investigated sulphur poisoning using several analytical techniques (TPO, XPS, XAS). To address these issues, Sato and Fujimoto [150] proposed a WO_3 promoted Ni/MgO-CaO biomass gasification catalyst with high resistance to sulfur containing species.

2.6.2.2   *Effect of Catalyst Support and Dopants*

The formulation of nickel catalysts may potentially involve the following components (i) an active component (i.e. Ni), (ii) a second added component (i.e. a dopant or promoter) and (iii) a support phase. Generally, higher nickel content results in lower tar yield and higher H_2 and CO yields. On the other hand, according to Bartholomew et al [146], the amount of nickel in the catalyst has a significant effect on the catalyst deactivation by coking. They suggested that a lower metal concentration, results in a stronger interaction with the support phase and a higher metal dispersion. Thus, by controlling the metal addition, one can have a catalyst which is more resistant to deactivation by carbon fouling. Metal dispersion can also be improved by the addition of dopants or promoters. It has been proven that the activation and deactivation of nickel based catalysts depend greatly on the type of support and the presence of additives/promoters. For instance, promoters may help to minimize the coke formation.

The support phase gives the catalyst mechanical strength and protection against severe conditions such as attrition and heat [25]. The pore structure of the support, the metal-support interactions, and the acidity-basicity of the support all significantly influence the metal dispersion, the metal crystallite size and the carbon deposition on the catalyst surface; thus affecting the overall catalytic performance and catalyst coking resistance [151,152]. Baker et al [26,153] also reported that the acidity of the support affects coke deposition and catalyst deactivation. For instance, higher acidity of the support materials favors tar cracking leading to higher carbon buildup on the catalyst surface. On the other hand, Mark and Maier [154] reported that the pore structure or type of support did not affect the rate of dry-reforming of methane. The role of the support is reported as stabilizing the metal surface, which, in turn, is responsible for catalyst activity.

Alumina-based materials are considered the primary support materials for most reforming catalysts. Gadalla and Bower [155] investigated the performance of α-Al_2O_3 and γ-Al_2O_3 supported Ni catalysts for the reforming of methane with CO_2. These authors reported that the Ni/α-Al_2O_3 catalyst provides lower methane conversion than the Ni/ γ-Al_2O_3, and this in spite of being constituted with a more stable allotropic α-Al_2O_3. This was attributed to the low surface area of α-Al_2O_3. They also showed that the Al_2O_3 supports containing MgO/CaO were more stable. However, the addition of silica on Ni/Al_2O_3 catalysts was not adequate given that it caused rapid deactivation. Wang and Lu [151,152] also reported higher conversion and lower deactivation rates for the Ni/γ-Al_2O_3 catalyst when compared to the Ni/α-Al_2O_3. They found that nickel aluminate ($NiAl_2O_4$) was formed due to the phase transformation of the γ-Al_2O_3 supported Ni catalyst during calcinations.

Nickel aluminate is difficult to reduce at lower temperatures. Temperatures higher than 800 °C are required for nickel aluminate reduction. As a result, the formation of nickel aluminate followed by its reduction has a negative impact on biomass gasification given the additional energy required. However, once $NiAl_2O_4$ is reduced, it is active for reforming reactions and is resistant to coking.

Table 2.8: Physical properties, catalytic activities and deactivation characteristics of various oxide-supported Ni (~ 5 wt%) catalysts [151,152]

Catalyst	Support S_{BET} (m²/g)	Catalyst S_{BET} (m²/g)	Ni crystallite size (nm) fresh (d_1)	Used (d_2)	CH$_4$ Conversion @ 800 °C (%)	Deactivation $\frac{Conv_{3h}}{Conv_{10min}}$	Carbon deposition (g of C/g of Cat)	Sintering d_2/d_1
Ni/La$_2$O$_3$	6.4	16.4	15.5	37.5	98	0.97	0.48	2.4
Ni/SiO$_2$	290	239	12	21.8	96.2	0.87	0.068	1.8
Ni/TiO$_2$	9.4	8.4	27.6		10			
Ni/α-Al$_2$O$_3$	0.8	1.2	31.7	37.5	92.4	0.72	0.15	1.2
Ni/γ-Al$_2$O$_3$		157			95.8	0.95		
Ni/MgO	147.8	55.5			95.6	1.1	0.049	
Ni/CeO$_2$	52	34			65	0.65	0.02	

Wang and Lu investigated the effect of various oxide-supports in the catalytic performance and stability of Ni catalysts for dry reforming of methane. Results of their investigation are summarized in Table 2.8. Ni crystallites which formed on the SiO_2 surface were smaller in size, given the high surface area and well developed porosity of these supports. Lower porosity of Ni/α-Al_2O_3 and Ni/TiO_2 resulted in lower dispersion of metal and thus in larger crystallite sizes. On the other hand, in spite of La_2O_3 being nonporous, the Ni crystallites that formed on it were smaller in size. La_2O_3 has a higher ability of dispersing metal particles on the surface. Regarding Ni catalysts supported on MgO, it is apparent that NiO-MgO catalysts form a solid phase. As a result, it is very hard to reduce the Ni in the Ni/MgO catalyst. It has to be pre-reduced at more than 800 °C to form active Ni crystallites.

Fluidizable γ-Al_2O_3 is one of the most promising supports for a Ni-based catalyst due to its high surface area and mechanical strength. However, γ-Al_2O_3 is not stable at high temperatures due to thermal sintering and phase transformation. Rare earth oxides have been investigated as a γ-Al_2O_3 stabilizer [33–37]. La_2O_3 is a reported inhibitor for γ-alumina surface area losses. Moreover, La_2O_3 has been used as a promoter of Ni/Al_2O_3 catalysts for steam gasification of biomass and its surrogate species [29,30,32,38–41]. When small amounts of La_2O_3 were added, they dispersed well on γ-Al_2O_3. These lanthanum species enhanced catalytic activity, acting as a Ni dispersant [37,42–51]. There is, however, a limit for lanthanum loading. Excess lanthanum may lead to formation of undesirable $LaAlO_3$ above 1000 °C [34,43,44,49,52,53]. Moreover, the controlled amount of basic La_2O_3 reduces the acidity and enhances the CO_2 adsorption capacity of γ-Al_2O_3 resulting in lower coke formation on the catalyst surface [30,39,46,54–57].

Furthermore, the catalyst preparation method also plays a crucial role influencing structural properties, metal-support interaction, reducibility and dispersion of active phase [58–60]. Conventionally, impregnated metal salts are decomposed to oxides by high temperature calcination in air followed by metal oxide reduction under hydrogen. Surface area, dispersion, and reducibility of nickel can be improved significantly

however, by direct decomposition of nickel salts to nickel in a reducing atmosphere without prior calcinations in air [58].

CREC researchers have also contributed significantly to the development of active and stable Ni-based catalysts for steam and dry reforming [88,156–159]. Most recently, a catalyst for steam gasification of biomass was developed using Ni on a fluidizable α-alumina support [18,68].

2.7 **Thermodynamic Analysis of Biomass Steam Gasification**

Biomass characteristics such as chemical and physical properties can vary widely as described in Section 2.2. This variability may have a potential effect on gasification conditions and product quality. With this in mind, thermodynamics can be a very useful engineering tool to assess how biomass composition, gasifier temperature and pressure, and steam/biomass ratio affect gasification.

Through thermodynamic analysis, one can determine the theoretical limits of the chemical species distributions at chemical equilibrium. Moreover, the thermodynamic efficiency, the available energy of a given biomass fuel and the optimum operating conditions can also be obtained by using this approach. Thermodynamic results are, in principle, independent of the reaction network, type of the reactor or/and reaction time [160]. However, in practice, thermodynamic predictions have inherent limitations, only being suitable for gasification processes with long reaction times. This is the result of the role played by gasification kinetics under these conditions [161].

2.7.1   **Thermodynamic Modelling of Biomass Gasification**

Modelling of biomass steam gasification is a challenging task as it involves a complex combination of reactions in the solid and gas phases [162]. Biomass is different from coal and other carbonaceous feedstocks given its high level of volatiles (70–75%), its different physical and structural characteristics, as well as its various reactivities. In spite of this, there is still vast experience with coal and other carbonaceous feedstocks that can be used to advance future development in biomass gasification.

Chemical equilibrium of biomass steam gasification can be determined by Gibbs Free Energy Minimization. Two approaches have been developed for equilibrium modelling: a) stoichiometric and b) non-stoichiometric. The "stoichiometric" approach requires a defined reaction incorporating all chemical species. In the "non-stoichiometric" formulation, on the other hand, no particular biomass chemical constituents are considered. The only input which must be specified is the feed elemental composition. These elemental C, O, H, S and N compositions can be readily obtained from ultimate analysis data. This method is particularly appropriate for reactions with uncertain mechanisms and feed streams like biomass whose precise chemical compositions are unknown. A numerical method is used to minimize the Gibbs Energy of a closed system to calculate the composition of the product mixture. This tool relies on thermodynamic databases that contain the values of the standard Gibbs Energy of the components. Most gaseous components can be found in such databases, but concerning solid phase, only pure carbon is taken into account. Such a model does not require any knowledge of the mechanisms of transformation. Moreover, the model is independent of the reactor configuration and not limited to a specified range of operating conditions.

Schuster et al [163], developed a model for the steam gasification of biomass by applying thermodynamic equilibrium calculations. Biomass was represented with an elemental composition. The influence of fuel composition (ultimate analysis and moisture content), temperature, and the amount of gasification agent were studied over a wide range of experimental conditions. Comparisons were made between the predictions of the equilibrium model and the experimental results. The results of the equilibrium model were in the range of measured results, though the CH_4 content in the product gas was overestimated.

Ginsburg and de Lasa [164], considered five components (H_2, CO, CO_2, H_2O, and CH_4) as the major species from biomass gasification and two main reactions in the gas phase at equilibrium: a) steam reforming of methane, and b) water-gas-shift. From the elemental analysis of the wood, they showed that the compositions of nitrogen and sulfur species evolving from the reactor are negligible in terms of the equilibrium calculations.

Although these and other thermodynamic studies [61,65,165–169] were useful in evaluating the influence of various operating parameters, in most cases, the observed synthesis gas compositions deviated from chemical equilibrium prediction significantly. Specifically, experimental methane and tar amounts deviate considerably from most of the model predicted values. The main reasons for these deviations are due to the inadequate assumptions adopted such as i) equilibrium conditions for some of the key reaction steps, ii) char and tar considered as solid carbon and iii) ash treated as an inert species.

Several semi-equilibrium models are also reported incorporating tars and char formation. Li et al [10,63] and Jand et al [170] considered additional empirical relations together with thermodynamics to calculate the carbon conversion and the yield of CH_4. These empirical-theoretical models provide good predictions, although they have limited applicability to the specific gasifiers under study. Whether extrapolations of these predictions to other gasifiers can be made is rather uncertain.

Li et al [10,63] found that the experimental results of a pilot-scale circulating fluidized bed gasifier deviated from chemical equilibrium due to kinetic limitations. They proposed a phenomenological model, adapted from the pure equilibrium model, incorporating experimental results regarding unconverted carbon and methane to account for non-equilibrium factors. This model allowed predicting product gas compositions, heating value and cold gas efficiency.

Melgar et al [171] proposed a mathematical model, which combined chemical equilibrium and thermal balance, in a downdraft biomass gasifier. According to the authors, this model helps to predict the behavior of different biomasses, and is a potentially useful tool for optimizing the design and operation of downdraft biomass gasifiers.

While most of the non-stoichiometric models analyzed in the technical literature, consider gasification under atmospheric pressure, Srinivas et al [172] examined a pressurized gasifier. This gasifier operates with compressed air and steam injection. According to this thermodynamic based analysis, there is a moderate effect of gasifier

pressure on gas composition. As a result, it is expected that gasifier pressure affects the heating value of the syngas produced, its temperature, and the exergy efficiency.

Moreover, most of the reported thermodynamic studies are on the air gasification of biomass. There is scarcity for a comprehensive equilibrium model for biomass steam gasification. Salaices et al [18] developed a comprehensive thermodynamic model for biomass steam gasification at atmospheric pressure. Elevated reactor pressure after biomass conversion was not considered in their model. In the present study, thermodynamic analysis of biomass steam gasification is conducted accounting for the equilibrium reactor pressure. This allows to make rigorous comparison between the equilibrium predictions and experimental results.

2.8 **Kinetic Modelling of Biomass Steam Gasification**

Steam gasification of biomass is a complex network of heterogeneous reactions. One can envision biomass gasification as a combination of primary and secondary reactions. *Primary* reactions break down the vaporized biomass molecules, forming coke and permanent gases:
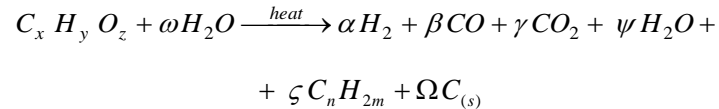
$$C_x\,H_y\,O_z + \omega H_2O \xrightarrow{\ heat\ } \alpha H_2 + \beta CO + \gamma CO_2 + \psi H_2O +$$
$$+\ \varsigma\, C_n H_{2m} + \Omega C_{(s)}$$

Secondary reactions crack the higher hydrocarbons into gases that further combust or become reduced:

$$C_n\,H_{2m}\ + nH_2O \longrightarrow nCO + (n+m)\,H_2$$

Furthermore, permanent gases react to alter the gas composition depending on gasifier conditions as indicated below:

$$CO + H_2O \longleftrightarrow H_2 + CO_2$$
$$CH_4 + H_2O \longleftrightarrow CO + 3H_2$$
$$CH_4 + CO_2 \longleftrightarrow 2CO + 2H_2$$

$$C + H_2O \longleftrightarrow H_2 + CO$$

$$C + CO_2 \longleftrightarrow 2CO$$

$$C + 2H_2 \longleftrightarrow CH_4$$
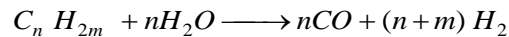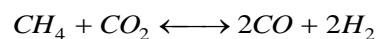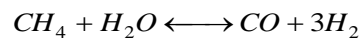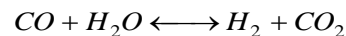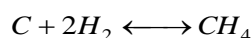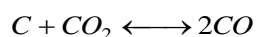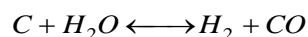
One can also provide a description of steam gasification on the basis of a single overall stochiometry where chemical species are grouped in "lumps" (char, gases and tar):

$$C_xH_yO_z + nH_2O \xrightarrow{\mathsf{T}} C_{x'}H_{y'}O_{z'} + gases + tar$$
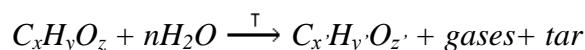
One possible approach towards successful gasification kinetic modelling is the use of biomass particles of a small enough size to ensure that the intrinsic kinetic is the controlling step. Another useful strategy is to use biomass surrogates such as glucose and/or phenolic species that allow the simulation of the main components of biomass (e.g. cellulose and lignin).

Various kinetic models of different complexity describing the gasification of various biomass feeds were proposed in the technical literature [173–178]. These models utilize subsets of reactions under a wide range of gasification conditions. In general, studies consider: (i) the kinetically limited steam reforming of methane, and (ii) the close to equilibrium water–gas shift reaction.

However, one can see that one of the main shortcomings of the proposed gasification kinetic models is that they lump together a complex network of heterogeneous reactions into one single kinetic rate equation. While this, in principle, circumvents the over-parametrization problem, the resulting rate equations provide an empirically fitted kinetics. These empirical models have little or no connection with the phenomenological events such as adsorption or intrinsic chemical reaction. In a previous study, Salaices et al [179] established that kinetic models for catalytic biomass steam gasification could be successfully developed using sound reaction engineering principles. Reaction rates for various species were expressed as the algebraic addition ("additive effect") of the dominant reactions. Based on their experimental studies, they considered water-gas shift, steam reforming of methane and dry reforming of methane as the dominant reactions. Mechanisms of these reactions are reviewed in detailed in the following sections:

2.8.1   Mechanism of Water Gas Shift (WGS)

Due to the industrial significance of the water gas shift (WGS) reaction, many researchers have investigated the reaction mechanism and developed kinetic models to reflect the behavior of the reaction over commercial industrial catalysts (i.e., copper, iron, or nickel-based). The results of several of these investigations suggest that the WGS reaction occurs largely via four specific mechanisms [180–182]: i) the *redox* mechanism; ii) the *formate* mechanism; iii) the *associative* mechanism; and iv) *the carbonate* mechanism.

The *redox* mechanism implies successive oxidation and reduction of the reactive catalyst surface by adsorbed oxygen (from water) and carbon monoxide (as it is oxidized to carbon dioxide), respectively.

$$H_2O + S \longrightarrow O \cdot S + H_2$$

$$O \cdot S + CO \longrightarrow CO_2 + S$$
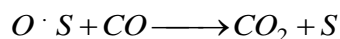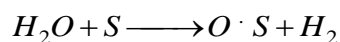
where S represents a surface site.

In the *formate* mechanism, adsorbed water dissociates into an adsorbed hydroxyl group and an adsorbed atomic hydrogen. The hydroxyl group then combines with adsorbed carbon monoxide to form adsorbed formate, which eventually decomposes into carbon dioxide and hydrogen, yielding the WGS products.

$$H_2O \cdot S + S \longrightarrow OH \cdot S + H \cdot S$$

$$CO \cdot S + OH \cdot S \longrightarrow HCOO \cdot S + S$$

$$HCOO \cdot S + S \longrightarrow CO_2 \cdot S + H \cdot S$$
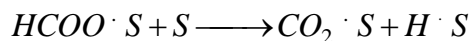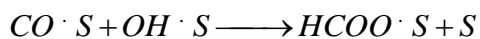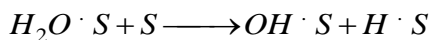
Campbell and Daube [182] explored the WGS reaction in terms of the *formate* mechanism, as given in Table 2.9:

Table 2.9: Formate Mechanism of WGS Reaction [182]

Formate Reaction Mechanism	
Step 1	$CO + S \longrightarrow CO \cdot S$
Step 2	$H_2O + S \longrightarrow H_2O \cdot S$
Step 3	$H_2O \cdot S + S \longrightarrow OH \cdot S + H \cdot S$
Step 4	$CO \cdot S + OH \cdot S \longrightarrow HCOO \cdot S + S$
Step 5	$HCOO \cdot S + S \longrightarrow CO_2 \cdot S + H \cdot S$
Step 6	$2H \cdot S \longrightarrow H_2 + 2S$
(overall)	$CO + H_2O \longrightarrow CO_2 + H_2$

An experimental investigation of the catalyst surface suggested that CO and H_2O coverage are very low under reaction conditions. This yields rates that are nearly independent of the partial pressure of CO and strongly influenced by the partial pressure of H_2O. The adequacy of this model was explained by the consideration of a hydroxyl intermediate formed from the surface dissociation of adsorbed water. Furthermore, in step 3, the dissociation of H_2O to form a surface hydroxyl and an adsorbed hydrogen atom were identified as the rate-limiting step. Campbell and Daube [182], also considered a *surface redox* mechanism in which the OH·S produced in step 3 of the *formate* mechanism further dissociates into O·S and H·S. The O·S was then assumed to be consumed rapidly by adsorbed CO in the following step:

$$CO \cdot S + O \cdot S \longrightarrow CO_2 + 2S$$
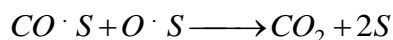
This alternate mechanism also assumes that step 3 is rate-limiting and is reinforced by the experimental findings. That is to say, the surface reaction proceeds rapidly to equilibrium. Campbell and Daube [182], also utilized the analytical expression proposed

earlier by van Hewijnen and de Jong [180], to correlate and predict their experimental results accurately. Assuming Langmuir adsorption, the numerical data are manipulated to indicate the form of the rate expression. The rate is reported, in general, as:

$$r_{WGS} = \frac{k_{WGS} \, p_{CO} \, p_{H_2O}}{1 + K^A_{CO_2} \, p_{CO_2} + K^A_{H_2O} \, p_{H_2O} + K^A_{H_2} \, p_{H_2} + K^A_{CO} \, p_{CO}} \left(1 - \frac{p_{CO_2} \, p_{H_2}}{K_{WGS} \, p_{CO} \, p_{H_2O}} \right) \quad (2.1)$$

where $k_{WGS} \, and \, K_{WGS}$ are the intrinsic kinetic constant and equilibrium constant of the water gas shift reaction, K^A_i represents the adsorption constants and p is the partial pressure.

In the third possible *associative* WGS reaction mechanism, adsorbed water dissociates into an adsorbed hydroxyl group and atomic hydrogen. The adsorbed hydroxyl then oxidizes the adsorbed carbon monoxide resulting in adsorbed carbon dioxide and atomic hydrogen.

In addition to the *redox*, *formate*, and *associative* mechanisms, researchers have also proposed that the WGS reaction may proceed via a *carbonate* species. Moreover, in attempts to model and predict the real behavior of the WGS reaction, some researchers have considered more general mechanisms often comprising of elementary reaction steps from the more recognized mechanisms as follows:

$$H_2O \cdot S + S \longrightarrow OH \cdot S + H \cdot S$$

$$CO \cdot S + OH \cdot S \longrightarrow CO_2 \cdot S + H . S$$

$$HCOO \cdot S + S \longrightarrow CO_2 \cdot S + H . S$$
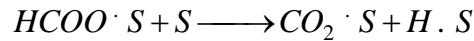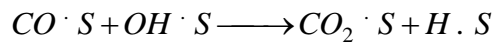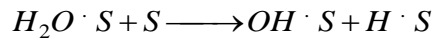
For the present study, the WGS reaction is assumed to occur via the *formate* mechanism assuming Langmuir adsorption.

2.8.2   Mechanism of Steam Reforming of Methane (SRM)

The chemical processes involved in the steam reforming of methane can be expressed using the following endothermic reforming reaction:

$$CH_4 + H_2O \longleftrightarrow CO + 3H_2$$
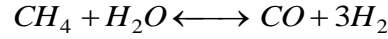
A considerable number of rate expressions for the steam reforming of methane have been proposed in literature. These kinetic models range in complexity from simple first order expressions that are dependent on methane and contain only two parameters to complex Langmuir-Hinshelwood models with over 10 parameters [183–185]. It is generally accepted that the rate of methane reforming displays a first order dependency on methane. Furthermore, it is also agreed that the rate determining step in the reforming process is the formation of adsorbed carbon [185].

$$CH_4 + * - \text{Metal site} \longleftrightarrow C_{Ads} - * + 2H_2$$
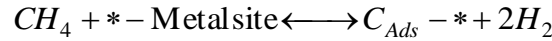
The formation of adsorbed carbon from methane is a stepwise process that requires a C-H bond to be broken while methane is in the gas phase. The resultant CH_3 species must then come into contact with an open site on the surface of the metal crystal. After being adsorbed to the surface of the metal crystal, the CH_3 is transformed into adsorbed carbon by stepwise dehydrogenation.

$$CH_4^{gas} \rightarrow CH_3^{gas} \rightarrow CH_3 - * \rightarrow CH_2 - * \rightarrow CH_1 - * \rightarrow C_{Ads} - *$$
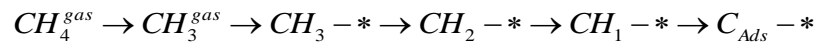
The kinetic expression reported by Munster and Grabke [185] was adopted for the steam reforming of methane reaction in the present study. In this model, adsorption of methane is assumed to play a role in determining the apparent rate of methane consumption as follows:

$$r_{CH_4} = \frac{k_{SRM} \, K^A_{CH_4} \, p_{CH_4}}{1 + K^A_{CH_4} \, p_{CH_4}} \left(1 - \frac{p_{CO} \, p^3_{H_2}}{K_{SRM} \, p_{CH_4} \, p_{H_2O}} \right) \tag{2.2}$$

where k_{SRM} and K_{SRM} are the intrinsic kinetic constant and equilibrium constants; K^A_i is the adsorption constant and p is the partial pressure.

In addition, the formation of an adsorbed carbon species is assumed to be the direct result of methane adsorption to the nickel crystal surface. The products, hydrogen and carbon monoxide, are not adsorbed. Water reacts directly with the adsorbed carbon species.

2.8.3   Mechanism of Dry Reforming of Methane (DRM)

Various rate models for the dry reforming of methane were fitted to the experimental data by numerically integrating the rate equations [159,186]. The best agreement was obtained with a rate model based on simplified noncompetitive Langmuir-Hinselwood [159], which is the mechanism adopted in the present study. This mechanism assumes that carbon dioxide is associatively adsorbed on the catalyst surface under adsorption equilibrium conditions. The slow and rate-determining step is the reaction of the adsorbed species with the other gas phase chemical species from the gas phase, which leads directly to the products.

Reaction steps of the considered mechanistic model include the following:

$$CO_2 + * \xleftrightarrow{\quad K_{CO_2} \quad} CO_2 - *$$

$$CO_2 - * + CH_4 \xleftrightarrow{\quad k_{ref} \quad} 2CO + 2H_2 + *$$
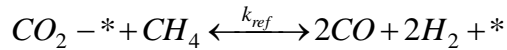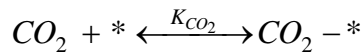
$$r_{DRM} = \frac{k_{DRM}\, P_{CO_2} P_{CH_4}}{1 + K^A_{CO_2} P_{CO_2}} \left(1 - \frac{P^2_{CO}\, P^2_{H_2}}{K_{DRM}\, P_{CO_2} P_{CH_4}} \right) \tag{2.3}$$

where $k_{DRM}\ and\ K_{DRM}$ are the intrinsic kinetic constant and equilibrium constant of the dry reforming of methane reaction; K^A_i is the adsorption constant and p is the partial pressure.

2.9 **Conclusions**

Based on the literature survey presented, the following are the main conclusions:

a) There is a great interest to develop and commercialize new catalysts for making biomass steam gasification in fluidized beds, a viable option. Disposable catalysts for steam biomass gasification such as dolomite and olivine are a possible alternative. These naturally occurring materials have attracted much attention since they are cheap and disposable. The main issue with them is that they are not specifically manufactured for the challenging conditions of fluidized beds: fluidization may be poor and attrition may be high.

b) Biomass steam gasification using synthetic catalysts is also a most valuable option with great potential. In particular, nickel based catalysts with adequate fluidizable supports and/or with the addition of dopants appears to open excellent possibilities for catalytic biomass gasifiers. These nickel-based catalysts can be specifically engineered to have the desired catalytic functions and the physical properties for low attrition and good fluidization.

c) Thermodynamic analysis provides a valuable tool for assessing the effect of various operating conditions in biomass gasifiers. Thermodynamic models help identify operating conditions leading to high hydrogen yields or to a synthesis gas of high H_2/CO ratio such as the one required for methanol synthesis. Thermodynamic models present limitations in terms of tars predictions and their applicability for short contact times.

d) The establishment of intrinsic kinetic models for steam gasification of biomass requires new approaches. One good example is the model proposed by Salaices et al [179] where the main gasification reactions are included as an algebraic addition of chemical reaction events.

CHAPTER 3

EXPERIMENTAL METHODS

3.1 Introduction

CHAPTER 3 describes the experimental procedures and methods involved in the preparation, characterization and reactivity evaluation of fluidizable Ni-based catalysts for the steam gasification of biomass. Section 3.2 reports catalyst preparation procedures. Following this, the background theory and the experimental procedures of various physiochemical techniques used to characterize the prepared catalysts are described in Section 3.3. Section 3.4 provides a detailed description of the fluidized bed CREC Riser Simulator reactor system and the experimental procedures considered for catalytic steam gasification of biomass surrogate species. In addition, a description of the analytical system used to quantify the reaction products is also included.

3.2 Catalyst Preparation

In this study, fluidizable Ni-based catalysts for biomass steam gasification were prepared via an 'incipient wetness' technique under vacuum conditions. According to El Solh [187], the incipient wetness technique offers proper control of the metal loading and also provides a higher degree of nickel reducibility. This is a simple and most frequently used procedure to prepare stable supported Ni catalysts at a commercial scale.

Two high surface area γ-Al_2O_3 samples are considered as the support: Alcan AA-100 Powder (Alcan Inc.) and Sasol Catalox® SSCa5/200 (Sasol North America Inc.). The γ-Al_2O_3 support was modified with La_2O_3 to control the thermal sintering, acidity and basicity of the metastable alumina phase. $Ni/La_2O_3/\gamma$-Al_2O_3 catalysts were prepared using successive impregnation: γ-Al_2O_3 was modified by adding La_2O_3, and following this, Ni was added on the modified γ-Al_2O_3 support. $La(NO_3)_3.6H_2O$ (CAS 10277-43-7) and $Ni(NO_3)_2 \cdot 6H_2O$ (CAS 13478-00-7) received from Sigma-Aldrich were used as precursors for the desired metal loading.
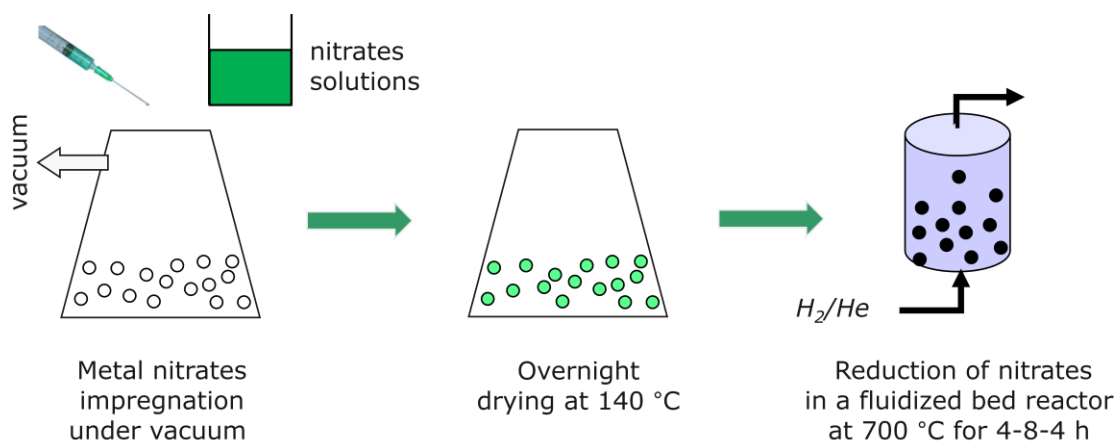
Figure 3.1: Schematic diagram of catalyst preparation procedure

Three main steps were involved in the catalyst preparation: a) support impregnation, b) drying, c) metal precursor's reduction. A schematic description of catalyst preparation steps is shown in Figure 3.1. The impregnation step was carried out in a quartz conical flask with a lateral outlet, which was connected to a vacuum system. In each batch, 20 g of support were added into the conical flask and its inlet was sealed with a rubber septum to maintain vacuum conditions throughout the impregnation process. The sample was stirred under a vacuum for 30 min to remove the trapped gases inside the porous support before impregnation.

An aqueous solution of La or Ni nitrate was prepared by dissolving a desired amount of the nitrate in water. The required amount of water was calculated based on the pore volume of the support. Following the support evacuation, the prepared nitrate solution was introduced drop-by-drop, contacting the support under vacuum and continuous mixing conditions. After adding the solution, the stirring was continued for an additional hour. Following this, the impregnated support was dried slowly at 140 °C overnight. The dried powder, was then transferred into the specially designed fluidized bed reactor and placed in a Thermolyne 48000 furnace in order to reduce the metal nitrate. During the reduction step, the reactor temperature was raised from ambient to 750 ^{o}C over 4 h and maintained at 750 ^{o}C for 8 h under the flow of a reducing gas mixture (10% hydrogen balanced with helium). Moreover, Ni was loaded employing multi-step impregnation to

reduce the nickel-aluminate formation as well as to increase the dispersion. Thus, impregnation, drying and reduction steps were repeated until the desired metal loading was attained.

The amount of La_2O_3 loading was varied from 0 to 15 wt% to study the effect La_2O_3 loading. Furthermore, concerning the nickel addition, it should be stated that an increase in the active metal content results in higher reactivity. However, excessive metal can cause the destabilization of the catalyst via metal sintering, phase transformation and particle agglomeration. This not only reduces the catalyst reactivity drastically, but also defluidizes the bed. The maximum limit of cumulative Ni loading was selected to be 20 wt%, aiming for a possible higher activity of biomass [188].

Table 3.1: Description of the Alcan γ-Al_2O_3 supported Ni (20 wt%) catalysts (H_2/He flow during catalyst reduction: 6 ml/mmol nitrates/min)

Sample	Nitrates decomposition method	La_2O_3 Loading (wt %)
Cat A	calcination	5
Cat B	reduction	0
Cat C	reduction	5
Cat D	reduction	10

Eight sets of Ni catalysts were prepared as described in Table 3.1 and Table 3.2. Cat B, Cat C and Cat D were supported on the Alcan γ-Al_2O_3 support containing 0, 5 and 10 wt% La_2O_3 respectively. Conventionally, Ni catalysts are prepared via decomposition of impregnated metal salts by high temperature calcination in air followed by metal oxide reduction under hydrogen. In this study, catalysts were prepared via direct reduction of metal salts in a fludized bed condition. In order to establish the value of the preparation method used, one set of catalyst was prepared using the conventional method (Cat A).

Table 3.2: Description of the Sasol γ-Al_2O_3 supported Ni (20 wt%) catalysts synthesized via direct reduction of metal nitrates

Sample	$La(NO_3)_3$ reduction gas flowrate (ml/mmol/min)	$Ni(NO_3)_2$ reduction gas flowrate (ml/mmol/min)	La_2O_3 Loading (wt %)
Cat E	8	2	5
Cat F	-	6	0
Cat G	16	6	5
Cat H	26	12	5

It was found that gas flow rate during catalysts reduction is a key preparation parameter. It determines the heat distribution and fluidization conditions inside the catalyst reduction chamber. To study the effect of reduction gas flow, several catalysts were prepared varying the reduction gas flow: a) Cat E using low flow (fixed bed condition), b) Cat F and Cat G using moderate flow (non-uniform fluidization), and c) Cat H using high flow (uniform fluidization).

3.3 Catalyst Characterization

Physicochemical characterization of the catalyst helps to predict structural properties and metal-support interactions. Moreover, the characterization of the supported metal catalyst is essential to understand its operation, and to compare its performance in a meaningful way with other catalyst samples. Thus, several physical and chemical properties of the prepared catalysts were evaluated using the characterization techniques described in the following sections.

3.3.1 Particle Size Distribution

Fluidizability is an important characteristic that a catalyst should have, for its application in a fluidized bed gasifier. Therefore, it is important to analyze the particle size and size distribution of the prepared catalyst to confirm its adequacy for fluidized bed conditions.

Besides the fluidization properties, the size of particles also plays a significant role in gas-solid reactions. On the other hand, excessively smaller particles can cause fluidization problems, channeling and loss of fines. Considering the importance of the above mentioned facts, the particle size of the prepared catalysts was determined using a Malvern Mastersizer 2000 size analyzer. During the measurement process, suspended dry particles were passed through a focused laser beam. The particles scatter light at an angle, which is inversely proportional to their size.

3.3.2 N_2 Physisorption

The specific surface area is another essential physical property of the supported metal catalyst involved in heterogeneous reactions. This is one of the important parameters that determine the dispersion of the active sites onto the support. The N_2 adsorption-desorption isotherm method is a well-known techniques to determine the specific surface area of a porous catalyst. Apart from surface area measurement, this nitrogen adsorption-desorption isotherm can also provide important structural properties of the material in terms of pore size distribution and pore geometry.

The specific surface area, the average pore diameter and pore volume of the prepared catalysts were determined in a Micromeritics ASAP 2010 Analyzer by using N_2 adsorption at 77 K. Before the analysis, 0.1–0.2 g of a catalyst sample was degassed at 200 °C until the pressure reached below 5 mm Hg. The adsorption-desorption isotherms were measured in a 10^{-6}–1 relative pressure ranges. The total pore volume was determined from the amount of N_2 desorption. The average pore size was estimated assuming cylindrical pore geometry and by using the relation, Pore diameter= (4 x pore volume/surface area). The pore size distribution was obtained by analyzing the desorption branch of the isotherm.

3.3.3   Temperature Programmed Studies

Temperature programmed reduction (TPR), temperature programmed oxidation (TPO), temperature programmed desorption (TPD) and pulse chemisorption experiments were conducted using a Micromeritics Autochem II 2920 Analyzer. In each experiment, 100 to

200 mg of catalyst sample was placed in a U-shape quartz tube and the tube was installed inside the heating chamber of the analyzer.

3.3.3.1 *Temperature Programmed Reduction (TPR)*

The TPR test provides valuable information about the reduction characteristics of a catalyst. Catalysts are subjected to repeated oxidation and reduction cycles in a gasifier. Regenerability of a catalyst depends on its metal reducibility and reduction temperature. TPR was performed to determine the amount of reducible species and the temperature range at which reduction occurs.

Before the hydrogen TPR experiments, the sample was pre-oxidized using a gas containing 5% oxygen in helium at 750 °C. The oxidized sample was, then, cooled down under argon flow to remove any gas phase oxygen trapped in the catalyst particles. Following this step, the sample reduction was performed using a gas containing 10% hydrogen in argon. This gas was circulated throughout the catalyst bed at a rate of 50 ml/min. While the gas was flown through the particle bed, the bed temperature was raised progressively from ambient to 950 °C at a rate of 10 °C/min. The gas leaving the quartz reactor was circulated through a cooling loop in order to remove the water (produced during the reduction reaction) before it reached a thermal conductivity detector (TCD). The cooling loop was refrigerated using a mixture of liquid nitrogen and iso-propanol. Once the bed temperature reached the reduction temperature, hydrogen reacted with the oxide(s) present in the sample. A thermal conductivity detector (TCD) was used to analyze the water-free exit gas concentration. The amount of hydrogen consumed (V_{H_2}) in the reduction of the catalyst sample was determined from the TCD signal. The reacted hydrogen was further related to the number of reducible species (Ni) in the catalyst sample as follows:

$$W_{Ni} = \frac{MW_{Ni}V_{H_2}}{v\rho_g} \tag{3.1}$$

where, MW_{Ni} represents the molecular weight of the reducible species (g), V_{H_2} stands for the volume of H_2 consumed at STP (cm^3), V_g denotes the gas molar volume at STP (cm^3/mol) and W_{Ni}^a represents the actual metal amount on the oxygen carrier (g). ν stands for the stoichiometric number based on the following reaction stoichiometry: $NiO + H_2 \rightarrow Ni + H_2O$.

The percentage reduction (R) was then calculated as follows:

$$R(\%) = \frac{W_{Ni}}{W_O} \times 100\% \qquad (3.2)$$

where, W_o represents the actual metal amount in the catalyst sample.

3.3.3.2 Temperature Programmed Oxidation (TPO)

The TPO examines the extent to which a catalyst can be oxidized or was previously reduced. During the present research, TPO experiments were developed following a TPR experiment. This was done, in order to re-oxidize the sample previously reduced in the TPR cycle. Before starting a TPO run, the system was cooled down to room temperature. During the cooling period, an inert gas (helium) flow was maintained to flush out any unreacted hydrogen from the system.

The steps of TPO were exactly the same as the ones of a TPR with the exceptions that in this case, the flowing gas stream had a composition of 5% O_2 and 95% He and the bed temperature was increased up to 700 °C. As with the TPR, the total amount of consumed O_2 calculated from processed TCD data, was used to measure the percentage of metal oxidation.

3.3.3.3 H₂ Pulse Chemisorption

H$_2$ pulse chemisorption was conducted to determine the active metal surface, the percent metal dispersion and the average active metal crystal size based on the monolayer of gas adsorbed on the catalyst. Regarding metal dispersion, it is important to mention that it can vary depending on several factors, such as: a) the type of metal/support selected, b) the

specific surface area of the support chosen, c) the sample preparation methods and d) the effects of the promoter employed.
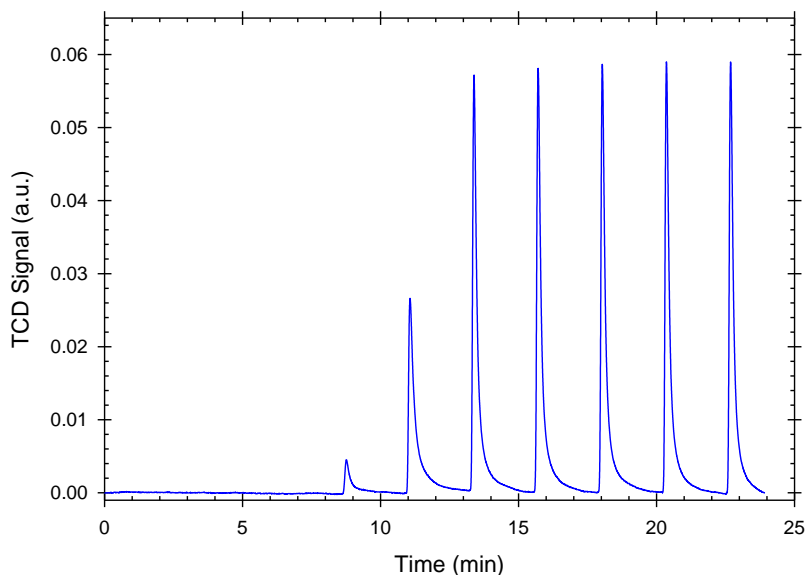
Figure 3.2: Typical TCD profile for H_2 pulse chemisorption experiments, where each peak pepresents the eluted hydrogen after each injection

H_2 pulse chemisorption was performed at ambient temperature following the TPR experiments. After reduction, a stream of argon gas was flown through the sample bed at a rate of 50 ml/min. Hydrogen gas was then injected as a series of consecutive pulses containing 1.0 ml each using a calibrated loop with a 1.5 min delay between each gas sequential injection. Each pulse generated a TCD peak which was recorded at the exit of the gas stream as shown in Figure 3.2. Peak areas changed for each injection as a result of the H_2 chemisorbed amount. When two consecutive peaks yielded essentially the same area (less than 1% difference), the sample was considered saturated with hydrogen. As a result, the total amount of hydrogen required for saturation was calculated as $X = \sum_i (N_{H2,in} - N_{H2,out})$. This X value describes the total hydrogen amount chemically adsorbed on the active sites of the catalyst. X can be used to calculate the percent metal dispersion as follows:

$$\% D = \frac{117 X}{W \times R} \tag{3.3}$$

where D is the metal dispersion, X stands for the total hydrogen chemisorbed (μmol of H$_2$ / g of catalyst), W denotes the metal wt% in the sample and R constitutes the percentage of metal reducibility.

Furthermore, the average crystal size (d$_v$) of the metal on the support was calculated from the percent metal dispersion using the following equation:

$$d_v = \frac{\varphi V_m}{S_m} \times \frac{1}{\% D} \tag{3.4}$$

where, φ represents the particle shape constant, V_m stands for the volume of metal atoms (nm^3) and S_m denotes the average surface area (nm^2) of metal particles exposed per surface metal atom.

3.3.3.4   *NH$_3$/CO$_2$ Temperature Programmed Desorption (TPD)*

Determining the quantity and strength of the acid sites on the support phase (γ-Al$_2$O$_3$) is of great importance for understanding and predicting the performance of the supported Ni catalyst. NH$_3$-TPD is one of the most widely used techniques to characterize the acid sites on oxide surfaces. Before the TPD experiment, the catalyst sample was pre-treated by flowing He or H$_2$ (in case of Ni loaded samples) through the bed at 700 ^{o}C. The catalyst sample was then brought to saturation by flowing a stream of gas containing 5% NH$_3$ in Helium at 50 ^{o}C for 1 hr. After NH$_3$ adsorption, the sample was purged by He again for 1 hr at the adsorption temperature. During the desorption, the temperature in the bed was raised at a linear rate (15 °C/min) from ambient to 950 °C while a stream of inert He gas was flown through the bed. Once the temperature in the bed overcame the energy of desorption, NH$_3$ was desorbed from the sample surface. A TCD detector was used to analyze the gas leaving the catalyst sample. The amount of desorbed NH$_3$ was calculated from the calibrated TCD signal. The total acidity of the catalyst sample is related directly to the amount of desorbed NH$_3$.

In order to establish the basicity and CO$_2$ adsorption capacity of the catalyst samples, CO$_2$-TPD was performed using a similar procedure as used for NH$_3$-TPD. After the pre-

treatment, CO_2 was chemisorbed onto the samples by flowing a stream of gas containing 10% CO_2 in Helium at 45 ^{o}C for 1 hr. Then, the samples were purged under He flow for another 30 min. Following this, CO_2-TPD profiles were recorded using a TCD detector up to 950 °C. In this case, a heating rate of 20 °C/min was used.

3.3.4   Pyridine FTIR

Pyridine FTIR was performed to evaluate the nature and strength of acid sites of the prepared catalysts using a Bruker IFS55 FTIR Spectrometer. Before pyridine adsorption, the samples were heat treated at 500 °C under N_2 flow for 2 hrs and then cooled to 100 °C. Following this, the samples were saturated using a N_2 gas stream containing pyridine for one hr. In the next step, the catalyst samples were purged with pure N_2 at 100 °C for 1 hr, to remove weakly adsorbed pyridine. Finally, diffuse reflectance infrared spectroscopy (DRIFTS) measurements were recorded at room temperature using the Bruker IFS55 FTIR Spectrometer having a 4 cm^{-1} resolution and data averaging over 100 scans.

3.3.5   X-ray Diffraction Analysis

XRD is one of the most widely used techniques for the identification of the crystalline structures in the supported metal catalyst. X-ray powder diffraction patterns were obtained on a Rigaku Miniflex Diffractometer using Ni filtered Cu Kα (λ = 0.15406 nm) radiation. A tube voltage of 40 kV and a tube current of 20 mA were used for each sample. The samples were scanned every 0.02° from 10 to 100° with a scan time constant of 2°/min. Identification of the phase was made with the help of the Joint Committee on Powder Diffraction Standards (JCPDS) files. The crystallite sizes of Ni were calculated using Scherrer's equation:

$$d = \frac{0.94\,\lambda}{(\beta - \beta_o)cos\theta} \tag{3.5}$$

where, d is the volume average diameter of the crystallite and $(\beta - \beta_o)$ is the full width at half maximum intensity of the peak.

3.4 **Biomass Steam Gasification in a CREC Riser Simulator**

3.4.1   **Biomass Surrogate Species**

Cellulose is a main carbohydrate constituent of biomass. Typically, cellulose content in biomass ranges from 22.5 to 50.3 wt% [13]. Cellulose is a polymer of glucose with a repeating unit of $C_6H_{10}O_5$ connected by ß-glycosidic linkages as shown in Figure 3.3. On this basis, glucose was chosen as a model compound for the cellulose contained in biomass, to evaluate the steam gasification performance of the prepared catalysts.
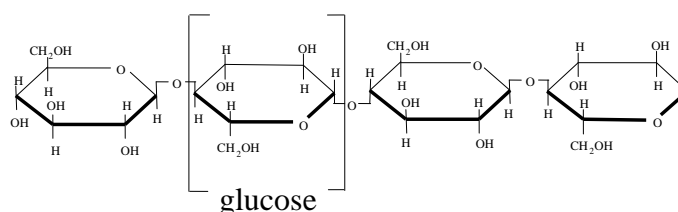
Figure 3.3: Chemical linkage in a cellulose polymer

On the other hand, lignin is the major noncarbohydrate, polyphenolic structural constituent of biomass. It is known as the main contributor to tar formation during the gasification process. Typical lignin content of biomass ranges from 10.9 to 28.8 wt%. It is a highly polymeric substance, with a complex, cross-linked, highly aromatic structure. Figure 3.4 shows the building blocks of the lignin polymer with three carbon chains attached to the rings of six carbon atoms. Therefore, the 2-methoxy-4-methylphenol, a typical monomeric structure in lignin as shown in Figure 3.4,   was selected as a model compound for representing biomass lignin content.
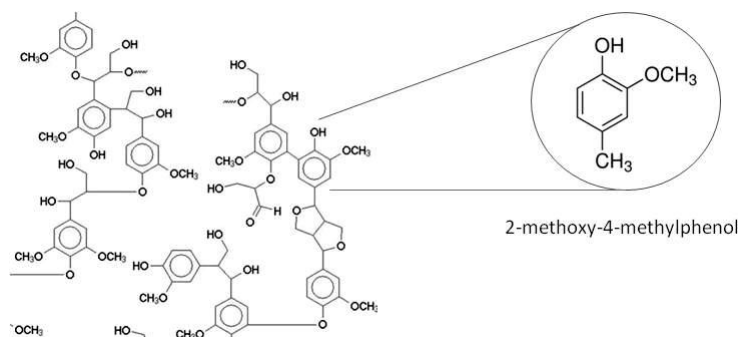
Figure 3.4: Chemical linkage in a lignin polymer

3.4.2 Experimental Setup

Thermal and catalytic steam gasification of glucose (a cellulose surrogate) and 2-methoxy-4-methylphenol (a lignin surrogate) experiments were developed using a CREC Riser Simulator [69]. The reactivity and regenerability of the prepared catalysts were evaluated under the operating conditions of an industrial fluidized bed gasifier. The CREC Riser Simulator is a bench-scale mini fluidized bed reactor with a volume of 50.7 cm^3. This mini fluidized reactor is especially designed for catalyst evaluation and kinetic studies under fluidized bed conditions.
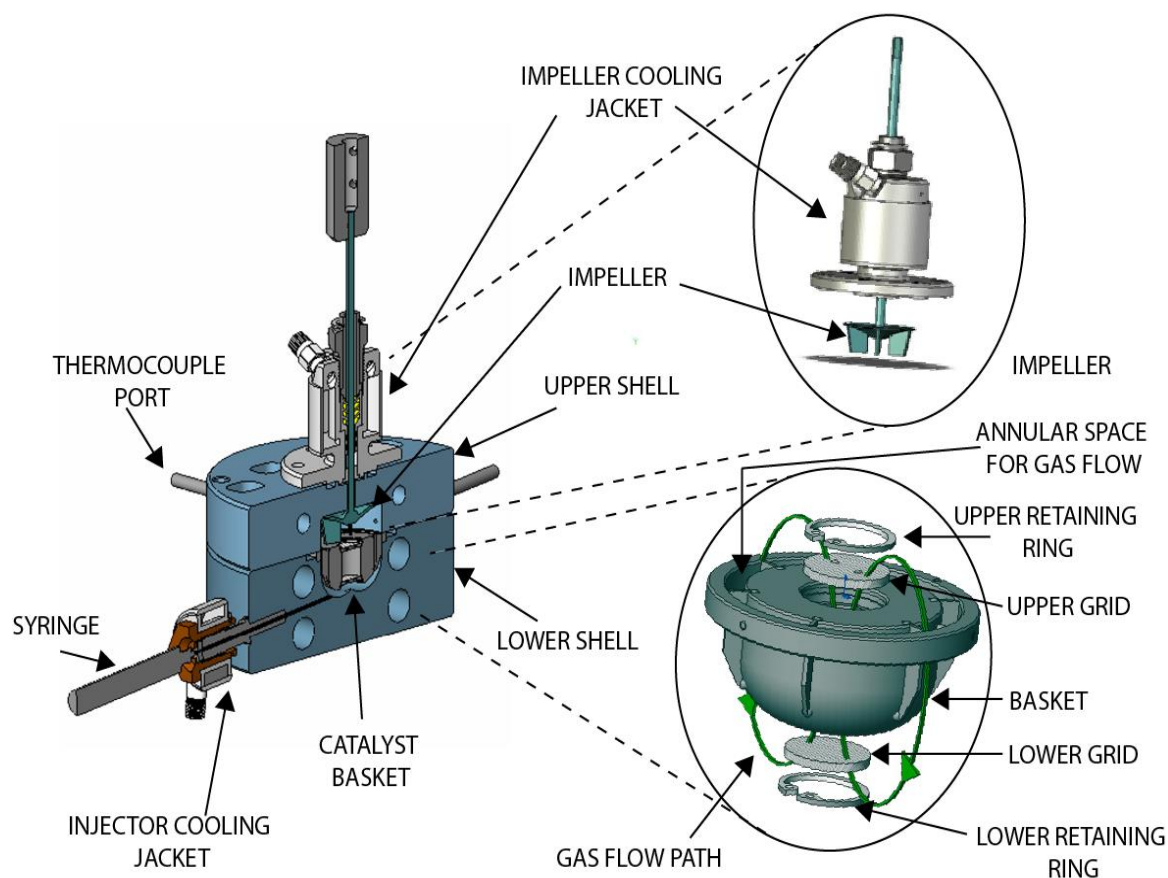
Figure 3.5: Sectional view of the reactor with detail assembly of the catalyst basket and impeller. The green line shows the gas flow path on rotation of the impeller.

The design and assembly of the different components of the CREC Riser Simulator is presented in Figure 3.5. It consists of two sections: the upper shell and the lower shell. These two shells allow easy access to load and unload catalyst in the reactor. The lower shell houses the reactor: half-moon shape hole that contains the catalyst basket. Two grids bind the solid containing basket, each at the top and bottom of the basket in order to trap the catalysts and to constrain their mobility within the basket.

A special design of the reactor allows creating an annular space between the outer portion of the basket and inner part of the reactor shell. This annular space facilitates the recirculation of the gaseous reactant/product/carrier by the rotation of a high-speed impeller positioned above the catalyst basket. A metallic gasket is used to seal the upper and lower shells of the reactor. Upon the rotation of the impeller at high speed (up to 6000 rpm), gas is forced both outward into the reactor section and downwards into the outer reactor annulus, causing the catalyst to become fully fluidized. An intense gas mixing inside the reactor can also be achieved by the high-speed rotation of the impeller.

The CREC Riser Simulator operates in conjunction with some other accessories, such as a vacuum box, sampling valves, a timer, two pressure transducers, two temperature controllers and a gas analysis system. A schematic diagram of the gasification experimental setup is illustrated in Figure 3.6.

The vacuum box, a stainless steel cylinder with a capacity of 1098.8 cm^3, is connected to the reactor by a four-port valve that enables the connection-isolation of the reactor and the vacuum box. A timer is connected to an actuator, which operates the four-port valve. The timer is used to set the reaction time for an experimental run. It starts with the manual injection of the feed, and when the preset time expires, various chemical species (recatants, products) are evacuated from the reactor to the vacuum box through the four-port valve. The evacuation process is almost instantaneous because of the significant pressure difference between the reactor and the vacuum box. Consequently, the reaction is terminated with the evacuation of chemical species from the reactor.
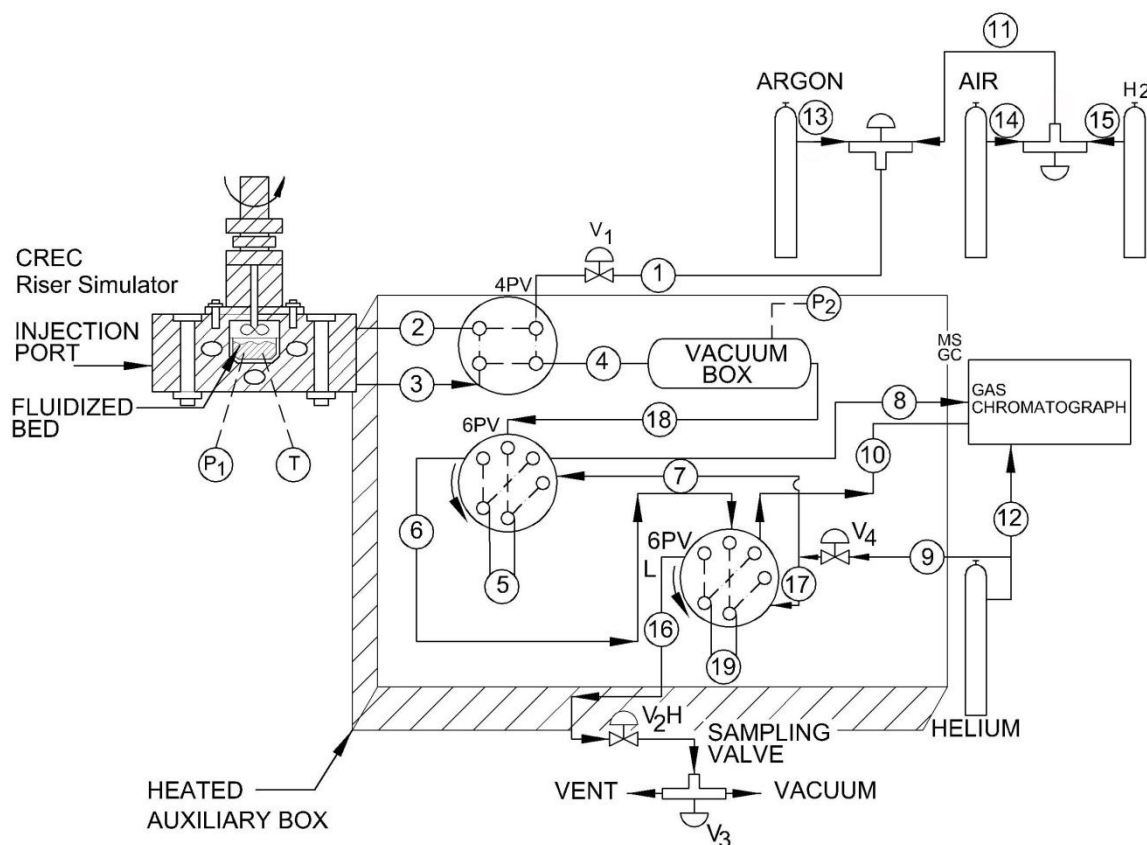
Figure 3.6: Schematic diagram of the gasification experimental Setup. The 4PV allows: i) the isolation of the reactor for gasification to take place (when 2-3 are connected) and ii) the reactor evacuation (when lines 3-4 are connected). The two 6PVs permit: i) loading sampling loops 5 and 19 with the lines 18-5-6 and 6-19-16 being connected, and ii) directing the sample to the capillary and packed-bed column of the GC system through connections 7-5-8 and 17-19-10, respectively.

Two pressure transducers (Omega DP series) are installed in both the reactor and vacuum box to allow the monitoring of the pressure during the experiment, as well as to make sure that complete and instantaneous evacuation occurs in the reactor. The pressure data of the reactor and vacuum box is saved on a computer disk using a Personal Daq acquisition card. Omega 400 KC temperature controllers are used in order to both display and control the temperature of various parts of the system which include the reactor, vacuum box, cooling jacket, flow lines.

As shown in Figure 3.6, the vacuum box in connected to the two sampling loops (5 and 19) using two 6-port valves. In the load position of the 6-port valves, both sampling loops are filled with reaction products. This path leads from the vacuum box to the vent/vacuum pump. The inject position connects the sample loops with the helium carrier gas supply, and sends the sample to the Shimadzu GC/MS and Shimatzu GC/TCD. The vacuum box temperature was set to 250 °C to avoid condensation of products. The temperature of the product transfer lines connecting the vacuum box and GCMS was also kept at 230 °C, using a heating tape.

3.4.3   Experimental Procedure

The Ni catalysts, already thermally treated during the preparation process, were loaded into the catalyst basket. The reactor system was sealed, leak tested and heated to the reaction temperature in an argon atmosphere. Then, the feed (glucose/2-methoxy-4-methylphenol and water) was injected, and once the reaction time was reached, the reaction products were evacuated from the reactor to the vacuum box. Reactor and vacuum box pressure data against time were recorded by the Personal Daq Acquisition Card.

Figure 3.7 displays the pressure changes in the reactor unit (upper curves) and vacuum box (lower curves) during glucose gasification. One can notice that as soon as the feed was injected, the pressure in the reactor increased sharply (first second) and then more gradually (remaining 20 seconds). These total pressure changes are likely due to the quick glucose solution vaporization and conversion (primary gasification reactions), followed by the much slower inter-conversion of gas phase species (secondary gasification reactions). Figure 3.7 also shows that as the temperature increases, higher reactor pressure readings were observed indicating higher gas yields.

From the vacuum box, gas samples were sent to a GCMS system via heated transfer lines. The GCMS system is equipped with a packed-bed column (HaysSep® D) and a capillary column (BPX5). The packed-bed column is connected to a thermal conductivity detector (TCD) and the capillary column is connected to a mass spectrometer (MS).
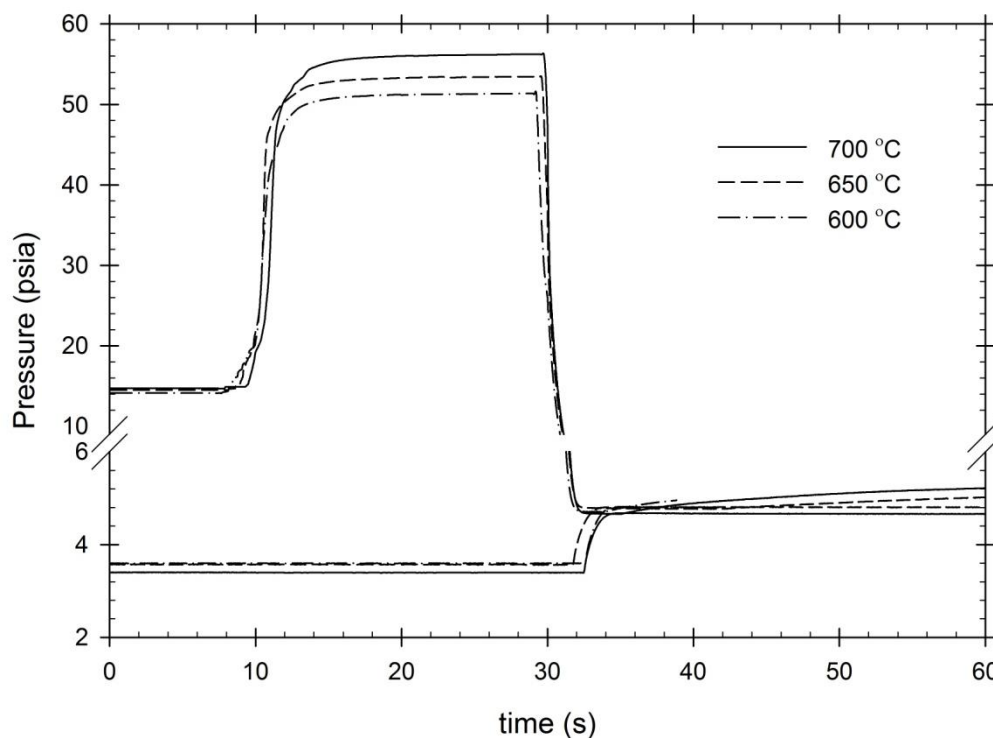
Figure 3.7: Pressure changes in the reactor and vacuum box of the CREC Riser Simulator during steam gasification of glucose at different temperatures. (S/B = 1.0 g/g and reaction time= 20 s).

To burn the coke deposited on the catalyst, a regeneration cycle was performed. The regeneration conditions were 10 min of air flow and 10 min of hydrogen flow (to re-reduce the catalyst). Under these conditions, coke was completely removed. Finally, the coke deposited on the used catalysts was measured as CO_2 in a Total Organic Carbon Analyzer (TOC-V) using a solid sample module (SSM-5000).

3.4.4 Analytical System

The gaseous products were analyzed in a Shimadzu GC/MS system with a thermal conductivity detector and a mass spectrometer. The biomass gasification products contained permanent gases, light and heavy hydrocarbons, as well as oxygenates. In the present study, C_{6+} organic compounds were considered as tars.

A Shimadzu 2010 GC/TCD (thermal conductivity detector) with a packed column HayeSep D 100/120 Pours Polymer, 30 ft x 1/8" O.D. S.S. was used for the separation of

permanent gases (H_2, CO, CO_2, CH_4), water, and light hydrocarbons up to C_6 hydrocarbons. A TCD signal was calibrated using certified standard gases. Figure 3.8 shows the chromatogram of permanent gases from GC/TCD during glucose gasification.
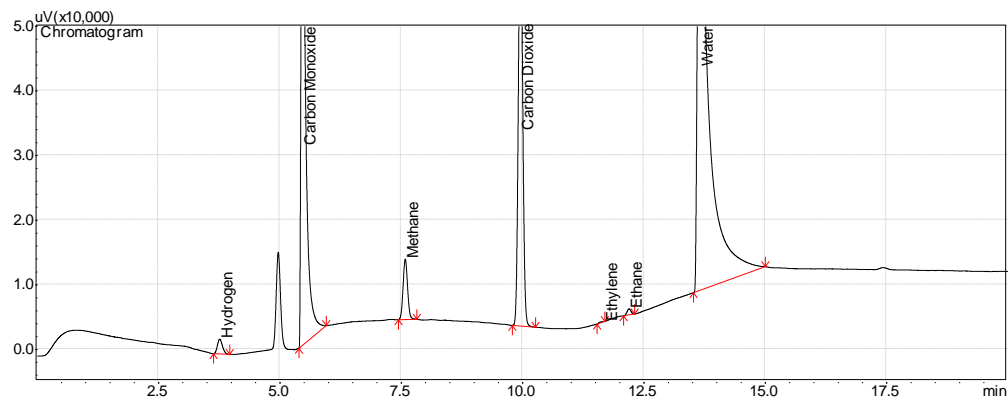
Figure 3.8: GC/TCD chromatogram of permanent gases obtained during glucose gasification at 650 °C, S/B = 1.0 g/g, Cat/B = 12.5 g/g, 20 s of reaction time using Cat H.
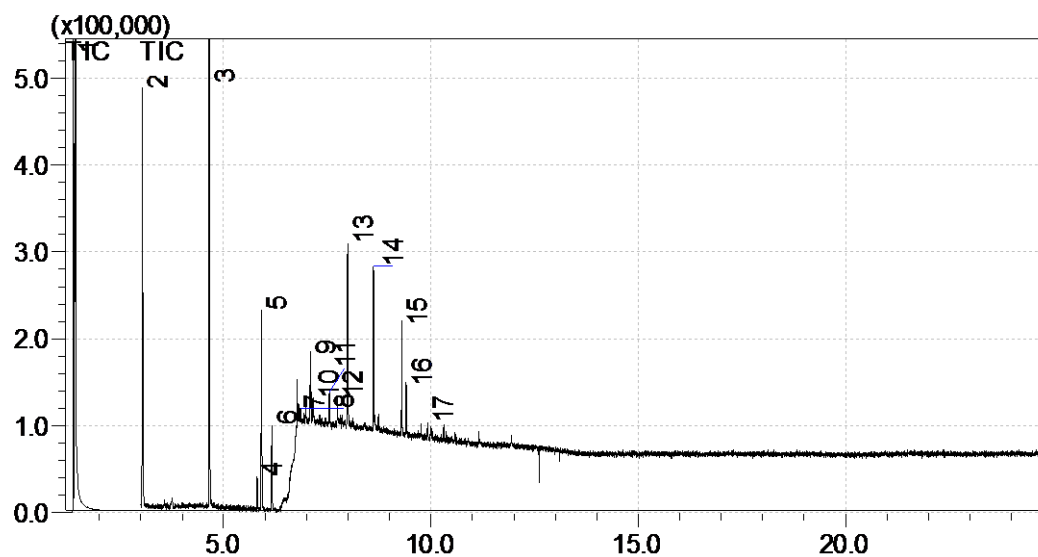
Figure 3.9: MS spectrum of tar compounds obtained during 2-Methoxy-4-Methylphenol gasification at 650 °C, S/B = 1.0 g/g, Cat/B = 12.5 g/g, 20 s of reaction time using Cat H. (1. methane, 2. benzene, 3. toluene, 4. ethylbenzene, 5. o-xylene, 6. p-xylene, 7. 1,2,3-trimethyl-benzene, 8. 1,2,4-trimethyl-benzene, 9. 1-ethenyl-3-methyl-benzene, 10. benzofuran, 11. indene, 12. 1-methyl-4-(1-methylethenyl)-benzene, 13. 7-methyl-benzofuran, 14. naphthalene, 15. 2-methyl-naphthalene, 16. 1-methyl-naphthalene and 17. 1,5-dimethyl-naphthalene).

While there was no tar formation during glucose gasification, considerable amounts of tars were obtained during 2-mehoxy-4-methylphenol gasification. A Shimatzu 2010 mass selective detector with a HP-5MS silica capillary column, 30 m×0.25 m I.D. (5% phenyl-95% methylpolysiloxane) was used for the separation, identification and quantification of the components present in the tars. A MS spectrum and the list of compounds identified in the tars is shown in Figure 3.9. The components present in the tars were quantified based on the size of the peaks in the MS spectrum in relation to the size of the methane peak in the same spectrum. Methane was visible in both the GC and MS spectrums. The amount of methane in the gasification product was obtained from the calibrated TCD signal. Thus, a mass/MS peak area ratio for methane was established, and compared to all peak areas in the MS spectrum. This led to the quantification of the unknown concentrations of all reported tar species.

3.5 **Conclusions**

The following are the most relevant conclusions of this chapter:

a) The Ni-based catalysts of the present study were prepared using carefully established procedures. These procedures involve direct reduction of lanthanum and nickel precursors in a fluidized bed condition instead of calcination.

b) The prepared catalysts were characterized using various well-established physiochemical techniques for particle size distribution, specific surface area, pore size distribution, acidity and basicity (TPD, FTIR), metal reducibility (TPR) and metal dispersion (chemisorptions).

c) The prepared Ni-based catalysts were tested under reaction conditions using the fluidized CREC Riser Simulator reactor and its analytical system. This allowed us to quantify the gasification products while using biomass surrogate species.

CHAPTER 4

CATALYST DEVELOPMENT

4.1 **Introduction**

This study focuses on the development of a high surface area and stable fluidizable Ni catalyst for steam gasification of biomass. A $Ni/\alpha-Al_2O_3$ catalyst was used for biomass steam gasification in a previous study conducted in the same laboratory [68]. In the present study, however, $\gamma-Al_2O_3$ is considered as the support for the development of a high surface area Ni catalyst with improved Ni dispersion. There are challenges when using $\gamma-Al_2O_3$, given its lower thermal stability and basicity, as well as its higher acidity. To overcome these challenges, La_2O_3 was used as a support modifier as well as a promoter. The effect of preparation methods, La_2O_3 loading and catalyst reduction conditions on the catalyst properties and biomass gasification reactivity are discussed in this chapter. Catalysts were characterized using various physico-chemical techniques. N_2 physisorption was used to assess the textural properties. Temperature programmed desorption of CO_2 was employed to determine total basicity and La_2O_3 dispersion, whereas catalysts acidity was studied using pyridine DRIFT and temperature programmed desorption of NH_3. Moreover, Ni reducibility and dispersion were assessed using H_2 temperature programmed reduction and pulse chemisorptions techniques. Finally, the performance of the catalysts for steam gasification of biomass surrogate species (glucose and 2-methoxy-4-methylphenol) was evaluated in a CREC riser simulator.

4.2 **Alcan and Sasol $\gamma-Al_2O_3$**

In this study, two high surface area $\gamma-Al_2O_3$ samples were tested: Alcan AA-100 Powder (Alcan Inc.) and Sasol Catalox® SSCa5/200 (Sasol North America Inc.). Particle density of the Alcan and Sasol samples were measured as 1.63 and 1.13 g/cc, respectively. Figure 4.1 reports the relatively narrow particle size distribution of Alcan $\gamma-Al_2O_3$and Sasol $\gamma-$

Al_2O_3 samples with a D_p^{50} of 109.5 and 85.4 µm, respectively. The volume weighted mean particle diameters of Alcan and Sasol γ-Al_2O_3 are 117.5 and 91.5 µm, respectively. Therefore, both samples belong to the Group A of the Geldart powder classification, indicating that both γ-Al_2O_3 supports are fluidizable. This was further verified experimentally using a flexi-glass model of the CREC Riser Simulator.
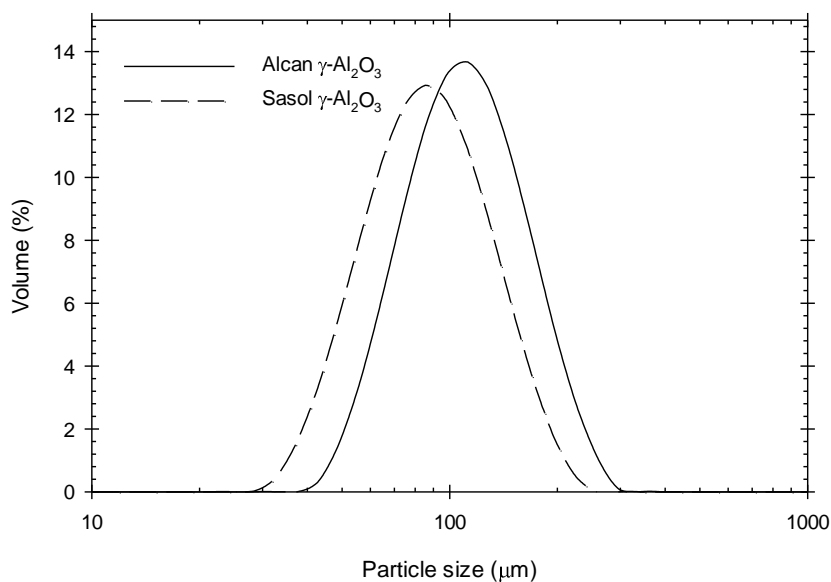
Figure 4.1: Comparison of particle size distribution for the Alcan γ-$Al_2O_3$and Sasol γ-Al_2O_3 samples.

Furthermore, Table 4.1 reports the BET surface area, the pore volume and the average pore diameter of the fresh and calcined samples. The pore size distribution, as described in Figure 4.2, was determined by analyzing the desorption branch of the isotherm using the BJH (Barrett-Joyner-Halenda) method. As shown in Table 4.1, the BET surface area of the fresh Alcan and Sasol γ-Al_2O_3 were found to be 233 and 193 m^2/g, respectively. These results are consistent with the value reported by the supplier. However, the surface area of the Alcan γ-Al_2O_3 was reduced drastically after calcination at 700 °C for 6 hrs, whereas the pore diameter increases from 38 to 72 Å due to calcination. According to the technical literature [36,189–191], this decrease in surface area with an increase in pore diameter can be attributed to the thermal sintering of γ-Al_2O_3.

Table 4.1: BET surface area, pore volume and pore diameter of the fresh and calcined γ-Al$_2$O$_3$ samples

Sample	S$_{BET}$ (m^2/g)	Pore volume (cm^3/g)	Avg pore dia (Å)
γ-Al$_2$O$_3$ (Alcan)	233	0.25	38
Alcan γ-Al$_2$O$_3$ calcined @ 700 °C	116	0.23	72
γ-Al$_2$O$_3$ (Sasol)	193	0.51	104
Sasol γ-Al$_2$O$_3$ calcined @ 700 °C	180	0.49	109
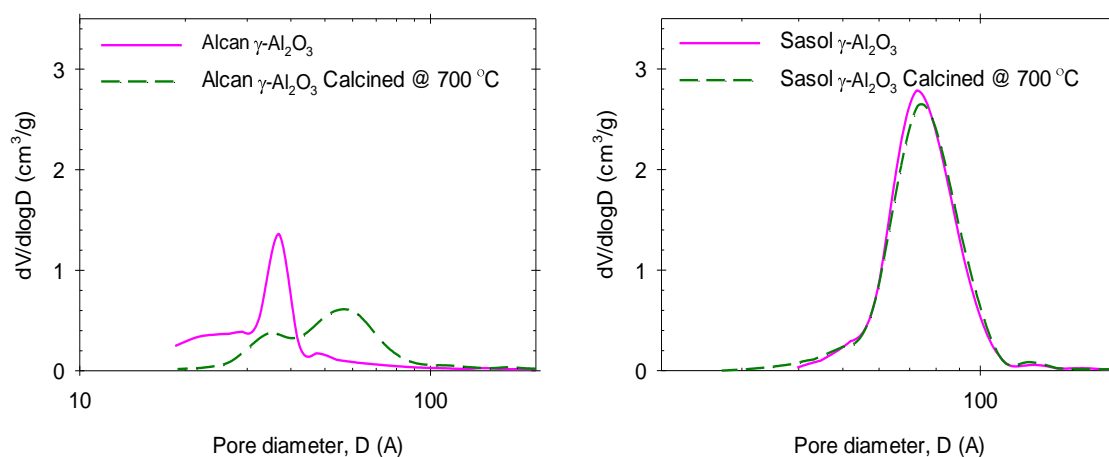
Figure 4.2: Pore size distribution based on the desorption branch of fresh and calcined γ-Al$_2$O$_3$ samples.

It was observed that Sasol γ-Al$_2$O$_3$ is more stable than Alcan γ-Al$_2$O$_3$. After calcination at 700 °C the surface area was only reduced from 193 m^2/g to 180 m^2/g. The changes in average pore size and pore volume due to the calcination were also comparatively less. In addition, the almost unchanged pore size distribution of Sasol γ-Al$_2$O$_3$ samples after calcination, as shown in Figure 4.2, also confirm its high thermal stability.

4.3 La$_2$O$_3$ Modified γ-Al$_2$O$_3$

4.3.1 Textural Properties

Table 4.2: BET surface area, pore volume and pore diameter of the La$_2$O$_3$ modified γ-Al$_2$O$_3$ samples

La$_2$O$_3$ Loading (%)	S$_{BET}$ (m^2/g)		Pore volume (cm^3/g)		Avg pore dia (Å)	
	Alcan	Sasol	Alcan	Sasol	Alcan	Sasol
0	116	180	0.25	0.49	72	109
2	124	182	0.28	0.50	84	107
5	130	183	0.26	0.48	75	104
10	115	162	0.23	0.45	74	107
15	100	144	0.22	0.42	79	111

Table 4.2 reports BET surface area, pore volume and average pore diameter of the La$_2$O$_3$ modified Alcan and Sasol γ-Al$_2$O$_3$ supports. It can be observed that the incorporation of La$_2$O$_3$ onto Alcan γ-Al$_2$O$_3$ in amounts as low as 2 wt%, increases the S$_{BET}$ from 116 to 124 m^2/g, with this being true while compared to the bare calcined Alcan γ-Al$_2$O$_3$. With the addition of 2 wt% La$_2$O$_3$, the surface area of Sasol γ-Al$_2$O$_3$ is also increased (180 to 182 m^2/g). However, due to its higher initial thermal stability, Sasol γ-Al$_2$O$_3$ exhibits comparatively lower improvement in S$_{BET}$ than Alcan γ-Al$_2$O$_3$. This increase in surface area for lanthanum modified γ-Al$_2$O$_3$ is in agreement with the data reported in the literature [36,189,192,193]. Lanthanum is considered to augment the γ-Al$_2$O$_3$ thermal resistance by reducing the number of sites where α-Al$_2$O$_3$ nucleation can occur [189]. On the other hand, with the addition of 2 wt% La$_2$O$_3$, the average pore diameter of Alcan γ-Al$_2$O$_3$ is increased from 72 to 84 Å. This suggests the blocking of some small pores by La$_2$O$_3$. Furthermore, when La$_2$O$_3$ content is increased up to 5 wt%, the specific surface area of both Sasol and Alcan γ-Al$_2$O$_3$ samples are further enhanced (Figure 4.3). The average pore diameters of both Sasol and Alcan samples are also decreased in this case (Table 4.2). This suggests good dispersion of La$_2$O$_3$ onto the pores of the γ-Al$_2$O$_3$, with La$_2$O$_3$ coating the inner pore surfaces.
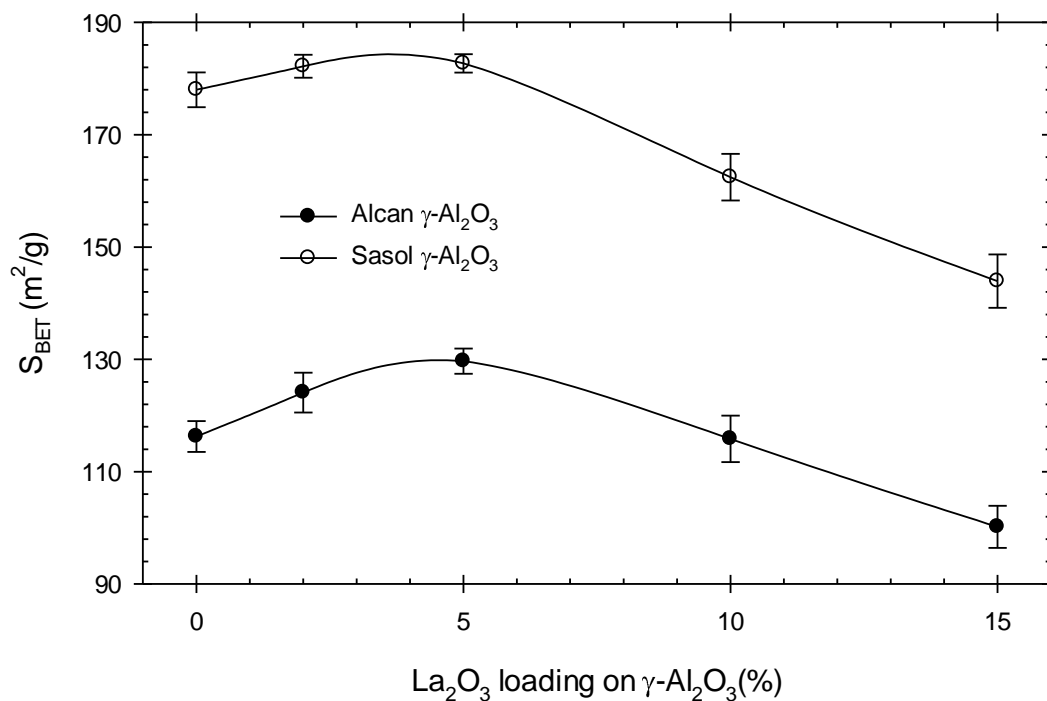
Figure 4.3: Effect of La_2O_3 loading on the surface area of Alcan and Sasol γ-Al_2O_3.

However, as shown in Figure 4.3, an increase in La_2O_3 in excess of 5 wt%, results in a decrease of surface area almost linearly for both Alcan and Sasol γ-Al_2O_3. This change is also accompanied with average pore diameter increases which can be attributed to the blocking of small pores by an excessive lanthanum addition. Therefore, 5 wt% La_2O_3 can be considered as the optimal La_2O_3 loading level to improve the thermal stability of γ-Al_2O_3.

4.3.2 Acid-Base Properties

The support acidity and basicity have a significant effect on the catalytic activity and the resistance to coke deposition. The type and nature of acidic sites present in Alcan and Sasol γ-Al_2O_3 and in the La_2O_3 modified Alcan and Sasol γ-Al_2O_3 support were evaluated with DRIFT using pyridine as a probe molecule. Pyridine interacts with different acid sites through the electron lone pair of its nitrogen atoms. Three types of adsorbed pyridine species have been reported as being present [194–196]: a) Molecularly adsorbed pyridine coordinating its lone electron pair from the nitrogen atom with surface Lewis acid sites (Al^{3+}), b) Hydrogen bonded pyridine interacting via its nitrogen atom to

weakly acidic hydroxy surface sites, and c) Pyridinium ion formed by extracting a proton from a Brønsted acid hydroxy surface site. In this respect, the "8a-8b" and "19a-19b" stretching vibrational modes of the pyridine ring are the most sensitive modes that can be evaluated to assess adsorption interaction strength using IR. More specifically, protonated pyridine on Brønsted centers give bands at 1640 and 1540 cm^{-1}. Furthermore, bands in the 1580–1630 cm^{-1} and the 1440–1455 cm^{-1} ranges are characteristic of pyridine coordinated with Lewis acid sites [194–197]. One should notice that the "19a" vibration band at around 1490 cm^{-1} is less informative, as it is associated with all three types of adsorbed pyridine.
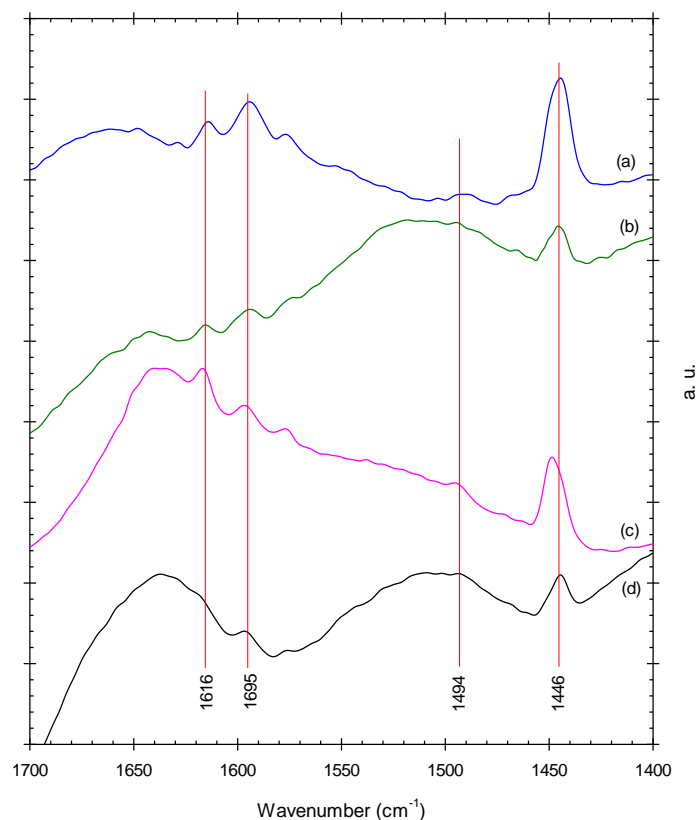
Figure 4.4: Pyridine DRIFT spectra of a) Alcan γ-Al$_2$O$_3$, b) 5% La$_2$O$_3$-Alcan γ-Al$_2$O$_3$, c) Sasol γ-Al$_2$O$_3$ and d) 5% La$_2$O$_3$-Sasol γ-Al$_2$O$_3$.

Figure 4.4 reports the IR spectra of the La$_2$O$_3$ doped and bare γ-alumina supports, following pyridine adsorption and evacuation at 100 °C, in the spectral region of 1700-1400 cm^{-1}. No bands at 1540 cm^{-1} for both Alcan γ-Al$_2$O$_3$ and Sasol γ-Al$_2$O$_3$ samples

were observed. This indicates that there are no Brønsted acid sites available on the γ-alumina surface, strong enough to form pyridinium ions. On the other hand, the appearance of the "19b" band at 1445 cm^{-1} and the "8a" band at 1590-1635 cm^{-1} in the DRIFT spectra of undoped alumina, demonstrates the presence of Lewis Acid sites. Based on the multiplicity of the "8a" band of coordinated pyridine, three types of Lewis acid sites with different strengths have been reported in the literature [195,198–200]: weak (1595-1610 cm^{-1}), moderate (1610-1620 cm^{-1}) and strong (1625 - 1635 cm^{-1}). Assignment of those peaks in terms of Al^{3+} configurations are further discussed in Section 4.7.4.

Both undoped Alcan and Sasol γ-Al$_2$O$_3$ exhibits peaks at 1595 cm^{-1} and 1613 cm^{-1} in the IR spectra (Figure 4.4) indicating the presence of weak to moderate Lewis acid sites. Moreover, the small peak at 1576 cm^{-1} corresponds to the "8b" vibrational mode is either hydrogen bonded or coordinated pyridine. Furthermore, in the case of the γ-Al$_2$O$_3$ modified with 5 wt% La$_2$O$_3$, the intensities of all the 19a,b and 8a bands were significantly decreased.
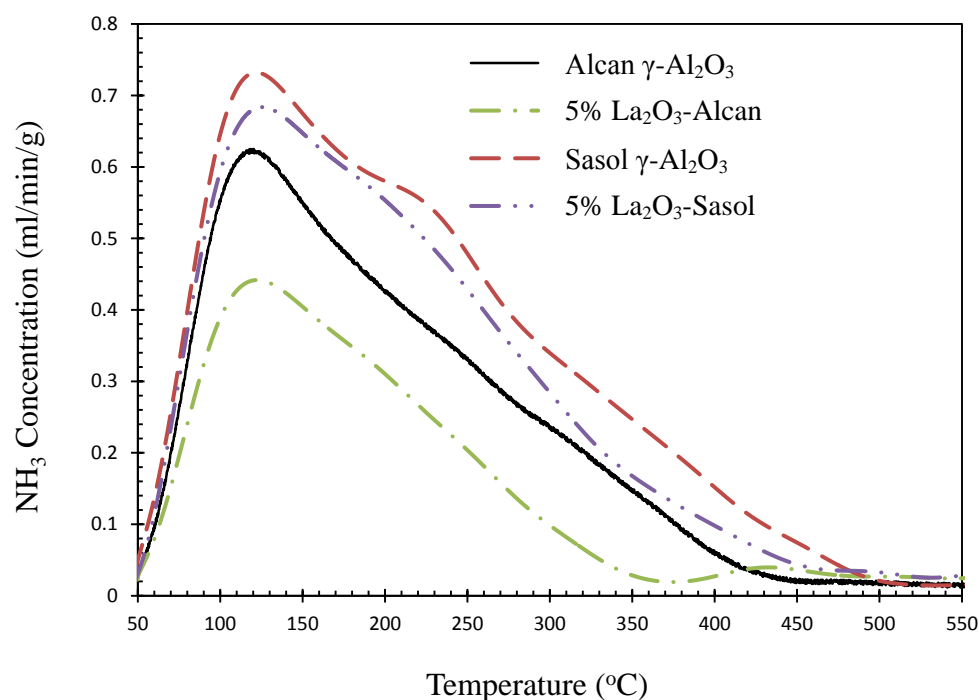
Figure 4.5: NH$_3$-TPD profile of bare and La2O3 modified γ-Al2O3 samples.

The acidity and basicity of the supports were further investigated by temperature programmed desorption (TPD) of NH_3 and CO_2, respectively. Figure 4.5 reports NH_3-TPD profiles for the undoped and La_2O_3 doped Alcan and Sasol γ-Al_2O_3 supports. One can notice that the γ-Al_2O_3 samples yield an asymmetric desorption peak in the low temperature range of 50 to 450 °C. This peak displays a maximum at around 120 °C and a long tail. The low temperature desorption peaks confirm the absence of Brønsted acid sites while the tail can be attributed to the presence of Lewis acid sites with different strengths. A clear bump at around 225 °C, observed in the NH_3-TPD profile of Sasol γ-Al_2O_3, can be correlated to the pyridine DRIFT peak of moderate strength Lewis acid sites at 1616 cm^{-1} (Figure 4.4 and Figure 4.5). These peaks almost disappeared from both the TPD profile and the IR spectra with the addition of 5 wt% La_2O_3.
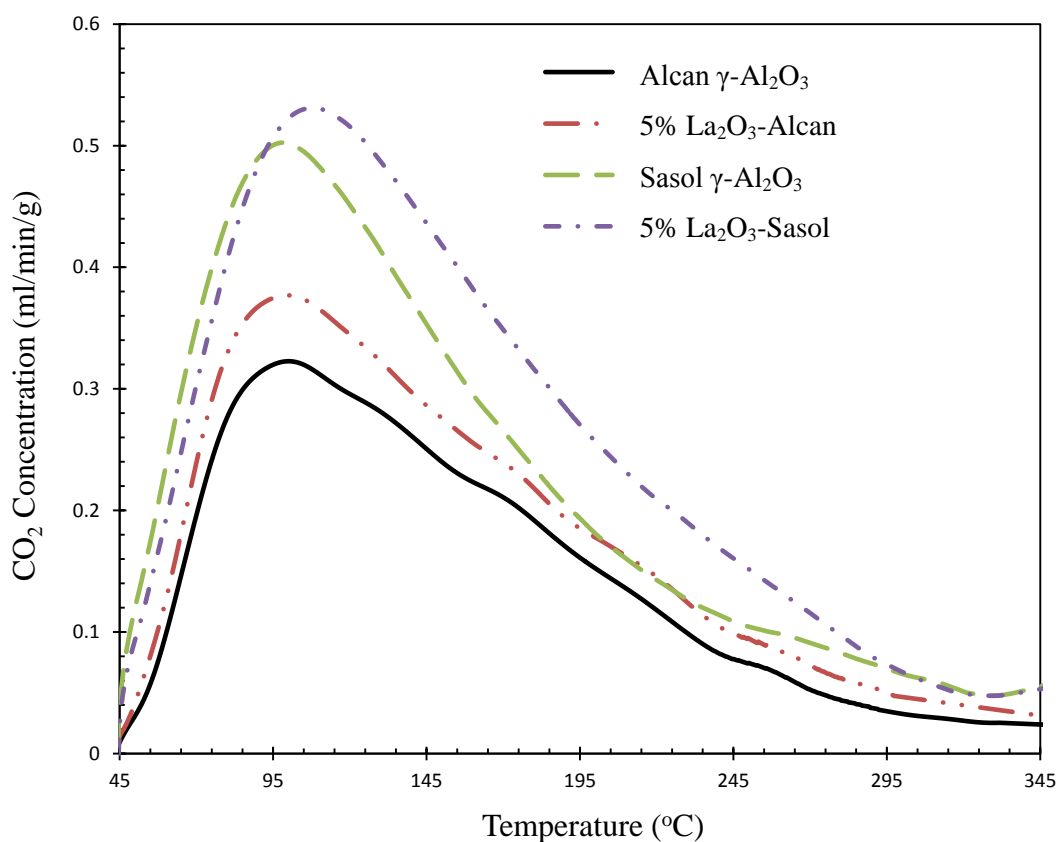
Figure 4.6: CO_2-TPD profile of bare and La_2O_3 modified γ-Al_2O_3 samples.

CO_2-TPD profiles of La_2O_3 doped and bare γ-Al_2O_3 samples are reported in Figure 4.6. γ-Al_2O_3 samples give a single asymmetric low-temperature (45 to 300 °C) peak of CO_2 desorption with a maximum value at 95 °C. According to Morterra et al [201], this low-temperature desorption peak can be attributed to the low-strength basic sites. These low-strength basicity sites can be traced to bicarbonates, which are formed as a result of the interaction between CO_2 and the weak basic surface hydroxyl groups. In addition, the asymmetric CO_2 desorption peak shows the coexistence of basic sites of different strengths. Figure 4.6 also reported that Sasol γ-Al_2O_3 exhibits significantly higher amount of CO_2 desorption (total Basicity) than Alcan γ-Al_2O_3. Moreover, La_2O_3 addition significantly increases basic density and site strength for both γ-Al_2O_3 samples.

Total acidity and basicity of the samples are considered equivalent to the amount of NH_3 and CO_2 desorbed, respectively and listed in Table 4.3. To distinguish between the role of La_2O_3 addition and structural change during the preparation stage on the acid-base properties of γ-Al_2O_3, concentration of acidic and basic sites on the surface are also reported in Table 4.3. As given in Table 4.3, higher total acidity and basicity were found in Sasol γ-Al_2O_3 samples than in Alcan γ-Al_2O_3 samples. This can be attributed to Sasol γ-Al_2O_3's higher thermal stability.

Table 4.3: Total acidity and basicity of the bare and La_2O_3 modified γ-Al_2O_3 samples as determined from NH_3-TPD and CO_2-TPD, respectively

La_2O_3 Loading (%)	Total acidity				Total basicity			
	μmol/g γ-Al_2O_3		μmol/m^2		μmol/g γ-Al_2O_3		μmol/m^2	
	Alcan	Sasol	Alcan	Sasol	Alcan	Sasol	Alcan	Sasol
0	370	511	3.18	2.84	91	116	0.79	0.65
2	272	467	2.15	2.51	105	129	0.83	0.70
5	251	458	1.85	2.39	131	170	0.96	0.88
10	250	464	1.96	2.60	156	261	1.23	1.46
15	246	471	2.14	2.84	164	313	1.43	1.90

To study the influence of La_2O_3 loading on the acidity and basicity of $\gamma\text{-}Al_2O_3$, NH_3 and CO_2 TPDs of $\gamma\text{-}Al_2O_3$ samples with different La_2O_3 content were performed. Regarding total acidity, one can notice in Table 4.3, that with the addition of the 2 wt% La_2O_3, the total acidity was decreased from 370 to 272 μmol NH_3/g $\gamma\text{-}Al_2O_3$ for Alcan $\gamma\text{-}Al_2O_3$ and from 511 to 467 μmol NH_3/g $\gamma\text{-}Al_2O_3$ for Sasol $\gamma\text{-}Al_2O_3$. 2 wt% La_2O_3 reduces the total acidity of Alcan $\gamma\text{-}Al_2O_3$ by 26%, whereas it reduced the total acidity of Sasol $\gamma\text{-}Al_2O_3$ by only 9%. The reduction of acidity in the La_2O_3 modified $\gamma\text{-}Al_2O_3$ supports is a combined effect of La_2O_3 addition and changes in the $\gamma\text{-}Al_2O_3$ structure due to the heat treatment involved during lanthanum impregnation. Heat treatment can damage $\gamma\text{-}Al_2O_3$ acid sites via dehydroxylation. A lesser degree of dehydroxylation occurs on Sasol $\gamma\text{-}Al_2O_3$ due to its higher thermal stability. Therefore, comparatively lower changes in total acidity were found for La_2O_3 modified Sasol $\gamma\text{-}Al_2O_3$.
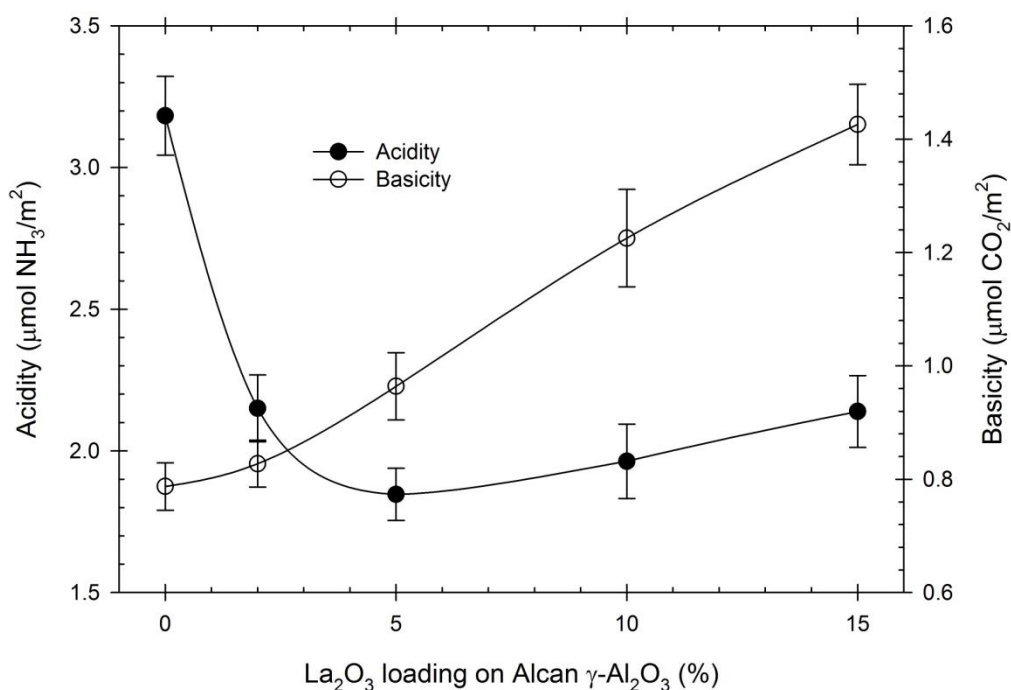
Figure 4.7: Effect of La_2O_3 loading on the acidity and basicity of the Alcan $\gamma\text{-}Al_2O_3$.

Moreover, the addition of the 5 wt% La_2O_3 yielded a further decrease in the acidity of both the Alcan and Sasol $\gamma\text{-}Al_2O_3$ surfaces. Figure 4.7 and Figure 4.8 report the concentration profiles of acidic and basic sites with the variation of La_2O_3 loadings on

Alcan and Sasol γ-Al_2O_3, respectively. As shown in Figure 4.7, the increase in La_2O_3 loading beyond 5 wt% resulted in the gradual rise of acid site concentrations. For example, acid site concentrations of 15 wt% La_2O_3-Alcan γ-Al_2O_3 was found to be equivalent to 2.14 µmol NH_3/m^2, whereas it was 1.84 µmol NH_3/m^2 for Alcan γ-Al_2O_3 modified with 5 wt% La_2O_3. The increase in total acidity and acid site concentrations for a La_2O_3 loading beyond 5 wt% was more apparent in the case of Sasol γ-Al_2O_3, as can be seen from Figure 4.8. This effect can be attributed to the presence of deficiently coordinated La^{3+} ions acting as Lewis acid sites [42,44,57]. One should notice, in this respect, that La^{3+} cations can mildly influence the acid site density.
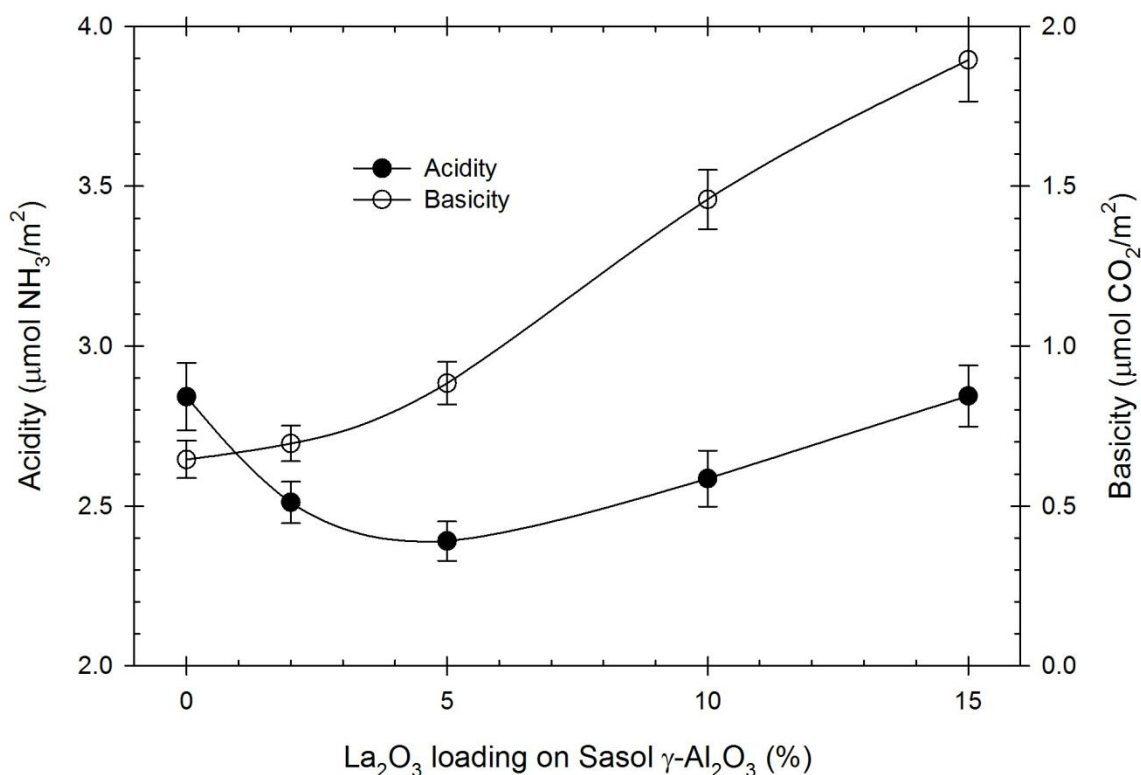
Figure 4.8: Effect of La_2O_3 loading on the acidity and basicity of the Sasol γ-Al_2O_3.

La_2O_3 addition improved, on the other hand, the CO_2 adsorption capacity of γ-Al_2O_3 by creating some basic sites. For the 2 wt% La_2O_3 loading, the total basicity (CO_2 adsorption capacity) was increased from 91 to 105 µmol CO_2/g γ-Al_2O_3 for Alcan γ-Al_2O_3 and from 116 to 129 µmol CO_2/g γ-Al_2O_3 for Sasol γ-Al_2O_3. As shown in Figure 4.7 and Figure 4.8, the increase in basic sites with La_2O_3 content is slow at low La_2O_3 loadings, as some

of the La_2O_3 is employed to neutralize the acid sites of γ-Al_2O_3. Then, at higher La_2O_3 loadings, it starts to increase more progressively given the availability of free dispersed La_2O_3. However, as the La_2O_3 content becomes much higher, the rate of basicity increase with La_2O_3 content becomes modest. In fact, when La_2O_3 content was augmented from 10 to 15 wt%, desorption of CO_2 only increased from 156 to 164 µmol per g γ-Al_2O_3 for Alcan γ-Al_2O_3 and from 261 to 313 µmol per g γ-Al_2O_3 for Sasol γ-Al_2O_3. The lower surface areas and lower La_2O_3 dispersion at 15 wt% La_2O_3 loading are likely to be responsible for this. In agreement with this, Bettman et al [43] also found that La_2O_3 remained in the dispersed phase up to a concentration of 8.5 µmol La/m^2 (~10 wt% La loading).

4.3.3   X-ray Diffraction Analysis
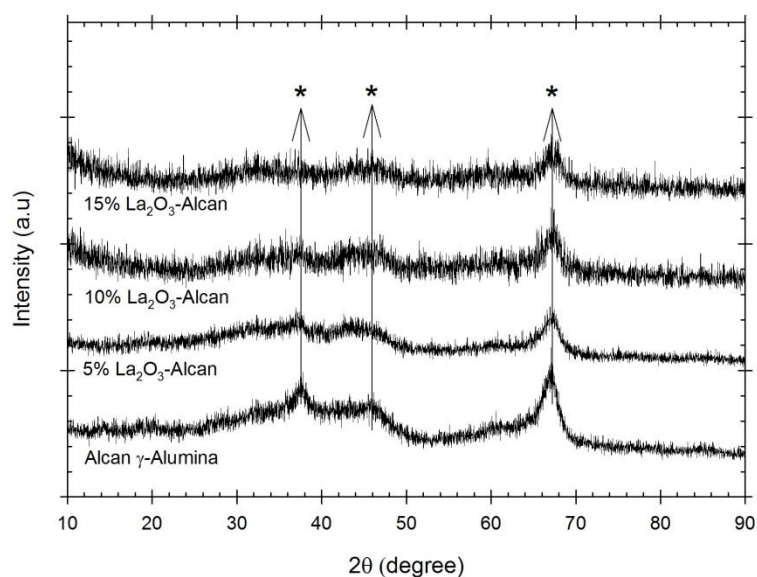
Figure 4.9: XRD patterns of the La_2O_3 doped Alcan γ-Al_2O_3 supports (⋆: γ-Al_2O_3).

XRD patterns of the Alcan and La_2O_3 modified Alcan γ-alumina are reported in Figure 4.9 with samples showing a mostly amorphous structure. According to JCPDS 10-0425, the low intensity peaks centered at $2\theta = 37.6°$, $45.8°$, $67.1°$ are the characteristic peaks of γ-Al_2O_3. As the La_2O_3 loading is increased, the diffraction patterns show a reduction in the intensities of γ-Al_2O_3 peaks. Diffraction lines corresponding to La-species were not observed. This indicates that La_2O_3 species are either incorporated into the pore network

of the γ-Al$_2$O$_3$ or highly dispersed on the alumina surface as amorphous phases contributing to undetectable crystallites. Similar XRD patterns were also observed for La$_2$O$_3$ modified Sasol γ-Al$_2$O$_3$ supports.

4.4 **Effect of the Catalyst Preparation Method**

The catalyst preparation method plays a crucial role influencing structural properties, metal-support interaction, metal reducibility and dispersion [58–60]. Conventionally, impregnated metal salts are decomposed to oxides by high temperature calcination in air followed by metal oxide reduction under hydrogen. In this study, catalysts were prepared via direct decomposition of impregnated metal nitrates under a reducing environment. To establish the value of the catalyst preparation method of the present study, a catalyst with the same composition was prepared using a conventional method:

a) Cat A - 20wt% Ni/5% La$_2$O$_3$-Alcan γAl$_2$O$_3$: the catalyst preparation involved the multi-step impregnation and calcination of metal precursors in air at 700 °C after each impregantion.

b) Cat C - 20wt% Ni/5% La$_2$O$_3$-Alcan γAl$_2$O$_3$: the catalyst preparation involved the multi-step impregnation and direct decomposition of metal precursors at 700 °C in a hydrogen atmosphere after each impregantion under fluidized bed conditions.

4.4.1   Characterization Results

Table 4.4 reports the BET surface area, the total acidity and the total basicity of the catalysts prepared via prior calcinations (Cat A) and using direct reduction (Cat C) of metal precursors. As can be seen in Table 4.4, a catalyst prepared by calcinations of metal nitrates (Cat A) possesses a higher surface area than a catalyst prepared by direct decomposition of metal nitrates in a reducing environment. This can be attributed to the highly exothermic reactions involved in the process of metal nitrate reduction. Details of the chemistry involved in the reduction of metal nitrates are discussed in the Section 4.7.

Table 4.4: BET surface area, total acidity and total basicity of the catalysts prepared via prior calcinations/direct reduction of metal precursors

Sample	S_{BET} (m^2/g)	Total acidity (μmol/g γ-Al$_2$O$_3$)	Total basicity (μmol/g γ-Al$_2$O$_3$)
20%Ni/5% La$_2$O$_3$-Alcan (Cat A)	70.5	162	69
20%Ni/5% La$_2$O$_3$- Alcan (Cat C)	55.5	97	83

The acidity and basicity of the catalysts were investigated by temperature programmed desorption (TPD) of NH$_3$ and CO$_2$, respectively. Total acidity and basicity of the samples were calculated from the amount of NH$_3$ and CO$_2$ desorbed. Table 4.4 also reports that the catalyst prepared with precursor calcinations instead of direct reduction (Cat A), exhibited significantly higher acidity (162 μmol NH3/g γ-Al$_2$O$_3$) than Cat C (97 μmol NH3/g γ-Al$_2$O$_3$). Acidity data from Cat A can be justified given the low exothermicity of the metal precursor decomposition under air, yielding modest losses in surface acidity. On the other hand, Cat C acidity data can be explained given the higher heat evolved when the Ni precursor is transformed under hydrogen, giving larger losses in surface acidity [58]. Moreover, lower CO$_2$ adsorption capacity (total basicity) was found for Cat A rather than C.

Reducibility (R), dispersion (D) and crystal size (d_v) of the active phase on the prepared catalysts are determined using temperature program reduction (TPR) and H$_2$ pulse chemisorptions experiments and are summarized in Table 4.5. The focus of this study is to conduct steam gasification of biomass at a temperature below 700 °C to avoid ash agglomeration and other operational issues with gasifiers. Therefore, reducibility below 700 °C ($R_{700 °C}$) is an important characteristic to investigate and is given in Table 4.5 as well. Figure 4.10 shows the TPR profiles of the prepared Ni catalysts as well as the profile of the La$_2$O$_3$ modified γ-Al$_2$O$_3$ support. The TPR profile of the La$_2$O$_3$-γAl$_2$O$_3$ support does not show any peak with the hydrogen consumed being negligible.
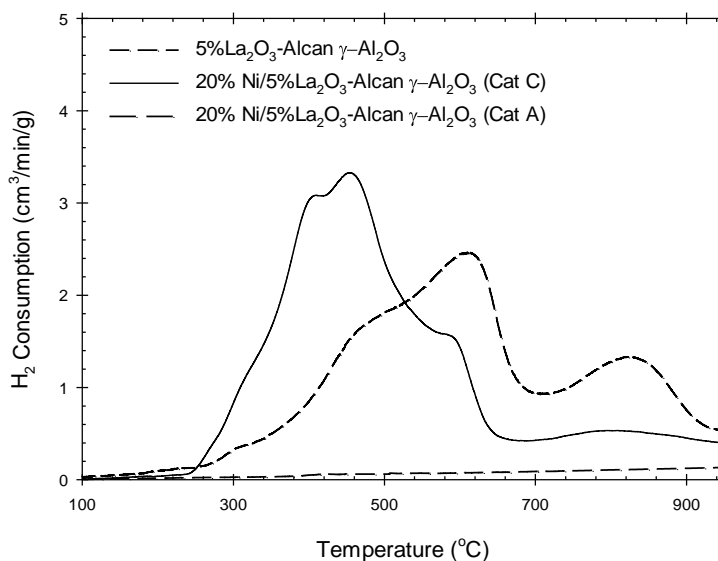
Figure 4.10: TPR profiles of the La_2O_3 modified γ-Al_2O_3 and supported Ni catalysts prepared via prior calcinations (Cat A) and direct reduction (Cat C) of metal precursors. (using 10% H_2/Ar at a flow rate of 50 cm^3/min and at a 10 °C/min heating rate).

Figure 4.10 shows that the Ni catalyst supported on 5 wt% La_2O_3- Alcan γ-Al_2O_3, prepared via direct reduction (Cat C) gives wide reduction peaks in the 350 °C to 950 °C range, with four peaks at 400, 460, 590 and 800 °C. The first peak (at 400 °C) can be assigned to the reduction of highly dispersed NiO species on the support surface [189,191,193]. According to the literature [39,189,191,202], the second peak (460 °C) and third peak (590 °C) can be attributed to the reduction of Ni^{+2} species having varying interactions with the oxide support. These could be highly dispersed, non-stoichiometric, amorphous nickel-aluminate spinels formed through metal support interaction. Finally, the reduction peak observed above 700 °C is related to the reduction of bulk nickel-aluminate ($NiAl_2O_4$) [39,188,189,191,193,202].

Table 4.5: Reducibility (R), dispersion (D) and crystal size (d_v) of Ni for the catalysts prepared via prior calcinations/direct reduction of metal precursors

Sample	R (%)	$R_{700\ °C}$ (%)	$D(\%) = \frac{117X}{WR}$	$d_v(nm) = \frac{97.1}{\%D}$
20%Ni/5% La_2O_3-Alcan (Cat A)	83	66	0.92	106
20%Ni/5% La_2O_3-Alcan (Cat C)	91	87	1.12	87

X stands for the total hydrogen chemisorbed (μmol of H_2/g cat); W denotes the metal loading (wt%)

Figure 4.10 also reports the TPR profile of the catalyst prepared with precursor decomposition via calcination (Cat A). It can be observed that Cat A yields significantly lower amounts of reducible species (only 83%) compared to Cat C (Table 4.5). Moreover, Cat C displays a significantly larger proportion of easily reducible surface NiO sites than Cat A, with Cat A having higher levels of undesirable $NiAl_2O_4$. According to Bartholomew and Farrauto [58], the calcination of Ni nitrates favors the formation of larger NiO particles as well as the formation of very stable $NiAl_2O_4$ through the interaction of NiO and Al_2O_3. Therefore, Cat A exhibited very low $R_{700\ °C}$ (66%) and dispersion of nickel. On the basis of these findings, one can argue that direct decomposition of the metal nitrates to a metallic species in hydrogen is critical especially when the metal loading onto the support is accomplished in several steps.

4.4.2   Gasification Results

Reactivity of the Ni catalysts prepared via prior calcinations (Cat A)/direct reduction (Cat C) of metal precursors for steam gasification of glucose, a biomass surrogate, were evaluated in a CREC Riser Simulator. Performance of the catalysts were evaluated in terms of a) carbon conversion to permanent gases, b) dry gas yield (moles of H_2, CO, CO_2, H_2O, and CH_4 produced/moles of glucose fed) and c) quality of synthesis gas obtained (H_2/CO). Table 4.6 compares the performance of the Cat A and Cat C for glucose gasification at 650 °C using a Steam/Biomass ratio of 1.0, a Cat/Biomass ratio of 12.5 and 20 s of reaction time.

Table 4.6: Glucose gasification performance of the catalysts prepared via prior calcinations (Cat A)/direct reduction (Cat C)

	Cat A	Cat C
Dry Gas Yield (mol/mol)	9.54	10.52
C-Conversion (%)	88.3	92.3
H_2/CO	1.77	1.90

It can be seen in Table 4.6 that the catalyst prepared via direct reduction of metal precursors (Cat C) exhibited better performance than the catalyst prepared via calcination

(Cat A). This enhanced performance of Cat C can be attributed to its better resulting surface structure, the higher Ni reducibity and dispersion, and the lower acidity and higher. The higher basicity of Cat C also facilitates H_2O and CO_2 adsorption resulting in higher reforming activity and less coking [29,30,203]. On the other hand, the catalyst prepared via precursor calcination (Cat A) displays a higher surface area than Cat C. However, the performance of Cat A was negatively affected by its poor reducibility, low metal dispersion and high acidity.

4.5 **Effect of Ni Loading**

The effect of Ni loading was studied using catalysts with varying Ni content supported on a 5 wt% La_2O_3-Alcan γ-Al_2O_3: 10 wt% Ni (Cat C-1), 15 wt% Ni (Cat C-2) and 20 wt% Ni (Cat C). These catalysts were characterized using various physicochemical techniques. The catalyst performance for biomass steam gasification was evaluated using glucose as a model compound.

4.5.1   **Characterization Results**

Table 4.7 reports the BET surface area, the total acidity and the total basicity of the catalysts with varying Ni content. As can be seen in Table 4.7, with the increase in Ni loading on La_2O_3 modified Alcan γ-Al_2O_3, both specific surface area and pore volume were reduced. There was also a gradual increase in pore diameter. This can be attributed to the blocking of support small pores with higher amounts of nickel.

Table 4.7: BET surface area, total acidity and total basicity of the catalysts with different Ni content

Sample	S_{BET} (m^2/g)	Total acidity (μmol/g γ-Al_2O_3)	Total basicity (μmol/g γ-Al_2O_3)
10%Ni/5% La_2O_3-Alcan (Cat C-1)	77.5	135	121
15%Ni/5% La_2O_3-Alcan (Cat C-2)	66.2	111	96
20%Ni/5% La_2O_3- Alcan (Cat C)	55.5	97	83

Table 4.7 also reports that total acidity and basicity were decreased gradually with the increase in Ni content. When Ni loading was augmented from 10 (Cat C-1) to 20 wt% (Cat C), the total acidity was decreased from 135 to 97 µmol NH_3/g γ-Al_2O_3 and the total basicity was reduced from 121 to 83 µmol CO_2/g γ-Al_2O_3. This was due to the blockage of support acidic and basic sites by excess nickel.
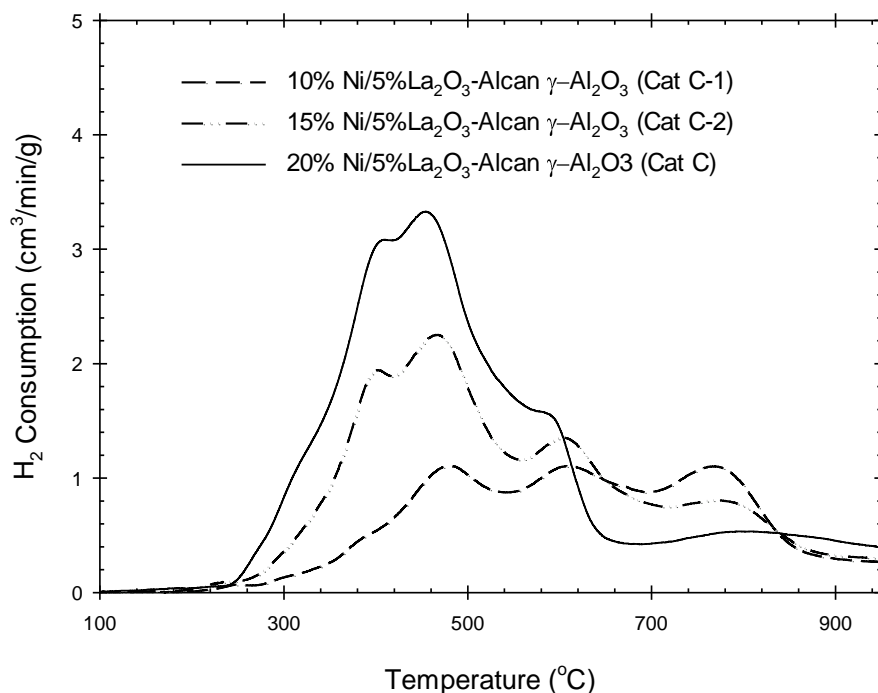
Figure 4.11: TPR profiles of catalysts with different Ni content (using 10% H_2 with balanced Ar at a flow rate of 50 cm^3/min and 10 °C/min heating rate).

Reducibility (R), dispersion (D) and crystal size (d_v) of the active phase are summarized in Table 4.8. Figure 4.11 reports TPR profiles of Ni/Alcan γ-Al_2O_3 catalysts modified with 5 wt% lanthanum oxide containing 10, 15 and 20 wt% Ni. It is, thus, apparent from Figure 4.11, that increasing Ni content, leads to a significant increase in the easily reducible NiO species. In fact, when Ni loading rises from 10 to 20%, R_{700} °C augments from 71% to 87%. This finding also confirms the advantage of the multi-step impregnation used in the catalyst preparation, yielding a higher density of reducible active sites.

Table 4.8: Reducibility (R), dispersion (D) and crystal size (d_v) of Ni for catalysts with different Ni content

Sample	R (%)	$R_{700\,°C}$ (%)	$D(\%) = \frac{117X}{WR}$	$d_v(nm) = \frac{97.1}{\%D}$
10%Ni/5% La$_2$O$_3$-Alcan (Cat C-1)	94	71	1.67	58
15%Ni/5% La$_2$O$_3$-Alcan (Cat C-2)	92	83	1.32	73
20%Ni/5% La$_2$O$_3$-Alcan (Cat C)	91	87	1.12	87

X stands for the total hydrogen chemisorbed (μmol of H$_2$/g cat); W denotes the metal loading (wt%)

4.5.2 Gasification Results

To study the effect of Ni loading, the reactivity of the catalysts with varying Ni content for the steam gasification of glucose, a biomass surrogate, were evaluated in a CREC Riser Simulator. Table 4.9 compares the performance of the prepared catalysts for glucose gasification at 650 °C using a Steam/Biomass ratio of 1.0, a Cat/Biomass ratio of 12.5 and 20 s of reaction time.

Table 4.9: Glucose gasification performance of the catalysts with different Ni content

	Cat C-1 10%Ni/5% La$_2$O$_3$-Alcan	Cat C-2 15%Ni/5% La$_2$O$_3$-Alcan	Cat C 20%Ni/5% La$_2$O$_3$-Alcan
Dry Gas Yield (mol/mol)	9.67	10.09	10.52
C-Conversion (%)	89.5	90.9	92.3
H$_2$/CO	1.83	1.88	1.90

As reported in Table 4.9, with the increase of Ni content, the reactivity of the catalyst was also increased. Glucose gasification using Cat C (20 wt% Ni) yielded 92.3% carbon conversion to permanent gases whereas 89.5% carbon conversion was obtained using Cat C-1 (10 wt% Ni). This favorable difference can be attributed to the higher nickel surface area of Cat C (1.48 m^2/g) compared to the nickel surface area on Cat C-1 (1.14 m^2/g).

4.6 **Effect of La$_2$O$_3$ loading on Ni /γ-Al$_2$O$_3$ Catalysts**

4.6.1 **Textural Properties**

At high temperatures, the structure of γ-Al$_2$O$_3$ is partially collapsed resulting in the loss of surface area. The BET surface area of the fresh Alcan γ-Al$_2$O$_3$ was found to be 233 m^2/g. However, both the surface area and the pore volume of the γ-Al$_2$O$_3$ were reduced drastically after calcination at 700 °C for 6 hrs, while the pore diameter increased from 38 to 72 Å due to calcinations (Table 4.1). The addition of small amounts of Lanthanum can augment the γ-Al$_2$O$_3$ thermal resistance by reducing the number of sites where α-Al$_2$O$_3$ nucleation can occur [189]. The role of La$_2$O$_3$ in improving the thermal stability of γ-Al$_2$O$_3$ is discussed in Section 4.3.1. It has been found that the addition of La$_2$O$_3$ up to 5 wt% helps to improve γ-alumina thermal stability, reducing thermal sintering. However, more than 5 wt% La$_2$O$_3$ content yielded a substantial decrease in the surface area of the La$_2$O$_3$ modified γ-Al$_2$O$_3$ due to the blocking of small pores by excessive lanthanum. Table 4.10 and Table 4.11 report the BET surface area, the pore volume and the average pore diameter of both the support materials and the Ni catalysts as determined using N$_2$ adsorption-desorption.

Table 4.10: BET surface area, pore volume and pore diameter of the catalysts supported on Alcan γ-Al$_2$O$_3$

Samples	S$_{BET}$ (m^2/g)	Pore volume (cm^3/g)	Avg pore dia (Å)
Alcan γ-Al$_2$O$_3$ calcined @ 700 °C	116	0.22	72
5% La$_2$O$_3$-Alcan γ-Al$_2$O$_3$	130	0.26	75
10% La$_2$O$_3$-Alcan γ-Al$_2$O$_3$	115	0.23	74
20% Ni/Alcan γ-Al$_2$O$_3$ (Cat B)	31.3	0.16	151
20% Ni/5% La$_2$O$_3$-Alcan γ-Al$_2$O$_3$ (Cat C)	55.5	0.19	124
20% Ni/10% La$_2$O$_3$-Alcan γ-Al$_2$O$_3$ (Cat D)	35.9	0.15	136

Table 4.10 shows that the incorporation of the active Ni phase on the Alcan γ-Al$_2$O$_3$ support, resulted in a substantial reduction in the specific surface area and pore volume. After 20 wt% Ni loading (Cat B), the surface area was reduced drastically from 116 to 31.3 m^2/g. It can also be observed that the average pore diameter of Cat B was increased to 151 Å after Ni loading. This is in agreement with the results reported by Navarro et al [191], and can be attributed to the thermal sintering and blocking of the support pores by metal particles.

For the Ni catalyst supported on 5 wt% La$_2$O$_3$ modified Alcan γ-Al$_2$O$_3$ (Cat C), the surface area was improved from 31.3 to 55.55 m^2/g. However, if lanthanum oxide loading is increased to 10 wt% (Cat D), the specific surface area after Ni loading was reduced to 35.88 m^2/g (Table 4.10) as in the case of La$_2$O$_3$ modified Alcan alumina. There was also an increase in pore diameter (124 to 136 Å) and a decrease in pore volume (0.19 to 0.15 cm^3/g) suggesting a greater extent of pore blocking in the catalyst containing 10 wt% La$_2$O$_3$ (Cat D). One should mention that the reduction of surface area and the blockage of alumina pores at higher La$_2$O$_3$ loadings was also reported in the literature [39,49]. This has been attributed to the blocking of alumina pores by the formation of LaAlO$_3$ at higher La$_2$O$_3$ loadings. This formation of lanthanum aluminates is confirmed in the present study using XRD analysis (Section 4.6.2).

Table 4.11: BET surface area, pore volume and pore diameter of the catalysts supported on Sasol γ-Al$_2$O$_3$

Samples	S$_{BET}$ (m^2/g)	Pore volume (cm^3/g)	Avg pore dia (Å)
Sasol γ-Al$_2$O$_3$ calcined @ 700 °C	180	0.49	109
5% La$_2$O$_3$- Sasol γ-Al$_2$O$_3$	183	0.48	104
20% Ni/Sasol γ-Al$_2$O$_3$ (Cat F)	128	0.39	113
20% Ni/5% La$_2$O$_3$- Sasol γ-Al$_2$O$_3$ (Cat G)	139	0.39	105

As given in Table 4.11, the incorporation of optimal amounts of La_2O_3 (5 wt%) to the comparatively stable Sasol-γ-Al_2O_3 support further improves its resistance to thermal sintering. One can notice that the surface area of the Sasol γ-Al_2O_3 showed a slight improvement from 180 m^2/g (for the bare calcined Sasol γ-Al_2O_3) to 183 m^2/g for the 5 wt% La_2O_3-Sasol γ-Al_2O_3. Table 4.11 also shows that Ni loading (20 wt%) on La_2O_3 modified Sasol γ-Al_2O_3 (Cat G) yielded a higher surface area and lower pore diameter while compared to the Ni catalyst supported on unmodified Sasol γ-Al_2O_3 (Cat F).

Furthermore, if one compares the catalyst supported on Alcan γ-alumina, with the one supported on Sasol γ-alumina, one can notice that the catalyst supported on Sasol γ-Al_2O_3 displayed better textural properties, with this including higher surface area, higher pore volume and a more stable network of pores.

4.6.2   X-ray Diffraction Analysis

XRD patterns of the fresh and used Ni catalysts supported on La_2O_3-Alcan γ-Al_2O_3 are reported in Figure 4.12. Figure 4.12 also presents the XRD pattern of Alcan γ-alumina showing a mostly amorphous structure. According to JCPDS 10-0425, the low intensity peaks centered at $2\theta = 37.6°$, $45.8°$, $67.1°$ are the characteristic peaks of γ-Al_2O_3.
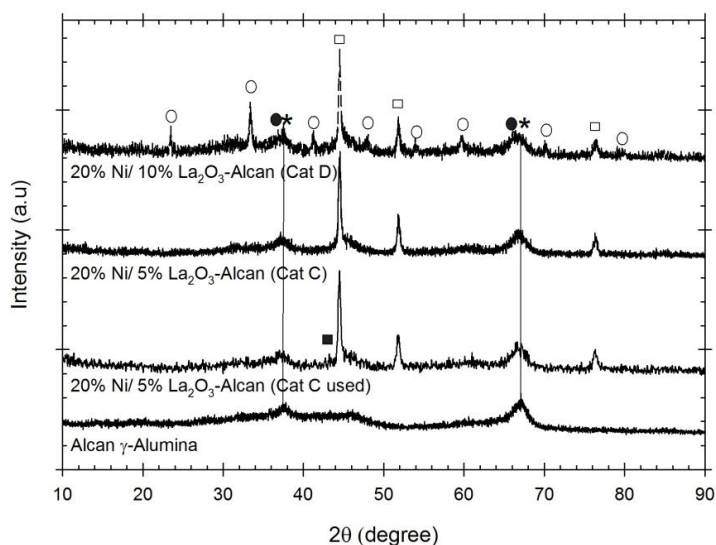
Figure 4.12: XRD patterns of the fresh and used (in 2-methoxy-4-methylphenol gasification) Ni catalysts supported on La_2O_3 doped Alcan γ-Al_2O_3. ($\star$: γ-Al_2O_3; $\square$: Ni; $\blacksquare$: NiO; $\bullet$: $NiAl_2O_4$; $\circ$: $LaAlO_3$).

As shown in Figure 4.12, the fresh Cat C (containing 20 wt% Ni on 5 wt% La_2O_3-Alcan support) gives diffraction lines for Ni (JCPDS 04-850) centered at $2\theta = 44.4°$, $51.8°$, $76.4°$. The γ-Al_2O_3 peak at $2\theta = 37.6°$ is slightly shifted to the left ($2\theta = 37.4°$) towards the difraction lines of $NiAl_2O_4$ ($2\theta = 36.96°$ JCPDS 01-1299). This suggests the presence of a solid mixture of both compounds with a relatively small proportion of $NiAl_2O_4$. With the increase of La_2O_3 content to 10 wt% (Cat D), reflections of $LaAlO_3$ crystals were observed at $2\theta = 23.4°$, $33.3°$, $41.2°$, $47.9°$, $54.0°$, $59.7°$, $70.2°$, $80.0°$ (JCPDS 09-0072). At higher La content formation of $LaAlO_3$ is also reported in the technical literature [34,43,44,49,204,205]. $LaAlO_3$ is formed by the solid phase interaction at high temperatures between Al_2O_3 and La_2O_3. According to Chen et al [34], at La/Al$\leq$0.02 (6.5wt% La_2O_3), the lanthanum species is highly dispersed on the alumina surface. Above this concentration level, La species is present as dispersed La_2O_3, $LaAlO_3$ and crystalline La_2O_3 phase depending on temperatures. For the purpose of comparison a quantitative estimation of the crystallite size of Ni was performed by applying the Scherrer equation (Eq. (3.5)). The broadening of the Ni (111) diffraction line at $45.4°$ gives slightly larger sizes of Ni crystallites on Cat D (31 nm) than that on Cat C (27 nm). This shows that the addition of La_2O_3 above the critical limit does not help in reducing the size of the Ni crystallites formed on the γ-Al_2O_3 surface. In the case of Cat D, the formation of $LaAlO_3$ reduces the Ni-alumina interactions resulting in larger Ni crystallites on the alumina support surface.

Furthermore, Figure 4.12 reports the XRD pattern of Cat C after being used in the gasification of 2-methoxy-4-methylphenol at 650 °C. Diffraction spectra of the fresh and used catalysts are almost the same except for the presence of a relatively small peak of NiO at $2\theta = 43.3°$ in the used catalyst. The diffraction lines of γ-Al_2O_3 for the used catalyst are also slightly shifted towards the $NiAl_2O_4$ compared to the fresh catalyst. The size of the Ni crystallites after being used for gasification remained essentially the same at 27.3 nm.

Figure 4.13 reports the X-ray diffractograms for Sasol γ-Al_2O_3 and catalysts prepared using Sasol γ-Al_2O_3. Catalysts supported on Sasol γ-Al_2O_3 exhibit similar γ-Al_2O_3 and Ni peaks. Comparatively smaller Ni crystallites are formed on the Sasol γ-Al_2O_3 surface. Ni

crystallites of 15.4 nm size are observed after the impregnation of 20 wt% Ni on Sasol γ-Al$_2$O$_3$ (Cat F). The stable structure of Sasol γ-Al$_2$O$_3$ with a higher surface area and pore volume (Table 4.1) helps in the formation of smaller Ni crystallites. Moreover, the pore size distribution of Sasol γ-Al$_2$O$_3$, as discussed in Section 4.2, suggests that its stable network of pores with larger pore diameters facilitates the dispersion of Ni onto the pores. Furthermore, the addition of 5 wt% La$_2$O$_3$ (Cat G) reduced the size of the Ni crystallites to 12.9 nm. This confirms the beneficial effect of La$_2$O$_3$ addition on Ni dispersion.
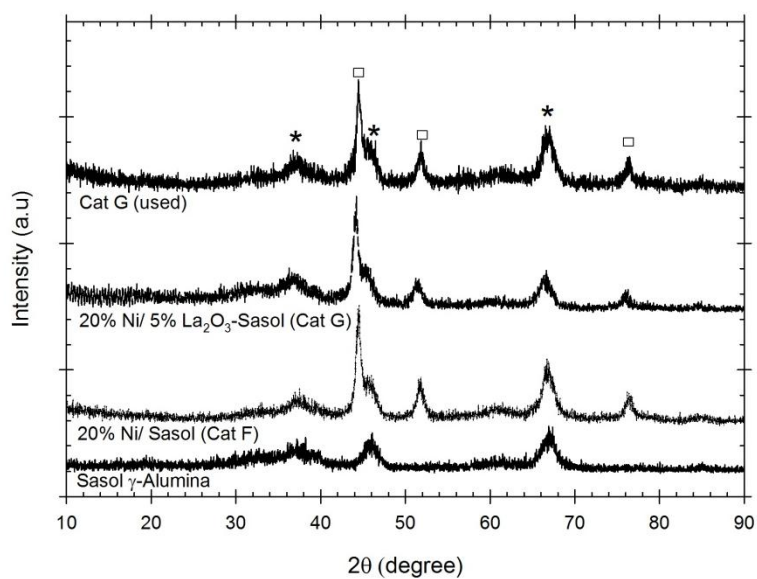
Figure 4.13: XRD patterns of the fresh and used (in 2-methoxy-4-methylphenol gasification) Ni catalysts supported on Sasol γ-Alumina. (★: γ-Al$_2$O$_3$; □: Ni; ■: NiO).

Figure 4.13 also shows the XRD diffractograms of Cat G following gasification of 2-methoxy-4-methylphenol. It was observed that Ni crystallites remain essentially unchanged with a 13.1 nm crystallites size. Furthermore, the XRD pattern of the used catalyst confirms the absence of graphitic carbon on the catalyst surface. This result suggests that this catalyst is stable for steam gasification of tars with negligible crystallite agglomeration.

4.6.3 Reducibility, Dispersion and Crystal Size

Figure 4.14 and Figure 4.15 report the reduction profiles of La_2O_3 doped and undoped Ni catalysts supported on Alcan γ-Al_2O_3 and Sasol γ-Al_2O_3, respectively. As shown in Figure 4.14, the Ni (20 wt%) catalyst supported on bare Alcan γ-Al_2O_3 (Cat B) exhibits wide reduction peaks in the 350 °C to 950 °C range, with four peaks at 400, 460, 640 and 800 °C. The first peak (at 400 °C) can be assigned to the reduction of highly dispersed NiO species on the alumina support surface [189,191,193]. According to the literature [39,189,191,202,206–209], the second peak (460 °C) and third peak (640 °C) can be attributed to the reduction of Ni^{+2} species with varying interactions with the oxide support. These could be highly dispersed non-stoichiometric amorphous nickel-aluminate spinels formed through metal support interaction. Surface nickel aluminate which is reducible at 500 °C can be attributed to the Ni^{+2} occupying the octahedral sites of γ-Al_2O_3, whereas surface $NiAl_2O_4$ formed with the tetrahedral sites of γ-Al_2O_3 requires higher reduction temperature [207,208,210]. Finally, the reduction peak observed above 700 °C is related to the reduction of bulk nickel-aluminates ($NiAl_2O_4$) [39,188,189,191,193,202].
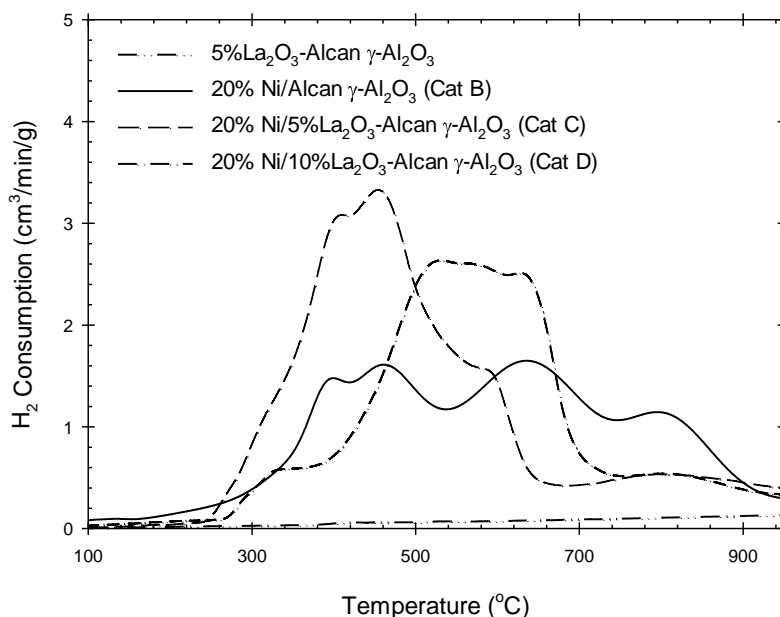
Figure 4.14: TPR profiles of the Ni catalysts supported on Alcan γ-Al_2O_3 with different La_2O_3 loadings (using 10% H_2 with balanced Ar at a flow rate of 50 cm^3/min and 10 °C/min heating rate).

For the 5 wt% La_2O_3 doped Ni/Alcan γ-Al_2O_3 catalyst (Cat C), reduction peaks were shifted to lower temperatures (Figure 4.14). Compared to the Ni catalyst on bare alumina, La_2O_3 addition yields a higher proportion of easily reducible Ni^{+2} species as well as reduced bulk $NiAl_2O_4$ significantly. Sanchez et al [39,202] and Mozahar et al [190], also reported similar findings for La_2O_3 doped Ni/Al_2O_3 catalysts.
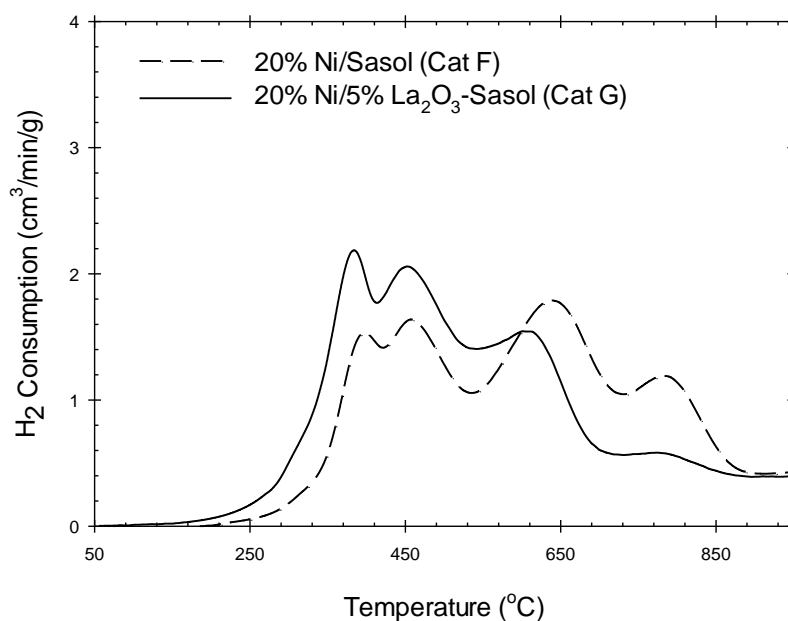
Figure 4.15: TPR profiles of Ni catalysts supported on bare and La_2O_3 modified Sasol γ-Al_2O_3 (using 10% H_2 with balanced Ar at a flow rate of 50 cm^3/min and 10 °C/min heating rate).

On the other hand, as shown in Figure 4.15, the TPR profile of the Ni catalyst supported on an undoped Sasol γ-Al_2O_3 support yields four major reduction peaks at 400, 460, 645 and 780 °C. Once again, the reduction profile of Ni catalysts supported on La_2O_3 doped Sasol γ-Al_2O_3 exhibits shifts in the reduction peak towards lower temperatures. This is an indication of the influence of La_2O_3 in decreasing the Ni-Al_2O_3 interaction.

Table 4.12 summarizes reducibility (R), dispersion (D) and crystallite size (d_v) as calculated using TPR and H_2 pulse chemisorptions. For both Alcan γ-Al_2O_3 and Sasol γ-Al_2O_3 supported catalysts, reducibility is increased with the incorporation of 5 wt% La_2O_3. It also improves the Ni dispersion by reducing the metal-support interactions; hence, smaller Ni crystals are formed on the support surfaces. Moreover, the focus of this

study is to conduct steam gasification of biomass at a temperature below 700 °C to avoid ash agglomeration and other operational issues with gasifiers. Therefore, the reducibility of the catalyst below 700 °C ($R_{700\ °C}$) is an important characteristic to investigate. As can be seen from Figure 4.14 and Figure 4.15, compared to Ni catalysts supported on bare γ-Al_2O_3, 5 wt% La_2O_3 addition yielded a higher proportion of easily reducible Ni^{+2} species (low temperature peaks). This is achieved by reducing $NiAl_2O_4$ formation (high temperature peaks). In this respect, La_2O_3 reduces the nickel-alumina interactions and limits nickel-aluminate formation [190]. Therefore, reducibility below 700 °C is significantly enhanced for catalysts containing 5 wt% lanthanum oxides, as reported in Table 4.12. One should also notice that La_2O_3 does not produce a significant effect on the textural properties of Sasol γ-Al_2O_3. The $R_{700\ °C}$ was, however, increased from 72 to 89% with the incorporation of 5 wt% La_2O_3 (Cat G) when compared to the unmodified Ni/Sasol γ-Al_2O_3 catalyst (Cat F).

Table 4.12: Reducibility (R), dispersion (D) and crystal size (d_v) of Ni for different catalysts

Sample	R (%)	$R_{700\ °C}$ (%)	$D(\%) = \frac{117X}{WR}$	$d_v(nm) = \frac{97.1}{\%D}$
20% Ni/Alcan-γ-Al_2O_3 (Cat B)	81	66	0.90	108
20% Ni/5% La_2O_3- Alcan γ-Al_2O_3 (Cat C)	91	87	1.12	87
20% Ni/10% La_2O_3- Alcan γ-Al_2O_3 (Cat D)	89	81	0.93	105
20% Ni/Sasol γ-Al_2O_3 (Cat F)	89	72	2.99	32
20% Ni/5% La_2O_3 – Sasol γ-Al_2O_3 (Cat G)	94	89	3.53	28

X stands for the total hydrogen chemisorbed (μmol of H_2/g cat); W denotes the metal loading (wt%)

Figure 4.14 also shows the TPR profiles of catalysts containing 5 wt% (Cat C) and 10 wt% (Cat D) lanthanum oxides. As shown in Figure 4.14, the increase of La_2O_3 loading from 5 to 10% resulted in a shift of reduction peaks to higher temperatures [39,49]. Moreover, the formation of $LaAlO_3$ on the Ni/γ-Al_2O_3 catalyst containing 10 wt% La_2O_3

(Cat D) was revealed by XRD (Figure 4.12). According to the technical literature [34,35,192,211,212], $LaAlO_3$ is formed on the relatively active surface sites of γ-Al_2O_3 via solid phase interactions between La_2O_3 and Al_2O_3. Furthermore, using Al NMR spectroscopy, Del Angel et al [55] showed that excess lanthanum content results in a higher relative abundance of aluminum in the tetrahedral symmetry. Therefore, for the catalyst containing 10 wt% La_2O_3, Ni is deposited on the relatively stable subsurface sites of γ-Al_2O_3 which are only reducible at higher temperatures.

The reduction profile of Cat D also exhibits a new peak of larger Ni particles at 320 °C. Liu et al [49] and Sanchez et al [39] also reported similar TPR data. This new peak can be attributed to the formation of $LaAlO_3$ on Cat D which may favor Ni crystallite agglomeration by blocking the Al_2O_3 active sites for Ni deposition. These results suggest that higher La_2O_3 loadings favor the formation of Ni species in strong interaction with the support as well as the formation of larger Ni particles which are susceptible to coke deposition. Therefore, $R_{700\ °C}$ was decreased from 87 to 81% when La_2O_3 loading augmented from 5 to 10% (Table 4.12). This also results in a reduced dispersion of nickel on the catalyst surface.

Finally, catalysts supported on Sasol γ-Al_2O_3 yield higher reducibility and metal dispersion when compared to the Alcan γ-Al_2O_3 supported catalysts. Significantly smaller Ni crystallites are formed when Sasol γ-Al_2O_3 is used instead of Alcan γ-Al_2O_3. Therefore, it can be hypothesized that better textural properties of Sasol γ-Al_2O_3 (higher surface area, pore diameter and thermal stability) facilitates the synthesis of catalysts with highly dispersed smaller Ni crystallites.

4.6.4 Acid-Base Properties

As confirmed using pyridine DRIFT in Section 4.3.2, both Alcan and Sasol γ-Al_2O_3 possess Lewis type acid sites only. The addition of basic La_2O_3 can influence the acidity and basicity of γ-Al_2O_3. The role of La_2O_3 on the acidity and basicity of γ-Al_2O_3 is discussed in section 4.3.2. It has been found that the addition of La_2O_3 helps to reduce the acidity and improve the basicity of γ-alumina. However, more than 5 wt% La_2O_3 content

results in a gradual rise of acid site concentration due to the presence of deficiently coordinated La^{3+} ions acting as Lewis acid sites.

The acidity and basicity of the Ni catalysts containing different amounts of La_2O_3 were investigated by the temperature programmed desorption (TPD) of NH_3 and CO_2, respectively. Table 4.13 and Table 4.14 report total acidity and basicity of the supports and Ni catalysts as determined from the amount of NH_3 and CO_2 desorption, respectively. To distinguish between the role of La_2O_3 addition and structural change during the preparation stage on the acid-base properties of γ-Al_2O_3, concentration of acidic and basic sites are also reported in Table 4.13.

Table 4.13: Total acidity and basicity of the catalyst supported on Alcan γ-Al_2O_3 as determined from NH_3-TPD and CO_2-TPD, respectively

Sample	Total acidity		Total basicity	
	µmol/g γ-Al_2O_3	µmol/m^2	µmol/g γ-Al_2O_3	µmol/m^2
Alcan γ-Al_2O_3	370	3.18	91	0.79
5% La_2O_3-Alcan γ-Al_2O_3	251	1.85	131	0.96
10% La_2O_3-Alcan γ-Al_2O_3	250	1.96	156	1.22
20% Ni/Alcan (Cat B)	137	3.63	38	1.01
20%Ni/5%La_2O_3-Alcan (Cat C)	97	1.39	83	1.19
20%Ni/10%La_2O_3-Alcan (Cat D)	110	2.27	70	1.49

Table 4.13 shows that after 20 wt% Ni addition on Alcan γ-Al_2O_3 (Cat B), the total acidity is substantially decreased from 370 to 137 µmol NH_3/g γ-Al_2O_3. One should mention that this significant reduction of acidity is mainly due to the changes in the γ-Al_2O_3 support during Ni impregnation. For instance, 20% Ni was loaded using 8 successive impregnations with overnight reduction at 700 °C following every impregnation step. Losses of γ-Al_2O_3 acid sites occur during heat treatment via dehydroxylation. Table 4.13 also reports that for the 20 wt% Ni/Alcan γ-Al_2O_3 catalyst containing 5 wt% La_2O_3 (Cat C), the total acidity is further reduced from 137 (for Cat B)

to 97 µmol NH$_3$/g γ-Al$_2$O$_3$. However, when La$_2$O$_3$ content is augmented to 10 wt%, the total acidity of the Ni/Alcan γ-Al$_2$O$_3$ catalyst (Cat D) is increased to 110 µmol NH$_3$/g γ-Al$_2$O$_3$.

Furthermore, the addition of the Ni on support reduces its basicity (CO$_2$ adsorption capacity). A substantial decrease in total basicity (from 91 to 38 µmol CO$_2$/g γ-Al$_2$O$_3$) was observed after loading 20 wt% Ni on bare Alcan γ-Al$_2$O$_3$ (Cat B). Significant improvement in the total basicity was found with the incorporation of 5 wt% La$_2$O$_3$ in the catalyst formulation (Cat C). Table 4.13 also reports that with the increase of La$_2$O$_3$ loading from 5 to 10 wt%, the basicity of the La$_2$O$_3$ modified Alcan γ-Al$_2$O$_3$ support was improved. However, adding Ni on a 10 wt% La$_2$O$_3$ (Cat D) yielded a lower basicity (70 µmol CO$_2$/g γ-Al$_2$O$_3$) than the catalyst containing 5 wt% La$_2$O$_3$ (Cat C) only. It is speculated that the formation of LaAlO$_3$ on Cat D is responsible for the reduction of its basicity.

Table 4.14: Total acidity and basicity of the catalyst supported on Sasol γ-Al$_2$O$_3$ as determined from NH$_3$-TPD and CO$_2$-TPD, respectively

Sample	Total acidity		Total basicity	
	µmol/g γ-Al$_2$O$_3$	µmol/m^2	µmol/g γ-Al$_2$O$_3$	µmol/m^2
Sasol γ-Al$_2$O$_3$	511	2.84	116	0.65
5% La$_2$O$_3$-Sasol γ-Al$_2$O$_3$	458	2.39	170	0.88
20% Ni/Sasol (Cat F)	547	3.55	98	0.64
20%Ni/5%La$_2$O$_3$-Sasol (Cat G)	510	2.94	153	0.91

As is the case for the Alcan γ-Al$_2$O$_3$, the addition of La$_2$O$_3$ to the Sasol γ-Al$_2$O$_3$ also diminishes acidity and improves basicity. The decrease in acidity when adding 5 wt% La$_2$O$_3$ to γ-Al$_2$O$_3$ is lower for Sasol γ-Al$_2$O$_3$ (511 to 458 µmol NH$_3$/g γ-Al$_2$O$_3$) than for Alcan (370 to 251 µmol NH$_3$/g γ-Al$_2$O$_3$). These modest acidity changes observed in Sasol γ-Al$_2$O$_3$ are mainly due to its higher thermal stability. On the other hand, Sasol exhibited higher improvements in basicity with the 5 wt% La$_2$O$_3$ addition ranging from 116 to 170

μmol CO_2/g γ-Al_2O_3. It is hypothesized that the higher specific surface area of Sasol γ-Al_2O_3 facilitates La_2O_3 dispersion.

Similarly, as reported in Table 4.14, a Ni catalyst supported on 5 wt% La_2O_3-Sasol γ-Al_2O_3 (Cat G) yielded lower acidity and substantially higher basicity when compared to the Ni catalyst supported on bare Sasol γ-Al_2O_3(Cat F). Furthermore, Ni catalysts supported on Sasol γ-Al_2O_3 exhibited higher acidity and basicity than the Alcan γ-Al_2O_3 supported catalysts. The higher acidity of Sasol γ-Al_2O_3 supported catalysts can be explained by their higher thermal stability. On the other hand, the higher basicity of the catalysts prepared on Sasol γ-Al_2O_3 can be associated to their higher surface area which facilitates La_2O_3 dispersion.

4.6.5   Stability over Repeated Oxidation-Reduction conditions

In biomass gasification, the catalyst undergoes repeated oxidation-reduction cycles in both the gasifier and the catalyst regeneration units. Therefore, a critical characteristic of a catalyst for biomass gasification is its stability under cyclic operation. To investigate these matters, successive TPO and TPR experiments were developed. Each cycle was composed of successive TPO, TPR, and pulse chemisorption experiments. Figure 4.16 Figure 4.16 reports Ni reducibility and dispersion of Cat C and Cat G under repeated oxidation and reduction cycles.
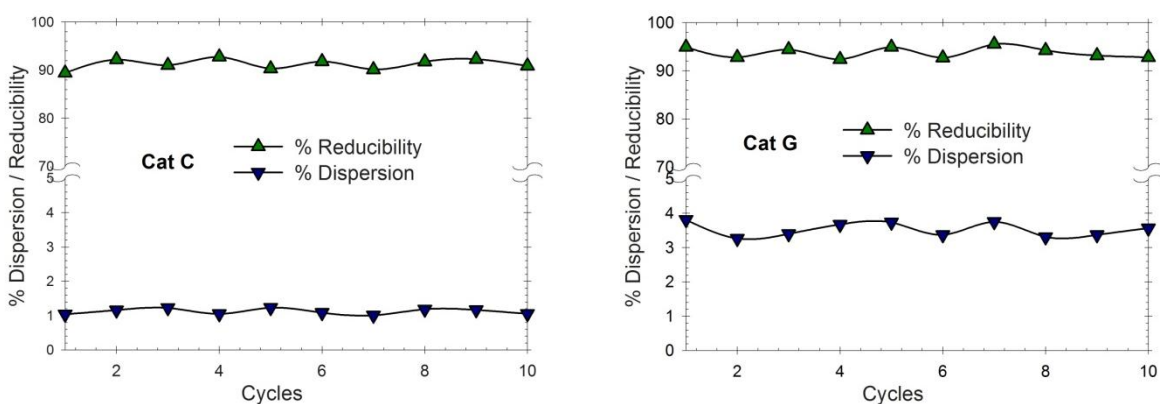
Figure 4.16: Ni reducibility and dispersion of 20%Ni/5% La_2O_3-Alcan γ-Al_2O_3 (Cat C) and 20%Ni/5% La_2O_3-Sasol γ-Al_2O_3 (Cat G) catalysts over TPO (up to 700 °C)/TPR (up to 950 °C) cycles. (oxidizing agent: 5% O_2 in He; reducing agent: 10% H_2 in Ar; flow rate: 50 cm³/min; heating rate: 10 °C/min)

One should mention that almost identical TPR profiles were found for the Ni catalysts supported on 5 wt% La_2O_3 modified Alcan (Cat C) and Sasol (Cat G) γ-Al_2O_3 even after ten cycles of TPO/TPR experiments. It can be further observed in Figure 4.16 that percentage reduction almost remained the same for the both catalysts under the repeated TPO/TPR cycles. The 20% Ni/5% La_2O_3-Sasol γ-Al_2O_3 (Cat G) showed stable reducibility under repeated oxidation-reduction cycles with an average reduction percentage of 94%. Pulse chemisorption results further confirm the negligible metal crystallite agglomeration of the catalyst over repeated oxidation-reduction conditions with consistent percentage dispersion of Ni. These results indicate that the catalyst preparation via multi-step impregnation with direct reduction of metal precursors after each impregnation in fluidized bed conditions is an effective way to prepare stable catalysts which can sustain the harsh operating conditions of an industrial gasifier unit.

4.6.6   Gasification Results

In this research, glucose and 2-methoxy-4-methylphenol were chosen as model compounds for the cellulose and lignin contained in biomass. This allowed evaluating the steam gasification performance of the Ni/γAl_2O_3 catalysts modified with different amount of La_2O_3. Steam gasification experiments of biomass surrogates were performed in a CREC fluidized Riser Simulator at reaction temperature of 650 °C, catalyst/biomass ratio (Cat/B) of 12.5 g/g and reaction time of 20 s. All the experiments were repeated at least 4 times to secure the reproducibility of results. Standard deviations for experimental repeats were in the 2-9% range with an average of 6%. An important observation from these runs was that the mass balance closures, which consider permanent gases (H_2, CO, CO_2, and CH_4), water, ethylene, ethane, propylene, acetaldehyde, and carbon deposited over the catalyst, were in the ±11% range, with most of the balances being in the ±5% range.

The performance of the prepared catalysts was evaluated based on the: i) dry gas yield (moles of H_2, CO, CO_2 and CH_4 produced/moles of biomass fed), ii) carbon conversion to permanent gases, iii) quality of synthesis gas, iv) coking, and v) tars formed. Aromatics and oxygenates of a C_6^+ structure in the produced gas were considered as tars. Experimental results were also compared to equilibrium data as calculated using the thermodynamic model described in CHAPTER 5. Elevated reactor pressure after the

conversion of biomass surrogate species in a constant volume CREC Riser Simulator was also considered to determine equilibrium under rigorous conditions. Coke and tars formation are also taken into account in the thermodynamic model as per the following overall reaction:

$$C_x H_y O_z + H_2O \xrightarrow{heat} H_2 + CO + CO_2 + H_2O + CH_4 + C_{(s)} + tars \qquad (6.1)$$
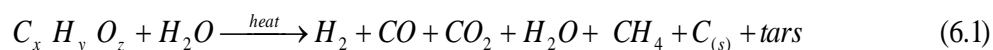
Figure 4.17 and Figure 4.18 compare the performance of the prepared catalysts in terms of carbon conversion, dry gases yield and tar formation for cellulose and 2-methoxy-4-methylphenol gasification, respectively. 100% conversion of glucose without any detectable tar formation was achieved at only 650 °C and 20 s of reaction time via catalytic steam gasification using La_2O_3 modified $Ni/\gamma\text{-}Al_2O_3$ catalysts. A maximum of only 2.3 mg of coke deposition per g of catalyst during glucose gasification was also observed.
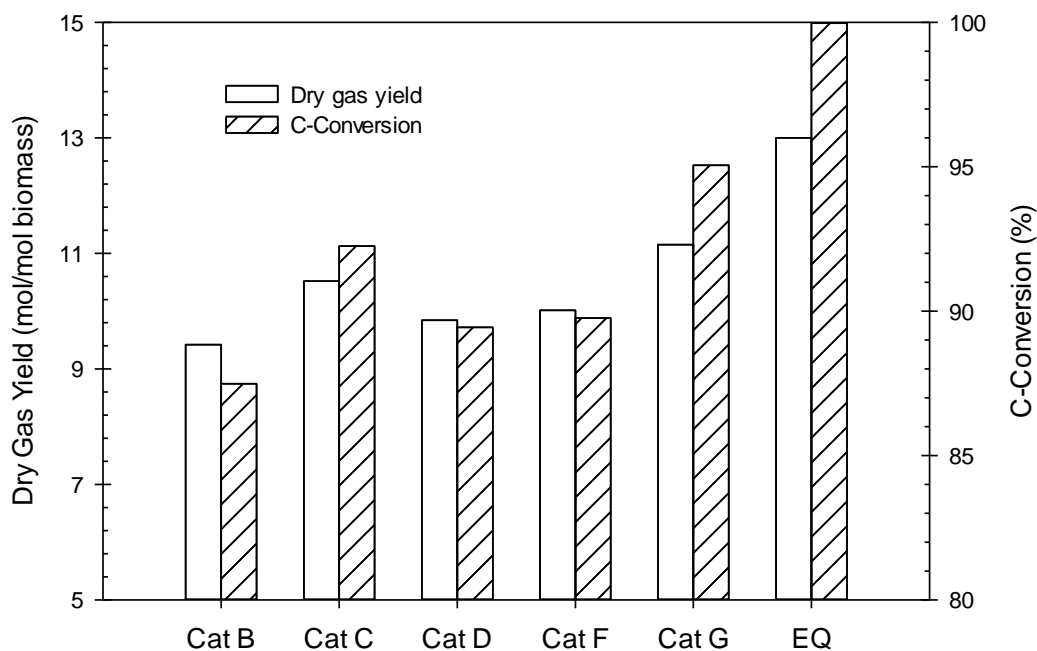
Figure 4.17: Dry gas yield and carbon-conversion during steam gasification of glucose at 650 °C, S/B = 1.0 g/g, Cat/B = 12.5 g/g and 20 s of reaction time using different catalysts: 20% Ni/Alcan γ-Al₂O₃ (Cat B), 20% Ni/5% La₂O₃-Alcan γ-Al₂O₃ (Cat C), 20% Ni/10% La₂O₃-Alcan γ-Al₂O₃ (Cat D), 20% Ni/Sasol γ-Al₂O₃ (Cat F) and 20% Ni/5% La₂O₃-Sasol γ-Al₂O₃ (Cat G).

On the other hand, 2-methoxy-4-methylphenol possesses significantly lower H/C and O/C ratios while compared to glucose. It is expected that steam gasification of 2-methoxy-4-methylphenol would yield lower carbon conversion to permanent gases and lower H_2/CO. It is also anticipated that, steam gasification of the lignin surrogate will lead to tar formation and higher coke deposition. Using the catalysts of this study, however, tars formation was limited to 10.5 wt% at 650 °C. Moreover, XRD results of the catalyst used in 2-methoxy-4-methylphenol gasification confirmed the absence of graphitic coke formation (Figure 4.12 and Figure 4.13).
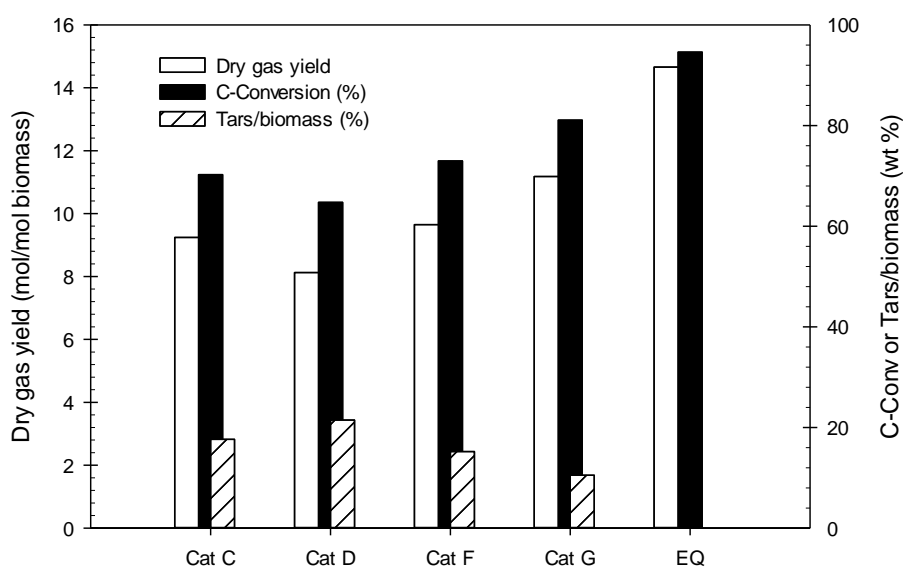
Figure 4.18: Dry gas yield, carbon-conversion and tars yield of 2-methoxy-4-methylphenol steam gasification at 650 °C, S/B = 1.5 g/g, Cat/B = 12.5 g/g and 20 s of reaction time using different catalysts: 20% Ni/5% La_2O_3-Alcan γ-Al_2O_3 (Cat C), 20% Ni/10% La_2O_3-Alcan γ-Al_2O_3 (Cat D), 20% Ni/Sasol γ-Al_2O_3 (Cat F) and 20% Ni/5% La_2O_3-Sasol γ-Al_2O_3 (Cat G).

Furthermore, Ni catalysts with different La_2O_3 content (Cat B: 0% La_2O_3, Cat C: 5% La_2O_3 and Cat D: 10% La_2O_3) were tested in the present study to understand the effect of lanthanum loading. As shown in Figure 4.17, a significant improvement in dry gas yield and carbon conversion can be achieved with the incorporation of 5 wt% La_2O_3 in the catalyst formulation (Cat C). A 5% La_2O_3 promoted Ni/Alcan γ-Al_2O_3 catalyst (Cat C) exhibited a high (92.3%) conversion of carbon to permanent gases producing 10.52 mol of dry gas per mole of glucose. However, both the dry gas yield and carbon conversion

from glucose gasification were reduced to 9.84 mol/mol and 89.4%, respectively, for a catalyst containing 10% lanthanum oxide (Cat D). These differences became more prominent in case of 2-methoxy-methylphenol gasification (Figure 4.18). Carbon conversion and dry gas yield during 2-methoxy-methylphenol gasification using Cat D were reduced from 70.2 to 64.1% and from 9.24 to 8.12 mol/mol, respectively, while compared to Cat C. These results can be explained given the lower surface area, Ni reducibility and dispersion of Cat D. XRD results as shown in Figure 4.12, provide evidence of $LaAlO_3$ formation on the catalyst containing 10 wt% La_2O_3 (Cat D). The formation of $LaAlO_3$ is undesirable as it partially blocks support pores and active sites. Therefore, an increase in La_2O_3 content from 5 (Cat C) to 10 wt% (Cat D) resulted in the reduction of catalyst surface area, $R_{700\ °C}$, and dispersion by 35%, 7% and 17%, respectively, which are mainly responsible for the observed decrease in gasification performance.

Cat D also exhibited higher coke deposition (Figure 4.19) than that of Cat C. As shown in Figure 4.14, it was found that higher La_2O_3 loadings favors nickel crystallite agglomeration forming larger nickel particles on the surface. Those surface Ni particles are susceptible to coking due to fast hydrocarbon cracking. Comparatively higher acidity and lower basicity of Cat D (Table 4.13) are also responsible for the observed increase in coke deposition. A catalyst containing 10 wt% La_2O_3 (Cat D) displayed 14% higher acidity and 16% lower basicity than the catalyst with 5 wt% La_2O_3 (Cat C). Regarding the influence of basicity, it has been reported that catalysts having a higher basicity support show stronger resistance to carbon fouling during steam and dry hydrocarbon reforming [29,30,213–217]. It is, thus, hypothesized that a basic support could improve the adsorption of acidic CO_2 and steam, so that more coke could be removed from the catalyst surface as a result of the Boudouard reaction $(C + CO_2 \longleftrightarrow 2CO)$ and the heterogeneous water-gas shift reaction $(C + H_2O \longleftrightarrow H_2 + CO)$. Furthermore, compared to Cat C, Cat D produced a synthesis gas with a 10% lower H_2/CO ratio during both glucose and 2-methoxy-4-methylphenol gasification (Figure 4.20). This lower H_2/CO ratio could be assigned to its lower CO_2 adsorption capacity.
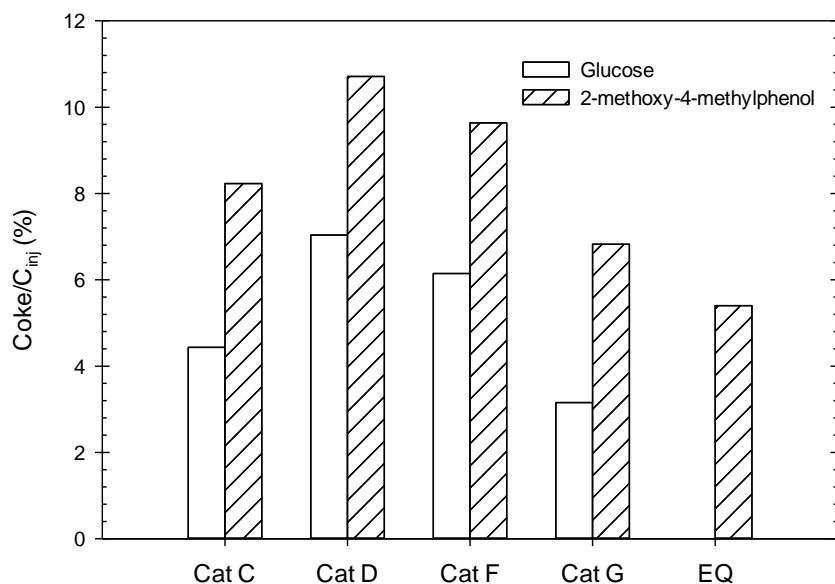
Figure 4.19: Coke deposition during steam gasification of glucose and 2-methoxy-4-methylphenol at 650 °C, Cat/B = 12.5 g/g and 20 s of reaction time using different catalysts: 20% Ni/5% La$_2$O$_3$-Alcan γ-Al$_2$O$_3$ (Cat C), 20% Ni/10% La$_2$O$_3$-Alcan γ-Al$_2$O$_3$ (Cat D), 20% Ni/Sasol γ-Al$_2$O$_3$ (Cat F) and 20% Ni/5% La$_2$O$_3$-Sasol γ-Al$_2$O$_3$ (Cat G).

Figure 4.17 to Figure 4.20 also compare the performance of Ni catalysts supported on bare Sasol γ-Al$_2$O$_3$ (Cat F) and Sasol γ-Al$_2$O$_3$ modified with 5% La$_2$O$_3$ (Cat G). Again, addition of 5% La$_2$O$_3$ (Cat G) resulted in the increase of carbon conversion to permanent gases from 89.7 to 95% and from 73 to 81% during glucose and 2-methoxy-4-methylphenol gasification, respectively. Cat G also yielded lower tars (15.2 to 10.5%) during 2-methoxy-4-methylphenol gasification (Figure 4.18). Moreover, as can be seen in Figure 4.19 and Figure 4.20, Cat G demonstrated lower coking and a higher H$_2$/CO ratio in the produced synthesis gas while compared to Cat F. These results confirm the promoting effect of La$_2$O$_3$ for reforming, water gas shift and coke conversion reactions. This enhanced reactivity can be linked to the higher surface area, the increased Ni reducibility, the higher metal dispersion, the higher basicity and the lower acidity achieved by lanthanum doping. In fact, the addition of 5 wt% La$_2$O$_3$ to the Ni/Sasol γ-Al$_2$O$_3$ catalyst improved the $R_{700\ °C}$ from 72 to 89% and the dispersion from 2.99 to 3.53%. Cat G also displayed an 8% higher surface area, a 37% higher basicity and a 6% lower acidity while compared to Cat F.

It can also be observed form Figure 4.17 to Figure 4.20 that Cat G displayed a significantly enhanced performance approaching chemical equilibrium while compared with all other catalysts used both for glucose and 2-methoxy-4-methylphenol gasification. Comparing the catalysts supported on Alcan γ-Al_2O_3 (Cat C) and Sasol γ-Al_2O_3 (Cat G), it can be noticed that significantly higher dry gas yield and carbon-conversion were achieved using Cat G especially in the case of 2-methoxy-4-methylphenol gasification. One should notice that the catalyst prepared on Sasol γ-Al_2O_3 showed significantly higher Ni dispersion (Table 4.12) and CO_2 adsorption capacity (Table 4.14). This was likely due to its higher thermal stability and stable pore network. In addition, the higher acidity found on Cat G versus the one on Cat C (Table 4.13 and Table 4.14) could be a factor on these findings. However, coke deposition was decreased from 4.44 to 3.15% (glucose gasification) and from 8.43 to 6.82% (2-methoxy-4-methylphenol gasification) using Cat G instead of Cat C. This can be attributed to a significantly higher CO_2 adsorption capacity of Cat G while compared to Cat C. As mentioned before, higher CO_2 adsorption facilitates the Boudouard reaction resulting in less net coke formation on acid sites.
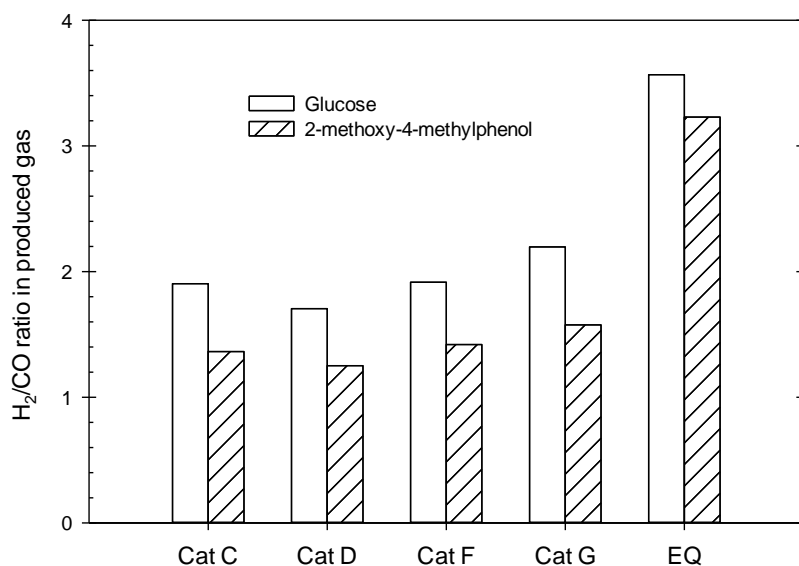
Figure 4.20: H_2/CO ratio of the synthesis gas obtained during steam gasification of glucose and 2-methoxy-4-methylphenol at 650 °C, Cat/B = 12.5 g/g and 20 s of reaction time using different catalysts: 20%Ni/5% La_2O_3-Alcan γ-Al_2O_3 (Cat C), 20%Ni/10% La_2O_3-Alcan γ-Al_2O_3 (Cat D), 20%Ni/Sasol γ-Al_2O_3 (Cat F) and 20%Ni/5% La_2O_3-Sasol γ-Al_2O_3 (Cat G).

Thus, it is demonstrated in the present study that La_2O_3 loadings on Ni/γ-Al_2O_3 catalyst has strong influence on its textural properties, acidity, basicity, Ni reducibility and metal dispersion and hence, influencing its biomass steam gasification performance.

4.7 **Effect of Catalyst Reduction Conditions**

Surface area loss of γ-Al_2O_3 at high temperature occurs due to: a) sintering via collapse of its pores and b) the phase transformation towards α-Al_2O_3 [34]. The sintering of particles is responsible for the surface area loss of γ-Al_2O_3 at temperatures below 1000 °C. At temperatures above 1000 °C, the phase transformation plays the major role in the γ-Al_2O_3 surface area loss. The addition of La_2O_3 improves the thermal resistance of γ-Al_2O_3 as shown in Section 4.3.1. Depending on loading and temperature, lanthanum is present as dispersed La_2O_3, crystalline La_2O_3 and $LaAlO_3$ [34,43,44,204,211,212]. At a lower loading, lanthanum exists as a dispersed phase, undetectable by XRD (Figure 4.9), and reduces the sintering of γ-Al_2O_3. Depending on the specific surface area, there is a concentration limit to which γ-Al_2O_3 can accommodate dispersed lanthanum. Beyond this concentration limit, lanthanum can form crystalline La_2O_3 and $LaAlO_3$ on a γ-Al_2O_3 surface [34,43,44,211,212]. At temperatures above 1000 °C, lanthanum reacts with alumina to form $LaAlO_3$ [34]. By XRD of lanthanum modified alumina, the formation of $LaAlO_3$ at 1000 °C was found on samples containing 5.8 wt% La_2O_3 [204] and 10 wt% La_2O_3 [212]. Beguin et al [211] also reported the formation of $LaAlO_3$ on 11 wt% La/Al_2O_3 after calcination at 1050 °C. The formation of $LaAlO_3$ helps to retard the phase transformation of γ-Al_2O_3 when the catalyst is exposed at temperatures above 1000 °C. However, the surface area is decreased due to pore blocking by added La_2O_3 and $LaAlO_3$ formation. In the present study, surface area loss of γ-Al_2O_3 due to sintering is the main focus as the process is operated at lower temperatures. Moreover, no evidence of phase transformation in the prepared catalysts was observed (Section 4.6.2).

However, the XRD results as shown in Figure 4.12 and Figure 4.21, revealed the formation of undesirable $LaAlO_3$ on the Ni/Alcan γ-Al_2O_3 catalyst containing 10 wt% La_2O_3 (Cat D). To investigate the reason behind the $LaAlO_3$ formation, XRDs of lanthanum modified γ-Al_2O_3 samples with different amounts of La_2O_3 were performed.

For up to 5 wt% La_2O_3 loading, no $LaAlO_3$ peak was observed on the diffractograms of the La_2O_3/γ-Al_2O_3 supports even after calcining at 1100 °C. Figure 4.21 reports the XRD profiles of the fresh and calcined 10 wt% La_2O_3/γ-Al_2O_3 support. As shown in Figure 4.21, $LaAlO_3$ formation was also not observed on freshly prepared 10 wt% La_2O_3/γ-Al_2O_3. In agreement with the literature [34,43,44,204,211,212], $LaAlO_3$ peaks on the 10 wt% La_2O_3/γ-Al_2O_3 support were only appeared after calcining the sample at 1000 °C for 8 hrs.
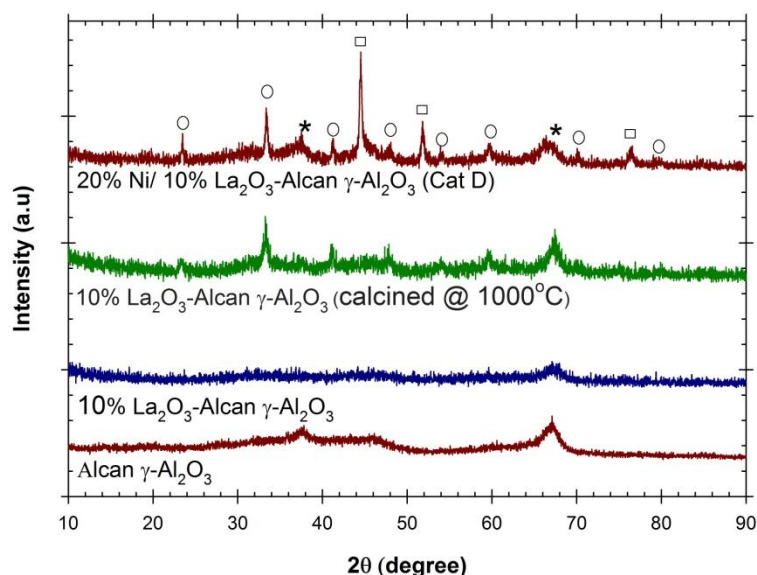
Figure 4.21: XRD patterns of 10 wt% La_2O_3 doped Alcan γ-Al_2O_3. ($\star$: γ-Al_2O_3; $\square$: Ni; $\blacksquare$: NiO; $\bullet$: $NiAl_2O_4$; $\circ$: $LaAlO_3$).

As $LaAlO_3$ was not observed on the support (10 wt% La_2O_3/γ-Al_2O_3) of Cat D, it is hypothesized that these species could have been formed during Ni impregnation. Cat D was prepared via direct reduction of impregnated nickel nitrates to nickel at a maximum temperature of 700 °C. Decomposition of nickel nitrates under an H_2 atmosphere involved the following possible reactions [58,218,219]:

$$Ni(NO_3)_2 + 9H_2 \rightarrow Ni + 2NH_3 + 6H_2O \qquad \Delta H^o = -267 \; kcal/mol$$

$$Ni(NO_3)_2 + 4H_2 \rightarrow Ni + 2NO + 4H_2O \qquad \Delta H^o = -87 \; kcal/mol$$

$$Ni(NO_3)_2 + 5H_2 \rightarrow Ni + N_2O + 5H_2O \qquad \Delta H^o = -168 \; kcal/mol$$

$$Ni(NO_3)_2 + 2H_2 \longrightarrow Ni + 2NO_2 + 2H_2O \quad \Delta H^o = 1.77\ kcal/mol$$

$$Ni(NO_3)_2 + 6H_2 \longrightarrow Ni + N_2 + 6H_2O \quad \Delta H^o = -245\ kcal/mol$$
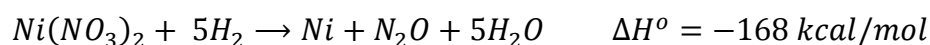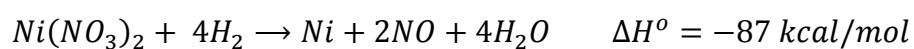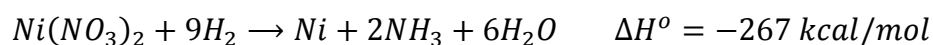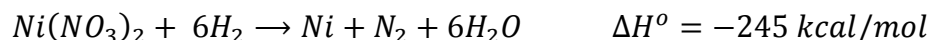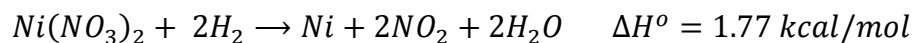
Thus, the heat evolved from these highly exothermic reactions involved in the reduction of nickel nitrates was the reason behind the LaAlO$_3$ formation by rising local temperature above 1000 °C. Failure to remove the heat released also resulted in excessive sintering. In fact, the catalyst surface area was dropped significantly after Ni impregnation (Table 4.10). Similar decomposition behaviour was also reported for lanthanum nitrate [220].Therefore, the flow during the catalyst reduction step is a crucial parameter to control sintering by quickly carrying out the heat evolved. In this study, 4 sets of catalysts were prepared by varying the reducing gas flow:

a) Low flow (2 ml/mmol nitrates/min):

Cat E - 20wt% Ni/5% La$_2$O$_3$-Sasol γ-Al$_2$O$_3$

b) Moderate flow (6 ml/mmol nitrates/min):

Cat F - 20wt% Ni/Sasol γ-Al$_2$O$_3$

Cat G - 20wt% Ni/5% La$_2$O$_3$-Sasol γ-Al$_2$O$_3$

c) High flow (12 ml/mmol nitrates/min):

Cat H - 20wt% Ni/5% La$_2$O$_3$-Sasol γ-Al$_2$O$_3$

The catalyst reduction chamber remained in a fixed bed condition at low gas flow. At the moderate flow, channeling in the catalyst bed was observed. The high gas flow ensured that the bed was in a uniform fluidized bed condition to achieve better heat distribution. Moreover, decomposition reactions started as the temperature approaches 270 °C at a very fast rate [58]. The fast decomposition was controlled by limiting the H$_2$ availability. At the high gas flow (12 ml/mmol nitrates/min), nitrates decomposition occurs at a faster rate. However, the high gas flow ensures the efficient removal and distribution of reaction heat. In contrast, at the low gas flow (2 ml/mmol nitrates/min), maximum nitrate decomposition occurred after the oven reached the maximum temperature (700 °C at a rate of 3 °C/min). Therefore, a significant rise of the local temperatures inside the catalyst

bed can be occurred at this condition given the limited release of the heat associated with the metal nitrate reduction reactions from the catalyst bed. In the following sections, effect of reduction gas flow rate on the textural properties, Ni reducibility and dispersion, acid-base properties, and gasification performance of the catalysts were discussed.

4.7.1 Textural Properties

Table 4.15 reports the BET surface area, pore volume and average pore diameter for both the support materials and Ni catalysts prepared varying gas flow during the reduction of impregnated metal nitrates. The pore size distribution, as described in Figure 4.22, was determined by analyzing the desorption branch of the isotherm and using the BJH (Barrett-Joyner-Halenda) method.

Table 4.15: BET surface area, pore volume and pore diameter of the supports and catalysts prepared varying reduction flow rate

Samples	Reduction Flow rate (ml/mmol/min)	S_{BET} (m^2/g)	Pore volume (cm^3/g)	Avg pore dia (Å)
5% La$_2$O$_3$-Sasol γ-Al$_2$O$_3$ (Cat E-1)	8	175	0.47	106
5% La$_2$O$_3$-Sasol γ-Al$_2$O$_3$ (Cat G-1)	16	1823	0.48	104
5% La$_2$O$_3$-Sasol γ-Al$_2$O$_3$ (Cat H-1)	26	186	0.48	102
20% Ni/5% La$_2$O$_3$-Sasol γ-Al$_2$O$_3$ (Cat E)	2	107	0.33	124
20% Ni/Sasol γ-Al$_2$O$_3$ (Cat F)	6	128	0.39	113
20% Ni/5% La$_2$O$_3$-Sasol γ-Al$_2$O$_3$ (Cat G)	6	139	0.39	105
20% Ni/5% La$_2$O$_3$-Sasol γ-Al$_2$O$_3$ (Cat H)	12	166	0.32	76

The main challenge in synthesising of Ni over γ-Al$_2$O$_3$ is to maintain the porous structure of the support. In the catalyst preparation stage, structure of γ-Al$_2$O$_3$ is altered by thermal sintering and pore blocking by added Ni loading. Sasol γ-Al$_2$O$_3$ possesses high thermal stability as shown in Section 4.2. However, pore size distribution of Sasol γ-Al$_2$O$_3$ after 20 wt% Ni addition (Cat F) showed the evidence of blocking and collapse of pores (Figure 4.22a). Figure 4.22a also shows that addition of 5 wt% La$_2$O$_3$ (Cat G), helps to

preserve its structure to some extent by improving thermal resistance. Gas flow during the reduction of impregnated lanthanum and nickel nitrates can play the major role in this regard, as shown in Table 4.15 and Figure 4.22a. Significant improvement in the specific surface area of both La_2O_3 modified γ-Al_2O_3 support and supported Ni catalyst were found using higher reducing gas flow rate. S_{BET} of a 20% Ni/5% La_2O_3-Sasol γ-Al_2O_3 can be increased from 107 to 166 m^2/g by augmenting the reduction flow on average from 8 to 26 and from 2 to 12 ml/mmol nitrates/min during lanthanum and nickel impregnation, respectively.
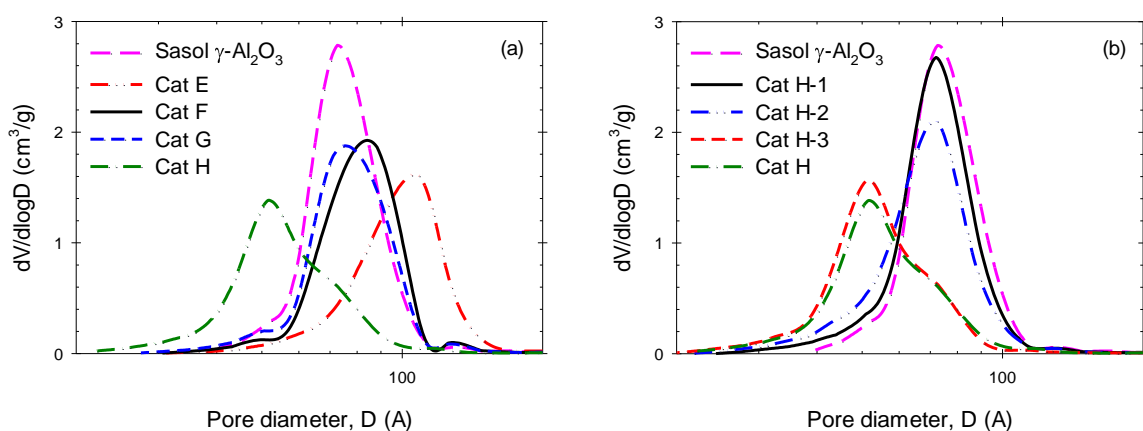
Figure 4.22: Pore size distribution based on desorption branch of a) Ni catalysts prepared varying reduction gas flow and b) Cat H at different loading steps (Cat H-1: 5% La_2O_3-Sasol γ-Al_2O_3; Cat H-2: 5% Ni/5% La_2O_3-Sasol γ-Al_2O_3; Cat H-3: 15% Ni/5% La_2O_3-Sasol γ-Al_2O_3).

Table 4.15 also reports that, the average pore diameter of the samples was significantly decreased with the use of a higher gas flow. It indicates the better dispersion of lanthanum and nickel on the γ-Al_2O_3 porous structure. Pore size distribution of the samples as shown in Figure 4.22, can give a better picture in this regard. The 20% Ni/5% La_2O_3-Sasol γ-Al_2O_3 catalyst prepared using low gas flow (Cat E) gave a wide range of pore size distributions indicating blockage of smaller pores and having significantly larger size pores due to sintering. With an increase in gas flow at the reduction step from 2 to 6 ml/mmol/min (Cat G), the sintering of pores could be significantly minimized. Pore size distribution of the catalyst prepared using high gas flow (Cat H) showed better dispersion of nickel and lanthanum onto the γ-Al_2O_3 pores resulting in significantly

higher specific surface area. The effect of the reduction gas flow on the samples structure can be explained by the exothermic decomposition of metal nitrate precursors in a H_2 atmosphere. This exothermic process facilitates temperature runaway in the catalyst bed and thus leads to metal sintering. Higher gas flow efficiently removed the heat evolved from the exothermic reactions. It can also quickly remove the water formed during nitrate decomposition. Moreover, at a lower gas flow, the channelling of gas through the catalyst bed was observed. Higher gas flow ensures uniform flow structure inside the catalyst reduction chamber. This could be another factor that can contribute to the better dispersion of nickel onto the γ-Al_2O_3 pores.

4.7.2　X-ray Diffraction Analysis

XRD patterns of the fresh and used Ni catalysts prepared by varying gas flow during the reduction of impregnated metal nitrates are reported in Figure 4.23. Figure 4.23 also presents the XRD pattern of Sasol γ-alumina showing a mostly amorphous structure. According to JCPDS 10-0425, the low intensity peaks centered at $2\theta = 37.6°$, $45.8°$, $67.1°$ are the characteristic peaks of γ-Al_2O_3.
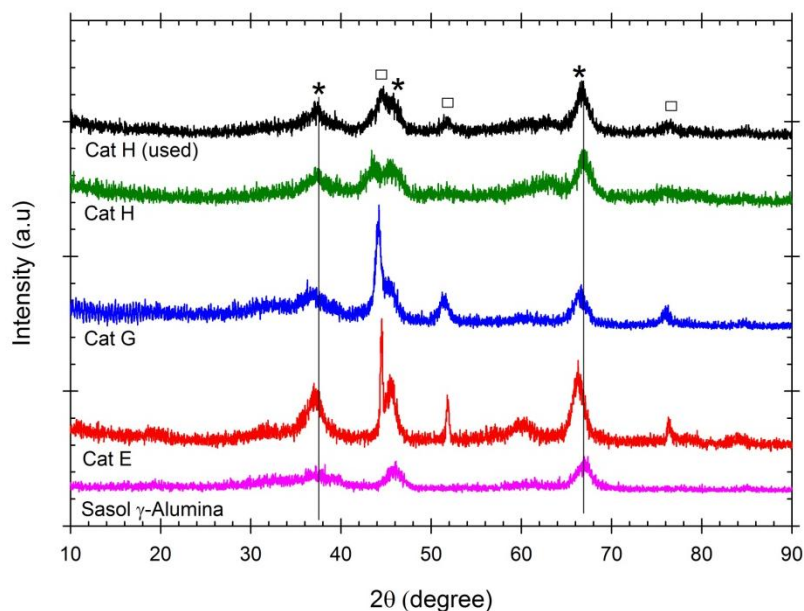
Figure 4.23: XRD patterns of the fresh and used (in 2-methoxy-4-methylphenol gasification) Ni catalysts prepared varying reduction gas flow. (★: γ-Al_2O_3; □: Ni).

As shown in Figure 4.23, Ni catalysts (containing 20 wt% Ni on 5 wt% La_2O_3-Sasol γ-Al_2O_3 support) gave reflections of Ni (JCPDS 04-850) centered at 2θ = 44.4°, 51.8°, 76.4°. For the catalysts prepared with lower gas flow (Cat E and Cat G) sharper and intense Ni peaks were observed indicating the formation of larger Ni crystals. On the other hand, catalyst prepared with high reduction flow (Cat H) gave broader Ni reflection peaks corresponding to well-dispersed small crystals on a thin layer of amorphous nickel species. This can be attributed to the better dispersion of Ni onto γ-Al_2O_3 pores as observed from the pore size distribution of Cat H (Figure 4.22). For the purpose of comparison, the crystallite size of Ni is determined by applying the Scherrer equation (Eq. (3.5)). The broadening of Ni (111) diffraction line at 45.4° was used to calculate the crystal size. For the Cat E and Cat G, the average crystal sizes of Ni were found to be 21 and 13 nm, respectively. On the other hand, Ni crystallites of 5.5 nm size were formed on Cat H. The size of the Ni crystallites of Cat H after being used in the 15 consecutive cycles of 2-methoxy-4-methylphenol gasification remained essentially the same (5.7 nm). Furthermore, the XRD pattern of the used catalyst confirms the absence of graphitic carbon on the catalyst surface. This result suggests that this catalyst is stable for steam gasification of tars with negligible crystallite agglomeration.

Figure 4.23 also shows that for the Cat E and Cat G, γ-Al_2O_3 diffraction lines were shifted especially at 2θ = 67.1°. Alteration of the γ-Al_2O_3 structure for the catalysts prepared with lower gas flow was also found by N_2 physisorption experiments as discussed in Section 4.7.1. Moreover, formation of amorphous like very small Ni crystallites on Cat H, indicates that catalysts prepared using higher gas flow at the reduction step possess stronger metal-support interactions. The metal-support interaction of the catalysts is investigated using temperature programmed reduction (TPR) in the next section.

4.7.3 Reducibility, Dispersion and Crystal Size
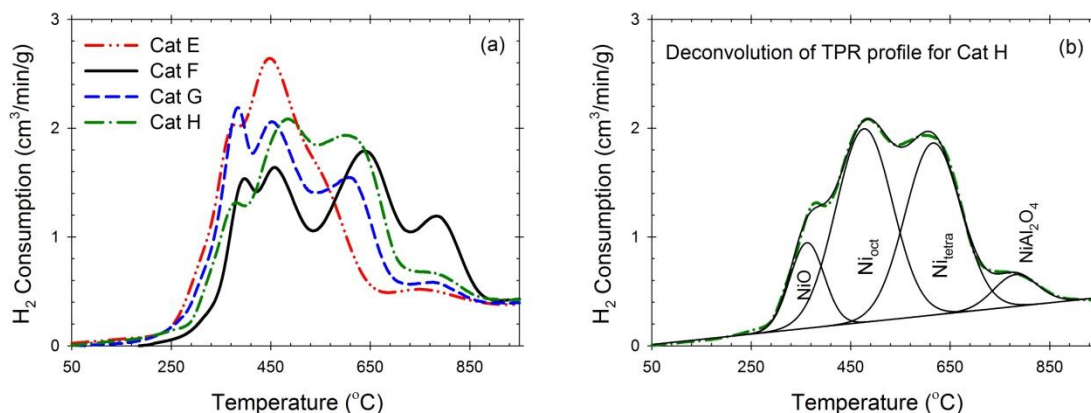
Figure 4.24: a) TPR profiles of the catalysts prepared varying reduction gas flow and b) deconvolution of the TPR profile for Cat H. (using 10% H_2 with balanced Ar at a flow rate of 50 cm^3/min and 10 °C/min heating rate).

Figure 4.24 report reduction profiles of catalysts prepared by varying gas flow during the reduction step. Ni reducibility (*R*), dispersion (*D*) and crystallite size (*d_v*) data as calculated from TPR and H_2 pulse chemisorptions area summarized in Table 4.16. As shown in Figure 4.24a, Ni (20 wt%) catalyst exhibits wide reduction peaks in the 300 °C to 950 °C range with four peaks at around 380, 470, 610 and 780 °C. The first peak (at 380 °C) can be assigned to the reduction of highly dispersed NiO species on the support surface [189,191,193]. According to the technical literature [39,189,191,202,206–209], the second and third peaks can be attributed to the reduction of NiO in varying interactions with the oxide support. The interaction of Ni with the support leads to the formation of surface nickel-aluminate spinels on the interface of Ni/Al_2O_3 catalysts. Moreover, γ-Al_2O_3 is a defective spinel phase of alumina with cation site vacancies randomly distributed throughout the crystal. Therefore, two types of surface spinels are formed by accommodating Ni ions in the tetrahedral and octahedral sites of alumina. Surface nickel aluminates that are reducible at 500 °C are attributed to the Ni^{2+} occupying the octahedral sites of γ-Al_2O_3, whereas surface $NiAl_2O_4$ formed with the tetrahedral sites of γ-Al_2O_3 requires higher reduction temperature [207,208,210]. Finally, the reduction peak observed at 780 °C is related to the reduction of bulk nickel-aluminate ($NiAl_2O_4$) [39,188,189,191,193,202].

Table 4.16: Reducibility (R), dispersion (D) and crystal size (d_v) of Ni for different catalysts

Samples	NiO (%)	Ni_{oct} (%)	Ni_{tetra} (%)	$NiAl_2O_4$ (%)	R (%)	$D(\%) = \frac{117X}{WR}$	$d_v(nm) = \frac{97.1}{\%D}$
Cat E	16.8	50.6	24.8	7.8	93	2.88	34
Cat F	10.7	30.3	45.1	14.0	89	2.99	32
Cat G	19.2	44.7	29.3	6.8	94	3.53	28
Cat H	11.7	44.0	38.7	5.6	95	4.52	21

X stands for the total hydrogen chemisorbed (μmol of H_2/g cat); W denotes the metal loading (wt%)

TPR profiles also showed differences in the relative proportion of Ni species with the variation of preparation conditions and La_2O_3 addition. Relative proportion of Ni species were determined by deconvoluting TPR profiles into four Gaussian peaks, as shown in Figure 4.24b for Cat H. As can be seen from Figure 4.24a and Table 4.16, decrease in gas flow at the catalyst reduction step from 12 (Cat H) to 6 (Cat G) ml/mmol nitrates/min, yielded higher proportion of NiO and Ni^{2+} in octahedral sites (Ni_{oct}) reducing Ni^{2+} occupying the tetrahedral sites of γ-Al_2O_3 (Ni_{tetra}). TPR profile of the unpromoted Ni/γ-Al_2O_3 catalyst (Cat F) showed increases in the reduction temperatures for all Ni species compared to the La_2O_3 promoted catalyst (Cat G) prepared at same conditions. Cat F also yielded higher proportion of Ni species requiring higher reduction temperatures (Ni_{tetra} and bulk $NiAl_2O_4$). This is attributed to the influence La_2O_3 in decreasing nickel-alumina interaction [39,190,202]. Moreover, at lower loading, La_2O_3 preferentially deposited on the tetrahedral Al^{3+} sites resulting in the decrease of Al^{3+}_{tetra}/Al^{3+}_{oct} ratio [55].

On the other hand, when reduction gas flow had been further reduced to 2 ml/mmol/min (Cat E), the intensities of the Ni_{oct} peak was increased significantly and the 3rd peak (which was assigned to Ni_{tetra}) shifted from 610 to 555 °C. The effect of the reduction gas flow on the relative proportion of Ni^{2+} in octahedral and tetrahedral γ-Al_2O_3 sites can be explained by the differences in the temperature rise during catalyst reduction. Reduction of all the catalysts was carried out at 700 °C. However, it was found that the local

temperatures in the catalyst reduction chamber could rise up to 1000 °C due to the heat released by the exothermic metal nitrates reduction reactions. The rise in local temperatures should be minimum at the high gas flow (12 ml/mmol/min) as it can carry out the reaction heat and can provide better distribution of heat in a fluidized bed condition. This was also confirmed by the lesser degree of sintering, as shown in Section 4.7.1, on the catalyst prepared using the high gas flow (Cat H).

The dehydroxylation of γ-Al_2O_3 during high temperature thermal treatment is considered as the main reason for the sintering. Due to the dehydroxylation, Al^{3+} starts to drop from the surface tetrahedral sites to the vacant interstices of the bulk structure to satisfy the valence requirements [195,221]. As the low reduction gas flow resulted in maximum rise in local temperatures, Cat E experienced higher degree of dehydroxylation. Therefore, unstable tetrahedral Al^{3+} was almost completely depleted from the surface of Cat E. In other words, higher dehydroxylation reduces the metal-support interactions resulting in lower reduction temperatures. On the other hand, the catalyst prepared with high gas flow possessed higher metal-support interaction and facilitated Ni dispersion (Table 4.16). However, a further increase in gas flow will result in lower Ni reducibility and dispersion below 700 °C.

4.7.4   Acid-Base Properties

Figure 4.25 reports the IR spectra of the Sasol γ-Al_2O_3 calcined at 700 °C and the prepared Ni catalysts following pyridine adsorption and evacuation at 100 °C, in the spectral region of 1700-1400 cm^{-1}. For all the samples, no band at 1540 cm^{-1} was observed. This indicates that there are no Brønsted acid sites available strong enough to form pyridinium ions. On the other hand, the appearance of the "19b" band at 1448 cm^{-1} and the "8a" bands at 1590-1635 cm^{-1} in the DRIFT spectra demonstrates the presence of Lewis Acid sites. It can also be seen from Figure 4.25 that addition of 5 wt% La_2O_3 (Cat G compared to Cat F) resulted in the reduction of intensity of the peak at 1448 cm^{-1}. It reconfirms the role of La_2O_3 in decreasing Lewis acidity of γ-Al_2O_3.
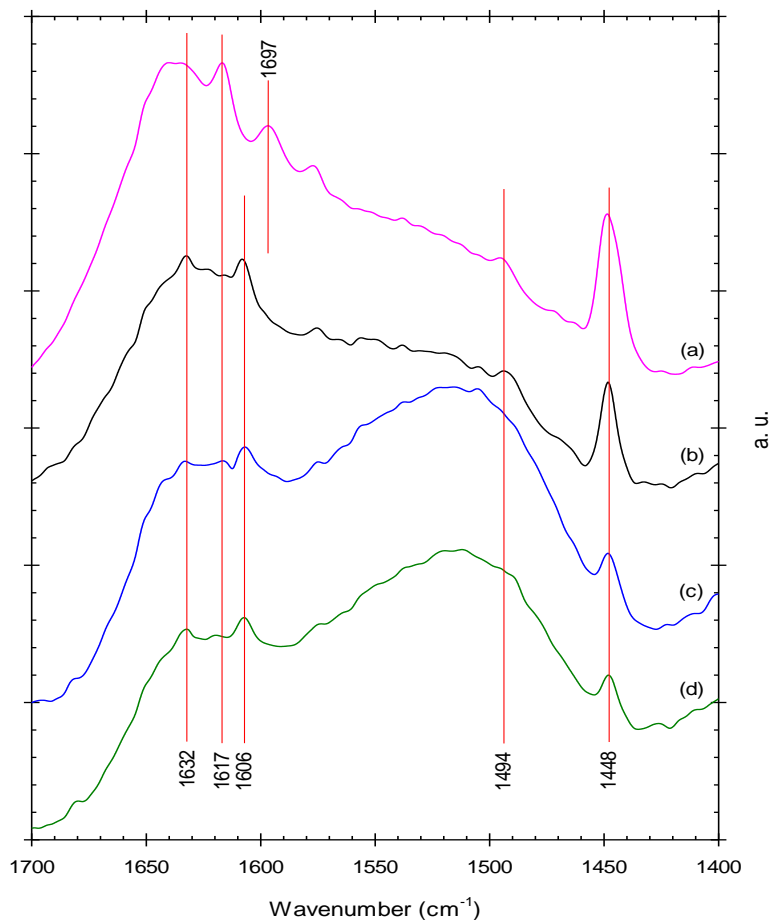
Figure 4.25: Pyridine DRIFT spectra of a) Sasol γ-Al$_2$O$_3$, b) 20% Ni/Sasol γ-Al$_2$O$_3$ prepared using moderate reduction gas flow (Cat F), 20% Ni/5% La$_2$O$_3$-Sasol γ-Al$_2$O$_3$ catalyst prepared c) using moderate reduction flow (Cat G) and d) using high reduction flow (Cat H)

The multiplicity of the "8a" band of coordinated pyridine as shown in Figure 4.25, indicates the presence of Lewis acid sites (Al^{3+}) in both octahedral and tetrahedral coordination [195,199,200]. Different configurations of Al^{3+} in γ-Al$_2$O$_3$ defect spinel are shown in Figure 4.26. Three types of Lewis acid sites with different strengths have been reported in the literature [195,198–200,222,223]: weak (1590-1610 cm^{-1}), moderate (1610-1620 cm^{-1}) and strong (1625 - 1635 cm^{-1}). The weak and strong Lewis sites are corresponds to five coordinated (quasi octahedral) and three coordinated (quasi tetrahedral) Al ions which are formed by dehydroxylation of octahedral and tetrahedral Al^{3+}, respectively. The moderate strength Lewis acid sites are attributed to four coordinated Al^{3+} [200,222,223]. On the other hand, Morterra and Magnacca[195]

assigned the moderate strength Lewis sites to the tetrahedral Al^{3+} with a cation vacancy ($\square$–O–Al^{IV}).

Al^{VI}—OH

octahedral Al^{3+}

$\square$ — O — Al^{VI}—OH

octahedral Al^{3+} with vacancy

$\square$ — O — Al^{IV}—OH

tetrahedral Al^{3+} with vacancy

Al^{IV}—OH

tetrahedral Al^{3+}
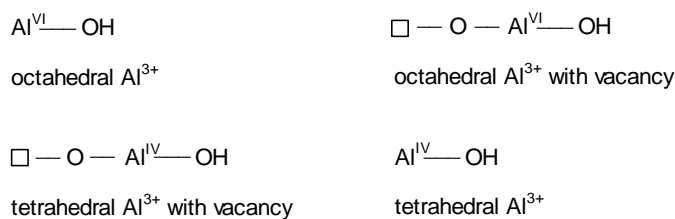
Figure 4.26: Different configurations of Al^{3+} in γ-Al_2O_3.

As shown in Figure 4.25, Sasol γ-Al_2O_3 exhibits peaks at 1597 cm^{-1} and 1617 cm^{-1} in the IR spectra indicating the presence of weak and moderate Lewis acid sites. The absence of pyridine coordination with tetrahedral Al^{3+} (strong Lewis acid) in Sasol γ-Al_2O_3 indicates that an activation temperature of more than 700 °C is required to expose those sites at the surface [195,223]. On the other hand, Ni catalysts exhibited IR bands at 1606 and 1632 cm^{-1} for pyridine co-ordination with the unsaturated Al^{3+} in octahedral and tetrahedral sites, respectively. The shift of the octahedral Al^{3+} peak from 1597 (for Sasol γ-Al_2O_3) to 1606 cm^{-1} indicates the increase of its strength after Ni impregnation. Furthermore, the absence of moderate strength sites on the Ni catalysts can be explained by the non-defective $NiAl_2O_4$ spinels formation on the catalyst surface at 20 wt% Ni loading.

Table 4.17: Total acidity and basicity of the La_2O_3 modified γ-Al_2O_3 supports and Ni catalyst prepared varying reduction gas flow as determined from NH_3- and CO_2-TPD

Samples	Reduction Flow rate (ml/mmol/min)	Total acidity (µmol/g γ-Al_2O_3)	Total basicity (µmol/g γ-Al_2O_3)
5% La_2O_3-Sasol γ-Al_2O_3 (Cat E-1)	8	435	168
5% La_2O_3-Sasol γ-Al_2O_3 (Cat G-1)	16	458	179
5% La_2O_3-Sasol γ-Al_2O_3 (Cat H-1)	26	476	195
20% Ni/5% La_2O_3-Sasol γ-Al_2O_3 (Cat E)	2	415	115
20% Ni/Sasol γ-Al_2O_3 (Cat F)	6	546	98
20% Ni/5% La_2O_3-Sasol γ-Al_2O_3 (Cat G)	6	510	153
20% Ni/5% La_2O_3-Sasol γ-Al_2O_3 (Cat H)	12	550	188

The acidity and basicity of the catalysts were quantitatively investigated by temperature programmed desorption (TPD) of NH_3 and CO_2, respectively. The total acidity and basicity of the La_2O_3 modified γ-Al_2O_3 supports and Ni catalyst prepared varying gas flow at the reduction step are listed in Table 4.17. The rise of acidity with the increase in reduction flow can be attributed to the lesser extent of thermal sintering (dehydroxylation) and to the higher specific surface area of samples prepared using higher gas flow. On the other hand, the improvement in CO_2 adsorption/total basicity for both the support and the Ni catalysts (Table 4.17 and Figure 4.27) with increase of reduction gas flow indicates that higher dispersion of La_2O_3 can be achieved using a higher reduction gas flow.
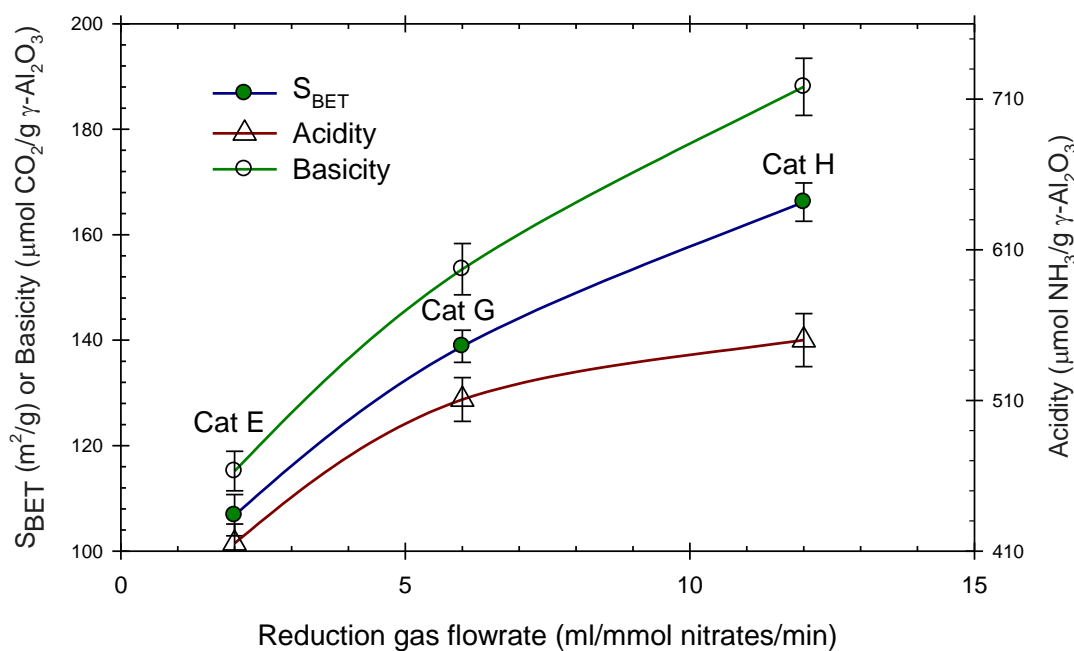
Figure 4.27: S_{BET}, total acidity and total basicity of the Ni catalysts with the variation of gas flow at the catalyst reduction step.

Figure 4.28a reports the NH_3-TPD profiles of the Ni catalysts prepared using different gas flow rate at the catalyst reduction step. In agreement with the pyridine DRIFT spectra (Figure 4.25), two peaks in the range of 50-500 °C were observed on the NH_3-TPD profiles of the Ni catalysts. According to Morterra and Magnacca [195], pyridine adsorbed on the weak Lewis sites (octahedral Al^{3+}) starts to desorbed at ambient

temperature, whereas evacuation of pyridine from tetrahedral Al^{3+} sites reuires more than 200 °C. Based on that the low and high temperature peak in the NH$_3$-TPD profiles are assigned to the octahedral Al^{3+} (weak) Lewis acid sites and tertrahedral Al^{3+} (strong) Lewis acid sites, respectively.
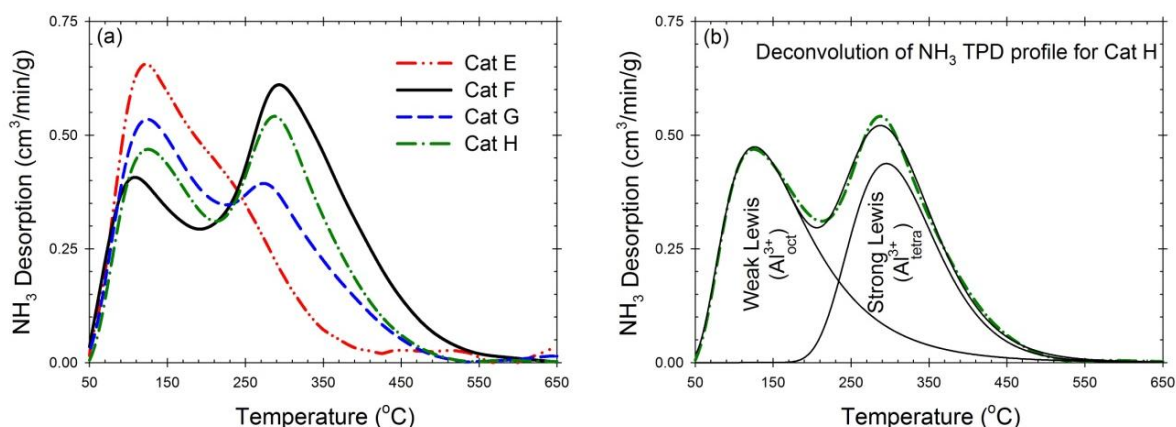
Figure 4.28: a) NH$_3$-TPD profiles of the catalysts prepared varying gas flow at the catalyst reduction step and b) deconvolution of the NH$_3$-TPD profile for Cat H.

Figure 4.28a also reports that for the catalysts prepared using lower reduction gas flow (from Cat H to Cat G and Cat E), Al^{3+}_{tetra} Lewis acid sites starts to diminish due to the greater extent of dehydoxylation as discussed in the previous sections. An increase in the amount of Al^{3+}_{oct} Lewis acid sites was also observed at the same time. However, according to the technical literature [195,199,223], the amount of surface octahedral and tetrahedral sites are independent of each other, i.e. one does not form at the expense of the other. In this respect, the findings of the present study do not disagree with the technical literature. The changes in relative proportion of Al^{3+}_{oct} and Al^{3+}_{tetra} can, in fact, be attributed to the La$_2$O$_3$ distribution over the octahedral and tetrahedral sites. The improvement in La$_2$O$_3$ dispersion with the increase of reduction gas flow was shown by CO$_2$-TPD (Table 4.17). On the other hand, the difference in the TPD profiles of unpromoted (Cat F) and La$_2$O$_3$ promoted (Cat G) catalysts prepared using same reduction gas flow, can be explained by the preferential neutralization of the tetrahedral Lewis acid sites with the addition of La$_2$O$_3$ [55].

Table 4.18: Ratio of octahedral and tetrahedral Al^{3+} sites

Samples	H$_2$ TPR Ni_{oct}/Ni_{tetra}	NH$_3$ TPD $Al^{3+}_{oct}/Al^{3+}_{tetra}$
Cat E	2.04	1.97
Cat F	0.67	0.68
Cat G	1.52	1.47
Cat H	1.14	1.16

The relative proportion of Al^{3+}_{oct} and Al^{3+}_{tetra} was determined by deconvoluting the NH$_3$-TPD profiles, as shown in Figure 4.24b for Cat H. It is interesting to note that the ratio of Al^{3+}_{oct} and Al^{3+}_{tetra} Lewis acid sites almost exactly match the ratio of surface NiAl$_2$O$_4$ in the octahedral and tetrahedral configuration, as given in Table 4.18. The same octahedral and tetrahedral ratios were obtained from the both methods because of Ni loading beyond the monolayer coverage as indicated by the presence of NiO peak in the TPR profiles (Figure 4.24a). Moreover, this finding confirms the applicability of classical NH$_3$ TPD and H$_2$ TPR techniques to efficiently determine the concentration of surface octahedral and tetrahedral Al^{3+} sites in γ-Al$_2$O$_3$. These techniques can also be used to measure the degree of dehydoxylation.

4.7.5 Gasification Results

Performance of the Ni catalysts prepared using different gas flows during the catalyst reduction step was evaluated for steam gasification of biomass surrogate species (glucose and 2-methoxy-4-methylphenol). Steam gasification experiments were performed in a CREC Riser Simulator at reaction temperature of 650 °C, catalyst/biomass ratio (Cat/B) of 12.5 g/g and reaction time of 20 s. All the experiments were repeated at least 4 times to secure the reproducibility of results. Standard deviations for experimental repeats were in

the 2-8% range with an average of 5%. An important observation from these runs was that the mass balance closures, which consider permanent gases (H_2, CO, CO_2, and CH_4), water, ethylene, ethane, propylene, acetaldehyde, and carbon deposited over the catalyst, were in the ±10% range, with most of the balances being in the ±5% range.

Catalysts reactivity were compared in terms of the: i) dry gas yield (moles of H_2, CO, CO_2 and CH_4 produced/moles of biomass fed), ii) carbon conversion to permanent gases, iii) quality of synthesis gas, iv) coking, and v) tars formed. Aromatics and oxygenates of C_6^+ structure in the produced gas were considered as tars. Experimental results were also compared to equilibrium data as calculated using the thermodynamic model described in CHAPTER 5. Elevated reactor pressure after the conversion of biomass surrogate species in a constant volume CREC Riser Simulator was also considered to determine equilibrium under rigorous conditions. Coke and tars formations are also taken into account in the thermodynamic model.
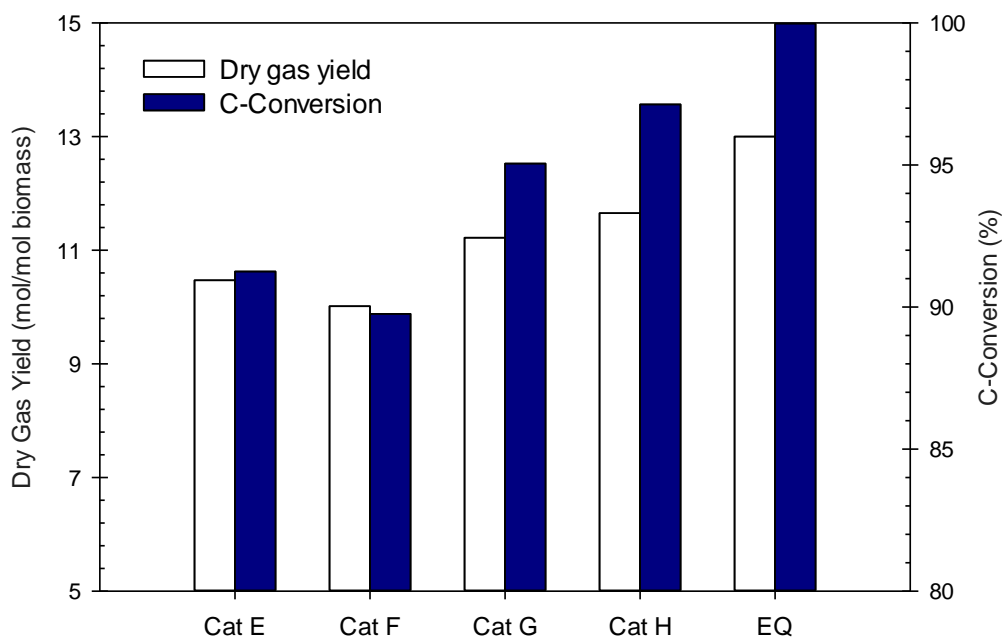
Figure 4.29: Dry gas yield and carbon-conversion during steam gasification of glucose at 650 °C, S/B = 1.0 g/g, Cat/B = 12.5 g/g and 20 s of reaction time using different catalysts: 20% Ni/Sasol γ-Al_2O_3 prepared using moderate flow (Cat F), 20% Ni/5% La_2O_3-Sasol γ-Al_2O_3 catalyst prepared using low flow (Cat E), moderate flow (Cat G) and high flow (Cat H). EQ represents equilibrium data.

Figure 4.29 and Figure 4.30 compare the performance of the Ni catalysts prepared varying the reduction gas flow in terms of carbon conversion, dry gases yields and tars formation for cellulose and 2-methoxy-4-methylphenol gasification, respectively. One can notice that 100% conversion of glucose was obtained without detectable tars formation at 650 °C and 20 s of reaction time. For the La_2O_3 modified Ni/γ-Al_2O_3 catalysts, a maximum of only 1.4 mg of coke deposition/g of catalyst was observed during glucose gasification.
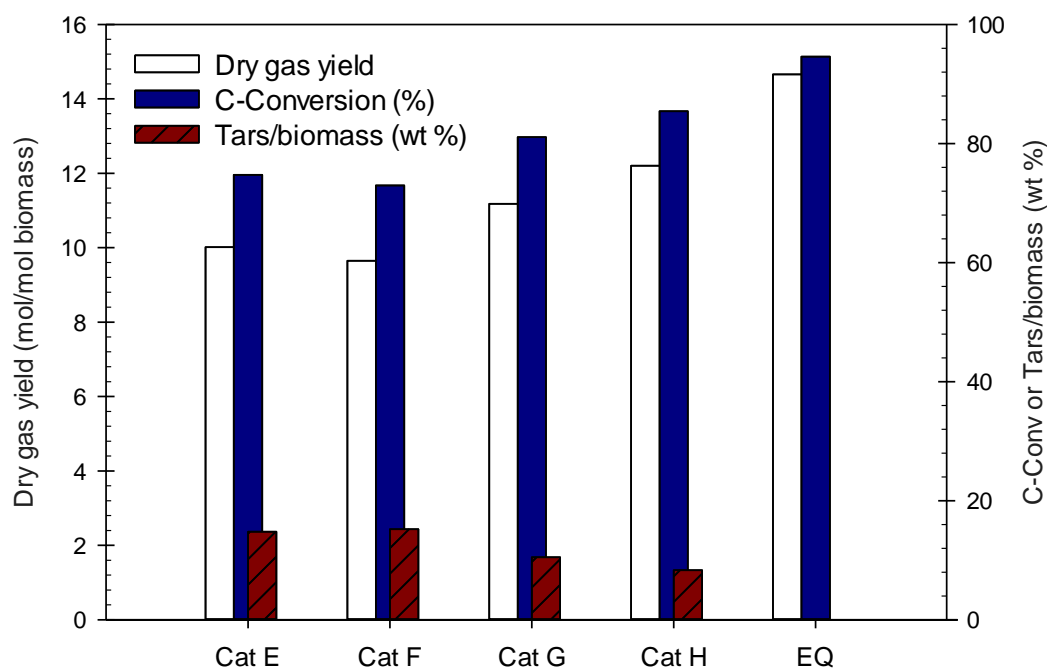
Figure 4.30: Dry gas yield, carbon-conversion and tars yield of 2-methoxy-4-methylphenol steam gasification at 650 °C, S/B = 1.5 g/g, Cat/B = 12.5 g/g and 20 s of reaction time using different catalysts: 20% Ni/Sasol γ-Al_2O_3 prepared using moderate flow (Cat F), 20% Ni/5% La_2O_3-Sasol γ-Al_2O_3 catalyst prepared using low flow (Cat E), moderate flow (Cat G) and high flow (Cat H). EQ represents equilibrium data.

On the other hand, it can be noticed from Figure 4.30 that catalytic steam gasification of 2-methoxy-4-methylphenol yielded tars as well as higher coke. This was assigned to the lower H/C and O/C ratios of 2-methoxy-4-methylphenol while compared to glucose. However, using the highly active catalyst developed in the present study tars can be kept as low as 8.3% at 650 °C. Moreover, XRD results of the catalyst used in 15 cycles of 2-

methixy-4-methylphenol gasification confirmed the absence of graphitic coke formation (Figure 4.23).
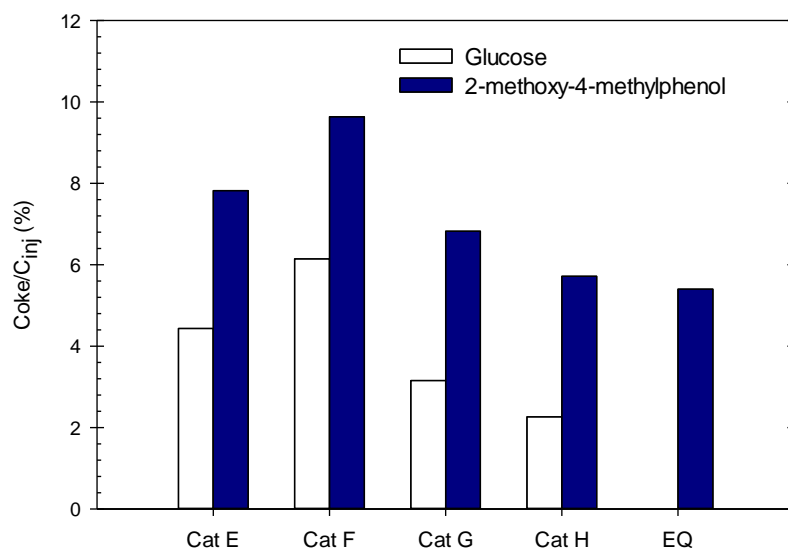
Figure 4.31: Coke deposition during steam gasification of glucose and 2-methoxy-4-methylphenol at 650 °C, Cat/B = 12.5 g/g and 20 s of reaction time using different catalysts: 20% Ni/Sasol γ-Al$_2$O$_3$ prepared using moderate flow (Cat F), 20% Ni/5% La$_2$O$_3$-Sasol γ-Al$_2$O$_3$ catalyst prepared using low flow (Cat E), moderate flow (Cat G) and high flow (Cat H). EQ represents equilibrium data.

Figure 4.29 to Figure 4.32 compare the gasification performance of unpromoted (Cat F) and La$_2$O$_3$ promoted (Cat G) Ni/γ-Al$_2$O$_3$ catalysts. These catalysts were prepared using same gas flow during the catalyst reduction step. Significant improvement in carbon conversion and dry gas yield were, however, obtained using the La$_2$O$_3$ promoted catalysts (Cat G) instead of the unprompted Cat F. These findings were consistent for both glucose and 2-methoxy-4-methylphenol gasification. Regarding the role of La$_2$O$_3$ vis-a-vis steam and dry reforming, water gas shift and coke conversion were already discussed in Section 4.6.6 of this chapter.

Regarding the effect of catalyst reduction conditions on dry gas yield and carbon conversion from glucose gasification, they were reported in Figure 4.29. This shows that, significant improvement in dry gas yield and carbon conversion can be achieved during glucose gasification using the catalysts prepared with higher flow at the catalyst reduction

step. Cat H provides an example of this improvement, exhibiting a 97% conversion of carbon to permanent gases yielding 11.68 mol of dry gas per mole of glucose. One can also notice as reported in Figure 4.30 that differences in the performance of catalysts prepared by varying reduction gas flow are more significant in the case of 2-methoxy-methylphenol gasification. For instance, steam gasification of 2-methoxy-4-methylphenol using Cat H showed 10 % improvement in carbon conversion, 21% enhancement in dry gas yield and a 6.5% reduction in tars while compared to Cat E. Figure 4.31 and Figure 4.32 also provide evidences of lower coking and higher H_2/CO ratio for the catalysts prepared with the higher reduction gas flows.
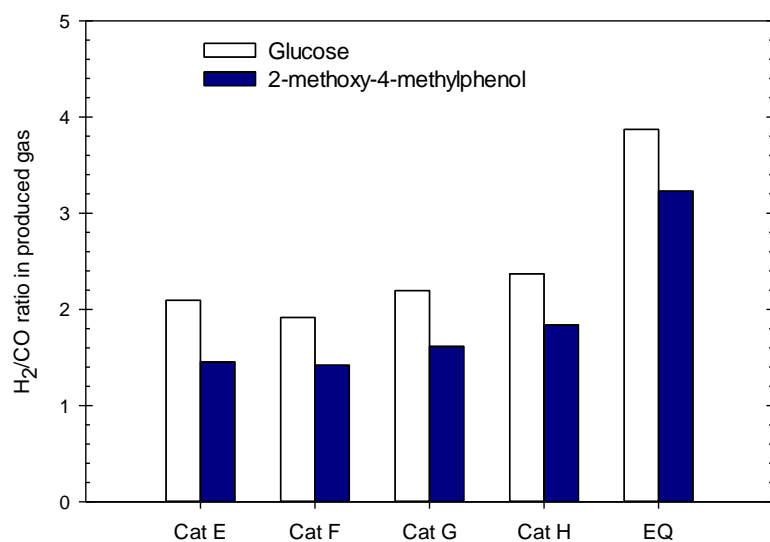
Figure 4.32: H_2/CO ratio in the products from steam gasification of glucose and 2-methoxy-4-methylphenol at 650 °C, Cat/B = 12.5 g/g and 20 s of reaction time using different catalysts: 20% Ni/Sasol γ-Al_2O_3 prepared using moderate flow (Cat F), 20% Ni/5% La_2O_3-Sasol γ-Al_2O_3 catalyst prepared using low flow (Cat E), moderate flow (Cat G) and high flow (cat H). EQ represents equilibrium data.

It is well established that dispersion of active phase (Ni) is a crucial determinant of catalyst reactivity. Figure 4.33a reports the carbon conversions obtained from glucose and 2-methoxy-4-methylphenol gasification as a function of Ni dispersion of the prepared catalysts. As can be seen from Figure 4.33a, performance of the catalysts for steam gasification of biomass surrogates species cannot be described by the properties of the active phase only.

Surface area, Ni reducibility and crystallite size are related to Ni dispersion. Total basicity and acidity are the two other independent properties of a Ni/Al_2O_3 catalyst. Regarding the influence of basicity, it has been reported that catalysts having a higher basicity support show stronger resistance to carbon fouling during steam and dry hydrocarbon reforming [29,30,213–217]. It is thus hypothesized that a basic support could improve the adsorption of acidic CO_2 and steam, so that coke deposited on the support acid sites and on the Ni surface can be removed as a result of the Boudouard reaction $(C + CO_2 \longleftrightarrow 2CO)$ and the heterogeneous water-gas shift reaction $(C + H_2O \longleftrightarrow H_2 + CO)$.
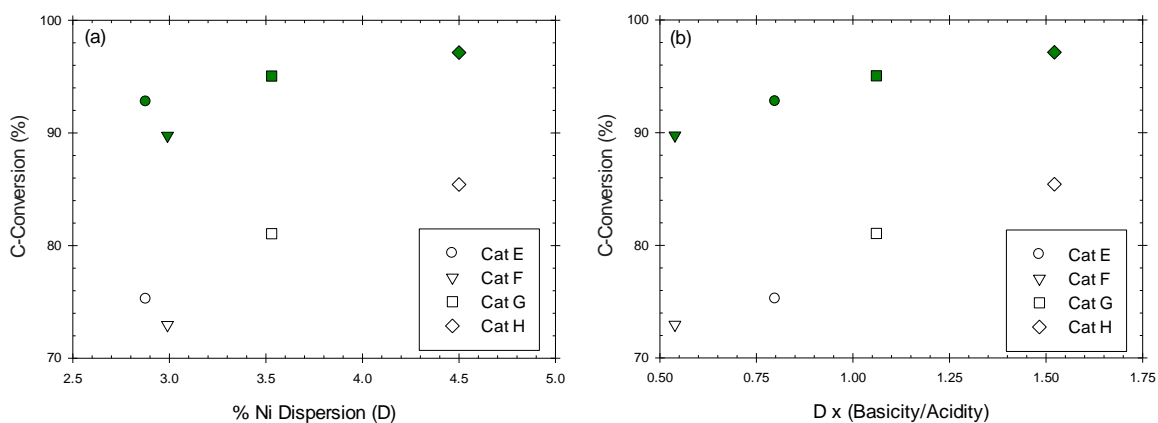
Figure 4.33: Plot of carbon conversion to permanent gases obtained during steam gasification of glucose (filled symbols) and 2-methoxy-4-methylphenol (open symbols) as a function of a) % Ni dispersion (D) and b) D x Basicity/Acidity.

Figure 4.33b shows that carbon conversions for different catalysts are well correlated as a function of the product of Ni dispersion and basicity/acidity ratio. Figure 4.34 also show that coke deposition, tars formation and H_2/CO ratio in the produced gas as a function of Ni dispersion and basicity/acidity ratio. As described in the previous section, gas flowrate at the catalyst reduction step have significant influence on these three properties. Hence, better performance of the catalyst prepared using high gas flow (Cat H) can be attributed to its higher Ni dispersion (4.52 % compared to 2.88% Ni dispersion on Cat E). Moreover, Cat H exhibited significantly greater basicity as higher gas flow facilities

dispersion of basic La_2O_3. Though Cat H possesses the highest acidity among the prepared catalysts, its higher basicity helped to reform the coke formed on the acid sites.
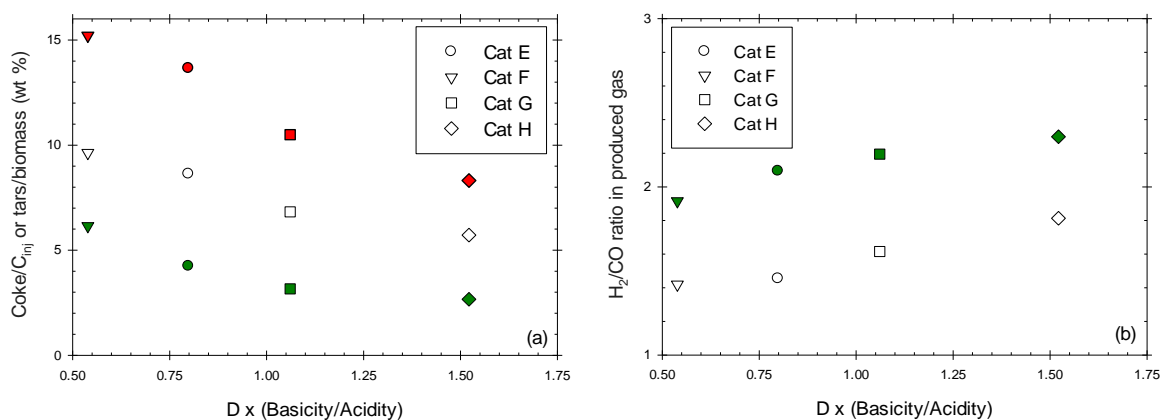
Figure 4.34: a) Coke deposition and tars formation, and b) H_2/CO ratio obtained during steam gasification of glucose (green symbols) and 2-methoxy-4-methylphenol (open symbols: coke deposition and red symbols: tars formation) as a function of D x Basicity/Acidity.

Thus, it is demonstrated that catalysts reduction conditions has significant influence on its properties. Higher reduction gas flow resulted in reduced sintering, higher Ni and La_2O_3 dispersions, and improved basicity. Hence, it yielded higher biomass steam gasification performance. However, excessive increase in reduction gas flow may result in reduced Ni reducibility and limited dispersion (especially below 700 °C) by increasing metal-support interaction. Furthermore, it is also proven that the fluidizable 20% Ni/5% La_2O_3-Sasol γ-Al_2O_3 catalyst (Cat H) prepared using high reduction gas flow is able to gasify surrogate biomass species performing very close to thermodynamic chemical equilibrium.

4.7.6 Catalyst Stability

Catalystic biomass gasification involves repeated oxidation-reduction cycles in the gasifier and the catalyst regeneration units. To investigate the stability of the prepared catalysts under repeated oxidation-reduction cycles, successive TPO and TPR experiments were developed. Each cycle was composed of successive TPO, TPR, and

pulse chemisorption experiments. Figure 4.35 reports Ni reducibility and dispersion of Cat H under repeated oxidation and reduction cycles.

It can be observed in Figure 4.35 that the 20% Ni/5% La_2O_3-Sasol γ-Al_2O_3 prepared using high reduction gas flow (Cat H) showed stable reducibility in repeated oxidation-reduction cycles with an average reduction percentage of 95%. Pulse chemisorption results further confirm the stability and negligible metal crystallite agglomeration of the catalyst over repeated oxidation-reduction conditions with consistent percentage dispersion of Ni.
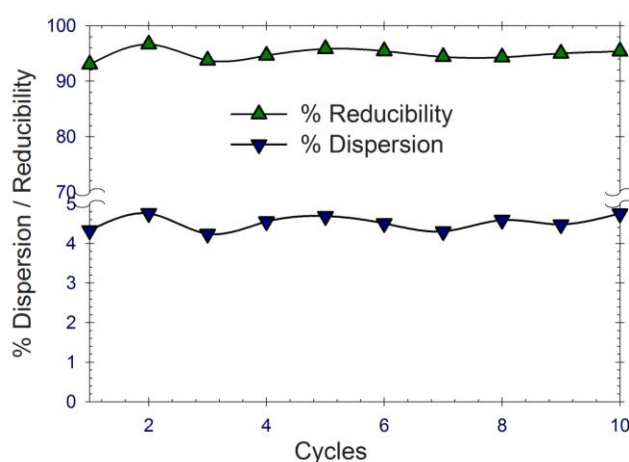
Figure 4.35: Ni reducibility and dispersion of Cat H over TPO (up to 700 °C)/TPR (upto 950 °C) cycles. (oxidizing agent: 5% O_2 in He; reducing agent: 10% H_2 in Ar; flow rate: 50 cm^3/min; heating rate: 10 °C/min)

Furthermore, to investigate the stability of Cat H in a biomass gasifier, multiple cycles gasification experiments were performed in the CREC riser simulator. Using Cat H, 35 cycles of glucose gasification at 650 °C, 1.0 g/g steam/biomass ratio, 12.5 g/g catalyst/biomass ratio and 20 s of reaction time in each cycle were conducted without catalyst regeneration in between. Glucose gasification products after a random number of cycles were analyzed. Figure 4.36 reports the carbon conversions to permanent gases obtained under the multiple cycles of steam gasification of glucose. Cat H showed stable glucose gasification performance over the cycles without significant deactivation. This result indicates that Cat H can be used efficiently for glucose gasification without requiring frequent catalyst regeneration.
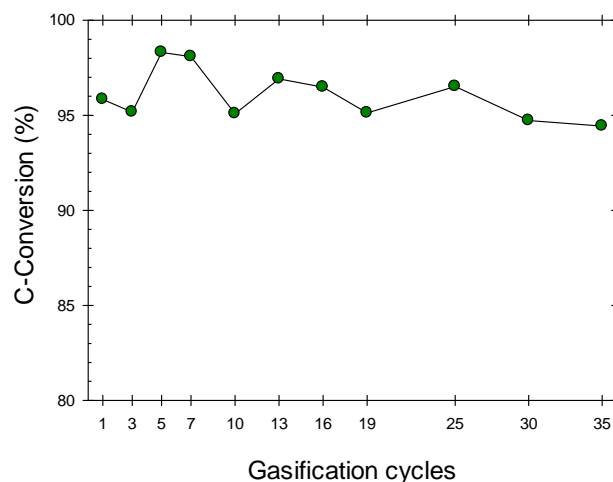
Figure 4.36: Carbon conversion to permanent gases obtained during multiple cycles (without catalyst regeneration) of steam gasification of glucose at 650 °C, S/B = 1.0 g/g, Cat/B = 12.5 g/g and 20 s of reaction cycle using Cat H.

Performance of the Cat H was also evaluated for 15 cycles of 2-methoxy-4-methylphenol gasification runs through consecutive reaction and regeneration cycles. In each cycle, 2-methoxy-4-methylphenol gasification was performed for 20 s at 650 °C, 1.5 g/g of steam/biomass ratio using a catalyst/biomass ratio of 12.5 g/g. After each gasification run, catalysts were regenerated in-situ. During the regeneration, deposited cokes were burned by following a O_2/He mixture and reduced using a H_2/Ar mixture. Figure 4.37 shows the carbon conversions to permanent gases obtained during successive steam gasification of 2-methoxy-4-methylphenol runs. Figure 4.37 reports that consistent 2-methoxy-4-methylphenol conversion can be achieved over successive gasification cycles using the Cat H. The absence of graphitic coke deposition on the used catalyst, as shown in Figure 4.23, makes catalysts regeneration easy. Moreover, Figure 4.35 shows the stability of the catalyst for repeated oxidation and reduction cycles. These results confirm the stability and regeneration ability of Cat H for 2-methoxy-4-methylphenol gasification.
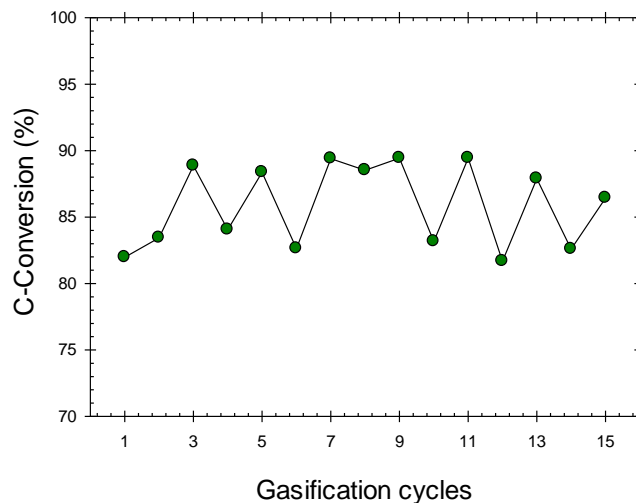
Figure 4.37: Carbon conversion to permanent gases obtained using during successive steam gasification of 2-methoxy-4-methylphenol at 650 °C, S/B = 1.5 g/g, Cat/B = 12.5 g/g and 20 s of reaction cycle with catalyst regeneration in between.

4.8 **Conclusions**

A Fluidizable La_2O_3 promoted Ni/γ-Al_2O_3 catalyst with high activity and stability for biomass steam gasification was developed. In this process, the effect of the catalyst preparation conditions and the catalyst composition were investigated using various well-established physic-chemical techniques. Structure-property and structure-reactivity relationships are established by comparing the catalyst characterization and gasification results. The developed catalyst performs close to the thermodynamic equilibrium and yields a high-quality synthesis gas (H_2/CO ratio > 2.0) by reducing tars at temperatures below 700 °C. It also shows excellent stability under repeated gasification and regeneration cycles which is the expected operating conditions of a circulating fluidized bed gasifier. Major findings on the catalyst development can be concluded as following:

a) It is shown that catalyst preparation via multi-step impregnation with direct reduction of metal precursors after each impregnation in fluidized bed conditions is an effective way to synthesis an active and stable Ni catalyst. Significantly higher basicity, nickel reducibility and dispersion are achieved employing the

preparation method of the present study instead of using calcination of metal precursors.

b) It is proven that addition of La_2O_3 up to 5 wt% helps to reduce thermal sintering and Lewis acidity of γ-Al_2O_3 as well as improves its basicity. Controlled La_2O_3 addition secures a positive impact on acid-base properties, and on surface structure limiting pore blocking. 5 wt% La_2O_3 addition also contributes to higher Ni dispersion and to a higher abundance of easily reducible species. However, excessive La_2O_3 facilitates undesirable $LaAlO_3$ formation resulting in Ni crystallite agglomeration and blocking of active sites. Therefore, the catalyst promoted with optimal amount of La_2O_3 (5 wt%) exhibits improved performance for both glucose and 2-methoxy-4-methylphenol gasification compared to the catalysts containing 0 and 10 wt % La_2O_3 content.

c) It is shown that during the catalyst reduction, local temperatures rise inside the catalysts bed occurs due to the exothermicity of the metal nitrates reduction process. This increase in bed temperature is responsible for the severe catalyst sintering via γ-Al_2O_3 dehydroxylation.

d) It is established that gas flow during catalyst reduction plays a central role on its properties. Surface structure, acid-base properties, metal dispersion and crystal size can be controlled by tuning this parameter. Higher reduction gas flow helps to maintain the structure of γ-Al_2O_3 (a transitional phase of alumina) by carrying out the heat evolved from exothermic nitrates reduction reactions. It also ensures better heat and mass distribution resulting in improved metal dispersion. However, excessive increase in reduction gas flow may results in reduced Ni reducibility and dispersion by increasing metal-support interaction.

e) It is proven that the relative proportion of octahedral and tetrahedral sites in γ-Al_2O_3, which is the main indicator of metal-support interaction and acid-base properties, can be assessed by the use of classical H_2 TPR and NH_3 TPD techniques.

f) It is demonstrated that the fluidizable La_2O_3 promoted Ni/Sasol γ-Al_2O_3 catalyst prepared using a fluidized bed reduction condition, is able to gasify surrogate biomass species performing very close to thermodynamic chemical equilibrium. It yields 100% glucose gasification without detectable tars formed at 650 °C. At the same temperature, gasification of methoxy-4-methylphenol gives 85.5% carbon conversion to permanent gases with only 8.3% tar formation and 5.7% carbon deposition as coke. These encouraging results are a strong indicator of the potential and capability for syngas production in a large scale fluidized biomass gasifier using the developed catalyst.

g) It is shown that catalysts gasification activities are well correlated with Ni dispersion and basicity/acidity ratio.

CHAPTER 5

THERMODYNAMIC ANALYSIS AND GASIFIER OPERATING CONDITIONS

5.1 Introduction

Gasifier operating conditions can significantly influence the biomass conversion, quality of the synthesis gas and tars yield, as well as catalyst deactivation [1,6,18,126,130,224]. In this chapter, the effect of the operating conditions is discussed using thermodynamic analysis and experimental gasification results.

The development of stoichiometric and non-stoichiometric equilibrium models for biomass steam gasification is illustrated in Section 5.3. Section 5.4 reports experimental results of the non-catalytic and the catalytic steam gasification of glucose and 2-methoxy-4-methylphenol. The effect of various operating variables such as temperature, steam biomass ratio and reaction time, on the carbon conversion, dry gas yield, product compositions and tars formation are evaluated. The experimental results are also compared with the chemical thermodynamic equilibrium as well as with the experimental results from a previous study [68].

5.2 Process Description

The steam gasification of biomass is a complex network of heterogeneous reactions. One can envision biomass gasification as a combination of primary and secondary reactions. *Primary* reactions break down the vaporized biomass molecules, forming permanent gases, higher hydrocarbons and coke:
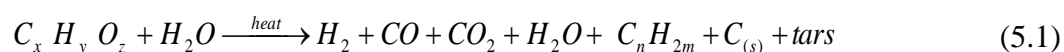
$$C_x H_y O_z + H_2O \xrightarrow{heat} H_2 + CO + CO_2 + H_2O + C_nH_{2m} + C_{(s)} + tars \qquad (5.1)$$

Secondary reactions crack the higher hydrocarbons into gases that further combust or become reduced:

$$C_n H_{2m} + nH_2O \longrightarrow nCO + (n+m) H_2 \qquad (5.2)$$
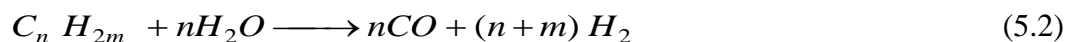
Furthermore, permanent gases react to alter the gas composition depending on gasifier conditions as indicated below:

	Chemical equation	$\Delta H^o_{298} \ (kJ/mol)$	
Water-gas shift	$CO + H_2O \longleftrightarrow H_2 + CO_2$	-41.16	(5.3)
Steam reforming methane	$CH_4 + H_2O \longleftrightarrow CO + 3H_2$	205.81	(5.4)
Dry reforming of methane	$CH_4 + CO_2 \longleftrightarrow 2CO + 2H_2$	246.98	(5.5)
Char gasification	$C + H_2O \longleftrightarrow H_2 + CO$	131.29	(5.6)
Boudouard reaction	$C + CO_2 \longleftrightarrow 2CO$	172.46	(5.7)
Hydrogenating gasification	$C + 2H_2 \longleftrightarrow CH_4$	-74.52	(5.8)
Ethylene formation	$2CO + 4H_2 \longleftrightarrow C_2H_4 + 2H_2O$	-111.65	(5.9)
Ethane formation	$2CO + 5H_2 \longleftrightarrow C_2H_6 + 2H_2O$	-212.78	(5.10)

5.3 **Chemical Thermodynamic Modelling**

Chemical thermodynamic equilibrium calculations allow one to develop feasibility studies before attempting experimental investigations. Chemical reaction equilibrium can be determined by Gibbs free energy minimization using either stoichiometric or non-stoichiometric approach. A stoichiometric model is based on equilibrium constants for a set of possible chemical reactions take place in the gasifier. On the other hand, the non-stoichiometric approach involves the minimization of the system Gibbs free energy for a set of specified components in the products. It does not require specifying the chemical reactions involved.

5.3.1 Stoichiometric Approach

A stoichiometric equilibrium model for biomass steam gasification can be developed based on the following simplifications, as in the case of other equilibrium models:

a) The presence of elements other than C, H, and O in biomass feedstocks is neglected. Thus, the possible contribution of biomass nitrogen and sulfur species are considered negligible in terms of the equilibrium calculations [61,163].

b) Biomass is ash free.

c) Char is approximated as carbon species neglecting its other possible constituents.

d) Gaseous products are assumed to behave as ideal gases.

e) Perfect mixing and uniform temperature distribution inside the gasifier are hypothesized. In case of gasification in a CREC Riser Simulator, these assumptions are very adequate.

f) The model is independent of reaction pathways.

g) Based on the experimental observations, H_2, CO, CO_2, H_2O, CH_4, C_2H_4 and C_2H_6 are considered as the significant compounds present in the gasification products.

h) Tar is modelled using selected compounds: a) toluene to represent all one-ring compounds, b) phenol to represent phenolic and other heterocyclic compounds, c) naphthalene to represent two-ring aromatics and d) pyrene to represent three-ring and higher aromatics.

Based on the above considerations, the overall chemical reaction of the biomass steam gasification reaction is given by:

$$C_x H_y O_z + mH_2O \xrightarrow{heat} A_1H_2 + A_2CO + A_3CO_2 + A_4H_2O + A_5CH_4 + A_6C_2H_4$$
$$+ A_7C_2H_6 + A_8C_{(s)} + A_9C_7H_8 + A_{10}C_6H_6O + A_{11}C_{10}H_8 + A_{12}C_{16}H_{10} \tag{5.11}$$
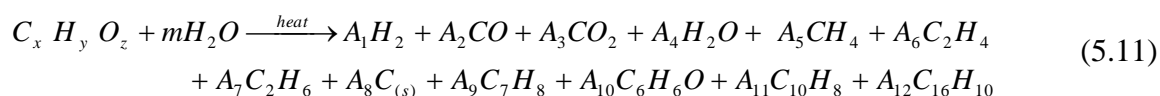
x, y and z can be obtained from ultimate analysis of biomass, and m depends on the steam/biomass ratio. Taking C, H and O elemental balances on the both sides on Eq. (5.11):

$$x = A_2 + A_3 + A_5 + 2A_6 + 2A_7 + A_8 + 7A_9 + 6A_{10} + 10A_{11} + 16A_{12} \tag{5.12}$$

$$y + 2m = 2A_1 + 2A_4 + 4A_5 + 4A_6 + 6A_7 + 8A_9 + 6A_{10} + 8A_{11} + 10A_{12} \tag{5.13}$$

$$z + m = A_2 + 2A_3 + A_4 + A_{10} \tag{5.14}$$

From the reactions involving permanent gases Eqs. ((5.3) to(5.10)), only the following five reactions are independent: a) water gas shift, b) steam reforming of methane, c) char gasification, d) ethylene formation and e) ethane formation reactions. In addition, for the tar compounds following reforming reactions are considered:

$$C_7H_8 + 7H_2O \leftrightarrow 11H_2 + 7CO \quad \Delta H^o_{298} = 882 \ kJ/mol \tag{5.15}$$

$$C_6H_6O + 5H_2O \leftrightarrow 8H_2 + 6CO \quad \Delta H^o_{298} = 1835 \ kJ/mol \tag{5.16}$$

$$C_{10}H_8 + 10H_2O \leftrightarrow 14H_2 + 10CO \quad \Delta H^o_{298} = 1178 \ kJ/mol \tag{5.17}$$

$$C_{16}H_{10} + 16H_2O \leftrightarrow 21H_2 + 16CO \quad \Delta H^o_{298} = 652 \ kJ/mol \tag{5.18}$$
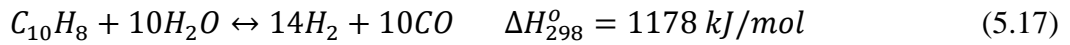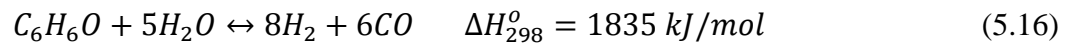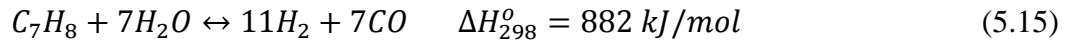
Equilibrium constants (K_{eq}) for a chemical reaction (aA+bB↔cC+dD) can be expressed in terms of reactants and products mole fractions considering ideal gas condition:

$$K_{eq} = \frac{y_C^c y_D^d}{y_A^a y_B^b} P^{(c+d-a-b)} \tag{5.19}$$

Total system pressure at equilibrium (P) can be calculated at constant volume and temperature from the total moles in the product using $PV=nRT$ relation. K_{eq} can be calculated from the thermodynamic properties (standard Gibbs free energy and heat capacity) and can be written as a function of temperature:

$$K_{eq} = \exp\left(-\left(\frac{\Delta G_0^o - \Delta H_0^o}{RT_0} + \frac{\Delta H_0^o}{RT} + \frac{1}{T}\int_{T_0}^{T}\frac{\Delta C_p^o}{R}dT - \int_{T_0}^{T}\frac{\Delta C_p^o}{R}\frac{dT}{T}\right)\right) \tag{5.20}$$

Thus, for the nine independent reactions, nine equations can be considered by combining Eqs. (5.19) and (5.20).

Regarding the twelve unknowns (A_1 to A_{12}) in Eq. (5.11), they were obtained by solving these nine non-linear equilibrium reaction expressions and three elemental balances (Eqs. (5.12)-(5.14)) using Newton-Raphson method in Matlab. Equilibrium dry gas yield, carbon conversions to permanent gases and composition of products are calculated using the model for different gasification temperatures and steam/biomass ratios.

5.3.2 Non-stoichiometric Approach

To verify the results obtained from the stoichiometric equilibrium model, a non-stoichiometric thermodynamic model was developed using Aspen Plus V8.0. Biomass surrogate species used in this study (glucose and 2-methoxy-4-methylphenol) were available as conventional components in Aspen Plus. In the case of biomass, it can be defined as a nonconventional component and its properties can be estimated incorporating both proximate and ultimate analysis into Aspen Plus. In addition, solid carbon was used as representative of char. A gasifier was simulated using RYield and RGibbs modules in Aspen Plus. The RYield reactor was employed to break down the biomass into its constituent elements/molecules. Then, these elements/molecules were fed to RGibbs reactor along with the gasifying agent (steam). All the experimentally observed compounds (permanent gases, carbon, hydrocarbons, and tar compounds) were specified as gasification products. Following these steps, equilibrium product compositions were calculated as a function of temperature, steam/biomass ratio and pressure by solving the RGibbs reactor.

Gasification experiments were conducted in a CREC Riser Simulator. Pressure in a constant volume batch reactor depends on the total moles of gas produced. Therefore, it is necessary to incorporate pressure rise due to the gasification in a RGibbs reactor for a meaningful comparison of equilibrium and experimental results. To simulate the constant volume batch CREC Riser Simulator, an optimization function was incorporated into continuous flow RGibbs reactor. The optimization function established the equilibrium pressure in the RGibbs reactor by minimizing the difference between the reactor pressure and the pressure of the product stream in the CREC Riser Simulator (P=nRT/V).

Similar results were obtained using the both Matlab and Aspen plus models, as reported by other researchers [62,225]. Moreover, H_2, CO, CO_2, CH_4, H_2O and carbon are found to be the significant components in the steam gasification products in the range of temperatures studied (500-900 °C). The concentration of the other hydrocarbons and tars remained less than 10^{-6} mol%. Similar findings were also reported for biomass gasification using air and/or steam [61,62,65,107,225].

5.4 **Gasifier Operating Conditions**

To study the effect of the gasifier operating conditions, thermal and catalytic gasification experiments were conducted in the CREC Riser Simulator varying temperature, steam/biomass ratios and reaction time. Based on the comparison of gasification performance of different catalysts as described in CHAPTER 4, the best performing Ni catalysts supported on Alcan γ-Al_2O_3 (Cat C) and supported on Sasol γ-Al_2O_3 (Cat H) were selected to evaluate the influence of various operating parameters. Each experiment was repeated at least 4 times to secure reproducibility of the results. Standard deviations for experimental repeats were in the 3-10% range with an average of 6%. An important observation from these runs was that the mass balance closures, which included H_2, CO, CO_2, H_2O, CH_4, ethylene, ethane, propylene, acetaldehyde, and carbon deposited over the catalyst, were in the $\pm11\%$ range, with most of the mass balances closing in the $\pm5\%$ range.

Gasification performance was evaluated in terms of a) carbon conversion to permanent gases, b) dry gas yield (moles of H_2, CO, CO_2, H_2O, and CH_4 produced/moles of glucose fed), c) product compositions, and d) tars yield. These results were compared with the ones reported by Salaices et al [18,68] using the same experimental conditions except the catalyst type and catalyst/biomass ratio. The experimental results were also compared with thermodynamic equilibrium data.

5.4.1 **Steam Gasification of Glucose**

Steam gasification of glucose was performed by varying the gasification temperature (600, 650 and 700 °C), steam/biomass (S/B) ratio (0.4, 0.6, 0.8 and 1.0 g/g) and reaction time (5, 10, 20 and 30 s). Catalytic glucose gasification was performed using 20% Ni/5% La_2O_3-Alcan γ-Al_2O_3 (Cat C) and 20% Ni/5% La_2O_3-Sasol γ-Al_2O_3 (Cat H) at a catalyst/biomass ratio of 12.5 g/g.

5.4.1.1   *Effect of Temperature*

Figure 5.1 reports the changes in equilibrium and experimental dry gas yield and carbon conversion obtained during glucose gasification at various temperatures. Both the dry gas yield and the carbon conversion are increased with temperature in both catalytic and non-catalytic experiments. It is considered that the higher temperatures favor steam and dry reforming of hydrocarbons, heterogeneous water-gas shift and Boudouard reactions. As shown in Figure 5.1, when temperature was raised from 600 to 700 °C, the dry gas yield was augmented from 10.07 to 12.94 mol/mol of glucose and the carbon conversion was increased from 91 to 98% in the case glucose gasification using a 20% Ni/5% La_2O_3-Sasol γ-Al_2O_3 (Cat H) catalyst.

Figure 5.1: Changes of (a) dry gas yield and (b) carbon conversion with temperature during non-catalytic and catalytic (Cat C: 20% Ni/5% La_2O_3-Alcan γ-Al_2O_3 and Cat H: 20% Ni/5% La_2O_3-Sasol γ-Al_2O_3) Steam Gasification of Glucose. Lines represent the corresponding equilibrium data. [S/B=1.0 g/g; catalyst/biomass = 12.5; 20 s reaction time]

It can also be noted that in Figure 5.1, both the dry gas yield and the carbon conversion improved substantially in all catalytic experiments while compared to the non-catalytic runs. In fact, the use of Cat H increased the dry gas yield on average by approximately 25%. However, the effect of the catalyst is more prominent at higher temperatures. This means that the catalyst activity for various gasification reactions increases with temperature, with this being especially true for steam and dry reforming of hydrocarbons. Moreover, the dry gas yield achieved for the catalytic gasification of glucose at 600 °C is

higher than the one for non-catalytic experiments at 700 °C. Similarly, using the Cat H, carbon conversion is increased by approximately 15% on average.
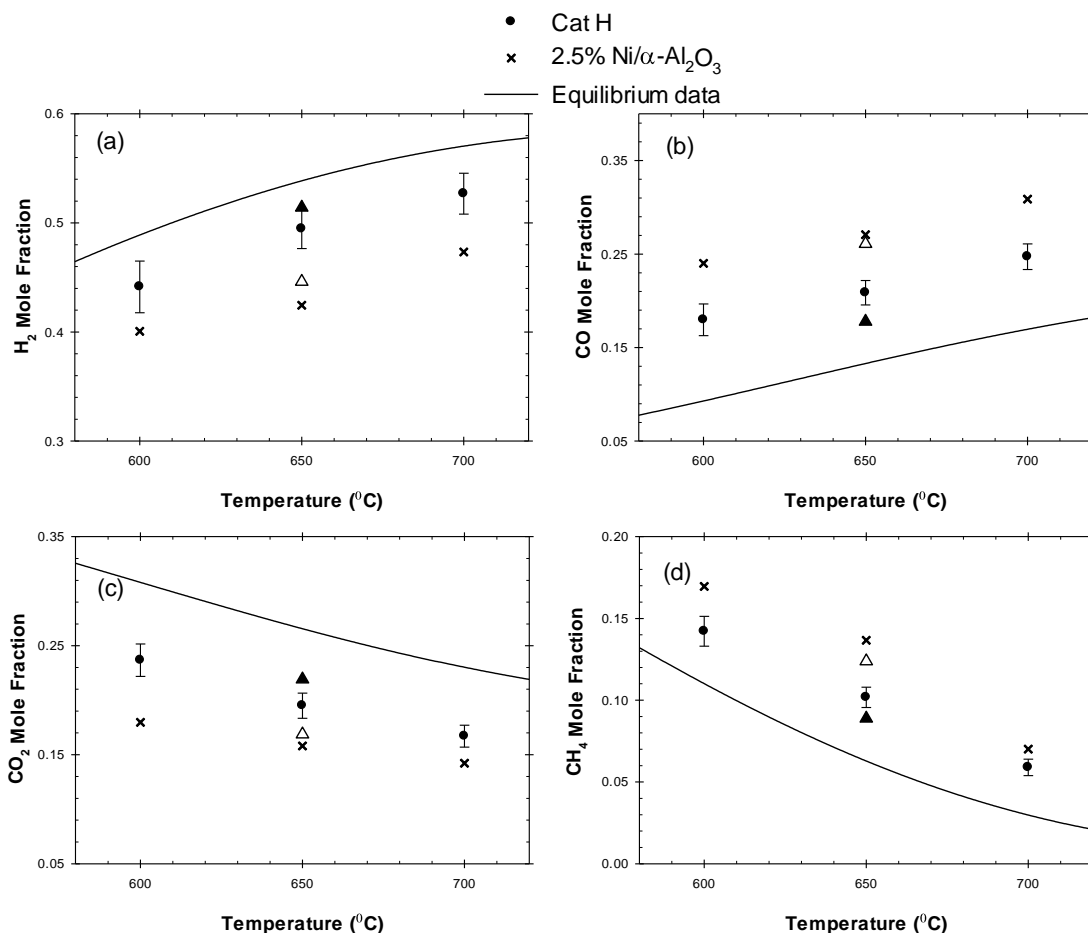
Figure 5.2: Changes of product gas composition (dry basis) with temperature (a) H_2, (b) CO, (c) CO_2 and (d) CH_4 from glucose gasification using Cat H (catalyst/biomass=12.5) and Ni/α-Al$_2$0$_3$ (catalyst/biomass=25; data taken from Salaices et al [18,68]). Lines represent the equilibrium data. Symbols Δ & $\blacktriangle$ represent experimental data using Cat H for 10 and 30 s reaction time, respectively. [S/B=1.0 g/g; 20 s reaction time].

Figure 5.2 reports the changes in H_2, CO, CO_2 and CH_4 compositions (dry basis) in the products with temperature, when using the Cat H. One can notice an increase in H_2 composition with the rise of temperature. This can be assigned to the higher influence of steam and dry reforming of hydrocarbons on the overall reaction network. Increasing the temperature also has important effects on CO composition. Due to the greater influence of reforming, heterogeneous water-gas shift and Boudouard reactions at higher thermal

levels, this also contributes to higher CO (Figure 5.2b). Furthermore, when temperature is increased from 600 to 700 °C, the CO composition increases almost linearly from 18 to 25%.

Figure 5.2c and d show that at higher thermal levels both the CO_2 and CH_4 compositions are decreased. In addition, one can notice the low methane concentrations in the product gas at higher temperatures (less than 6% at 700 °C). These low methane levels are a primary indication of the high–methane reforming activity of the catalyst used in this study.

Salaices et al [18,68] also reported H_2, CO, CO_2 and CH_4 product compositions (dry basis) obtained from glucose gasification and their changes with the temperature. These data were obtained at the same operating conditions as the ones of present study. In the experiments by Salaices et al [18,68], a 2.5% Ni/α-Al_2O_3 catalyst was used with a 25 g/g catalyst/biomass ratio. This catalyst/biomass ratio was double with respect to the 12.5 g/g of the present study. Comparing the results obtained by Salaices et al [18,68] to the findings of the present study, one can notice that significantly higher H_2 and CO_2, and lower CO and CH_4 compositions were obtained in this study using half the amount of catalyst, as shown in Figure 5.2. These data confirmed that the 20% Ni/5% La_2O_3-γAl_2O_3 catalyst displays higher steam reforming, dry reforming and water-gas shift activity than the 2.5%Ni/α-Al_2O_3. This higher catalytic activity can be attributed to the following: i) higher Ni content (20 wt% instead of 2.5 wt%), ii) higher specific surface area (166.2 instead of 22.4 m^2/g), iii) higher reducibility (95% versus 76%), and iv) La_2O_3 addition which is known to catalyze coke reforming reactions.

Figure 5.2 also reports that thermodynamic data overpredicts H_2 and CO_2 yields and underpredicts CO and CH_4 experimental compositions. Figure 5.2 also shows the synthesis gas composition obtained in the present study is in closer agreement with the equilibrium compositions than the ones reported by Salaices et al [18,68]. One should also notice that experimental results with variation of reaction times at 650 °C are also reported in Figure 5.2. As can be seen, the permanent gases approach thermodynamic equilibrium compositions with the increase of reaction times from 10 to 30 s.

5.4.1.2   Effect of Steam/Biomass ratio

Figure 5.3 describes equilibrium and experimental dry gas yields and carbon conversions obtained during glucose gasification at various steam/biomass ratios(S/B). It can be observed that an increase in the S/B ratio from 0.4 to 1.0 augments the dry gas yield as well as the carbon conversion. This is true for both the catalytic and non-catalytic experiments. Thus, it appears that higher S/B ratios promote the steam reforming of hydrocarbons and water-gas shift reactions. For instance, when the S/B ratio was increased from 0.4 to 1.0 g/g at a constant temperature of 650 °C, a higher dry gas yield (9.35 to 11.68 mol/mol of glucose) and an increased carbon conversion (87.45 to 97.13%) were obtained using a 20% Ni/5% La$_2$O$_3$-Sasol γ-Al$_2$O$_3$ (Cat H). However, the rate of change in both the dry gas yield and the carbon conversion was reduced at a higher range of S/B ratios. Thus, by changing the S/B from 0.4 to 0.6 g/g, the dry gas yield and the carbon conversion can be improved by approximately 12% and 5.5%, respectively. On the other hand, when the S/B ratio is raised from 0.8 to 1.0 g/g, the dry gas yield and the carbon conversion are enhanced by 4.1% and 3.7% respectively. This reduction in the rate of change in both the dry gas yield and the carbon conversion at higher S/B ratios can be attributed to gasification being close to equilibrium.
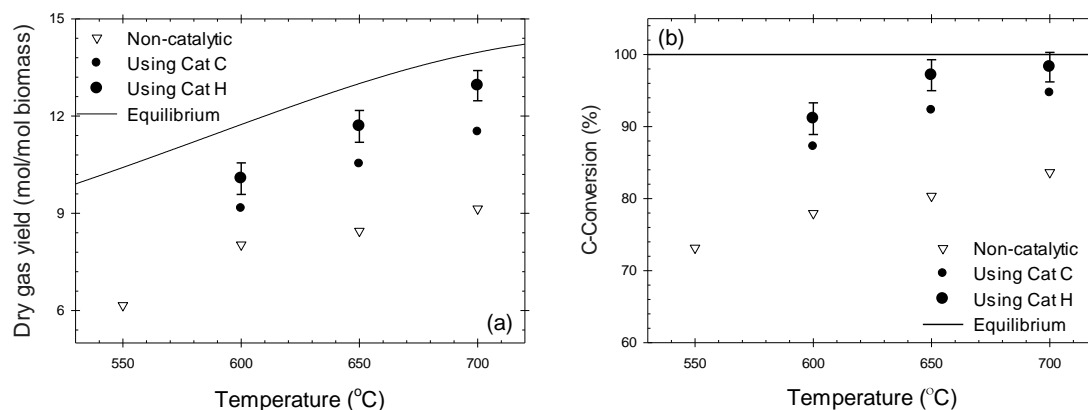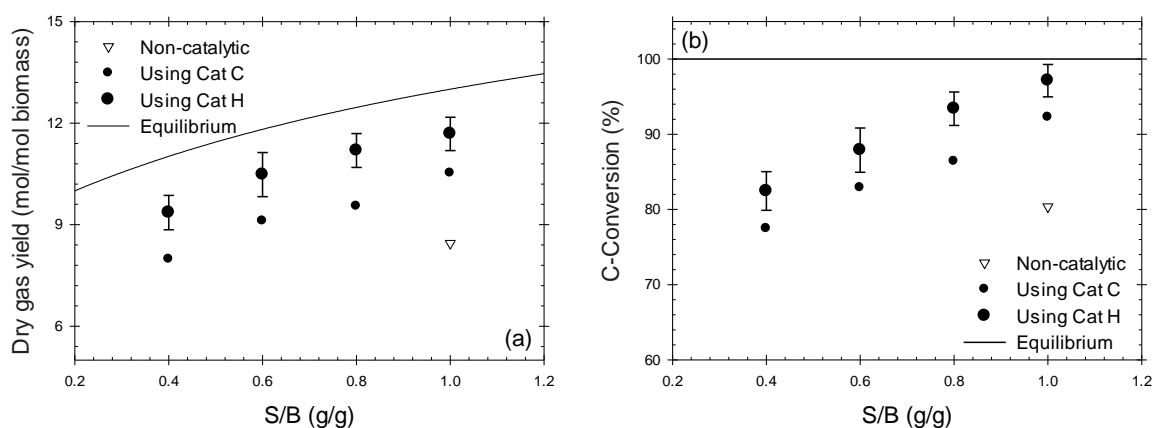

Figure 5.3: Profiles of (a) dry gas yield and (b) carbon conversion with S/B ratio during non-catalytic and catalytic (Cat C: 20% Ni/5% La$_2$O$_3$-Alcan γ-Al$_2$O$_3$ and Cat H: 20% Ni/5% La$_2$O$_3$-Sasol γ-Al$_2$O$_3$) steam gasification of glucose. Lines represent the corresponding equilibrium data. [Temperature=650 °C; catalyst/biomass = 8.75 to 12.5; 20 s reaction time].
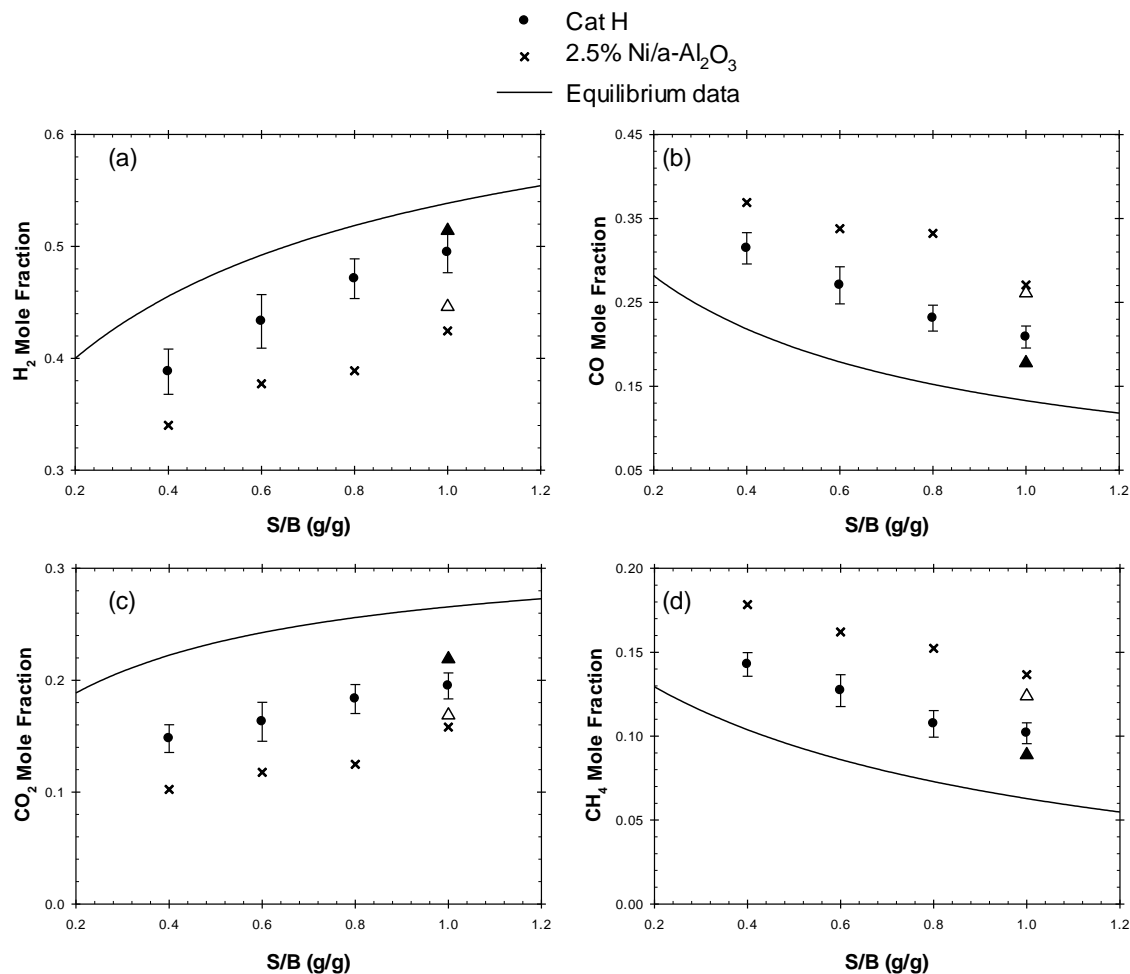
Figure 5.4: Variation of product gas composition (dry basis) with S/B ratio (a) H_2, (b) CO, (c) CO_2 and (d) CH_4, from glucose gasification using Cat H (catalyst/biomass=8.75 to 12.5) and a Ni/α-Al_2O_3 catalyst(catalyst/biomass=17.5 to 25); data taken from Salaices et al [18,68]). Lines represent the equilibrium data. Symbols Δ and $\blacktriangle$ represent experimental data using Cat H for 10 and 30 s reaction times, respectively. [Temperature=650 °C; catalyst/biomass = 8.75 to 12.5; 20 s reaction time].

Figure 5.4a, b, c and d report the H_2, CO, CO_2 and CH_4 compositions (dry basis) in the product gas obtained from glucose gasification at various S/B ratios using Cat H. Figure 5.4a shows that a higher S/B ratio leads to an increased H_2 composition. This is a likely result of the higher extents of steam reforming, water-gas shift and char gasification reactions. Figure 5.4b and c report that CO_2 composition increases with S/B ratio while CO concentration decreases. These trends can also be attributed to an increased influence of the water-gas shift reaction. Furthermore, Figure 5.4d reports a decreasing CH_4

composition with the S/B ratio. This behavior can be assigned to a more prevalent steam reforming reaction influence. One should also notice that the variations of H_2, CO, CO_2 and CH_4 compositions with S/B, become milder at higher S/Bs, as the reactions approach equilibrium.

Figure 5.4 also reports the equilibrium composition (dry basis) for H_2, CO, CO_2 and CH_4 in the product gas while performing glucose gasification at various S/B ratios. One can notice the close agreement of the experimental concentrations with the equilibrium model predictions. In general, experimental H_2 and CO_2 compositions appear to remain below the thermodynamic levels, while CO and CH_4 compositions appear to be above. One should notice that the relatively short reaction time used appears to be the reason for the difference between the experimental data and the thermodynamic predictions. In the specific case of a S/B=1.0 g/g, experiments were developed by changing the reaction time as also reported in Figure 5.4. One can observe that increasing reaction times leads to gas compositions very close to those at chemical reaction equilibrium.
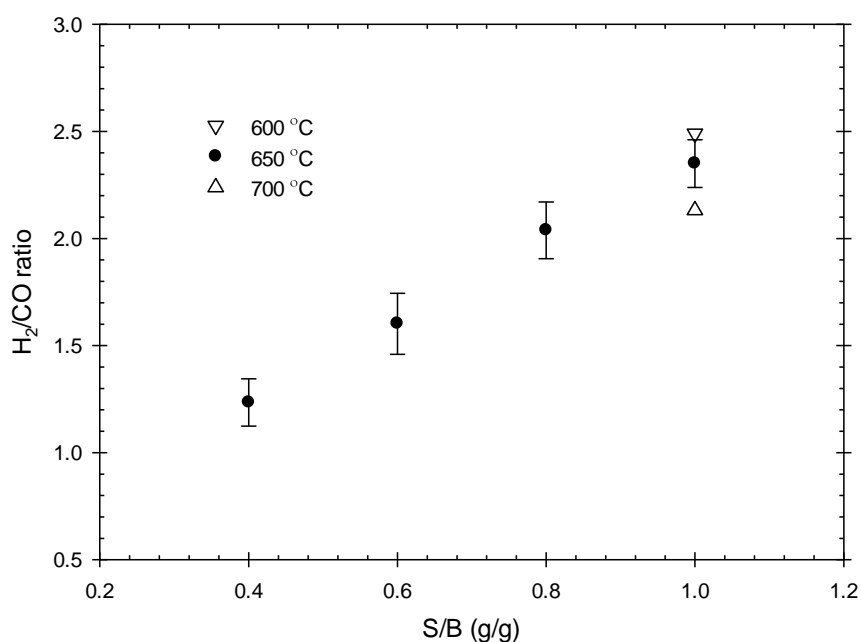
Figure 5.5: H_2/CO ratio of product gas from glucose gasification using Cat H at different S/B ratios (at 650 °C) and at different temperatures (at S/B=1.0 g/g). [Catalyst/biomass = 8.75 to 12.5 g/g; 20 s reaction time].

A crucial parameter in biomass gasification is the H_2/CO ratio. This parameter determines the quality of a synthesis gas. Figure 5.5 reports the H_2/CO ratios at the end of 20 s reaction time for various S/B ratios and temperatures. One can observe that increasing S/B ratio, leads to a higher H_2/CO ratio. The H_2/CO ratio increased from 1.23 to 2.34, when the S/B ratio was augmented from 0.4 to 1.0 g/g at 650 °C and at 20 s of reaction time. This can be attributed to the higher influence of the water-gas shift reaction due to the increased steam partial pressure. On the other hand, the H_2/CO ratio of the produced gas is decreased when temperature is augmented (Figure 5.5). The observed H_2/CO ratio diminished from 2.49 to 2.13 as the gasifier operation temperature was raised from 600 to 700 °C at a S/B =1.0 g/g and at 20 s reaction time. Once again, a reduced reaction extent of the exothermic water-gas shift reaction (WGSR) at higher temperatures, could be the reason behind this experimental finding.

5.4.2   Steam gasification of 2-methoxy-4-methylphenol

Catalytic steam gasification of 2-methoxy-4-methylphenol was performed at different temperatures (600, 650 and 700 °C). A 20% Ni/5% La_2O_3-Sasol γ-Al_2O_3 (Cat H) was used in 2-methoxy-4-methylphenol gasification experiments at a catalysts/biomass ratio of 12.5 g/g, steam/biomass (S/B) ratio of 1.5 g/g and 20 s of reaction time. Experimental results were also compared with equilibrium data obtained using the thermodynamic model developed in this study.

Figure 5.6 reports the dry gas yield, the carbon conversion, the tar yield and the coke/char deposition resulting from steam gasification of 2-methoxy-4-methylphenol. Figure 5.6 shows that experimental results for only 20 s of 2-methoxy-4-methylphenol gasification using Cat H are comparable with the thermodynamic prediction. It can be also observed in Figure 5.6a and b that both the dry gas yield and the carbon conversion to permanent gases are improved with the increase in temperature. When gasification temperature augmented from 600 to 700 °C, carbon conversion was increased by 10.25% yielding a 34% higher amount of dry gas. Figure 5.6c and d show that a higher gasification temperature also results in reduced tar and char/coke formation.

In agreement with the technical literature [61,64,65,225], the equilibrium model developed in the present study also predicted negligible amounts of tar from the steam gasification of 2-methoxy-4-methylphenol (Figure 5.6c). It can also be observed from Figure 5.6b and d that, thermodynamically, a complete gasification of 2-methoxy-4-methylphenol can be achieved at 684 °C using a S/B ratio of 1.5 g/g. This temperature is known as the carbon boundary point (CBP). Above this point, the char/coke yield becomes zero.
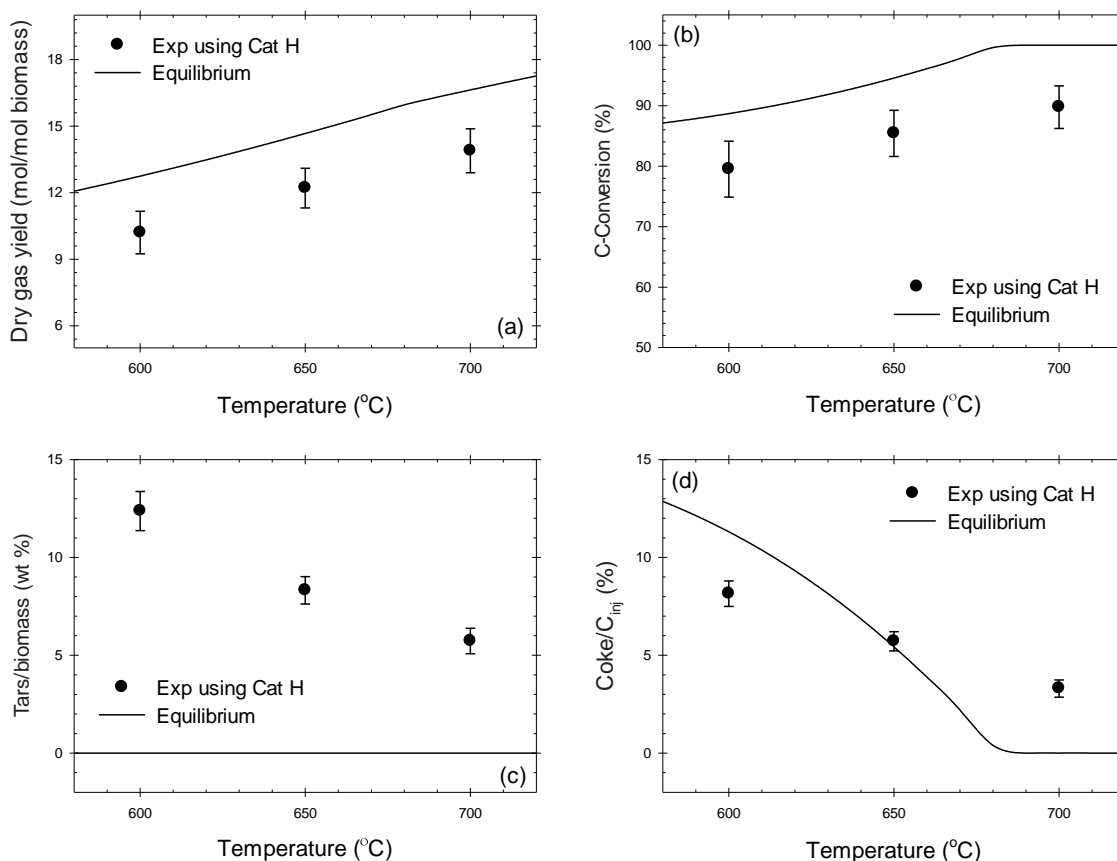
Figure 5.6: Profiles of (a) dry gas yield, (b) carbon conversion, (c) tar yield and (d) coke/char deposition with the variation of temperature from steam gasification of 2-methoxy-4-methylphenol using Cat H (20% Ni/5% La$_2$O$_3$-Sasol γ-Al$_2$O$_3$). Lines represent the corresponding equilibrium data. [S/B = 1.5 g/g; catalyst/biomass = 12.5; 20 s reaction time].

Figure 5.6a and b also report that the thermodynamic equilibrium model over predicts the dry gas yield and carbon conversion in comparison to the experimental results. On the

other hand, one should notice that a coke deposition less than the equilibrium prediction was obtained at 600 °C. This can be attributed to the significant difference in tar yield between the experimental and the equilibrium results. Moreover, in the thermodynamic model, char was simplified as solid carbon. Thus, the thermodynamic model overestimates coke below CBP to compensate for char and tar.
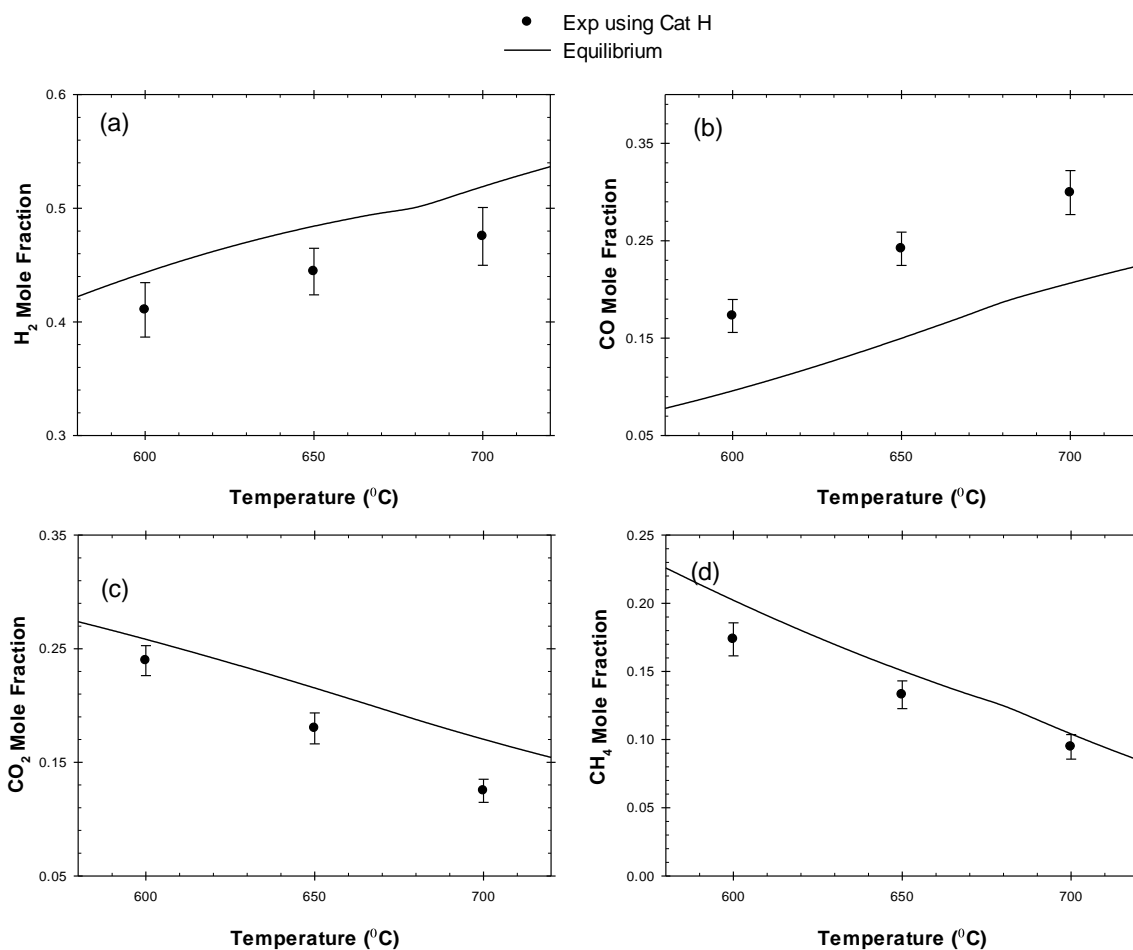
Figure 5.7: Variation of product gas composition (dry basis) with temperature (a) H_2, (b) CO, (c) CO_2 and (d) CH_4, from 2-methoxy-4-methylphenol gasification using Cat H (20% Ni/5% La_2O_3-Sasol γ-Al_2O_3). Lines represent the corresponding equilibrium data. [S/B = 1.5 g/g; catalyst/biomass = 12.5; 20 s reaction time].

Figure 5.7 compares the experimental and equilibrium composition of the dry gas at different temperatures. It shows that the fractions of H_2 and CO in the produced gas increased with the temperature due to the greater extent of hydrocarbon and tar

reforming. Figure 5.7d also reports that the thermodynamic model over predicts CH_4 composition as in the case of coke deposition. It indicates that presence of CH_4 is more favourable at the equilibrium than the tar compounds.

Figure 5.8 describes the H_2/CO ratio of the product gas from steam gasification of 2-methoxy-4-methylphenol at different temperatures. As in the case of glucose gasification, the H_2/CO ratio was diminished at higher temperatures due to the decrease in the extent of the exothermic water gas shift reaction. Moreover, steam gasification of 2-methoxy-4-methylphenol yielded a lower H_2/CO ratio than glucose gasification due to its lower H/C ratio.
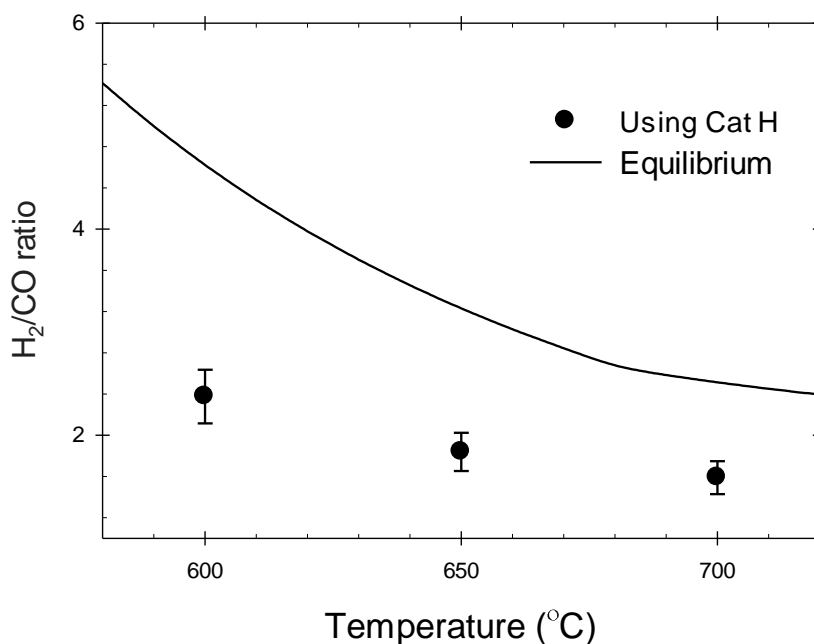
Figure 5.8: Variation of the H_2/CO ratio of product gas with temperature from 2-methoxy-4-methylphenol gasification using Cat H (20% Ni/5% La_2O_3-Sasol γ-Al_2O_3). Lines represent the corresponding equilibrium data. [S/B = 1.0 g/g; catalyst/biomass = 12.5; 20 s reaction time].

5.5 **Conclusions**

The following are the main conclusions of this chapter:

a) Thermodynamic equilibrium models for steam gasification of biomass are developed using both stoichiometric and non-stoichiometric approaches. Both the models give essentially the same results. Coke and tar compounds were considered in the equilibrium calculations together with the permanent gases.

b) Conditions of the constant volume batch CREC Riser Simulator are accounted for in the developed models to establish a rigorous comparison with experimental results.

c) The catalyst developed in the present study perform closer to thermodynamic equilibrium versus the ones of the previous study [18,68] using a $Ni/\alpha\text{-}Al_2O_3$ catalyst.

d) Both the carbon conversion and gas yield can be also improved by increasing the temperature and the steam/biomass ratio. However, there is a limit from the point of energy efficiency. Moreover, to avoid operation problems such as ash agglomeration, operating temperatures are limited to 700 °C.

e) Changes in the observed gasification product composition with the variation of operating parameters are in agreement with thermodynamic model predictions. Moreover, product composition approaches chemical equilibrium as the reaction time is increased. This indicates that the overall steam gasification process is kinetically controlled.

CHAPTER 6

KINETIC MODELLING

6.1 **Introduction**

The differences between the experimental gasification results and the thermodynamic model predictions for short contact times, as described in Chapter 5, indicate that the biomass steam gasification process is kinetically controlled. Therefore, non-equilibrium kinetic models are required, to be able to predict various chemical species in a catalytic gasifier.

Various kinetic models of different complexity describing the gasification of various biomass feeds were proposed in the technical literature [173–178]. These reported models lump together a complex network of heterogeneous reactions into one single kinetic rate equation. While this, in principle, circumvents the over-parametrization problem, the resulting rate equations provide an empirically fitted kinetics. These models have little or no connection with the phenomenological events. In a previous study, Salaices et al [179] established that kinetic models for catalytic biomass steam gasification can be successfully developed using sound reaction engineering principles. This was done using a linear combination of dominant reactions for glucose gasification using a 2.5%Ni/α-Al$_2$O$_3$ catalyst.

In the present study, a similar mechanistic kinetic approach is proposed by considering the water gas-shift reaction, the steam reforming of methane and the reverse dry reforming of methane as the dominant reactions. The rates of each of these reactions are modeled using Langmuir-Hinshelwood type equations, which take into consideration both the adsorption of chemical species on the catalyst surface as well as the intrinsic reaction kinetics. Thus, the net rate of either formation or disappearance of various chemical species in the product gas is considered as the result of the algebraic addition of the dominant reactions. The kinetic parameters are estimated using experimental data

with the variation of gasification temperature. The proposed model and estimated kinetic parameters are also validated using experimental data with the variation of the steam/biomass (S/B) ratio.

6.2 **Mechanism of Biomass Steam Gasification**

In a biomass catalytic gasifier, biomass molecules are decomposed into permanent gases, higher hydrocarbons, tars and coke. H_2, CO, CO_2, CH_4 and H_2O are found to be the main species in the gas phase [1,18,87,174,226,227]. As a result, the global steam gasification process can be described by:

$$C_x H_y O_z + H_2O \xrightarrow{heat} H_2 + CO + CO_2 + H_2O + C_n H_{2m} + C_{(s)} + tars$$

(6.1)
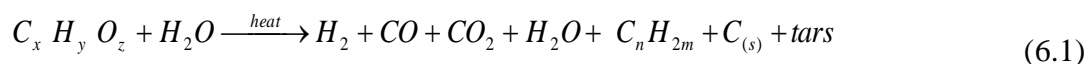
Coke and tar formation depend on the gasifier operating conditions and additives used. The final gas composition of the gasification process is the result of the combination of a series of complex and competing reactions [18,88,174,227–229]:

Water gas shift (WGS)	$CO + H_2O \longleftrightarrow H_2 + CO_2$	$\Delta H^o = $ -41.2 KJ/mol	(6.2)
Steam reforming of methane (SRM)	$CH_4 + H_2O \longleftrightarrow CO + 3H_2$	$\Delta H^o = $ 206 KJ/mol	(6.3)
Dry reforming of methane (DRM)	$CH_4 + CO_2 \longleftrightarrow 2CO + 2H_2$	$\Delta H^o = $ 247 KJ/mol	(6.4)
Char gasification (CG)	$C + H_2O \longleftrightarrow H_2 + CO$	$\Delta H^o = $ 131.3 KJ/mol	(6.5)
Boudouard reaction (BR)	$C + CO_2 \longleftrightarrow 2CO$	$\Delta H^o = $ 172.5 KJ/mol	(6.6)
Hydrogenating gasification (HG)	$C + 2H_2 \longleftrightarrow CH_4$	$\Delta H^o = $ -74.5 KJ/mol	(6.7)
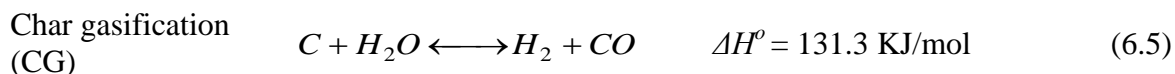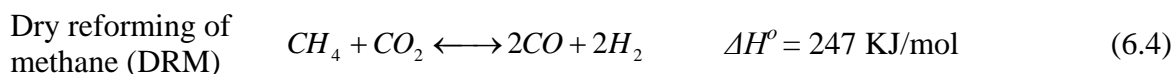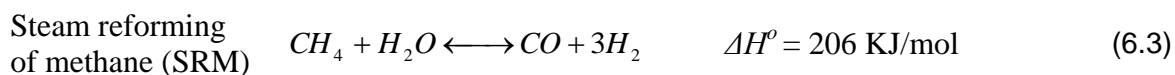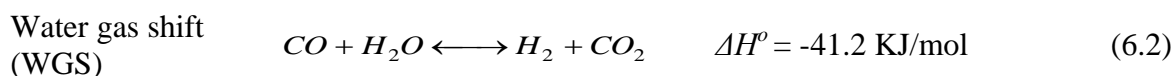
The Langmuir-Hinshelwood (L-H) mechanism is frequently used to express the rate of a catalytic reaction. Considering both the adsorption and chemical reactions, L-H type rate equations have been used extensively for water gas-shift, steam and dry reforming, char

gasification reactions [179,184,227,228,230,231]. The general form of a Langmuir-Hinshelwood rate equation can be written as:

$$r_i = \frac{k_i\, K_i^A\, p_i}{(1 + \sum\limits_{j=1}^{n} K_j^A\, p_j)^{m'}}$$ (6.8)

where, r_i is the rate of reaction of component "i" in $mol/g_{cat}\,min$, k_i is the kinetic constant for component "i" in $mol/g_{cat}.s$, K_i^A is the adsorption constant for component "i" in $1/bar$, p is the partial pressure of component "i" in bar. The term "n" is the number of chemical species, while "j" is a subscript to denote each component in the denominator term and "m'" is the number of catalyst sites involved in the catalytic reaction.

At the expected high operating temperature of a gasifier, H_2 and CO adsorption effects are usually considered negligible due to the weaker adsorption interaction with the catalys. According to Maestri et al [230], at temperatures above 550 °C, the CO and H_2 inhibition effects are not significant. Thus, the Langmuir-Hinselwood expression for WGS, SRM and reverse dry reforming of methane (RDRM) reactions can be written as:

$$r_{WGS} = \frac{k_{WGS}\, K_{H_2O}^A\, K_{CO}^A\, p_{CO}\, p_{H_2O}}{(1 + K_{CH_4}^A\, p_{CH_4} + K_{CO_2}^A\, p_{CO_2})^2} \left(1 - \frac{p_{H_2}\, p_{CO2}}{K_{WGS}\, p_{CO}\, p_{H_2O}}\right)$$ (6.9)

$$r_{SRM} = \frac{k_{SR}\, K_{CH_4}^A\, K_{H_2O}^A\, p_{CH_4}\, p_{H_2O}}{(1 + K_{CH_4}^A\, p_{CH_4} + K_{CO_2}^A\, p_{CO_2})^4} \left(1 - \frac{p_{CO}\, p_{H_2}^3}{K_{SR}\, p_{CH_4}\, p_{H_2O}}\right)$$ (6.10)

$$r_{RDRM} = \frac{k_{RDRM}\, K_{CO}^A\, K_{H_2}^A\, p_{CO}^2\, p_{H_2}^2}{(1 + K_{CH_4}^A\, p_{CH_4} + K_{CO_2}^A\, p_{CO_2})^4} \left(1 - \frac{p_{CO_2}\, p_{CH_4}}{K_{RDRM}\, p_{CO}^2\, p_{H_2}^2}\right)$$ (6.11)

It can be noticed that each of these equations include relevant physicochemical intrinsic kinetic parameters, k_j and adsorption constants, K_j^A.

6.3 **Model Formulation**

The gathered experimental data shows that H_2, CO, CO_2, CH_4 and H_2O are the five major species with negligible amounts of C_2H_4 (< 0.12 mol%) and C_2H_6 (< 0.1 mol%) in the product gas from steam gasification of biomass surrogate species. Coke deposition was also found to be negligible with less than 1 wt% coke in case of glucose gasification. Carbon deposition on the catalyst surface was related to char gasification (CG), Boudouard reaction (BR) and hydrogenating gasification (HG) reactions (6.5(6.7). As a result of these three reactions, different amounts of coke may have been formed with this depending on the S/B ratio, the operating temperature and pressure. To develop a thermodynamic feasibility analysis of the above coking reactions, their equilibrium constants were calculated using Eq. 6.20. The driving force for these reactions can be written in terms of the experimental partial pressures of the species involved:

$$Driving\ Force = \ 1 - \frac{\Pi P_{products}^{v_p}}{K_{eq}\Pi P_{reactanst}^{v_r}} \qquad (6.12)$$

Table 6.1: Driving Force of the char gasification (CG), Boudouard reaction (BR) and hydrogenating gasification (HG) reactions for glucose gasification at S/B = 1.0 g/g

Reaction time (sec)	600 °C			650 °C			700 °C		
	CG	BR	HG	CG	BR	HG	CG	BR	HG
5	0.64	-3.65	-2.22	0.62	-9.34	-1.05	0.76	-29.20	-1.39
10	0.55	-2.61	-0.68	0.64	-1.82	-0.63	0.73	-0.83	-0.46
20	0.49	-1.23	-0.05	0.60	-0.26	0.08	0.68	0.21	0.29
30	0.44	-0.61	0.21	0.58	0.14	0.29	0.66	0.44	0.47

To check the direction of char gasification (CG), Boudouard reaction (BR) and hydrogenating gasification (HG) reactions, their driving forces were calculated at the experimental conditions and summarized in Table 6.1. One can notice that experimental conditions always favour the forward CG reaction diminishing coke deposition. Initially,

BR and HG reactions proceed in the backward direction to form coke. However, with the increase of reaction times, these two reactions also shifted to the forward direction. As a result, a good approximation is to consider that, on balance, the net formation of carbon is negligible. This hypothesis is also consistent with the very small amount of coke found during the gasification experiments. Therefore, the contribution of the reactions involving coke can be considered insignificant.

Thus, once Eqs (6.5), (6.6) and (6.7) are discarded in the analysis, the remaining relevant reactions in the kinetic modelling are the following: a) water gas-shift reaction (WGS), b) steam reforming of methane (SRM), and c) dry reforming of methane (DRM). Moreover, the driving force for the DRM reaction indicates that it occurs in the backward direction at the experimental conditions. Therefore, reverse dry reforming of methane (RDRM) reaction is considered instead of DRM to model the steam gasification process. One can model the overall rate of formation/disappearance of the five major chemical species as an algebraic addition of the individual reactions, as follows:

$$r_i = v_{WGS,i} r_{WGS} + v_{SRM,i} r_{SRM} + v_{RDRM,i} r_{RDRM} \qquad (6.13)$$

where $v_{j,i}$ is the stoichiometric coefficients of species "i" in reaction "j" and $r_{j,}$ is the rate for the reaction "j".

Moreover, for the CREC Riser Simulator, a well mixed batch reactor, reaction rates for each component "i" can be expressed as follows:

$$r_i = \frac{V}{W} \frac{d\left(\dfrac{p_i}{R\,T}\right)}{dt} \qquad (6.14)$$

where V is the volume of the reactor in cm^3, W is the weight of the catalyst in $grams$, p_i is the partial pressure of species "i", R is the gas constant in $cm^3 atm K^{-1} mol^{-1}$, T is the reactor temperature in K and t is the time in seconds.

By combining Eqs. (6.8) and (6.14), a rate of reaction can be established for every chemical species as a function of partial pressures as follows:

$$\frac{d\,p_i}{dt} = \frac{\dfrac{W}{V}RTk_i' p_i}{(1+\sum\limits_{j=1}^{n} K_j^A p_j)^{m'}} \tag{6.15}$$

where, kinetic constants, $k_i' = k_i K_j^A$, represent lump adsorption and intrinsic kinetic parameters.

Regarding the contributions of H_2, CO and CH_4 adsorption in the kinetics, one can assume that these are insignificant considering the range of operating temperatures [230]. Moreover, by doing adsorption experiments in a CREC Riser Simulator, Salaices [68] found that CH_4 adsorption on a Ni/Al_2O_3 catalyst is negligible.

Thus, a differential equation for each of the five major species can be written in terms of the rate of WGS, SRM and RDRM reactions as follows:

$$
\begin{aligned}
\frac{dp_{H_2}}{dt} &= \frac{\dfrac{W}{V}RTk'_{WGS}\,p_{CO}\,p_{H_2O}}{(1+2K^A_{CO_2}\,p_{CO_2})}\left(1-\frac{p_{H_2}\,p_{CO2}}{K_{WGS}\,p_{CO}\,p_{H_2O}}\right) \\[2mm]
&+3\frac{\dfrac{W}{V}RTk'_{SRM}\,p_{CH_4}\,p_{H_2O}}{(1+4K^A_{CO_2}\,p_{CO_2})}\left(1-\frac{p_{CO}\,p^3_{H_2}}{K_{SRM}\,p_{CH_4}\,p_{H_2O}}\right) \\[2mm]
&-2\frac{\dfrac{W}{V}RTk'_{RDRM}\,p^2_{CO}\,p^2_{H_2}}{(1+4K^A_{CO_2}\,p_{CO_2})}\left(1-\frac{p_{CO_2}\,p_{CH_4}}{K_{RDRM}\,p^2_{CO}\,p^2_{H_2}}\right)
\end{aligned} \tag{6.16}
$$

$$
\begin{aligned}
\frac{dp_{CO}}{dt} &= -\frac{\dfrac{W}{V}RTk'_{WGS}\,p_{CO}\,p_{H_2O}}{(1+2K^A_{CO_2}\,p_{CO_2})}\left(1-\frac{p_{H_2}\,p_{CO2}}{K_{WGS}\,p_{CO}\,p_{H_2O}}\right) \\[2mm]
&+\frac{\dfrac{W}{V}RTk'_{SRM}\,p_{CH_4}\,p_{H_2O}}{(1+4K^A_{CO_2}\,p_{CO_2})}\left(1-\frac{p_{CO}\,p^3_{H_2}}{K_{SRM}\,p_{CH_4}\,p_{H_2O}}\right) \\[2mm]
&-2\frac{\dfrac{W}{V}RTk'_{RDRM}\,p^2_{CO}\,p^2_{H_2}}{(1+4K^A_{CO_2}\,p_{CO_2})}\left(1-\frac{p_{CO_2}\,p_{CH_4}}{K_{RDRM}\,p^2_{CO}\,p^2_{H_2}}\right)
\end{aligned} \tag{6.17}
$$

$$\frac{dp_{CO_2}}{dt} = \frac{\frac{W}{V}RTk'_{WGS}\, p_{CO}\, p_{H_2O}}{(1+2K^A_{CO_2}\, p_{CO_2})}\left(1-\frac{p_{H_2}\, p_{CO2}}{K_{WGS}\, p_{CO}\, p_{H_2O}}\right)$$
$$+\frac{\frac{W}{V}RTk'_{RDRM}\, p^2_{CO}\, p^2_{H_2}}{(1+4K^A_{CO_2}\, p_{CO_2})}\left(1-\frac{p_{CO_2}\, p_{CH_4}}{K_{RDRM}\, p^2_{CO}\, p^2_{H_2}}\right)$$

(6.18)

$$\frac{dp_{CH_4}}{dt} = -\frac{\frac{W}{V}RTk'_{SRM}\, p_{CH_4}\, p_{H_2O}}{(1+4K^A_{CO_2}\, p_{CO_2})}\left(1-\frac{p_{CO}\, p^3_{H_2}}{K_{SRM}\, p_{CH_4}\, p_{H_2O}}\right)$$
$$+\frac{\frac{W}{V}RTk'_{RDRM}\, p^2_{CO}\, p^2_{H_2}}{(1+4K^A_{CO_2}\, p_{CO_2})}\left(1-\frac{p_{CO_2}\, p_{CH_4}}{K_{RDRM}\, p^2_{CO}\, p^2_{H_2}}\right)$$

(6.19)

$$\frac{dp_{H_2O}}{dt} = -\frac{\frac{W}{V}RTk'_{WGS}\, p_{CO}\, p_{H_2O}}{(1+2K^A_{CO_2}\, p_{CO_2})}\left(1-\frac{p_{H_2}\, p_{CO2}}{K_{WGS}\, p_{CO}\, p_{H_2O}}\right)$$
$$-\frac{\frac{W}{V}RTk'_{SRM}\, p_{CH_4}\, p_{H_2O}}{(1+4K^A_{CO_2}\, p_{CO_2})}\left(1-\frac{p_{CO}\, p^3_{H_2}}{K_{SRM}\, p_{CH_4}\, p_{H_2O}}\right)$$

(6.20)

where k'_{WGS}, k'_{SRM} and k'_{RDRM} are the kinetic constants for the water gas shift (WGS), the steam reforming of methane (SRM) and reverse dry reforming of methane (RDRM) reactions, respectively; K_{WGS}, K_{SR} and K_{RDRM} are the thermodynamic equilibrium constants of the WGS, SRM and RDRM reactions at the reaction temperature; $K^A_{CO_2}$ is the adsorption constant for carbon dioxide; and p is the partial pressure.

To obtain the intrinsic kinetic parameters (activation energies/heat of adsorption and pre-exponential factors), Arrhenius relationships centered on an average temperature (650°C) were used:

$$k'_i = k^o_i \exp\left(-\frac{E_i}{R}\left(\frac{1}{T}-\frac{1}{T_{avg}}\right)\right)$$

(6.21)

$$K_{CO_2}^A = K_{CO_2}^o \exp\left(-\frac{\Delta H_{CO_2}^{ads}}{R}\left(\frac{1}{T} - \frac{1}{T_{avg}}\right)\right) \tag{6.22}$$

where $k_i^{'}$ is the rate reaction constant, k_i^o is the apparent pre-exponential factor, E_i is the apparent activation energy, $K_{CO_2}^o$ is the carbon dioxide adsorption constant, $\Delta H_{CO_2}^{ads}$ is the carbon dioxide heat of adsorption, R is the universal gas constant, and T_{avg} is the average temperature.

In terms of Eqs. (6.21) and (6.22), one should notice that the centered Arrhenius form reduces the correlation between the pre-exponential factor and the activation energy, thereby improving the statistical properties of the estimates for the intrinsic kinetic parameters.

6.4 CO_2 Adsorption Constant

These postulated rate expressions inevitably lead to mathematical models that are nonlinear with respect to their parameters, particularly when the adsorption constants appear both in the numerator and in the denominator of the expression. The non-linearity in the parameters can result in over-parametrization given a high degree of parameter correlation. One should notice that this parameter correlation is amplified given the mathematical form of the Langmuir-Hinshelwood equation where parameters to be fitted are both in the numerator and in the denominator of the rate equation.

One of the highlights of the mini-fluidized CREC Riser Simulator is given by the fact that the determination of adsorption and intrinsic kinetic parameters can be *decoupled*. As a result, one can obtain in the CREC Riser Simulator, experimental data suitable for the analysis of either adsorption or reaction models with a limited number of parameters. To independently determine the CO_2 adsorption parameters of a 20% Ni/5% La_2O_3-γ-Al_2O_3 (Cat H), adsorption experiments were conducted in the CREC Riser Simulator varying the CO_2 partial pressures. CO_2 adsorption isotherms were determined at 600, 650 and 700 °C. Adsorption constants were determined by fitting the experimental data against the

Langmuir adsorption isotherm (Eq. 6.23). An Arrhenius equation (Eq. 6.22) centered on an average temperature (650 °C) was incorporated to establish the effect of temperature. Table 6.2 reports the CO_2 adsorption constant and heat of adsorption for the 20% Ni/5% La_2O_3-γ-Al_2O_3 (Cat H).

$$\frac{V_{CO_2}^A}{V_m} = \frac{K_{CO_2}^A p_{CO_2}}{1+K_{CO_2}^A p_{CO_2}} \tag{6.23}$$

Where $V_{CO_2}^A$ is the volume of CO_2 adsorption on the catalyst, V_m is the volume of monolayer coverage, $K_{CO_2}^A$ is the carbon dioxide adsorption constant, p_{CO_2} is the carbon dioxide partial pressure.

Table 6.2: CO_2 Adsorption Parameters for a 20% Ni/5% La_2O_3-γ-Al_2O_3 (Cat H)

Parameter	Value	Span for 95% C.I.
$K_{CO_2}^o$ (bar^{-1})	0.557	± 0.167
$\Delta H_{CO_2}^{ads}$ (kJ/mol)	-20.79	± 9.31

6.5 Parameter Estimation

Non-linear regression analysis was performed using MATLAB. The Eqs. (6.16) to (6.20) were solved using a built-in ordinary differential equation solver (ODE45). The kinetic parameters k_i^0 and E_i for the water gas shift (WGS), the steam reforming of methane (SRM) and the reverse dry reforming of methane (RDRM) were estimated using the least square curve fitting function (LSQCURVEFIT), which minimizes the error between the experimental observations and numerical solutions of ODE45.

To estimate these kinetic parameters, glucose gasification experiments were conducted using 20% Ni/5% La_2O_3-γ-Al_2O_3 (Cat H) by varying the reaction time (5, 10, 15, 20 and 30 s) and temperature (600, 650 and 700 °C) at a constant steam/biomass (S/B) ratio of 1.0 g/g and using a catalyst/biomass ratio of 12.5 g/g. Each experiment was repeated at

least 3 times to secure reproducibility of the results. Standard deviations for experimental repeats were in the 3-9% range with an average of 5%. Experimental results at 5 s reaction time were used as the initial conditions to solve the differential equations.
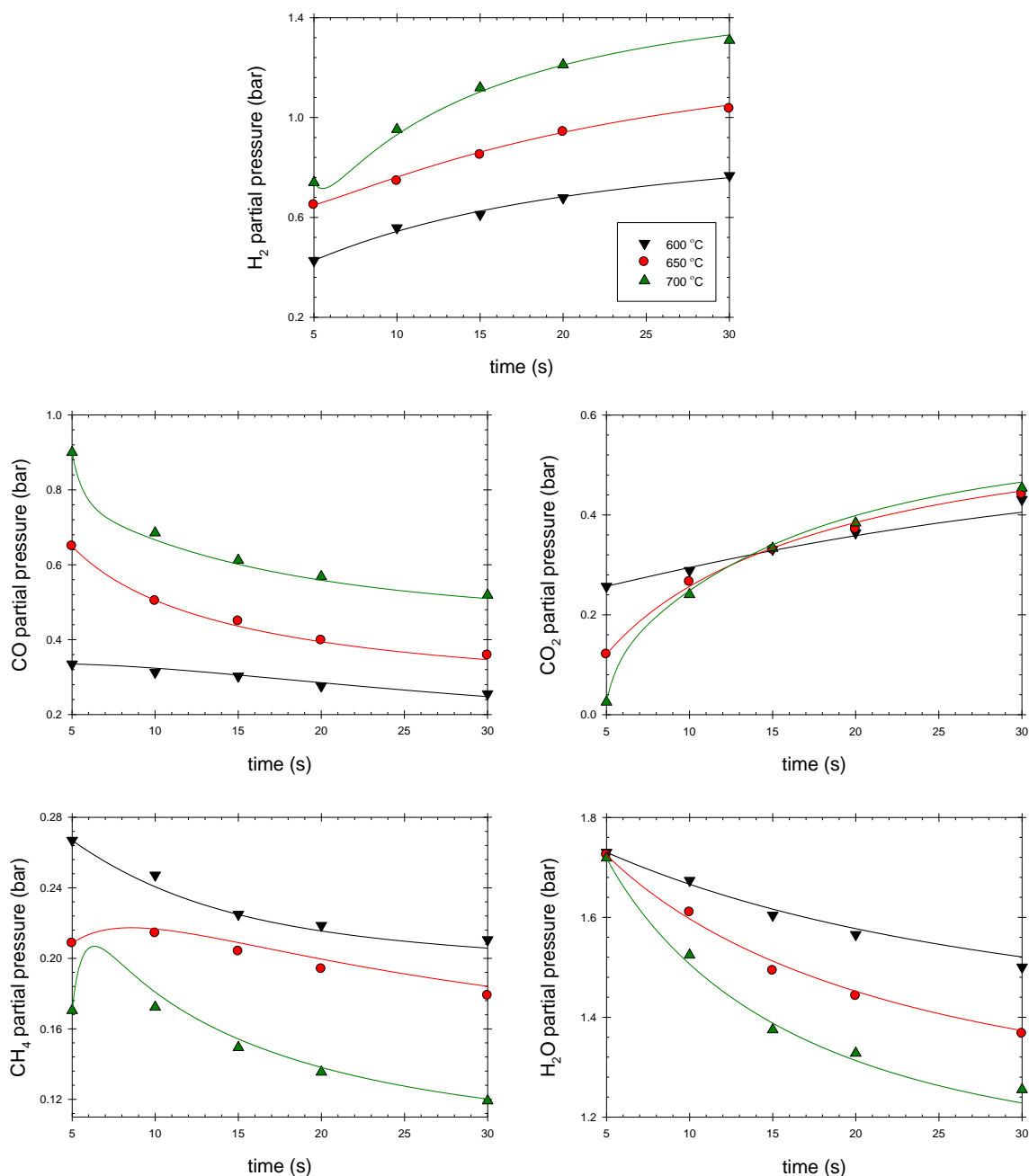
Figure 6.1: Estimation of kinetic parameters: experimental H_2, CO, CO_2, CH_4 and H_2O partial pressure vs the model predictions for steam gasification of glucose using 20% Ni/5% La_2O_3-γ-Al_2O_3 (Cat H) at S/B = 1.0 g/g and Catalyst/Biomass = 12.5 g/g. [R^2= 0.9917; sum of squares error = 4E-3; DOF = 69].

Figure 6.1 shows the fitting of the experimental H_2, CO, CO_2, CH_4 and H_2O partial pressures with the model predictions. The proposed model was well fitted with the experimental results with an R^2 value over 0.99. The profile of CH_4 partial pressure with time is interesting to mention here. It was found that the decrease in CH_4 was slow initially (5 to 10 s). At 650 and 700 °C, the amount of methane increased from 5 to 10 s of reaction time. This can be attributed to a higher driving force of the reverse dry reforming reaction (RDRM) at shorter reaction times. After 10 s, CH_4 started to decrease progressively due to the greater extent of the steam reforming (SRM) reaction. One can notice in Figure 6.1, that the proposed model well described the changes in methane formation (RDRM) and consumption (SRM) rates with time.

Table 6.3: Estimated kinetic parameters with their 95% confidence intervals for glucose gasification using 20% Ni/5% La_2O_3-γ-Al_2O_3 (Cat H)

Parameter	Present study using 20% Ni/5% La_2O_3-γ-Al_2O_3 (Cat H)		Salaices et al [179] Ni/α-Al_2O_3
	Value	Span for 95% C.I.	Value
k^o_{WGS} (mol/gcat.s.bar^2)	6.1E-05	± 1.2E-06	3.07E-6
E_{WGS} (kJ/mol)	33.36	± 13.06	53.1
k^o_{SRM} (mol/gcat.s.bar^2)	1.16E-4	± 4.18E-05	9.21E-10
E_{SRM} (kJ/mol)	68.11	± 9.88	93
k^o_{RDRM} mol/gcat.s.bar^4)	3.81E-4	± 1.98E-4	2.22E-9
E_{RDRM} (kJ/mol)	89.71	± 19.73	75.8

Table 6.3 summarizes the estimated intrinsic kinetic parameters with their 95% confidence intervals. A cross-correlation matrix of the estimated parameters is given in Table 6.4. When the results of the parameter estimation are inspected, it can be seen that all the six kinetic parameters are significant at the 95% confidence interval. In addition,

the temperature centering was successful in reducing the correlation between the pre-exponential factor and the activation energy to very moderate levels. Kinetic parameters for water gas shift and steam reforming reactions (k^o_{WGS} & k^o_{SRM}; and E_{WGS} & E_{SRM}) shows some degree of correlation. These correlations can be attributed to the fact that only two reactions are independent out of three dominant reactions considered.

Table 6.4: Cross-correlation matrix for the estimated parameters

	k^o_{WGS}	E_{WGS}	k^o_{SRM}	E_{SRM}	k^o_{RDRM}	E_{RDRM}
k^o_{WGS}	1.00					
E_{WGS}	0.38	1.00				
k^o_{SRM}	-0.78	-0.49	1.00			
E_{SRM}	-0.44	-0.79	0.60	1.00		
k^o_{RDRM}	-0.67	-0.40	0.64	0.48	1.00	
E_{RDRM}	-0.11	-0.60	0.23	0.57	0.18	1.00

It is important to review the magnitude of the activation energies (E_i), obtained in the context of the present study and to compare them with energies of activation for the same water gas shift, the steam methane reforming and the dry methane reforming reported in the literature. Regarding the steam reforming of methane (SRM), the activation energies for the dissociation of CH_4 on Ni range from 70 to 141 kJ/mol [232]. Maestri et al [230] reported the activation energy for methane steam reforming to be in the range of 55-70 kJ/mol. As a result, the activation energy of 68.1 kJ/mol determined in the present study for glucose, is in agreement with literature data. For the dry reforming of methane (DRM), Bradford et al [186] reported activation energies in the 93.3 to 123.2 kJ/mol range for similar nickel based catalysts. The activation energies calculated for the RDRM reaction in the present study are close that range. Furthermore, Maestri et al [230] reported activation energies for the water gas shift reaction to be in the range of 27-40 kJ/mol, which include the ones calculated in the present study.

The kinetic parameters obtained in the present study for Cat H are also compared with the results reported by Salaices et al [179] for a Ni/α-Al$_2$O$_3$, as shown in

Table 6.3. One can notice that the pre-exponential factors for all the three reactions have been significantly increased in the present study. This is an indication of the higher catalytic activity of Cat H, with this being attributed to its enhanced properties while compared to the Ni/α-Al$_2$O$_3$ catalyst. This enhanced reaction behaviour of Cat H can be linked to the following properties: i) higher specific surface area (167 vs 22.4 m^2/g), ii) higher Ni content (20 wt% vs 2.5 wt%), iii) higher reducibility (91% vs 76%), and iv) La$_2$O$_3$ addition.

6.6 **Model validation**

The proposed model and the estimated parameters were validated using the experimental data obtained with the variation of the steam/biomass ratio (S/B = 1.0. 0.8 and 0.6 g/g). Figure 6.2 compares the experimental data and model predictions using the estimated kinetic parameters. The model predictions predict quite well with the experimental data with a R^2 value of .988. These results indicate that the set of adsorption and kinetic parameters established are accurate enough for predicting hydrogen, carbon monoxide, carbon dioxide, methane and water concentrations. Moreover, it also demonstrated that one can perform controlled reaction experiments using a CREC Riser Simulator.

On this basis, it can be established that the proposed model is adequate for describing the steam gasification process. It can also be concluded that given the sound reaction engineering basis of the proposed kinetic model, it could be used to predict biomass conversion in large scale circulating fluidized bed gasifiers.
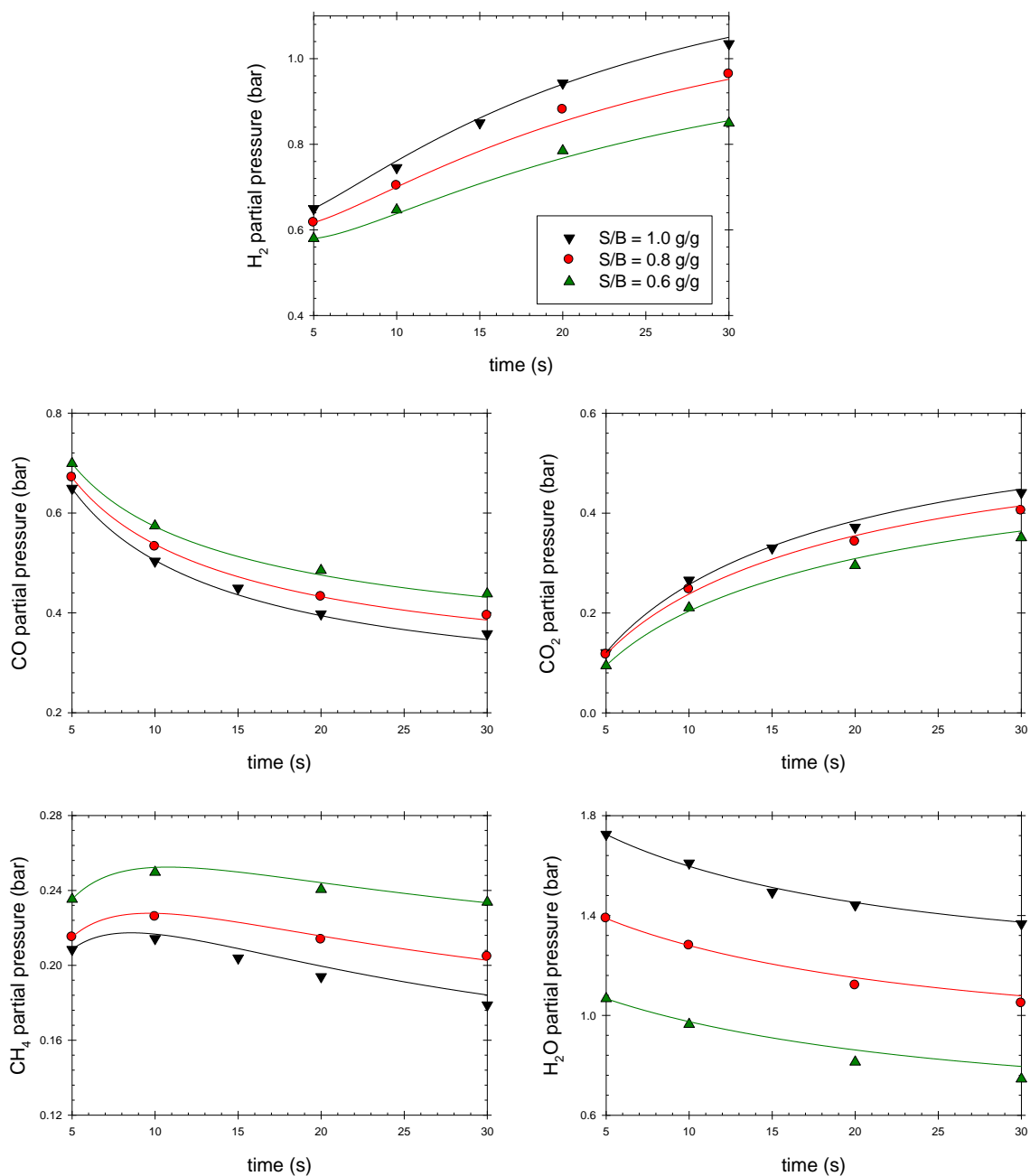
Figure 6.2: Validation of the developed model: experimental H_2, CO, CO_2, CH_4 and H_2O partial pressure with the variation of steam/biomass ratio vs the model predictions for glucose gasification using 20% Ni/5% La_2O_3-γ-Al_2O_3 (Cat H) at 650 °C. [R^2= 0.9887; sum of squares error = 6E-3].

6.7 **Conclusions**

The following are the main conclusions of this chapter:

f) It is shown that a three reaction additive kinetic model is adequate to represent the steam gasification of biomass surrogates. The model proposed successfully accounts for various product gas species (H_2, CO, CO_2, H_2O and CH_4).

g) It is proven that the experimental-modelling procedure, where intrinsic kinetic parameters and adsorption constants are *decoupled* in their evaluation, as accomplished in the CREC Riser Simulator, eliminates over-parameterization.

h) It is proven that the resulting energies of activation, in the case of glucose gasification, are in agreement in their magnitudes with those reported in the literature using single component reactions. This shows the likelihood that the proposed model includes phenomenologically-based parameters that can be linked to intrinsic reaction kinetics.

i) It is demonstrated that the proposed model and the estimated kinetic parameters can predict the steam gasification process in a wide range of operating parameter variation.

CHAPTER 7

CONCLUSIONS AND RECOMMENDATIONS

7.1 Conclusions

In this study, a high surface area, active and stable La_2O_3 promoted Ni/γ-Al_2O_3 catalyst was developed for biomass steam gasification. Glucose and 2-methoxy-4-methylphenol were used as biomass surrogate species representing cellulose and lignin components. Catalytic steam gasification experiments were developed at the expected operating conditions of a twin circulating fluidized bed gasifier using a CREC Riser Simulator. Catalyst structure-property and structure-reactivity relationships were established using characterization and gasification results. On this basis, a phenomenologically based kinetic model was also established considering the various product species.

The major findings of this study can be concluded as follows:

I. It is shown that catalyst preparation via multi-step impregnation with direct reduction of metal precursors after each impregnation in fluidized bed conditions is an effective way to prepare active and stable Ni catalysts. Significantly higher basicity, nickel reducibility and dispersion are achieved employing the preparation method of the present study instead of using calcination of metal precursors in air.

II. It is demonstrated that 5 wt% La_2O_3 is an optimal loading in terms of acid-base properties, textural properties, Ni reducibility and dispersion. Excessive La_2O_3 facilitates undesirable $LaAlO_3$ formation resulting in Ni crystallite agglomeration and hence, higher coke formation. Therefore, the catalyst promoted with 5 wt% La_2O_3 exhibits better performance for both glucose and 2-methoxy-4-methylphenol gasification compared to the catalysts with 0 and 10 wt % La_2O_3 content.

III. It is shown that the reactivity of a catalyst is well correlated with its Ni dispersion and basicity/acidity ratio. Higher Ni dispersion improves conversion and synthesis gas yield. It is also hypothesized that acid sites of γ-Al_2O_3 are responsible for coke deposition via hydrocarbon cracking, whereas basic sites facilitated coke reforming.

IV. It is established that surface structure, acid-base properties, metal dispersion and crystal size can be controlled by tuning a single parameter, which is the gas flow rate at the catalyst reduction step. Higher reduction gas flow helps to maintain the structure of γ-Al_2O_3 by carrying out the heat evolved from exothermic nitrates reduction reactions. It also ensures better heat and mass distribution resulting in improved metal dispersion. However, an excessive increase in reduction gas flow may result in reduced Ni reducibility and dispersion by increasing metal-support interaction.

V. It is proven that the relative proportion of octahedral and tetrahedral sites in γ-Al_2O_3, which is the main indicator of metal-support interaction and acid-base properties, can be assessed by the use of classical H_2 TPR and NH_3 TPD techniques.

VI. It is demonstrated that the fluidizable La_2O_3 promoted Ni/γ-Al_2O_3 catalyst developed in this study, is able to gasify surrogate biomass species performing very close to thermodynamic chemical equilibrium. It yields 100% glucose gasification without detectable tars formed at 650 °C. At the same temperature, gasification of methoxy-4-methylphenol gives 85.5% carbon conversion to permanent gases with only 8.8% tar formation and 5.7% carbon deposition as coke. The developed catalyst also exhibits stability under successive gasification and regeneration cycles.

VII. It is shown that both the stoichiometric and the non-stoichiometric thermodynamic equilibrium models developed in this study give essentially the same results. Coke and tar compounds were considered in the equilibrium calculations together with the permanent gases. Moreover, conditions of the

constant volume batch CREC Riser Simulator are incorporated into the developed models to establish a rigorous comparison with experimental results.

VIII. It is observed that increase of temperature and steam/biomass ratio yields higher conversions and dry gas yields. This finding should, however, be considered carefully in the context of energy efficiency and other operational challenges such as ash agglomeration, to determine best operating conditions.

IX. It is demonstrated that changes in the observed gasification product composition with the variation of operating parameters are in agreement with thermodynamic model predictions. Moreover, product composition approaches chemical equilibrium as the reaction time is increased. This indicates that the overall steam gasification process is kinetically controlled.

X. It is shown that a mechanistic kinetic model considering adsorption, desorption and surface chemical reactions is able to predict the catalytic steam gasification of biomass surrogates. Water gas shift, steam reforming of methane and reverse dry reforming of methane are considered as the dominant reactions. In this respect, the proposed model successfully accounts for various product gas species (H_2, CO, CO_2, H_2O and CH_4). Successful validation of the kinetic model and estimated intrinsic kinetic parameters using a different set of experimental results, shows the applicability in a wide range of operating conditions.

7.2 **Recommendations**

Based on the encouraging results of this study, the following future works are recommended:

I. Incorporation of a small amount of noble metals such as Rh, Pt, Ru in the catalyst formulation. Nobel metal addition is expected to enhance the catalyst stability especially in the case of refractory tars gasification.

II.   Further research should focus on the understanding of the effect of catalyst properties on the tar compositions. It will be interesting to explore the effect of octahedral and tetrahedral Lewis acid sites on the yields of different tar compounds. This study should also involve the understanding of possible reaction pathways for tar conversion.

III.   A mixture of steam and air could be considered as gasifying agents to achieve autothermal gasification. This interesting approach to biomass gasification could be considered using multiple injection ports in a CREC Riser Simulator.

IV.   Combined catalytic biomass gasification and CO_2 capture could be another promising area to explore.

REFERENCES

[1]   H.I. de Lasa, E. Salaices, J. Mazumder, R. Lucky, Catalytic steam gasification of biomass: catalysts, thermodynamics and kinetics., Chem. Rev. 111 (2011) 5404–33.

[2]   P. Parthasarathy, K.S. Narayanan, Hydrogen production from steam gasification of biomass: Influence of process parameters on hydrogen yield – A review, Renew. Energy. 66 (2014) 570–579.

[3]   G.W. Huber, S. Iborra, A. Corma, Synthesis of transportation fuels from biomass: chemistry, catalysts, and engineering., Chem. Rev. 106 (2006) 4044–98.

[4]   B. Hejazi, J.R. Grace, X. Bi, A. Mahecha-Botero, Steam gasification of biomass coupled with lime-based CO2 capture in a dual fluidized bed reactor: A modeling study, Fuel. 117 (2014) 1256–1266.

[5]   J. Udomsirichakorn, P.A. Salam, Review of hydrogen-enriched gas production from steam gasification of biomass: The prospect of CaO-based chemical looping gasification, Renew. Sustain. Energy Rev. 30 (2014) 565–579.

[6]   L. Wang, C.L. Weller, D.D. Jones, M. a. Hanna, Contemporary issues in thermal gasification of biomass and its application to electricity and fuel production, Biomass and Bioenergy. 32 (2008) 573–581.

[7]   P. McKendry, Energy production from biomass (Part 1): Overview of biomass., Bioresour. Technol. 83 (2002) 37–46.

[8]   V. Kirubakaran, V. Sivaramakrishnan, R. Nalini, T. Sekar, M. Premalatha, P. Subramanian, A review on gasification of biomass, Renew. Sustain. Energy Rev. 13 (2009) 179–186.

[9]   L. Devi, K.J. Ptasinski, F.J.J.G. Janssen, A review of the primary measures for tar elimination in biomass gasification processes, Biomass and Bioenergy. 24 (2003) 125–140.

[10]   X.T. Li, J.R. Grace, C.J. Lim, a. P. Watkinson, H.P. Chen, J.R. Kim, Biomass gasification in a circulating fluidized bed, Biomass and Bioenergy. 26 (2004) 171–193.

[11]   P. McKendry, Energy production from biomass (Part 2): Conversion technologies., Bioresour. Technol. 83 (2002) 47–54.

[12]   M. Asadullah, Barriers of commercial power generation using biomass gasification gas: A review, Renew. Sustain. Energy Rev. 29 (2014) 201–215.

[13]   M. Balat, Gasification of Biomass to Produce Gaseous Products, Energy Sources, Part A Recover. Util. Environ. Eff. 31 (2009) 516–526.

[14]   A.A. Khan, W. de Jong, P.J. Jansens, H. Spliethoff, Biomass combustion in fluidized bed boilers: Potential problems and remedies, Fuel Process. Technol. 90 (2009) 21–50.

[15]   A.V. Bridgwater, The technical and economic feasibility of biomass gasification for power generation, Fuel. 74 (1995) 631–653.

[16]   P. McKendry, Energy production from biomass (Part 3): Gasification technologies., Bioresour. Technol. 83 (2002) 55–63.

[17]   A.V. Bridgwater, Renewable fuels and chemicals by thermal processing of biomass, Chem. Eng. J. 91 (2003) 87–102.

[18]   E. Salaices, B. Serrano, H.I. de Lasa, Biomass Catalytic Steam Gasification Thermodynamics Analysis and Reaction Experiments in a CREC Riser Simulator, Ind. Eng. Chem. Res. 49 (2010) 6834–6844.

[19]   D. Sutton, B. Kelleher, J.R.H. Ross, Review of literature on catalysts for biomass gasification, Fuel Process. Technol. 73 (2001) 155–173.

[20]   A.V. Bridgwater, Catalysis in thermal biomass conversion, Appl. Catal. A Gen. 116 (1994) 5–47.

[21]   J. Han, H. Kim, The reduction and control technology of tar during biomass gasification/pyrolysis: An overview, Renew. Sustain. Energy Rev. 12 (2008) 397–416.

[22]   S. Nanda, P. Mohanty, K.K. Pant, S. Naik, J. a. Kozinski, A.K. Dalai, Characterization of North American Lignocellulosic Biomass and Biochars in Terms of their Candidacy for Alternate Renewable Fuels, BioEnergy Res. 6 (2012) 663–677.

[23]   L. Garcia, A. Benedicto, E. Romeo, M.L. Salvador, J. Arauzo, R. Bilbao, Hydrogen Production by Steam Gasification of Biomass Using Ni - Al Coprecipitated Catalysts Promoted with Magnesium, Energy & Fuels. 16 (2002) 1222–1230.

[24]   E. Gusta, A.K. Dalai, M.A. Uddin, E. Sasaoka, Catalytic Decomposition of Biomass Tars with Dolomites, Energy & Fuels. 23 (2009) 2264–2272.

[25]   Z. Abu El-Rub, E.A. Bramer, G. Brem, Review of Catalysts for Tar Elimination in Biomass Gasification Processes, Ind. Eng. Chem. Res. 43 (2004) 6911–6919.

[26]   E.G. Baker, L.K. Mudge, M.D. Brown, Steam gasification of biomass with nickel secondary catalysts, Ind. Eng. Chem. Res. 26 (1987) 1335–1339.

[27]   J. Ashok, S. Kawi, Steam reforming of toluene as a biomass tar model compound over CeO2 promoted Ni/CaO–Al2O3 catalytic systems, Int. J. Hydrogen Energy. 38 (2013) 13938–13949.

[28]   P. Lan, Q.-L. Xu, L.-H. Lan, D. Xie, S.-P. Zhang, Y.-J. Yan, Steam Reforming of Model Compounds and Fast Pyrolysis Bio-oil on Supported Nickle Metal Catalysts for Hydrogen Production, Energy Sources, Part A Recover. Util. Environ. Eff. 34 (2012) 2004–2015.

[29]   L. Garcia, R. French, S. Czernik, E. Chornet, Catalytic steam reforming of bio-oils for the production of hydrogen: effects of catalyst composition, Appl. Catal. A Gen. 201 (2000) 225–239.

[30]   R. Martínez, E. Romeo, L. García, R. Bilbao, The effect of lanthanum on Ni–Al catalyst for catalytic steam gasification of pine sawdust, Fuel Process. Technol. 85 (2003) 201–214.

[31]   K. Tomishige, T. Kimura, J. Nishikawa, T. Miyazawa, K. Kunimori, Promoting effect of the interaction between Ni and CeO2 on steam gasification of biomass, Catal. Commun. 8 (2007) 1074–1079.

[32]   A. Iriondo, V.L. Barrio, J.F. Cambra, P.L. Arias, M.B. Güemez, R.M. Navarro, et al., Influence of La2O3 modified support and Ni and Pt active phases on glycerol steam reforming to produce hydrogen, Catal. Commun. 10 (2009) 1275–1278.

[33]   S. Bona, P. Guillen, J. Alcalde, L. Garcia, R. Bilbao, Toluene steam reforming using coprecipitated Ni/Al catalysts modified with lanthanum or cobalt, Chem. Eng. J. 137 (2008) 587–597.

[34]   X. Chen, Y. Liu, G. Niu, Z. Yang, M. Bian, A. He, High temperature thermal stabilization of alumina modified by lanthanum species, Appl. Catal. A Gen. 205 (2001) 159–172.

[35]   F. Oudet, P. Courtine, A. Vejux, Thermal Stabilization of Transition Alumina by Structural Coherence with LnA1O3 (Ln = La , Pr , Nd), J. Catal. 114 (1988) 112–120.

[36]   H. Schaper, E.B.M. Doesburg, P.H.M. de Korte, L.L. van Reijen, Thermal Stabilization of High Surface Area Alumina, Solid State Ionics. 16 (1985) 261–265.

[37] R. Yang, X. Li, J. Wu, X. Zhang, X. Xi, Z. Zhang, Promotion Effects of La and Ce on Ni/γ-Al2O3 Catalysts in Hydrotreating of Crude 2-Ethylhexanol, Catal. Letters. 132 (2009) 275–280.

[38] Q. Xu, P. Lan, B. Zhang, Z. Ren, Y. Yan, Preparation of Syngas via Catalytic Gasification of Biomass with a Nickel-based Catalyst, Energy Sources, Part A Recover. Util. Environ. Eff. 35 (2013) 848–858.

[39] M. Sanchez-Sanchez, R. Navarro, J. Fierro, Ethanol steam reforming over Ni/La–Al2O3 catalysts: Influence of lanthanum loading, Catal. Today. 129 (2007) 336–345.

[40] H. Cheng, X. Lu, Y. Zhang, W. Ding, Hydrogen Production by Reforming of Simulated Hot Coke Oven Gas over Nickel Catalysts Promoted with Lanthanum and Cerium in a Membrane Reactor, Energy & Fuels. 23 (2009) 3119–3125.

[41] B. Valle, A. Remiro, A.T. Aguayo, J. Bilbao, A.G. Gayubo, Catalysts of Ni/α-Al2O3 and Ni/La2O3-αAl2O3 for hydrogen production by steam reforming of bio-oil aqueous fraction with pyrolytic lignin retention, Int. J. Hydrogen Energy. 38 (2013) 1307–1318.

[42] R. Alvero, A. Bernal, I. Carrizosa, A. Odriozola, Characterization of Lanthanide Oxide-promoted Rhodium Alumina Catalysts, Inorganica Chim. Acta. 140 (1987) 45–47.

[43] M. Bettman, R.E. Chase, K. Otto, W.H. Weber, Dispersion Studies on the System La2O3/y-Al2O3, J. Catal. 117 (1989) 447–454.

[44] L.P. Haack, J.E. deVries, K. Otto, M.S. Chattha, Characterization of lanthanum-modified γ-alumina by X-ray photoelectron spectroscopy and carbon dioxide absorption, Appl. Catal. A Gen. 82 (1992) 199–214.

[45] R. Yang, X. Li, J. Wu, X. Zhang, Z. Zhang, Promotion Effects of Copper and Lanthanum Oxides on Nickel/Gamma-Alumina Catalyst in the Hydrotreating of Crude 2-Ethylhexanol, J. Phys. Chem. C. 113 (2009) 17787–17794.

[46] C. Cerritos, R.F. Ramírez, A.F.A. Alvarado, J.M.M. Rosales, V. García, I.R.G. Esquivel, Steam Reforming of Ethanol over Ni/Al2O3 - La2O3 Catalysts Synthesized by Sol - Gel, Ind. Eng. Chem. Res. 50 (2011) 2576–2584.

[47] Y. Cui, H. Zhang, H. Xu, W. Li, The CO2 reforming of CH4 over Ni/La2O3/α-Al2O3 catalysts: The effect of La2O3 contents on the kinetic performance, Appl. Catal. A Gen. 331 (2007) 60–69.

[48]   P. Kumar, Y. Sun, R.O. Idem, Comparative Study of Ni-based Mixed Oxide Catalyst for Carbon Dioxide Reforming of Methane, Energy & Fuels. 22 (2008) 3575–3582.

[49]   Z.-W. Liu, H.-S. Roh, K.-W. Jun, Carbon Dioxide Reforming of Methane over Ni/La2O3/Al2O3, J. Ind. Eng. Chem. 9 (2003) 267–274.

[50]   S. Natesakhawat, O. Oktar, U.S. Ozkan, Effect of lanthanide promotion on catalytic performance of sol–gel Ni/Al2O3 catalysts in steam reforming of propane, J. Mol. Catal. A Chem. 241 (2005) 133–146.

[51]   S.-S. Lim, H.-J. Lee, D.-J. Moon, J.-H. Kim, N.-C. Park, J.-S. Shin, et al., Autothermal reforming of propane over Ce modified Ni/LaAlO3 perovskite-type catalysts, Chem. Eng. J. 152 (2009) 220–226.

[52]   M. Scheithauer, H. Knozinger, M.A. Vannice, Raman Spectra of La2O3 Dispersed on g-Al2O3, J. Catal. 705 (1998) 701–705.

[53]   A. Slagtern, U. Olsbye, R. Blom, I.M. Dahl, H. Fjellvag, Characterization of Ni on La modified A1203 catalysts during CO2 reforming of methane, Appl. Catal. A Gen. 165 (1997) 379–390.

[54]   X. Junke, Z. Wei, W. Jihui, L. Zhaojing, M. Jianxin, Characterization and Analysis of Carbon Deposited during the Dry Reforming of Methane over Ni/La2O3/Al2O3 Catalysts, Chinese J. Catal. 30 (2009) 1076–1084.

[55]   G. Del Angel, C. Guzmán, a. Bonilla, G. Torres, J.M. Padilla, Lanthanum effect on the textural and structural properties of γ-Al2O3 obtained from Boehmite, Mater. Lett. 59 (2005) 499–502.

[56]   G. Del Angel, a. Bonilla, Y. Peña, J. Navarrete, J.L.G. Fierro, D.R. Acosta, Effect of lanthanum on the catalytic properties of PtSn/γ-Al2O3 bimetallic catalysts prepared by successive impregnation and controlled surface reaction, J. Catal. 219 (2003) 63–73.

[57]   Y. Zhang, Y. Zhou, H. Liu, Y. Wang, Y. Xu, P. Wu, Effect of La addition on catalytic performance of PtSnNa/ZSM-5 catalyst for propane dehydrogenation, Appl. Catal. A Gen. 333 (2007) 202–210.

[58]   C.H. Bartholomew, R.J. Farrauto, Chemistry of Nickel-Alumina Catalysts, J. Catal. 45 (1976) 41–53.

[59]   Y.-J. Huang, J.A. Schwarz, The Effect of Catalyst Preparation on Catalytic Activity: II. The Design of Ni/A1203 Catalysts Prepared by Wet Impregnation, Appl. Catal. 30 (1987) 255–263.

[60] Y. Kim, C. Kim, P. Kim, J. Yi, Effect of preparation conditions on the phase transformation of mesoporous alumina, J. Non. Cryst. Solids. 351 (2005) 550–556.

[61] P. Chaiwatanodom, S. Vivanpatarakij, S. Assabumrungrat, Thermodynamic analysis of biomass gasification with CO2 recycle for synthesis gas production, Appl. Energy. 114 (2014) 10–17.

[62] M. J. Prins, K. J. Ptasinski, F. J. J. G. Janssen, Thermodynamics of gas-char reactions: first and second law analysis, Chem. Eng. Sci. 58 (2003) 1003–1011.

[63] X. Li, J.R. Grace, A.P. Watkinson, C.J. Lim, A. Ergudenler, Equilibrium modeling of gasification : a free energy minimization approach and its application to a circulating fuidized bed coal gasifier, Fuel. 80 (2001) 195–207.

[64] S. Vivanpatarakij, S. Assabumrungrat, Thermodynamic analysis of combined unit of biomass gasifier and tar steam reformer for hydrogen production and tar removal, Int. J. Hydrogen Energy. 38 (2013) 3930–3936.

[65] A. Abuadala, I. Dincer, G.F. Naterer, Exergy analysis of hydrogen production from biomass gasification, Int. J. Hydrogen Energy. 35 (2010) 4981–4990.

[66] C.C. Sreejith, C. Muraleedharan, P. Arun, Equilibrium modeling and regression analysis of biomass gasification, J. Renew. Sustain. Energy. 4 (2012) 063124.

[67] G. Song, L. Chen, J. Xiao, L. Shen, Exergy evaluation of biomass steam gasification via interconnected fluidized beds, Int. J. Energy Res. 37 (2013) 1743–1751.

[68] E. Salaices, PhD Thesis, Catalytic Steam Gasification of Biomass Surrogates: A Thermodymaic and Kinetic Approach, The University of Western Ontario, London, ON, Canada, 2010.

[69] H.I. de Lasa, Riser Simulator, US Patent 5102628, 1992.

[70] P.L. Dhepe, A. Fukuoka, Cellulose conversion under heterogeneous catalysis., ChemSusChem. 1 (2008) 969–75.

[71] A. Demirbas, Modernization of Biomass Energy Conversion Facilities, Energy Sources, Part B Econ. Planning, Policy. 2 (2007) 227–235.

[72] L. Garcia, M.. Salvador, J. Arauzo, R. Bilbao, CO2 as a gasifying agent for gas production from pine sawdust at low temperatures using a Ni/Al coprecipitated catalyst, Fuel Process. Technol. 69 (2001) 157–174.

[73] J. Gil, J. Corella, P. Aznar, M.A. Caballero, Biomass gasification in atmospheric and bubbling fuidized bed : Effect of the type of gasifying agent on the product distribution, Biomass and Bioenergy. 17 (1999) 389–403.

[74] L. Devi, K.J. Ptasinski, F.J.J.G. Janssen, S.V.B. van Paasen, P.C. a. Bergman, J.H. a. Kiel, Catalytic decomposition of biomass tars: use of dolomite and untreated olivine, Renew. Energy. 30 (2005) 565–587.

[75] M.F. Demirbas, Nitrogenous Chemicals from Carbon Based Materials, Energy, Explor. Exploit. 23 (2005) 215–224.

[76] P.C. Roy, A. Datta, N. Chakraborty, Assessment of cow dung as a supplementary fuel in a downdraft biomass gasifier, Renew. Energy. 35 (2010) 379–386.

[77] M. Ni, D.Y.C. Leung, M.K.H. Leung, K. Sumathy, An overview of hydrogen production from biomass, Fuel Process. Technol. 87 (2006) 461–472.

[78] W. Rulkens, Sewage Sludge as a Biomass Resource for the Production of Energy : Overview and Assessment of the Various Options, Energy & Fuels. 44 (2008) 9–15.

[79] F. Jappe Frandsen, Utilizing biomass and waste for power production—a decade of contributing to the understanding, interpretation and analysis of deposits and corrosion products, Fuel. 84 (2005) 1277–1294.

[80] S. Munir, S.S. Daood, W. Nimmo, a M. Cunliffe, B.M. Gibbs, Thermal analysis and devolatilization kinetics of cotton stalk, sugar cane bagasse and shea meal under nitrogen and air atmospheres., Bioresour. Technol. 100 (2009) 1413–8.

[81] Y. Chen, Y. Luo, W. Wu, Y. Su, Experimental Investigation on Tar Formation and Destruction in a Lab-Scale Two-Stage Reactor, Energy & Fuels. 23 (2009) 4659–4667.

[82] H. Kosstrin, Direct formation of pyrolysis oil from biomass, in: Spec. Work. Fast Pyrolysis Biomass, Copper Mountain, CO, USA, 1980: pp. 105–120.

[83] D. Mohan, C.U. Pittman,, P.H. Steele, Pyrolysis of Wood/Biomass for Bio-oil: A Critical Review, Energy & Fuels. 20 (2006) 848–889.

[84] M.J. Antal,, S.G. Allen, D. Schulman, X. Xu, R.J. Divilio, Biomass Gasification in Supercritical Water, Ind. Eng. Chem. Res. 39 (2000) 4040–4053.

[85] L. Wei, S. Xu, L. Zhang, C. Liu, H. Zhu, S. Liu, Steam gasification of biomass for hydrogen-rich gas in a free-fall reactor, Int. J. Hydrogen Energy. 32 (2007) 24–31.

[86]   K. Tomishige, M. Asadullah, K. Kunimori, Syngas production by biomass gasification using Rh/CeO2/SiO2 catalysts and fluidized bed reactor, Catal. Today. 89 (2004) 389–403.

[87]   C. Franco, F. Pinto, I. Gulyurtlu, I. Cabrita, The study of reactions influencing the biomass steam gasification process, Fuel. 82 (2003) 835–842.

[88]   J. Ginsburg, H.I. de Lasa, Catalytic Gasification of Biomass in a CREC Fluidized Riser Simulator, Int. J. Chem. React. Eng. 3 (2005) 1–18.

[89]   M.P. Aznar, M.A. Caballero, J.A. Sancho, E. Francés, Plastic waste elimination by co-gasification with coal and biomass in fluidized bed with air in pilot plant, Fuel Process. Technol. 87 (2006) 409–420.

[90]   J. Hrdlicka, C. Feik, D. Carpenter, M. Pomeroy, Parametric Gasification of Oak and Pine Feedstocks Using the TCPDU and Slipstream Water-Gas Shift Catalysis, 2008.

[91]   V. Skoulou, E. Kantarelis, S. Arvelakis, W. Yang, a. Zabaniotou, Effect of biomass leaching on H2 production, ash and tar behavior during high temperature steam gasification (HTSG) process, Int. J. Hydrogen Energy. 34 (2009) 5666–5673.

[92]   M. Tanaka, H. Ozaki, A. Ando, S. Kambara, H. Moritomi, Basic Characteristics of Food Waste and Food Ash on Steam Gasification, Ind. Eng. Chem. Res. 47 (2008) 2414–2419.

[93]   K. Raveendran, A. Ganesh, K.C. Khilart, Influence of mineral matter on biomass pyrolysis characteristics, Fuel. 74 (1995) 1812–1822.

[94]   A. van der Drift, J. Van Doorn, J.W. Vermeulen, Ten residual biomass fuels for circulating uidized-bed gasiÿcation, Biomass and Bioenergy. 20 (2001) 45–56.

[95]   L. Wang, M. a. Hanna, C.L. Weller, D.D. Jones, Technical and economical analyses of combined heat and power generation from distillers grains and corn stover in ethanol plants, Energy Convers. Manag. 50 (2009) 1704–1713.

[96]   P. Maa, R. Bailie, Influence of particle sizes and environmental conditions on high temperature pyrolysis of cellulose material, Combust. Sci. Technol. 7 (1973) 257–269.

[97]   R.J. Evans, T.A. Milne, Molecular Characterization of the Pyrolysis of Biomass. 1. Fundamentals, Energy & Fuels. 1 (1987) 123–137.

[98]   P. Fu, S. Hu, L. Sun, J. Xiang, T. Yang, A. Zhang, et al., Structural evolution of maize stalk/char particles during pyrolysis., Bioresour. Technol. 100 (2009) 4877–83.

[99]   D.C. Elliott, Relation of reaction time and temperature to chemical composition of yrolysis oils. In: Soltes EJ, Milne TA, editors. 1988, in: Proc. ACS Symp. Ser. 376, Pyrolysis Oils from Biomass, 1988.

[100] T.A. Milne, R.J. Evans, Biomass Gasifier " Tars ": Their Nature, Formation, and Conversion, 1998.

[101] H.B. Goyal, D. Seal, R.C. Saxena, Bio-fuels from thermochemical conversion of renewable resources: A review, Renew. Sustain. Energy Rev. 12 (2008) 504–517.

[102] L. Fagbemi, L. Khezami, R. Capart, Pyrolysis products from different biomasses : application to the thermal cracking of tar, Appl. Energy. 69 (2001) 293–306.

[103] Q. Yu, C. Brage, G. Chen, K. Sjöström, Temperature impact on the formation of tar from biomass pyrolysis in a free-fall reactor, J. Anal. Appl. Pyrolysis. 40-41 (1997) 481–489.

[104] C. Hanping, L. Bin, Y. Haiping, Y. Guolai, Z. Shihong, Experimental Investigation of Biomass Gasification in a Fluidized Bed Reactor, Energy & Fuels. 22 (2008) 3493–3498.

[105] S. Luo, B. Xiao, Z. Hu, S. Liu, X. Guo, M. He, Hydrogen-rich gas from catalytic steam gasification of biomass in a fixed bed reactor: Influence of temperature and steam on gasification performance, Int. J. Hydrogen Energy. 34 (2009) 2191–2194.

[106] N. Gao, A. Li, C. Quan, A novel reforming method for hydrogen production from biomass steam gasification., Bioresour. Technol. 100 (2009) 4271–7.

[107] M. Mahishi, D. Goswami, Thermodynamic optimization of biomass gasifier for hydrogen production, Int. J. Hydrogen Energy. 32 (2007) 3831–3840.

[108] C.M. Kinoshita, Y. Wang, J. Zhou, Tar formation under different biomass gasification conditions, J. Anal. Appl. Pyrolysis. 29 (1994) 169–181.

[109] I. Narvaez, A. Orio, M.P. Aznar, J. Corella, Biomass Gasification with Air in an Atmospheric Bubbling Fluidized Bed . Effect of Six Operational Variables on the Quality of the Produced Raw Gas, Ind. Eng. Chem. Res. 5885 (1996) 2110–2120.

[110] J. Herguido, J. Corella, J. Gonzalez-Saiz, Steam Gasification of Lignocellulosic Residues in a Fluidized Bed at a Small Pilot Scale . Effect of the Type of Feedstock, Ind. Eng. Chem. Res. 31 (1992) 1274–1282.

[111] P. Aznar, M.A. Caballero, J. Gil, J.A. Martın, J. Corella, Commercial Steam Reforming Catalysts To Improve Biomass Gasification with Steam - Oxygen Mixtures . 2 . Catalytic Tar Removal, Ind. Eng. Chem. Res. 37 (1998) 2668–2680.

[112] R.A. Knight, Experience with raw gas analysis from pressurized gasification of biomass, Biomass and Bioenergy. 18 (2000) 67–77.

[113] J. Corella, M.-P. Aznar, J. Gil, M. a. Caballero, Biomass Gasification in Fluidized Bed: Where To Locate the Dolomite To Improve Gasification?, Energy & Fuels. 13 (1999) 1122–1127.

[114] W. Chaiwat, I. Hasegawa, K. Mae, Examination of the Low-Temperature Region in a Downdraft Gasifier for the Pyrolysis Product Analysis of Biomass Air Gasification, Ind. Eng. Chem. Res. 48 (2009) 8934–8943.

[115] M. Bartels, W. Lin, J. Nijenhuis, F. Kapteijn, J.R. van Ommen, Agglomeration in fluidized beds at high temperatures: Mechanisms, detection and prevention, Prog. Energy Combust. Sci. 34 (2008) 633–666.

[116] G.M. Banowetz, S.M. Griffith, H.M. El-Nashaar, Mineral Content of Grasses Grown for Seed in Low Rainfall Areas of the Pacific Northwest and Analysis of Ash from Gasification of Bluegrass (Poa pratensis L.) Straw †, Energy & Fuels. 23 (2009) 502–506.

[117] M. Asadullah, K. Fujimoto, K. Tomishige, Catalytic Performance of Rh/CeO2 in the Gasification of Cellulose to Synthesis Gas at Low Temperature, Ind. Eng. Chem. Res. 40 (2001) 5894–5900.

[118] B. Digman, S. Joo, D. Kim, Recent Progress in Gasification / Pyrolysis Technologies for Biomass Conversion to Energy, Environ. Prog. Sustain. Energy. 28 (2009) 47–51.

[119] M.A. Dietenberger, M. Anderson, Vision of the U.S. Biofuel Future: A Case for Hydrogen-Enriched Biomass Gasification, Ind. Eng. Chem. Res. 46 (2007) 8863–8874.

[120] L.K. Mudge, E.G. Baker, D.H. Mitchell, M.D. Brown, Catalytic Steam Gasification of Biomass for Methanol and Methane Production, J. Sol. Energy Eng. 107 (1985) 88–92.

[121] J. Nishikawa, K. Nakamura, M. Asadullah, T. Miyazawa, K. Kunimori, K. Tomishige, Catalytic performance of Ni/CeO2/Al2O3 modified with noble metals in steam gasification of biomass, Catal. Today. 131 (2008) 146–155.

[122] J. Arauzo, D. Radlein, J. Piskorz, D.S. Scott, Catalytic Pyrogasification of Biomass. Evaluation of Modified Nickel Catalysts, Ind. Eng. Chem. Res. 36 (1997) 67–75.

[123] A. Olivares, P. Aznar, M.A. Caballero, J. Gil, E. France, Biomass Gasification : Produced Gas Upgrading by In-Bed Use of Dolomite, Ind. Eng. Chem. Res. (1997) 5220–5226.

[124] L. Garcia, M.L. Salvador, R. Bilbao, J. Arauzo, Influence of Calcination and Reduction Conditions on the Catalyst Performance in the Pyrolysis Process of Biomass, Energy & Fuels. 12 (1998) 139–143.

[125] J. Arauzo, D. Radlein, J. Piskorz, D.S. Scott, A New Catalyst for the Catalytic Gasification of Biomass, Energy & Fuels. 8 (1994) 1192–1196.

[126] L. García, M.L. Salvador, J. Arauzo, R. Bilbao, Catalytic Steam Gasification of Pine Sawdust. Effect of Catalyst Weight/Biomass Flow Rate and Steam/Biomass Ratios on Gas Production and Composition, Energy & Fuels. 13 (1999) 851–859.

[127] M.A. Caballero, J. Corella, M.-P. Aznar, J. Gil, Biomass Gasification with Air in Fluidized Bed. Hot Gas Cleanup with Selected Commercial and Full-Size Nickel-Based Catalysts, Ind. Eng. Chem. Res. 39 (2000) 1143–1154.

[128] M.A. Caballero, P. Aznar, J. Gil, J.A. Martı, E. France, Commercial Steam Reforming Catalysts To Improve Biomass Gasification with Steam - Oxygen Mixtures . 1 . Hot Gas Upgrading by the Catalytic Reactor, Ind. Eng. Chem. Res. 36 (1997) 5227–5239.

[129] J. Corella, A. Orı, P. Aznar, Biomass Gasification with Air in Fluidized Bed : Reforming of the Gas Composition with Commercial Steam Reforming Catalysts, Ind. Eng. Chem. Res. 37 (1998) 4617–4624.

[130] C.M. Kinoshita, Y. Wang, J. Zhou, Effect of Reformer Conditions on Catalytic Reforming of Biomass-Gasification Tars, Ind. Eng. Chem. Res. 34 (1995) 2949–2954.

[131] M. Asadullah, K. Tomishige, K. Fujimoto, A novel catalytic process for cellulose gasification to synthesis gas, Catal. Commun. 2 (2001) 63–68.

[132] N.H. Florin, A.T. Harris, Enhanced hydrogen production from biomass with in situ carbon dioxide capture using calcium oxide sorbents, Chem. Eng. Sci. 63 (2008) 287–316.

[133] A.K. Dalai, E. Sasaoka, H. Hikita, D. Ferdous, Catalytic Gasification of Sawdust Derived from Various Biomass, Energy & Fuels. 17 (2003) 1456–1463.

[134] G. Hu, S. Xu, S. Li, C. Xiao, S. Liu, Steam gasification of apricot stones with olivine and dolomite as downstream catalysts, Fuel Process. Technol. 87 (2006) 375–382.

[135] G. Xu, T. Murakami, T. Suda, S. Kusama, T. Fujimori, Distinctive Effects of CaO Additive on Atmospheric Gasification of Biomass at Different Temperatures, Ind. Eng. Chem. Res. 44 (2005) 5864–5868.

[136] S.W. Lee, S.S. Nam, S.B. Kim, K.W. Lee, C.S. Choi, The effect of Na2CO3 on the catalytic gasification of rice straw over nickel catalysts supported on kieselguhr, Korean J. Chem. Eng. 17 (2000) 174–178.

[137] P.A. Simell, J.K. Leppalahtia, J.B. Bredenberg, Catalytic purification of tarry fuel gas with carbonate rocks and ferrous materials, Fuel. 71 (1992) 211–218.

[138] S. Juutilainen, P. Simell, a Krause, Zirconia: Selective oxidation catalyst for removal of tar and ammonia from biomass gasification gas, Appl. Catal. B Environ. 62 (2006) 86–92.

[139] J.R. Rostrup-Nielsen, J.H. Hansen, CO2-Reforming of Methane over Transition Metals, J. Catal. 144 (1993) 38–49.

[140] D.C. Elliott, E.G. Baker, R.S. Butner, L.J. Sealock, Bench-Sole Reactor Tests of Low Temperature , Catalytic Gasification of Wet Industrial Wastes, J. Sol. Energy Eng. 115 (1993) 52–56.

[141] M.P. Aznar, J. Corella, Steam Gasification of Lignocellulosic Residues in a Fluidized Bed with Commercial Steam Reforming Catalysts, Ind. Eng. Chem. Res. 32 (1993) 1–10.

[142] D.L. Trimm, Coke formation and minimisation during stem reforming reactions, Catal. Today. 37 (1997) 233–238.

[143] H. Bartholomew, L. Sorensen, Sintering Kinetics of Silica- and Alumina-Supported Hydrogen Atmosphere Nickel in, J. Catal. 81 (1983) 131–141.

[144] D.N. Bangala, N. Abatzoglou, E. Chornet, Steam Reforming of Naphthalene on Ni-Cr / Al , O , Catalysts Doped with MgO , TiO ,, and L % O ,, AIChE J. 44 (1998) 927–936.

[145] J.R. Rostrup-Nielsen, Industrial relevance of coking, Catal. Today. 37 (1997) 225–232.

[146] C.H. Bartholomew, G.D. Weatherbee, G.A. Jarvi, Effects of Carbon Deposits on the Specific Activity of Nickel and Nickel Bimetallic Catalysts, Chem. Eng. Commun. 5 (1980) 125–134.

[147] H.C. Dibbern, P. Olesen, J.R. Rostrup-Nielse, P.B. Tottrup, N.R. Udengaard, Make low hydrogen syngas using sulfur passivated reforming, Hydrocarb. Process. 65 (1986) 71–74.

[148] K. Tomishige, M. Asadullah, K. Kunimori, Novel catalysts for gasification of biomass with high conversion efficiency, Catal. Surv. from Asia. 7 (2003) 219–233.

[149] R.P.W.J. Struis, T.J. Schildhauer, I. Czekaj, M. Janousch, S.M. a. Biollaz, C. Ludwig, Sulphur poisoning of Ni catalysts in the SNG production from biomass: A TPO/XPS/XAS study, Appl. Catal. A Gen. 362 (2009) 121–128.

[150] K. Sato, K. Fujimoto, Development of new nickel based catalyst for tar reforming with superior resistance to sulfur poisoning and coking in biomass gasification, Catal. Commun. 8 (2007) 1697–1701.

[151] S. Wang, G.Q.M. Lu, Catalytic Activities and Coking Characteristics of Oxides-Supported Ni Catalysts for CH4 Reforming with Carbon Dioxide, Energy & Fuels. 12 (1998) 248–256.

[152] S. Wang, G.Q.M. Lu, CO2 reforming of methane on Ni catalysts : Effects of the support phase and preparation technique, Appl. Catal. B Environ. 16 (1998) 269–277.

[153] E.G. Baker, L.K. Mudge, Mechanisms of catalytic biomass gasification, J. Anal. Appl. Pyrolysis. 6 (1984) 285–297.

[154] M.F. Mark, W.F. Maier, CO2-Reforming of Methane on Supported Rh and Ir Catalysts, J. Catal. 162 (1996) 122–130.

[155] A.M. Gadalla, B. Bower, The role of catalyst support on the activity of nickel for reforming methane with CO2, Chem. Eng. Sci. 43 (1988) 3049–3062.

[156] J.M. Ginsburg, J. Pin, T. El Solh, H.I. de Lasa, Coke Formation over a Nickel Catalyst under Methane Dry Reforming Conditions : Thermodynamic and Kinetic Models, Ind. Eng. Chem. Res. 44 (2005) 4846–4854.

[157] K. Jarosch, H.I. de Lasa, Novel Riser Simulator for methane reforming using high temperature membranes, Chem. Eng. Sci. 54 (1999) 1455–1460.

[158] T. El Solh, K. Jarosch, H.I. de Lasa, Fluidizable catalyst for methane reforming, Appl. Catal. A Gen. 210 (2001) 315–324.

[159] T. El Solh, K. Jarosch, H.I. de Lasa, Catalytic Dry Reforming of Methane in a CREC Riser Simulator Kinetic Modeling and Model Discrimination, Ind. Eng. Chem. Res. 42 (2003) 2507–2515.

[160] S. Aktaş, M. Karakaya, A.K. Avcı, Thermodynamic analysis of steam assisted conversions of bio-oil components to synthesis gas, Int. J. Hydrogen Energy. 34 (2009) 1752–1759.

[161] M. Baratieri, P. Baggio, L. Fiori, M. Grigiante, Biomass as an energy source: thermodynamic constraints on the performance of the conversion process., Bioresour. Technol. 99 (2008) 7063–73.

[162] H.-J. Huang, S. Ramaswamy, Modeling biomass gasification using thermodynamic equilibrium approach, Appl. Biochem. Biotechnol. 154 (2009) 14–25.

[163] G. Schuster, G. Loffler, K. Weigl, H. Hofbauer, Biomass steam gasification - an extensive parametric modeling study, Bioresour. Technol. 77 (2001) 71–79.

[164] J. Ginsburg, H.I. de Lasa, Catalytic Gasification of Biomass in a CREC Fluidized Riser Simulator, Int. J. Chem. React. Eng. 3 (2005) A38.

[165] M.K. Cohce, I. Dincer, M. a. Rosen, Thermodynamic analysis of hydrogen production from biomass gasification, Int. J. Hydrogen Energy. 35 (2010) 4970–4980.

[166] P.T. Diniz Filho, J.L. Silveira, C.E. Tuna, W.D.Q. Lamas, Energetic, ecologic and fluid-dynamic analysis of a fluidized bed gasifier operating with sugar cane bagasse, Appl. Therm. Eng. 57 (2013) 116–124.

[167] P.-C. Kuo, W. Wu, W.-H. Chen, Gasification performances of raw and torrefied biomass in a downdraft fixed bed gasifier using thermodynamic analysis, Fuel. 117 (2014) 1231–1241.

[168] C.C. Sreejith, P. Arun, C. Muraleedharan, Thermochemical Analysis of Biomass Gasification by Gibbs Free Energy Minimization Model—Part: I (Optimization of Pressure and Temperature), Int. J. Green Energy. 10 (2013) 231–256.

[169] C.C. Sreejith, C. Muraleedharan, P. Arun, Thermo-Chemical Analysis of Biomass Gasification by Gibbs Free Energy Minimization Model-Part: II (Optimization of Biomass Feed and Steam to Biomass Ratio), Int. J. Green Energy. 10 (2013) 610–639.

[170] N. Jand, V. Brandani, P.U. Foscolo, Thermodynamic Limits and Actual Product Yields and Compositions in Biomass Gasification Processes, Ind. Eng. Chem. Res. 45 (2006) 834–843.

[171] A. Melgar, J.F. Pérez, H. Laget, A. Horillo, Thermochemical equilibrium modelling of a gasifying process, Energy Convers. Manag. 48 (2007) 59–67.

[172] T. Srinivas, a. V.S.S.K.S. Gupta, B. V. Reddy, Thermodynamic Equilibrium Model and Exergy Analysis of a Biomass Gasifier, J. Energy Resour. Technol. 131 (2009) 031801.

[173] J.J.M. Orfao, F.J.A. Antunes, J.L. Figueiredo, Pyrolysis kinetics of lignocellulosic materials-three independent reactions model, Fuel. 78 (1999) 349–358.

[174] J. Corella, A. Sanz, Modeling circulating fluidized bed biomass gasifiers. A pseudo-rigorous model for stationary state, Fuel Process. Technol. 86 (2005) 1021–1053.

[175] D. Fiaschi, M. Michelini, A two-phase one-dimensional biomass gasiÿcation kinetics model, Biomass and Bioenergy. 21 (2001) 121–132.

[176] R. Radmanesh, Y. Courbariaux, J. Chaouki, C. Guy, A unified lumped approach in kinetic modeling of biomass pyrolysis, Fuel. 85 (2006) 1211–1220.

[177] E. Ranzi, A. Cuoci, T. Faravelli, A. Frassoldati, G. Migliavacca, S. Pierucci, et al., Chemical Kinetics of Biomass Pyrolysis, Energy & Fuels. 22 (2008) 4292–4300.

[178] M. Sedighi, K. Keyvanloo, J. Towfighi, Kinetic study of steam catalytic cracking of naphtha on a Fe/ZSM-5 catalyst, Fuel. 109 (2013) 432–438.

[179] E. Salaices, H.I. de Lasa, B. Serrano, Steam Gasification of a Cellulose Surrogate over a Fluidizable Ni/a-alumina Catalyst : A Kinetic Model, AIChE. 58 (2012) 1588–599.

[180] T. van Herwijnen, W.A. de Jong, Kinetics and Mechanism of the CO shift on Cu / ZnO I. Kinetics of the Forward and Reverse CO Shift Reactions, J. Catal. 63 (1980) 83–93.

[181] T. van Herwijnen, W.A. de Jong, Kinetics and Mechanism of the CO shift on Cu / ZnO II. Kinetics of the Decomposition of Formic Acid, J. Catal. 63 (1980) 94–101.

[182] C.T. Campbell, K.A. Daube, A Surface Science Investigation of the Water-Gas on Cu (111), J. Catal. 104 (1987) 109–119.

[183] J.-W. Snoeck, G.F. Froment, M. Fowles, Steam/CO2 Reforming of Methane. Carbon Formation and Gasification on Catalysts with Various Potassium Contents, Ind. Eng. Chem. Res. 41 (2002) 3548–3556.

[184] K. Jarosch, T. El Solh, H.I. de Lasa, Modelling the catalytic steam reforming of methane: discrimination between kinetic expressions using sequentially designed experiments, Chem. Eng. Sci. 57 (2002) 3439–3451.

[185] P. Munster, H. Grabke, Kinetics of the Steam Reforming of Methane with Iron, Nickel and Iron–Nickel Alloys as Catalysts, J. Catal. 72 (1981) 279–287.

[186] M.C.J. Bradford, M. V Albert, Catalytic reforming of methane with carbon dioxide over nickel catalysts II . Reaction kinetics, Appl. Catal. A Gen. 142 (1996) 97–122.

[187] T. El Solh, PhD Thesis, Dry Reforming Of Methane In A Fast Fluidized Bed Reactor: Catalysis & Kinetics, The University of Western Ontario, London, ON, Canada, 2002.

[188] M.M. Hossain, H.I. de Lasa, Reactivity and Stability of Co-Ni/Al2O3 Oxygen Carrier in Multicycle CLC, AIChE J. 53 (2007) 1817–1829.

[189] M.C. Alvarez-Galvan, R.M. Navarro, F. Rosa, Y. Briceño, F.G. Alvarez, J.L.G. Fierro, Performance of La,Ce-modified alumina-supported Pt and Ni catalysts for the oxidative reforming of diesel hydrocarbons, Int. J. Hydrogen Energy. 33 (2008) 652–663.

[190] M.M. Hossain, D. Lopez, J. Herrera, H.I. de Lasa, Nickel on lanthanum-modified γ-Al2O3 oxygen carrier for CLC: Reactivity and stability, Catal. Today. 143 (2009) 179–186.

[191] R.M. Navarro, M.C. Álvarez-Galván, F. Rosa, J.L.G. Fierro, Hydrogen production by oxidative reforming of hexadecane over Ni and Pt catalysts supported on Ce/La-doped Al2O3, Appl. Catal. A Gen. 297 (2006) 60–72.

[192] H. Schaper, E.B.M. Doesburg, L.L. van Reijen, The Influences of Lanthanum Oxide on the Thermal Stability of Gamma Alumina Catalyst Supports, Appl. Catal. 7 (1983) 211–220.

[193] Y. Jilei, L. Zengxi, D. Huachao, L. Yuan, Lanthanum Modified Ni/y-A1203 Catalysts for Partial Oxidation of Methane, J. Rare Earths. 24 (2006) 302–308.

[194] E.P. Parry, An Infrared Study of Pyridine Adsorbed on Acidic Solids. Characterization of Surface Acidity, J. Catal. 2 (1963) 371–379.

[195] C. Morterra, G. Magnacca, A case study: surface chemistry and surface structure of catalytic aluminas, as studied by vibrational spectroscopy of adsorbed species, Catal. Today. 27 (1996) 497–532.

[196] A.A. Khaleel, K.J. Klabunde, Characterization of Aerogel Prepared High-Surface-Area Alumina: In Situ FTIR Study of Dehydroxylation and Pyridine Adsorption, Chem. - A Eur. J. 8 (2002) 3991–3998.

[197] V. La Parola, G. Deganello, S. Scirè, A.M. Venezia, Effect of the Al/Si atomic ratio on surface and structural properties of sol–gel prepared aluminosilicates, J. Solid State Chem. 174 (2003) 482–488.

[198] C. Morterra, S. Coluccia, A. Chiorino, F. Boccuzzi, Infrared Study of the Adsorption of Pyridine on a-Al2O3, J. Catal. 54 (1978) 348–364.

[199] C. Morterra, A. Chiorino, G. Ghiotti, E. Garrone, Surface Acidity of n-Alumina Part 1.- Pyridine Chemicsorption at Room Temperature, J. Chem. Soc. Faraday Trans. 1. 75 (1979) 271–288.

[200] X. Liu, R.E. Truitt, DRFT-IR Studies of the Surface of γ-Alumina, Jounal Am. Chem. Soc. 119 (1997) 9856–9860.

[201] C. Morterra, A. Zecchina, S. Coluccia, A. Chiorino, No Title, J. Chem. Soc. Faraday Trans. 1. 73 (1977) 1544–1560.

[202] M. Sanchez-Sanchez, R. Navarro, J. Fierro, Ethanol steam reforming over Ni/MxOy–Al2O3 (M=CeM=Ce, La, Zr and Mg) catalysts: Influence of support on the hydrogen production, Int. J. Hydrogen Energy. 32 (2007) 1462–1471.

[203] T. Horiuchi, H. Hidaka, T. Fukui, Y. Kubo, M. Horio, K. Suzuki, et al., Effect of added basic metal oxides on CO2 adsorption on alumina at elevated temperatures, Appl. Catal. A Gen. 167 (1998) 195–202.

[204] N.E. Bogdanchikova, S. Fuentes, M. Avalos-Borja, M.H. Farias, A. Boronin, G. Diaz, Structural properties of Pd catalysts supported on Al2O3-La2O3 prepared by sol-gel method, Appl. Catal. B Environ. 17 (1998) 221–231.

[205] T. Yamamoto, T. Tanaka, T. Matsuyama, T. Funabiki, S. Yoshida, Structural analysis of La/Al2O3 catalysts by La K -edge XAFS, J. Synchrotron Radiat. 8 (2001) 634–636.

[206] V. Gonzalezdelacruz, J. Holgado, R. Pereniguez, a Caballero, Morphology changes induced by strong metal–support interaction on a Ni–ceria catalytic system, J. Catal. 257 (2008) 307–314.

[207] F.-W. Chang, M.-S. Kuo, M.-T. Tsay, M.-C. Hsieh, Effect of calcination temperature on catalyst reducibility and hydrogenation reactivity in rice husk ash–alumina supported nickel systems, J. Chem. Technol. Biotechnol. 79 (2004) 691–699.

[208] M. Wu, D.M. Hercules, Studies of supported nickel catalysts by x-ray photoelectron and ion scattering spectroscopies, J. Phys. Chem. 83 (1979) 2003–2008.

[209] G. Li, L. Hu, J.M. Hill, Comparison of reducibility and stability of alumina-supported Ni catalysts prepared by impregnation and co-precipitation, Appl. Catal. A Gen. 301 (2006) 16–24.

[210] J. Choi, S. Zhang, J.M. Hill, Reducibility and toluene hydrogenation activity of nickel catalysts supported on γ-Al2O3 and κ-Al2O3, Catal. Sci. Technol. 2 (2012) 179.

[211] B. Beguin, E. Garbowski, M. Primet, Stabilization of alumina by addition of lanthanum, Appl. Catal. 75 (1991) 119–132.

[212] L. Wachowski, P. Kirszensztejn, R. Łopatka, B. Czajka, Studies of physicochemical and surface properties of alumina modified with rare-earth oxides I. Preparation, structure and thermal stability, Mater. Chem. Phys. 37 (1994) 29–38.

[213] C. Choong, L. Huanga, Z. Zhonga, J. Lina, L. Hong, L. Chen, Effect of calcium addition on catalytic ethanol steam reforming of Ni/Al2O3: II. Acidity/basicity, water adsorption and catalytic activity, Appl. Catal. A Gen. 407 (2011) 155–162.

[214] V. Guggilla, J. Akyurtlu, A. Akyurtlu, I. Blankson, H2 Production by Autothermal Reforming of n-Dodecane over Highly Active Ru–Ni–Ce–Al2O3 Catalyst, Ind. Eng. Chem. Res. 49 (2010) 8164–8173.

[215] W. Gac, Acid–base properties of Ni–MgO–Al2O3 materials, Appl. Surf. Sci. 257 (2011) 2875–2880.

[216] G. Xu, K. Shi, Y. Gao, H. Xu, Y. Wei, Studies of reforming natural gas with carbon dioxide to produce synthesis gas X. The role of CeO and MgO promoters, J. Mol. Catal. A Chem. 147 (1999) 47–54.

[217] H. Liu, D. He, Properties of Ni/Y2O3 and its catalytic performance in methane conversion to syngas, Int. J. Hydrogen Energy. 36 (2011) 14447–14454.

[218] B. Jang, M. Helleson, C. Shi, A. Rondinone, V. Schwartz, C. Liang, et al., Characterization of Al2O3 Supported Nickel Catalysts Derived from RF Non-thermal Plasma Technology, Top. Catal. 49 (2008) 145–152.

[219] S. Yuvaraj, L. Fan-yuan, C. Tsong-huei, Y. Chuin-tih, Thermal Decomposition of Metal Nitrates in Air and Hydrogen Environments, J. Phys. Chem. 107 (2003) 1044–1047.

[220] S. Mentus, D. Jeli, V. Grudi, Lanthanum Nitrate Dexomposition by both Temperature Programmed Heating and Citrate Gel Combustion Comparative study, J. Therm. Anal. Calorim. 90 (2007) 393–397.

[221] K. Sohlberg, S.J. Pennycook, S.T. Pantelides, The Bulk and Surface Structure of γ-Alumina, Chem. Eng. Commun. 181 (2000) 107–135.

[222] D. Coster, a. L. Blumenfeld, J.J. Fripiat, Lewis Acid Sites and Surface Aluminum in Aluminas and Zeolites: A High-Resolution NMR Study, J. Phys. Chem. 98 (1994) 6201–6211.

[223] X. Liu, DRIFTS Study of Surface of γ -Alumina and Its Dehydroxylation, J. Phys. Chem. 2 (2008) 5066–5073.

[224] C. Wu, P.T. Williams, Effects of Gasification Temperature and Catalyst Ratio on Hydrogen Production from Catalytic Steam Pyrolysis-Gasification of Polypropylene, Energy & Fuels. 22 (2008) 4125–4132.

[225] R. Karamarkovic, V. Karamarkovic, Energy and exergy analysis of biomass gasification at different temperatures, Energy. 35 (2010) 537–549.

[226] C. Dupont, G. Boissonnet, J.-M. Seiler, P. Gauthier, D. Schweich, Study about the kinetic processes of biomass steam gasification, Fuel. 86 (2007) 32–40.

[227] D.G. Roberts, D.J. Harris, Char gasification in mixtures of CO2 and H2O: Competition and inhibition, Fuel. 86 (2007) 2672–2678.

[228] Y. Wang, C.M. Kinoshita, Kinetic Model of Biomass Gasification, Sol. Energy. 51 (1993) 19–25.

[229] A.N. Fatsikostas, X.E. Verykios, Reaction network of steam reforming of ethanol over Ni-based catalysts, J. Catal. 225 (2004) 439–452.

[230] M. Maestri, D. Vlachos, a Beretta, G. Groppi, E. Tronconi, Steam and dry reforming of methane on Rh: Microkinetic analysis and hierarchy of kinetic models, J. Catal. 259 (2008) 211–222.

[231] T. El Solh, K. Jarosch, H. de Lasa, Catalytic Dry Reforming of Methane in a CREC Riser Simulator Kinetic Modeling and Model Discrimination, Ind. Eng. Chem. Res. 42 (2003) 2507–2515.

[232] E. Nikolla, J. Schwank, S. Linic, Comparative study of the kinetics of methane steam reforming on supported Ni and Sn/Ni alloy catalysts: The impact of the formation of Ni alloy on chemistry, J. Catal. 263 (2009) 220–227.

CURRICULUM VITAE

Name: A S M Jahirul Islam Mazumder

Post-secondary Bangladesh University of Engineering & Technology
Education and Dhaka, Bangladesh
Degrees: 2000-2004 B.Sc. in Chemical Engineering

University of Western Ontario
London, Canada
2006-2008 M.E.Sc. in Chemical Engineering

University of Western Ontario
London, Canada
2009-2014 Ph.D. in Chemical Engineering

Honors and Ontario Graduate Scholarships
Awards: 2011-2012

Related Work Research and Teaching Assistant
Experience: University of Western Ontario, London, Canada
2006-2014

Publication:

(a) Articles published in refereed journals

1. Mazumder, J., de Lasa, H., Fluidizable Ni/La$_2$O$_3$-γAl$_2$O$_3$ Catalyst for Steam Gasification of Biomass, *App Catal B Environ* (Accepted # APCATB-D-14-00121R1).

2. Mazumder, J., de Lasa, H., Ni Catalysts for Steam Gasification of Biomass: Influence of La$_2$O$_3$ Loading, *Catal Today* (Accepted # CATTOD 8906).

3. de Lasa, H., Salaices, E., Mazumder, J., Lucky, R., Catalytic Steam Gasification of Biomass: Catalysts, Thermodynamics and Kinetics, *Chem Rev* 111, 5404 (2011).

4. Mazumder, J., Zhu, J-X., Ray, A.K., Optimal Design of Liquid-Solid Circulating Fluidized Bed for Continuous Protein Recovery, *Powder Technol* 199, 32 (2010).

5. Mazumder, J., Zhu, J-X., Bassi, A.S., Ray, A.K., Modeling and Simulation of Liquid-Solid Circulating Fluidized Bed Ion-Exchange System for Continuous Protein Recovery, *Biotechnol Bioeng* 104, 111 (2009).

6. Mazumder, J., Zhu, J-X., Bassi, A.S., Ray, A.K., Multi-Objective Optimization of the Operation of a Liquid-Solid Circulating Fluidized Bed Ion Exchange System for Continuous Protein Recovery, *Biotechnol Bioeng* 103, 873 (2009).

(b) Articles submitted/to be submitted in refereed journals

1. Mazumder, J., de Lasa, H., Ni Catalysts for Steam Gasification of Biomass: Influence of Preparation Conditions, *J Catal* (anticipated submission date: May 20, 2104).

2. Mazumder, J., de Lasa, H., Steam Gasification of Biomass: Thermodynamic Analysis and gasification in a CREC Riser Simulator, Applied *Catalysis B: Environmental* (anticipated submission date: Jun 10, 2014).

3. Mazumder, J., de Lasa, H., Kinetic Modeling of Steam Gasification of Biomass using Ni/La_2O_3-γAl_2O_3, *AIChE Journal* (anticipated submission date: Jun 30, 2014).

(c) Significant conference presentations

1. Mazumder, J., de Lasa, H., *23rd NAM*, Louisville, KY, June 2-7 (2013).

2. Mazumder, J., de Lasa, H., *3rd North American Symp on Chemical Reaction Eng*, Houston, Mar 17-20 (2013).

3. Al-Bogami, S., Mazumder, J., de Lasa, H., *3rd North American Symp on Chemical Reaction Eng*, Houston, Mar 17-20 (2013).

4. Mazumder, J., de Lasa, H., *AIChE Annual Meeting*, Pittsburgh, Oct 28- Nov 02 (2012).

5. Mazumder, J., de Lasa, H., *3rd Int Symp on Chemical Reaction Eng*, Netherlands, Sept 2-5 (2012).

6. Mazumder, J., de Lasa, H., *22nd Can Symp on Catalysis*, Quebec City, May 13-16 (2012).

7. Mazumder, J., Carrillo, D., Salaices, E., de Lasa, H., *22nd NAM,* Detroit, June 5-10 (2011).

8. Mazumder, J., Lucky, R., de Lasa, H., *21st Can Sym on Catalysis*, Banff, May 9-12 (2010).

9. Mazumder, J., Zhu, J., Ray, A., *AIChE Annual Meeting*, Philadelphia, Nov 16-21 (2008).

10. Mazumder, J., Zhu, J., Bassi, A., Ray, A., *CSChE Conf*, Ottawa, Oct 19-22 (2008).